

**Electron Transfer through Thin Organic Films and Highly Curved Donor-Bridge-Acceptor
Molecules.**

by

Andrew Michael Napper

B. Sc. (Hons.), University of Wales, Swansea. U. K., 1996

Submitted to the Graduate Faculty of
Arts and Sciences in partial fulfillment
of the requirements for the degree of
Doctor of Philosophy

University of Pittsburgh

2002

UNIVERSITY OF PITTSBURGH
FACULTY OF ARTS AND SCIENCES

This dissertation was presented

By

Andrew M. Napper

It was defended on

30th August 2002

and approved by

Prof. Kenneth D. Jordan

Prof. Gilbert C. Walker

Prof. Matthew B. Zimmt

Prof. David H. Waldeck

Committee Chairperson

Electron Transfer through Thin Organic Films and Highly Curved Donor-Bridge-Acceptor Molecules.

Andrew M. Napper, Ph. D.

University of Pittsburgh, 2002

Abstract

Electron-transfer rate constants were measured for a variety of molecular systems. The rate constant was found to depend upon the nature of the medium between the electron donor and acceptor moieties. Using a superexchange model to calculate the electronic coupling between donor and acceptor, the effect of orbital energetics was studied. For photoinduced electron transfer, aromatic moieties with large electron affinities promote large electronic coupling magnitudes. In the electrochemical systems studied involving a gold electrode and an immobilized ferrocene tethered alkanethiol, alkane chains were found to be more efficient at promoting electron transfer than chains incorporating ether linkages. This indicates a dominant hole-transfer mechanism for the electrochemical systems. Chemical modification of adjacent diluent alkanethiols also resulted in alteration of the rate constant. This suggests intermolecular interactions are important in electron transfer in these systems.

Acknowledgements.

I'd like to thank the many people who have made this work possible. First and foremost, I must acknowledge the efforts of my advisor: David Waldeck. His door was always open and he was always willing to entertain questions no matter how crazy they may have been. Without his calm manner and scientific integrity, the doctoral years would have been much more difficult.

Of my co-workers, I have many fond memories. The 'original' Waldeck group consisted of Zhe Lin, Yupeng (George) Gu, Natasha Balabai, Alexander Sukharevsky, Hiromichi Yamamoto, and Ian Anthony Read. All the original group members helped to define who I was in the laboratory, and were all willing to put up with my questioning and observations. I am truly grateful towards Ian Read for his many patient hours showing me how to use and optimize the TCSPC system. He really was a patient teacher.

In the latter years, I was able to overlap with some wonderful new researchers. Luckily for me, Haiying Liu had just joined the group as a postdoctoral researcher around about the time I started working on electrochemical systems. He taught me a great deal about the black-art of electrochemistry! It is truly amazing how quickly Haiying was able to synthesize and purify the compounds needed in my electrochemical experiments. In my last few months here, I have also overlapped with Min – a very talented young laser spectroscopist who will no doubt achieve success with the laser system through her patient determination.

My research revolves around the abilities of other people to synthesize and purify the many amazing molecules that we study. Of these people, I would like to thank Dr. Krishna Kumar who first synthesized the molecular C-Clamp A9DCE. This one molecule has proven to be extremely fruitful, resulting in many papers and many more hours of trying to understand the

results of our experiments. Dr. Ruth Kaplan provided even more (milligrams!) of A9DCE, as well as other interesting curved donor-bridge-acceptor molecules. Joceyln Nadeau made a brief appearance in our lab in the June of 2002, bringing with her a few milligrams of an equally interesting DBA type molecule. It was great to finally meet someone from Professor Matthew Zimmt's lab – who have provided us with many hours of entertainment over the years.

Of course, I would be amiss if I didn't thank Professor Matthew Zimmt, or just Matt as he is informally known as in the Waldeck lab. Although I failed to meet him in the many years we were doing experiments on his systems, we have exchanged many, many e-mails over the years in our ongoing efforts to understand these electron transfer systems. We couldn't do it without you!

Last, but by no means least, are my family members who have encouraged me and supported me during my stay here in Pittsburgh. My eldest son, Alex was a mere baby upon first arriving in Pittsburgh in the summer of 1996 – and is now about ready to enter first grade. It's amazing how quickly they grow. His smiles and hugs were of great importance to me. My youngest son, Aaron, was born in the summer of 1999. He has been a constant delight since he was born. My wife, Jennifer. Well – let's just say I couldn't have done it without her. She has been more supportive than I could imagine. My parents, Michael and Maureen, started me off on this wonderful journey and deserve the original credit for all of this. And of course my younger sister, Catherine – who beat me to the mark almost a year ago. Congratulations, Dr. Catherine Napper.

TABLE OF CONTENTS

Chapter 1. Introduction.....	1
1.1 Overview	1
1.2 Marcus Theory	4
1.3 Semi-Classical Theory.....	7
1.4 Photoinduced Electron Transfer.....	11
1.5 Electron Transfer at an Electrode.....	12
1.6 Reorganization Energy	19
1.6.1 Continuum Approaches to $\Delta_r G$ and λ_0	20
1.6.2 Molecular Approach to $\Delta_r G$ and λ_0 :	22
1.7 Electronic Coupling.....	23
Chapter 2. Solvent-Mediated Electronic Coupling: The Role of Solvent Placement	28
2.1 Introduction.....	28
2.2. Experimental Section	33
2.2.1 Materials and Equipment.....	33
2.2.2 Kinetic and Thermodynamic Analyses.....	34
2.3 Analyses.....	40
2.4 Modeling $\Delta_r G(T)$ and $\lambda_0(T)$	48
2.5 Determination of $ V $ and λ_0	53
2.6 Discussion and Conclusion.....	58
2.7 Appendix 2.A.....	61

2.8 Appendix 2.B	63
2.9 References.....	64
Chapter 3. Electron Transfer in Aromatic Solvents: The Importance of Quadrupolar Interactions	67
3.1 Introduction.....	67
3.2 Background.....	72
3.2.1. Continuum Prediction of $\Delta_r G$ and λ_0	72
3.2.2. Molecular Model for $\Delta_r G$	73
3.2.3. Molecular Model for the Reorganization Energy, λ_0	79
3.3 Results and Discussion	81
3.3.1. Calculation of $\Delta_r G$	81
3.3.2. Calculation of the Reorganization Energy.....	88
3.3.3. Fitting the Rate Constants.....	89
3.4 Conclusions.....	96
3.5 Acknowledgment.....	97
3.6 Appendix: Polynomial Forms of the Perturbation Integrals.....	98
3.7 References.....	100
Chapter 4. An Unequivocal Demonstration of the Importance of Nonbonded Contacts in the Electronic Coupling between Electron Donor and Acceptor Units of Donor-Bridge-Acceptor Molecules.....	103

4.1 References.....	111
Chapter 5. Solvent Mediated Coupling Across 1 nm: Not a π Bond in Sight.....	113
5.1 References.....	119
Chapter 6. The Nature of Electronic Coupling between Ferrocene and Gold through Alkanethiolate Monolayers on Electrodes. The Importance of Chain Composition, Interchain Coupling, and Quantum Interference.....	122
6.1 Introduction.....	122
6.2 Experimental.....	127
6.2.1 Reagents.....	127
6.2.2 Electrode Fabrication.....	128
6.2.3 Synthesis of $\text{CH}_3(\text{CH}_2)_4\text{O}(\text{CH}_2)_6\text{SH}$	128
6.2.4 Synthesis of $(\eta^5\text{C}_5\text{H}_5)\text{Fe}(\eta^5\text{C}_5\text{H}_4)\text{CO}_2(\text{CH}_2)_{12}\text{SH}$	128
6.2.5 Synthesis of $(\eta^5\text{C}_5\text{H}_5)\text{Fe}(\eta^5\text{C}_5\text{H}_4)\text{CO}_2(\text{CH}_2)_5\text{O}(\text{CH}_2)_6\text{SH}$	130
6.2.6 Electrochemical Measurements.....	130
6.3 Background.....	131
6.3.1 The electron transfer rate constant.....	131
6.3.2 Obtaining Rate Constants from Voltammograms.....	133
6.4 Results.....	135
6.5 Discussion.....	140
6.6 Conclusions.....	150
6.7 Acknowledgements.....	150

6.8 References.....	151
Chapter 7. Solvent Mediated Superexchange in a C-Clamp Shaped Donor-Bridge-Acceptor Molecule: The Correlation between Solvent Electron Affinity and Electronic Coupling.....	155
7.1 Introduction.....	155
7.2 Background.....	161
7.2.1 Continuum Approaches to $\Delta_r G$ and λ_0	164
7.2.2 Molecular Approach to $\Delta_r G$ and λ_0	165
7.2.3 Internal Reorganization Parameters.....	166
7.2.4 Kinetic Analysis.....	166
7.3 Experimental Section.....	167
7.4 Results and Discussion.....	169
7.4.1 Molecular Model.....	173
7.5 Summary and Conclusions.....	182
7.6 References.....	185
Chapter 8 The Role Played by Orbital Energetics in Solvent Mediated Electronic Coupling.....	188
8.1 Introduction.....	188
8.2 Experimental Details.....	192
8.3 Results and Analysis.....	193

8.4	Calibrating the FCWDS	194
8.5	Experimental Rate Ratios (3:1) for Linear Systems	202
8.6	Experimental Rate Ratios (2:1) for the C-shaped Molecule.....	204
8.7	Origin of the Solvent Dependent Values of $ V(2) $	206
8.8	Discussion.....	208
8.8.1	Characterizing the <i>fcwds</i>	209
8.8.2	The Solvent Dependence of $ V $	213
8.9	Conclusion.....	215
8.10	Acknowledgments.....	215
8.11	References.....	216

Chapter 9. Electron Transfer Reactions of C-shaped Molecules in Alkylated Aromatic Solvents: Evidence that the Effective Electronic Coupling Magnitude Is Temperature-Dependent	220
9.1 Introduction.....	220
9.2 Data, Rate Constant, and Δ_rG Determinations.....	225
9.2.1 Kinetic and Thermodynamic Analyses.....	227
9.3 Rate Constant Temperature Dependence and Possible Explanations	228
9.4 Pros, Cons, and Consequences of the Two Explanations.....	238
9.5 Conclusion.....	247
9.6 References.....	250

Chapter 10. Use of U-shaped Donor-Bridge-Acceptor Molecules to Study Electron Tunneling Through Non-bonded Contacts.....	255
10.1 Introduction.....	255
10.2 Experimental and Computational Details.....	258
10.3 Evaluation of Through-Bond Mediated Electron Transfer	263
10.4 Determination of λ_i and $h\nu$	264
10.4.1 Charge Transfer Spectra	265
10.4.2 Theoretical Calculations	266
10.5 Determination of $\Delta_r G$	270
10.6 Determination of λ_o	274
10.7 Determination of the Electronic Coupling, $ V $	275
10.8 Conclusions.....	284
10.9 Appendix A.....	285
10.10 References.....	289
Chapter 11. Conclusions.....	293
11.1 References.....	297

LIST OF TABLES

Table 1.1 The three common electron transfer motifs in electrochemical systems.....	16
Table 2.1 Kinetic Parameters for 2 in Different Solvents as a Function of Solvent Polarity.....	36
Table 2.2 Solvent Parameters Used in the Matyushov Modeling.....	51
Table 2.3 Best Fit Values for $ V $ and λ_0 Using the Experimentally Determined $\Delta_r G(T)$:	
Method 1	52
Table 2.4 Best Fit $ V $ and $\lambda_0(295)$ Using the Matyushov Model for $\Delta_r G(T)$	52
Table 2.5	63
Table 3.1 Best Fit Parameters Used in $\Delta_r G$ Calibrations.	80
Table 3.2 Solvent Parameters Used in Matyushov Modeling	82
Table 3.3 Diagonal Quadrupole Moment Tensor Components Used To Compute $\langle Q \rangle$	82
Table 3.4 Experimental and Calculated $\Delta_r G$ (eV) at 295 K	85
Table 3.5 Regression Estimates of the Electronic Couplings and Reorganization Energies Obtained Using the Matyushov Solvation Model	92
Table 3.6 Values of the Coefficients for the Polynomial Forms	98
Table 3.7 Individual Contributions to $\Delta_r G$ and λ_0 (All Values in eV).....	99
Table 4.1 Comparison of Rate Constants k_{ET} and Relative Electronic Couplings $ V_{rel} $ in Acetonitrile Solvent at 300 K.	108

Table 5.1 ϵ_S , n_D , EA_V , and k_{CS} for 1 and 2 and k_{DB} at 295 K	114
Table 5.2 Regression Values of $ V $ and $\lambda_S(295\text{ K})$ [$\lambda_S(295\text{ K})$ Predicted by a Two Sphere Continuum Model, for the Same Range of Radii, Are Also Shown]	116
Table 6.1 Kinetic Data for the Four Model Systems	137
Table 6.2 Electronic couplings for the radical cation and anion determined from electronic structure calculations.....	143
Table 6.3 NBO Pathway Decomposition of the Electronic Coupling through Part of the Bonding Orbital Manifold for Two-Model Diradicals.....	146
Table 6.4 Effect of Oxygen Parameters on the Electronic Coupling through the Bonding Orbital Manifold for Two Model Diradicals	148
Table 7.1 Reaction Free Energies $\Delta_r G$, Reorganization Energies λ_o , and FCWDS Are Given at $T = 295\text{ K}$ for the Electron Transfer Reaction Using Different Models	161
Table 7.2 This Data Provides Physical Parameters of the Solvents Used in This Study.....	176
Table 7.3 The Best Fit $ V $, the Electron Affinity EA, and the Ionization Potential IP	177
Table 8.1 Electron Transfer and Donor Only Decay Rate Constants for 1 - 4 in fourteen solvents.	191
Table 8.2 Solvent Properties.....	195

Table 9.1 Calibrated Solvation Model Predictions of $\lambda_s(295\text{ K})$, Its First Derivative, and Experimental Values of $\lambda_s(295\text{ K})$ Determined by Fitting $k_{\text{for}}(T)$ and $k_{\text{back}}(T)$ Data	235
Table 10.1 Selected Data for the Ground and CS States of 4 - 7 and 7' Obtained from Geometry Optimizations at the (U)HF/3-21G Level	262
Table 10.2 Parameters used in the molecular solvation model.	271
Table 10.3 Best Fit $ V $ and $\lambda_o(295\text{ K})$ values for the aromatic systems.....	276
Table 10.4 Free energy and reorganization energies for 1 and 2 in the more polar solvents....	276

LIST OF FIGURES

- Figure 1.1** Chemical structure and CPK rendering of A9DCE, a C-Clamp shaped donor-bridge-acceptor molecule. 2
- Figure 1.2** Chemical structure of three donor-bridge-acceptor molecules studied in this thesis. The R-Group is in direct line-of-sight between a substituted naphthalene electron donor and a dicyanoethylene electron acceptor. 3
- Figure 1.3** A schematic of a mixed self-assembled monolayer on a gold surface. Chemical modification of the alkanethiol molecules allows for the introduction of either an alkane or an ether linkage in the center of the film. Modification of both the electroactive and diluent alkanethiols leads to a change in the electron-transfer rate constant, as determined by cyclic voltammetry..... 3
- Figure 1.4** Non-adiabatic free-energy curves for reactant and product states of an electron transfer reaction are shown..... 4
- Figure 1.5** Non-adiabatic free-energy profiles for reactant (R) and product (P) states are shown as a function of the free energy of reaction. Inset I shows the profile when the reaction lies in the normal region. An increase in reaction driving force, $-\Delta G^0$ lowers the intersection point of the two free-energy curves leading to increased thermal activation for a given temperature. Inset II shows the optimal driving force for the reaction. At this point the free energy of activation is zero. Beyond this driving force, ΔG^\ddagger increases with increasing $-\Delta G^0$, leading to the Marcus inverted region. 6

Figure 1.6 Logarithmic plots of experimental rate constants obtained at room temperature in methyltetrahydrofuran (A), di-*n*-butylether (B), and isooctane (C) versus free energy changes of the electron transfer reactions indicated in the figure (structures are the various acceptors). Solid lines are from the semi-classical equation (eq. 1.7) with the parameters listed in the figures..... 9

Figure 1.7 Comparison of theories with data on *C. Vinosum* cytochrome oxidation. Data are points; various theoretical models yield the curves. Note the nonvanishing rate constant at low temperature. The line indicated by short dashes is the best fit using the semiclassical equation (equation 1.7) with the following parameters: $|V| = 2.4 \times 10^{-3}$ eV, $\lambda_s = 2.10$ eV, $h\nu = 387$ cm⁻¹, $\Delta G^0 = -0.45$ eV, and $S=43.9$. Reproduced from: DeVault, D. *Quantum Mechanical Tunneling in Biological Systems*; Cambridge University Press: Cambridge, 1984. Copyright 1984 Cambridge University Press. 10

Figure 1.8 Energy diagram for electron transfer from an electrode to a redox couple. $f(E)$ represents the density of donor states in the electrode and $D_{ox}(E)$ represents the density of acceptor states for the redox couple. The HOMO and LUMO levels for a typical alkane spacer are also shown in the middle. For an overpotential $\eta = 0$ V, then center of the gaussian distributed acceptor states lies above the Fermi level of the electrode by the reorganization energy, λ 14

Figure 1.9 Synthetic linear sweep voltammograms were generated for the following $\log(v/k^0)$ parameters: $A = -2.0$, $B = -1.0$, $C = 0$, $D = 1.0$, $E = 2.0$, $F = 3.0$. A value of 5.0 s⁻¹ was chosen for k^0 , and λ is 0.8 eV. 18

- Figure 1.10** The frequently used continuum model used to calculate the reorganization energy assumes that the charge separated state can be approximated by two spheres separated by a distance of R_{cc} immersed in a dielectric continuum with a low frequency dielectric constant of ϵ_s and a high frequency dielectric constant equal to the square of the optical refractive index, n^2 . Equation 1.16 assumes a single positive and negative charge is formed and the radius of the electron donor (cation) is r_D and the acceptor (anion) is r_A 20
- Figure 1.11** Another continuum approach used to calculate the reorganization energy and free energy of reaction is to assume the charge separated state can be modeled as a dipole moment embedded in a spherical cavity of radius a_0 which is immersed in a dielectric continuum, with a low frequency dielectric constant of ϵ_s and a high frequency dielectric constant equal to the square of the optical refractive index, n^2 21
- Figure 1.12** The energy diagram for a superexchange interaction given by equation 1.22 is shown. H_{ij} represents the exchange interaction between sites i and j in the system. The coupling pathway shown in the figure using the LUMO levels of the bridge is said to be electron mediated. ϵ_t is the tunneling energy..... 24
- Figure 2.1** A fluorescence decay profile (circles) is shown for A9DCE in mesitylene at 50°C. The instrument function (+) is also shown. The best fit to a double exponential (line) gives $\tau_1 = 0.909$ ns (51.7%); $\tau_2 = 19.3$ ps (48.3%); and a $\chi^2 = 1.5$. The residuals for the fit are also shown. 35
- Figure 2.2** This diagram shows the kinetic scheme used to interpret the fluorescence intensity decay from **2** in the alkylated benzene solvents. 36

Figure 2.3 The temperature dependence of the forward (filled symbols) and backward (open symbol) electron-transfer rate constants are shown. Panel A shows the data for benzene (●,○), toluene (■,□), and mesitylene (▲,△). Panel B shows the data for benzene (●,○), cumene (▼,▽), and triisopropylbenzene (◆,◇). The lines are fits to the data using the Matyushov model for $\Delta_r G(T)$ and $d\lambda_o(T)/dT$ 39

Figure 2.4 The temperature dependence of $\Delta_r G$ for the electron-transfer reaction is shown. Panel A shows the data for benzene (●), toluene (■), and mesitylene (▲). Panel B shows the data for benzene (●), cumene (▼), and triisopropylbenzene (◆). 41

Figure 2.5 This figure illustrates the parameter coupling between $|V|$ and λ_o . Panel A shows the data for benzene (295 K, solid line), benzene (342 K, dashed line), cumene (270 K, dotted line), cumene (345 K, dash-dot line). Panel B shows the data for cumene (270 K, solid line), triisopropylbenzene (260 K, dashed line), triisopropylbenzene (270 K, dotted line), triisopropylbenzene (283 K, dash-dot line). The 270 and 283 K curves overlap in panel B. 45

Figure 2.6 The temperature-dependent values of λ_o that are needed to reproduce the $k_{\text{for}}(T)$. Panel A shows the data for benzene (●,○), toluene (■,□), and mesitylene (▲,△). Panel B shows the data for benzene (●,○), cumene (▼,▽), and triisopropylbenzene (◆,◇). The filled symbols give values of λ_o for $|V| = 6 \text{ cm}^{-1}$. The open symbols give values of λ_o for $|V| = 10 \text{ cm}^{-1}$ for all the solvents except TIP where it was set to $|V| = 1 \text{ cm}^{-1}$ 47

Figure 2.7 The temperature dependence of the forward (filled symbols) and backward (open symbol) electron-transfer rate constants is shown. Panel A shows the data for benzene (●,○), toluene (■,□), and mesitylene (▲,△). Panel B shows the data for benzene (●,○),

<p>cumene ($\blacktriangledown, \triangledown$), and triisopropylbenzene (\blacklozenge, \lozenge). The lines are fits to the data using the Matyushov model for $\Delta_r G(T)$ and $\lambda_o(T)$. The dashed curves show the fits for benzene and the solid curves are for the other solvents.</p>	56
<p>Figure 2.8 The calculated slope of $\ln(k_{\text{for}}(T)\sqrt{T})$ versus $1/T$ is plotted as a function of λ_o for benzene and TIP. The solid curve is for benzene, and the dashed curve is for TIP. The left panel shows the result for 0-0.03 eV. The horizontal line with circles indicates the experimental slope for TIP. The right panel shows the result for 0.04-0.2 eV. The horizontal line with diamonds indicates the experimental slope for benzene.</p>	57
<p>Figure 3.1 Molecular structure of the DBA molecules used in this work.</p>	69
<p>Figure 3.2 Behavior of the polarity response function for the dipole (solid line, $\langle Q \rangle = 0 \text{ D \AA}$) and dipole-quadrupole (dashed line, $\langle Q \rangle = 3 \text{ D \AA}$) models are shown as a function of the solute radius.</p>	76
<p>Figure 3.3 The lines show the temperature-dependent free energies calculated using the dipole model in panel A and the dipole-quadrupole model in Panel B. The solid lines show the predicted free energies in alkylbenzenes, the dashed line shows the predicted free energy in acetonitrile and the dashed-dotted line shows the predicted free energy in benzonitrile. Experimental data is shown for benzene (\bullet), toluene (\blacksquare), cumene(\blacktriangledown), mesitylene (\blacktriangle), TMB (\square) and TIP (\blacklozenge). Note that the y-axis is broken in both plots.....</p>	86
<p>Figure 3.4 Experimental rate data is shown for acetonitrile (O, Panel A) and benzonitrile (\blacklozenge, Panel B). The solid lines represent fits using the free energy and reorganization energy calculated using the dipole-quadrupole model. The dashed lines represent the calculated</p>	

rate constants when the free energies and the temperature dependence of λ_o was calculated using the dipole-quadrupole model but λ_o (295 K) was varied. 91

Figure 3.5 Experimental rate data (k_{et}) are shown for benzene (●), toluene (■), cumene(▼), mesitylene(▲), TMB (□), and TIP (◆). Panel A shows the fits using the free energy and temperature dependence of the outer sphere reorganization energy predicted by the dipole model. Panel B shows the fits using the energies predicted by the dipole- quadrupole model. The dotted curve shows the fit for the benzene data, the solid curve shows the fits for the singly substituted benzenes (toluene and cumene), and the dashed curves show the fits for the triply substituted benzenes (mesitylene, 1,2,4-trimethylbenzene, TIP). In each case, the electronic coupling and reorganization energy at 295 K were fitting parameters.. 93

Figure 3.6 Temperature-dependent electronic couplings are shown. These values are calculated from eq 3.1 using the absolute Δ_rG and λ_o values from the dipole-quadrupole model. Data are shown for benzene (●), toluene (■), cumene (▼), mesitylene (▲), TMB (□), TIP (◆), acetonitrile (O), and benzonitrile (◇)..... 94

Figure 4.1 These plots show the temperature dependence of the ET rate constant k_{ET} in three solvents: acetonitrile (squares), dichloromethane (diamonds), and tetrahydrofuran (circles). The filled symbols represent the data for **1**, the open symbols with an x represent the data for **2**, and the open symbols represent the data for **3**. The lines are linear regression fits to the data. 106

Figure 4.2 This figure shows ball-and-stick renderings of MM2 optimized structures of the DBA molecules **1** and **2**. The phenyl ring of the pendant group in **2** is on the line-of-sight between the donor and acceptor units. 107

Figure 6.1 Schematic illustration of the four systems studied.	126
Figure 6.2 Synthetic linear sweep voltammograms were generated for the following $\log(v / k^\circ)$ parameters: A = -2.0, B = -1.0, C = 0, D = 1.0, E = 2.0, F = 3.0. A value of 5.0 s^{-1} was chosen for k° , and λ is 0.8 eV.....	134
Figure 6.3 This figure shows a typical cyclic voltammogram for the O/A system, at a scan rate of 3200 mV/s. The supporting electrolyte is 1.0 M HClO ₄ , and the surface coverage of electroactive thiols is about 10%.	135
Figure 6.4 Plot of anodic ($E_p - E^\circ$) vs. \log (sweep rate) for all four systems studied. The solid lines are the best fit to the data points using the Marcus model described in the text. λ is taken to be 0.8 eV and $T = 298 \text{ K}$. The data points are from a specific run, and the calculated k° is 52.8 s^{-1} for A/A (filled squares) 37.3 s^{-1} for A/O (open squares), 12.2 s^{-1} for O/A (filled triangles), and 4.4 s^{-1} for O/O (open triangles).....	136
Figure 6.5 This figure shows fits to the peak separation data for A/A using different values of the reorganization energy. The dotted lines show the fits of the rate data to reorganization energies of 0.6 and 1.0 eV at a fixed rate constant of 52.8 s^{-1}	139
Figure 6.6 Panel A shows the four dominant pathways for the all methylene diradical model compound, along with the contribution each one makes to the electronic coupling. Panel B shows the four dominant pathways for the ether linked diradical model compound, along with the contribution each one makes to the electronic coupling. The diagrams are intended to reflect the molecules connectivity, not its stereochemistry.....	145

- Figure 7.1** A fluorescence decay profile is shown for **1** in 2,5-dichlorotoluene at 338 K. The best fit parameters are 311 ps (90%), 11.15 ns (10%) and a χ^2 of 1.14. The top graph plots the residuals for the best-fit decay law (thick line through data points). For clarity, only every tenth data point is plotted here. The inset shows the level kinetics used to interpret these data. 159
- Figure 7.2** This diagram illustrates the energy level scheme that is used in the superexchange model to calculate $|I|$ 160
- Figure 7.3** The experimental $\Delta_r G$ data for 2,5-dichlorotoluene (open squares), 1,2,4-trimethylbenzene (filled squares), toluene (+), benzene (open circle), and mesitylene (open diamonds) are shown here. Panel A shows an expanded view of the data for which experimental $\Delta_r G$ data are available. The best fit predictions from the molecular model are shown as solid lines for each data set (see text for details). Panel B shows the predicted free energies for all the solvents. The long dashed curve is the prediction for benzonitrile, the short dashed curve is the prediction for chlorobenzene, the dotted curve is the prediction for *m*-chlorotoluene, and the dashed-dotted curve is the prediction for *m*-dichlorobenzene. .. 171
- Figure 7.4** The temperature-dependent rate data are fit to the semiclassical expression in each of the solvents. The data are plotted in two panels for clarity, however the axis scales are identical. Part A plots the data for *m*-dichlorobenzene (filled triangles), *m*-chlorotoluene (open triangles), 2,5-dichlorotoluene (open squares), 1,2,4-trimethylbenzene (filled squares), and mesitylene (open diamonds). Part B plots the data for benzonitrile (filled circles), chlorobenzene (filled diamonds), benzene (open circles), and toluene (+). The lines represent best fit curves using the semiclassical equation (see Figure 7.3 for convention on line type)..... 172

- Figure 7.5** The temperature-dependent reorganization energies, predicted by the molecular-based model, are presented here for each of the solvents. The symbol convention is the same as that in Figure 7.4. 179
- Figure 7.6** The inverse of the electronic coupling is plotted as a function of -EA for different solvents. EA values are taken from ref 27. The line represents a best fit to the monosubstituted and di-substituted benzene data (filled circles). The open squares are the trisubstituted benzene data. 181
- Figure 8.1** Panel **A** shows a plot of the Franck Condon Weighted Density of States (FCWDS) calculated for **1** at 295 K using continuum models for $\Delta_r G$ and λ_o vs. the experimental transfer rate constants of **1**. Panel **B** shows a similar plot for **3**. For both panels, the filled circles indicate non-aromatic solvents and the empty circles indicate aromatic solvents. Points for 1,3-dithiolane are not included as ϵ_S of this solvent is unavailable. 199
- Figure 8.2** Plots of calculated continuum FCWDS ratios at 295 K for **3** : **1** (circles, left axis) and **2** : **1** (diamonds, right axis) versus the experimental transfer rate constants for **1**. Filled symbols indicate non-aromatic solvents; empty symbols indicate aromatic solvents. 200
- Figure 8.3** Plots of experimental rate constant ratios $k_{eT}(X) : k_{eT}(1)$ versus the experimental transfer rate constants of **1**. $X = 3$ (circles) and $X = 2$ (diamonds). The solvent corresponding to each pair of points is indicated 202
- Figure 8.4** The reciprocal D/ A coupling magnitude for **2** ($|V(2)|^{-1}$) in each solvent is plotted as a function of the HF 6-31G** LUMO energy of that solvent molecule. 207

Figure 9.1 Fluorescence decay for **1** in 1,3-diisopropylbenzene at 290 K and the best fit to the data (solid line hidden by the raw data). The impulse response function (\times) and the residuals (\square , at top) are also shown. The fitted curve gives rate constants of 814 ps (68%), 17.7 ns (32%), and a χ^2 of 1.08. The inset shows an energy level diagram for the kinetics.

..... 226

Figure 9.2 (Panel A) Charge separation (k_{for} , \circ) and charge recombination (k_{back} , \blacklozenge) rate constants for molecule **1** as a function of temperature in 1,3-diisopropylbenzene. Panel B plots the free energy change for charge separation (k_{for} , \diamond) as a function of temperature for **1** in 1,3-diisopropylbenzene. The solid line represents a best fit of the data to a quadratic equation. 229

Figure 9.3 Plots of the charge separation (k_{for} , \circ) and charge recombination (k_{back} , \blacklozenge) rate constants versus the free energy change for charge separation. To minimize overlap, both plots use the charge separation $\Delta_r G$ as the abscissa. The solid lines were calculated using eq 9.2 assuming $|V| = 2.25 \text{ cm}^{-1}$ and $\lambda_S = 0.033 \text{ eV}$. The dashed lines were calculated using the parametrized Matyushov model to predict $\lambda_S(T)$ and the regression estimates of $|V(T)|$ (see text). 230

Figure 9.4 Correlation between $|V|$ and λ_S for **1** derived from the experimental transfer rate constant at 297 K, where $\Delta_r G = 0 \text{ eV}$ 232

Figure 9.5 Values of $\lambda_S(T)$ obtained from the experimental rate constant data, eq 9.2 and an assumed value of $|V|$. The data in panel A were obtained with $|V|$ set to 2.25 cm^{-1} . The data

- in panel B were obtained by setting $|V|$ equal to 6.0 cm^{-1} . The solid line in panel B shows the $\lambda_S(T)$ prediction from the calibrated Matyushov model..... 234
- Figure 9.6** Values of the electronic coupling for **1** in 1,3-diisopropylbenzene, obtained by fitting the experimental rate constant data using the calibrated Matyushov model to calculate $\lambda_S(T)$, plotted as a function of temperature: (k_{back} , O), (k_{for} , \blacklozenge)..... 237
- Figure 9.7** Examples of rate constant versus reaction free energy plots calculated using a one-quantized mode (—) and a two quantized mode (\square) model. For both models, $|V| = 6 \text{ cm}^{-1}$, $\lambda_S = 0.033 \text{ eV}$, $h\nu_1 = 0.175 \text{ eV}$, $h\nu_2 = 0.087 \text{ eV}$, and the total internal reorganization energy is 0.39 eV . For the two quantized mode calculation, the internal reorganization energies are λ_{ν_1} (0.175 eV mode) = 0.33 eV and λ_{ν_2} (0.087 eV mode) = 0.06 eV . For the one quantized mode calculation, λ_{ν} (0.175 eV mode) = 0.39 eV 240
- Figure 9.8** Temperature dependence of the electronic coupling for **1** in benzene (\blacklozenge), cumene (\square), mesitylene (\bullet), and 1,3,5-triisopropylbenzene (\triangle), obtained by fitting the experimental rate constant data and using the calibrated Matyushov model to calculate $\lambda_S(T)$. Regression lines are drawn through the data for each solvent. The best fit line to the 1,3-diisopropylbenzene $|V(T)|$ data (— —) is reproduced from Figure 9.6. 243
- Figure 10.1** Profiles of the ground (left) and CS (right) optimized geometries for the systems **4** (top) - **7** (bottom) obtained at the (U)HF/3-21G level. 268
- Figure 10.2** The experimental $\Delta_r G$ values are plotted for **1** in toluene (open square) and mesitylene (filled square). The experimental values for **2** in mesitylene are shown as filled

triangles. The lines show the $\Delta_r G$ values predicted for all four aromatic systems by the molecular model with the parameters given in Table 10.2. The experimental values for 2 in toluene could not reliably be determined from the fluorescence lifetime data. The $\Delta_r G$ values predicted by the model for 2 in toluene are indicated by the bottom dot-dashed line. See text for details..... 273

Figure 10.3 Experimental rate data (k_{for}) are plotted versus $1/T$, for 1 in toluene (open square), 1 in mesitylene (filled square), 2 in toluene (open triangle), and 2 in mesitylene (closed triangle). The lines represent the best fits to eq 10.1; see text for details. 278

Figure 10.4 Experimental rate data (k_{for}) are plotted versus $1/T$, for 1 in CH_3CN (open circle), CH_2Cl_2 (open square) and THF (open diamond) and 2 in CH_3CN (filled circle), CH_2Cl_2 (filled square), and THF (filled diamond). The lines represent the best fits to eq 10.1; see text for details. 279

Figure 10.5 A schematic of the potential energy surface for photo-induced electron transfer is shown here. D-A is the ground state surface; $\text{D}^*\text{-A}$ is the locally excited state surface; and $\text{D}^+\text{-A}^-$ is the CS state surface. At the avoided crossing, the energy gap between the locally excited and CS states, ΔE , is twice the electronic coupling matrix element for electron transfer, $|V|$ 281

Figure 10.6 The internal reorganization energy is systematically partitioned between a 1600 cm^{-1} and a 990 cm^{-1} mode. The three-dimensional plot demonstrates the ratio of $|V|$ that is obtained between 1 and 2 for a given percentage of 1600 cm^{-1} mode. The lower frequency mode corresponds to a pyramidalization of the cyanoethylene acceptor group, whereas the higher frequency mode corresponds to a skeletal breathing mode of the naphthalene donor. 283

Chapter 1. Introduction

1.1 Overview

Electron transfer occurs in a number of fundamental processes in nature. The photosynthetic reaction center uses a light driven electron transfer to produce a charge imbalance across a membrane which can subsequently be used to drive a series of reactions resulting in the production of ATP. Electron transfer from metal surfaces to molecular oxygen is responsible for atmospheric oxidation, corrosion. An understanding of how molecular structure influences and controls the electron transfer event is critical to our ability to design and create systems that can mimic nature.

It has long been known that the rate at which electron transfer occurs between electron donor and electron acceptor molecules is related to their separation in space. Large separations typically result in small transfer rate constants, k_{eT} . Empirically, an exponential dependence is often observed

$$k_{eT} \propto \exp(-\beta l) \quad (1.1)$$

where l is the separation and β represents the attenuation factor which is highly dependent upon the chemical structure of the intervening medium. The exponentially decaying electron transfer rate constant is related to the decay of the electronic wavefunction at large distance. Values of β ranging from 0.25 to 2.0 \AA^{-1} have been reported in the literature. Systems containing electron donor and acceptor groups separated by highly conjugated bridges such as $-(\text{C}\equiv\text{C}-\text{C}_6\text{H}_4)_n-$ typically exhibit small attenuation factors and have been termed molecular wires by some researchers.

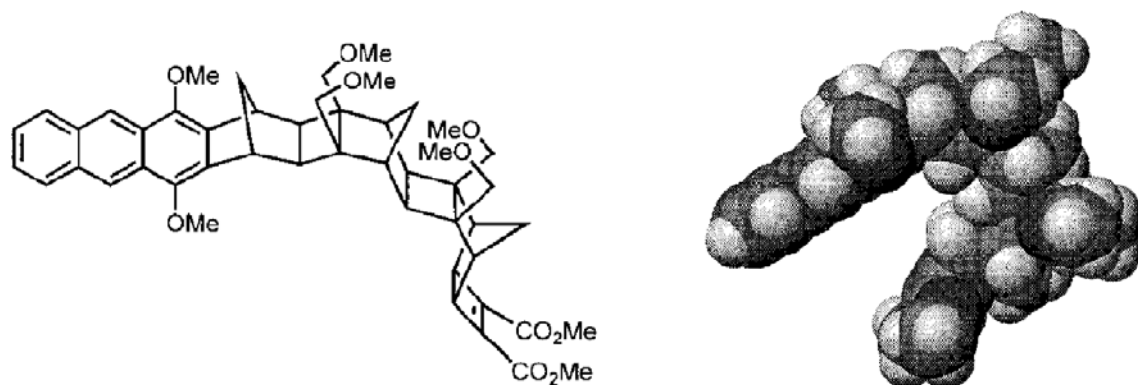


Figure 1.1 Chemical structure and CPK rendering of A9DCE¹, a C-Clamp shaped donor-bridge-acceptor molecule.

The work described in this thesis examines three different electron-transfer systems in detail. Chapters 2, 3, 5, 7, 8, and 9 examine a class of donor-bridge-acceptor molecules in which the bridging group enforces a pronounced curvature upon the molecule. The resulting geometry places an electron donor and acceptor group on either side of a cleft whose size is amenable to occupation by a lightly substituted benzene ring, or a small aliphatic molecule. Occupation of this cleft by solvent molecules results in enhanced electron transfer, presumably due to the possibility of solvent mediated superexchange which enhances the electronic coupling between donor and acceptor groups.

Chapters 4 and 10 deal with another curved donor-bridge-acceptor molecule that has a pendant group in direct line of sight in-between electron donor and acceptor groups. Variations in solvent choice leads to variations in reaction free energies and solvent reorganization parameters, but little or no change in the degree of electronic coupling.

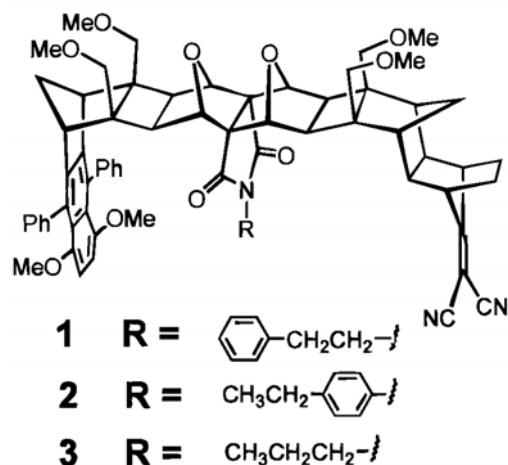


Figure 1.2 Chemical structure of three donor-bridge-acceptor molecules² studied in this thesis. The R-Group is in direct line-of-sight between a substituted naphthalene electron donor and a dicyanoethylene electron acceptor.

Thirdly, Chapter 6 deals with electron transfer from a gold electrode to a ferrocene molecule through a self-assembled monolayer formed from alkanethiols.

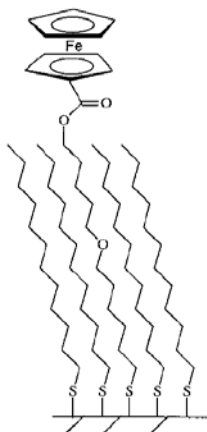


Figure 1.3 A schematic of a mixed self-assembled monolayer on a gold surface. Chemical modification of the alkanethiol molecules allows for the introduction of either an alkane or an ether linkage in the center of the film. Modification of both the electroactive and diluent alkanethiols leads to a change in the electron-transfer rate constant, as determined by cyclic voltammetry.

The chemical structure of the alkanethiol which is covalently attached to the ferrocene group affects the electronic coupling between the gold surface and the ferrocene. Interestingly, there is a subtle but noticeable dependence upon the electronic coupling when adjacent ‘diluent’ alkanethiols are chemically modified. We have attributed this to electron tunneling pathways from the gold to the ferrocene that involve adjacent alkanethiols.

1.2 Marcus Theory

Marcus introduced a description³ of electron transfer reactions in 1956 that sought to quantify the rate at which electron transfer can take place. Two parabolic potential energy surfaces representing the reactant and product state are considered, each one having a curvature related to a parameter λ and a zero-point energy separation equal to ΔG^0 . λ represents the energy

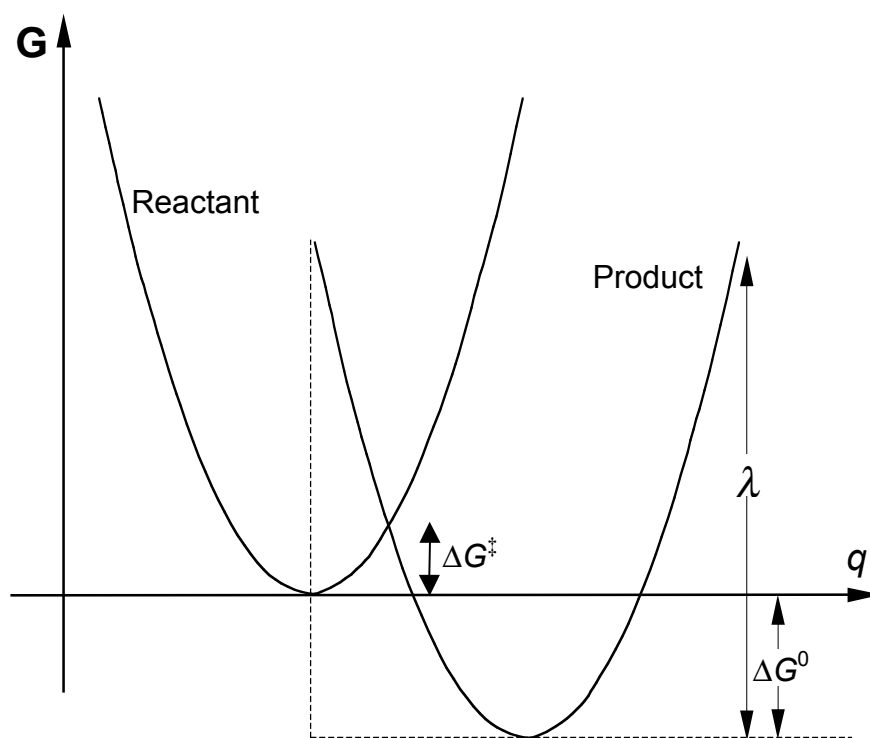


Figure 1.4 Non-adiabatic free-energy curves for reactant and product states of an electron transfer reaction are shown.

required to reorganize the reactant system into the equilibrium geometry of the product without undergoing an electron transfer, and ΔG^0 represents the difference in free energies between the reactant and the product.

The rate of the reaction is determined by the frequency at which the reactant crosses the point of intersection of the two parabolas and the probability that the reactant will transfer from one curve to the other. The electron transfer rate constant can be written as

$$k_{eT} = A \exp \left[-\frac{(\Delta G^0 + \lambda)^2}{4\lambda k_B T} \right] \quad (1.2)$$

for which the free energy of activation energy is

$$\Delta G^* = \frac{(\Delta G^0 + \lambda)^2}{4\lambda} \quad (1.3)$$

The prefactor A is a convolution of the frequency at which the crossing is attempted and the electronic transmission factor, which is close to unity for adiabatic reactions and significantly smaller for nonadiabatic reactions. Equation 1.2 is referred to as the Marcus equation. One of its most famous predictions is the existence of an inverted region, whereupon an increase in the reaction driving force ($-\Delta G^0$) leads to a decrease in the rate of electron transfer.

Figure 1.5 illustrates the turnover from the normal region (whereby an increase in reaction driving force leads to an increase in reaction rate) to the inverted region. Inset I shows the relative positioning of the reactant and product energy curves whilst in the normal region. As the reaction driving force increases, the intersection point between the two curves is lowered and the reaction proceeds at a faster rate. Inset II shows the maximal rate – at this driving force there is no activation barrier and the reaction rate is determined by the prefactor of eq. 1.2.

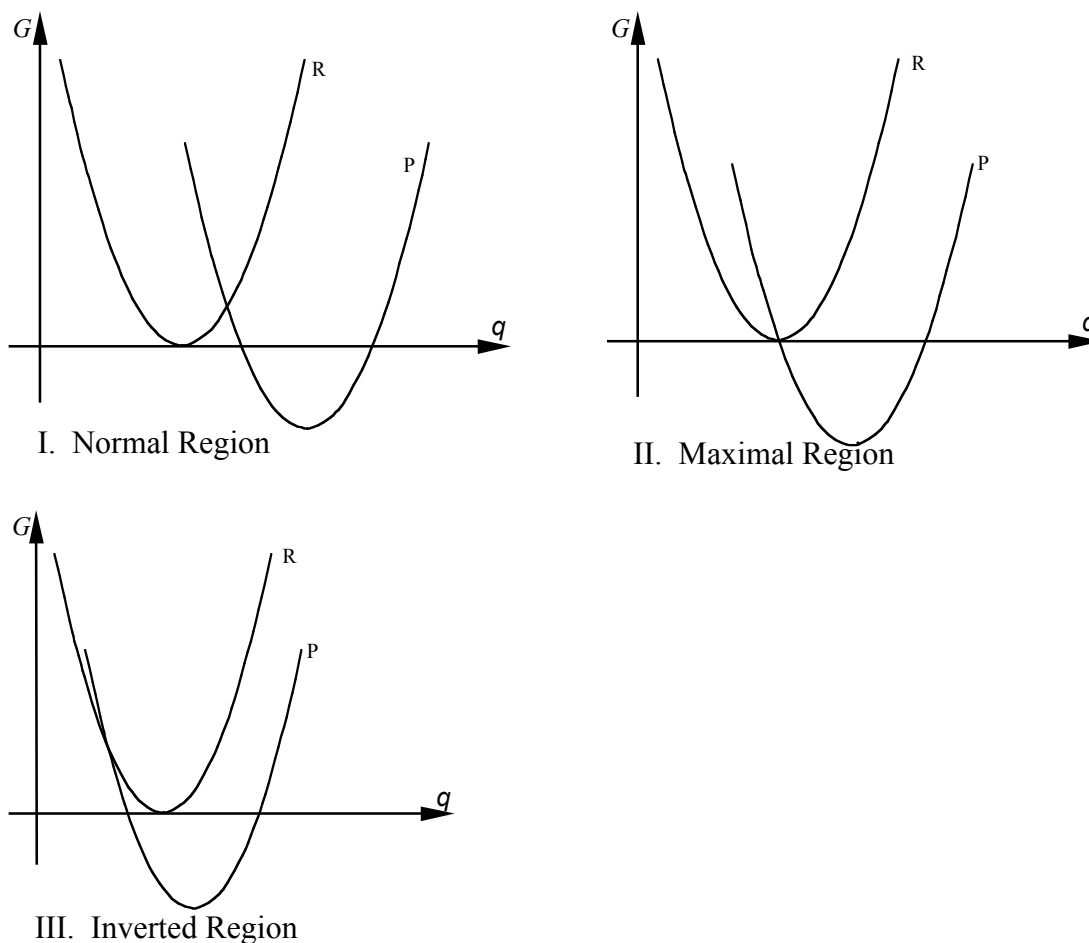


Figure 1.5 Non-adiabatic free-energy profiles for reactant (R) and product (P) states are shown as a function of the free energy of reaction. Inset I shows the profile when the reaction lies in the normal region. An increase in reaction driving force, $-\Delta G^0$ lowers the intersection point of the two free-energy curves leading to increased thermal activation for a given temperature. Inset II shows the optimal driving force for the reaction. At this point the free energy of activation is zero. Beyond this driving force, ΔG^* increases with increasing $-\Delta G^0$, leading to the Marcus inverted region.

Inset III shows the situation when the driving force becomes larger than the reorganization energy, λ . The activation energy barrier now increases with an increasing driving force. Figure 1.5 shows convincing data to support the existence of the inverted region. Although earlier experimental data had hinted at the existence of an inverted region, the experiments had tended to focus on intermolecular electron transfer in solution. For very rapid electron transfer, the

observed rate constant may reach a limiting value. This rate constant, k_{obs} , depends upon the intrinsic electron transfer rate constant, k_{eT} , and the rate of diffusion of the two species to form a precursor complex, $k_{\text{diffusion}}$. The relationship between k_{obs} and k_{eT} is given by equation 1.4

$$\frac{1}{k_{\text{obs}}} = \frac{1}{k_{\text{eT}}} + \frac{1}{k_{\text{diffusion}}} \quad (1.4)$$

For fast electron transfer (when the reaction approaches the maximal region and $k_{\text{eT}} \gg k_{\text{diffusion}}$) the observed rate constant, $k_{\text{obs}} \approx k_{\text{diffusion}}$.

In reality, the simple Marcus relationship given by equation 1.2 predicts a much greater fall off in rate constant in the inverted region than is actually observed. This can be rectified by taking into account nuclear tunneling between the two states, which allows for the reaction to proceed along a non-activated path. The turnover prediction is still present in these quantum mechanical modifications, but not as rapid as the quadratic dependence predicted by equation 1.2. Section 1.3 discusses one of the most frequently applied extensions to the simple Marcus theory (a hybrid of Marcus' classical theory and a quantum mechanical treatment of nuclear tunneling) in more detail.

1.3 Semi-Classical Theory

The Marcus expression has been widely applied and found to be reasonably successful in its native form. Deviations have been observed which have demanded the modification and refinement of the original expression. One problem with the original Marcus expression is the prediction of a vanishingly small rate constant as the absolute temperature approaches zero, however experimental data for systems such as *Chromatium vinosium* clearly exhibit non-zero low temperature rate constants as well as activation energies close to zero in this region (See

Figure 1.7). The Marcus expression also predicts an excessively rapid fall-off in k_{eT} with $-\Delta G^0$ and an exaggerated temperature dependence in the inverted region. The introduction of the possibility of quantum mechanical nuclear tunneling through the barrier leads to a modified expression which accounts for these experimental observations. Nuclear tunneling allows for the possibility of traversing from the reactant state to the product without having the classical energy required to reach the transition state. Nuclear tunneling is a temperature independent process, so at low temperatures there should be little variation in k_{eT} with T . When $-\Delta G^0 > \lambda$ (the inverted region) nuclear tunneling allows for the reaction to proceed without passing through the transition state.

A commonly used description of the electron transfer kinetics assumes that two effective modes are directly coupled to the electron transfer event. The lower frequency mode is typically of low enough energy relative to the thermal bath that it can be treated classically, whereas the higher frequency mode, which is typically of the order of 1000 cm^{-1} must be treated quantum mechanically. The low frequency mode is often assumed to be solvent based, whereas the higher frequency mode is due to intramolecular vibrations. The quantum-classical nature of this expression leads the formulation to be known as the semi-classical expression.

For non-adiabatic electron transfer, the Fermi golden rule expression is used as a basis with which to calculate transition rates between degenerate states. In its simplest form, it can be shown that the transition rate between two degenerate states is given by the following form:

$$k(E) = \frac{2\pi}{\hbar} |V|^2 \rho(E) \quad (1.5)$$

Where $k(E)$ represents the rate of transfer between two degenerate states of energy, E , which are electronically coupled to an extent $|V|$, and whose density of electronic states are $\rho(E)$.

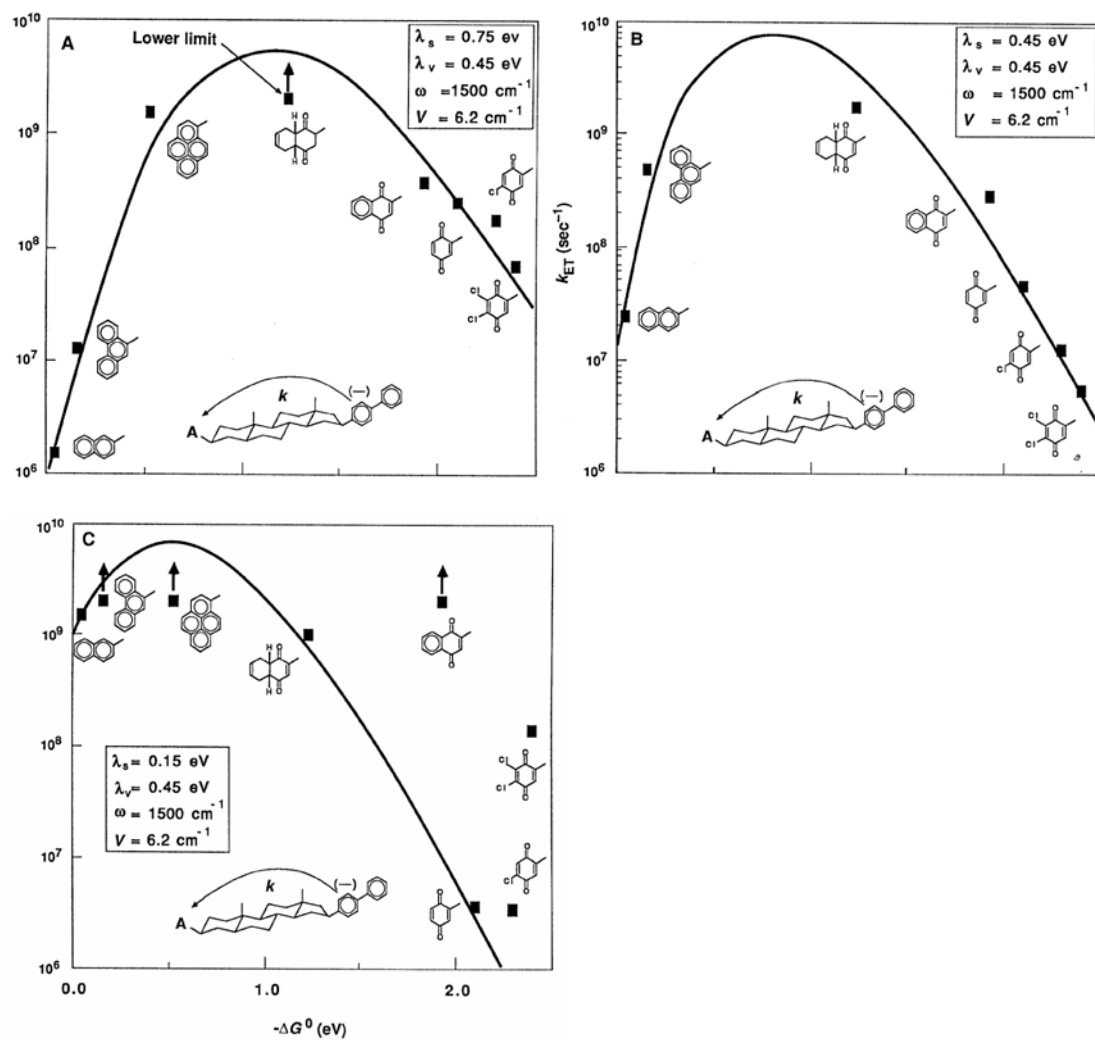


Figure 1.6 Logarithmic plots of experimental rate constants obtained at room temperature in methyltetrahydrofuran (A), di-*n*-butylether (B), and isooctane (C) versus free energy changes of the electron transfer reactions indicated in the figure (structures are the various acceptors). Solid lines are from the semi-classical equation (eq. 1.7) with the parameters listed in the figures.⁴

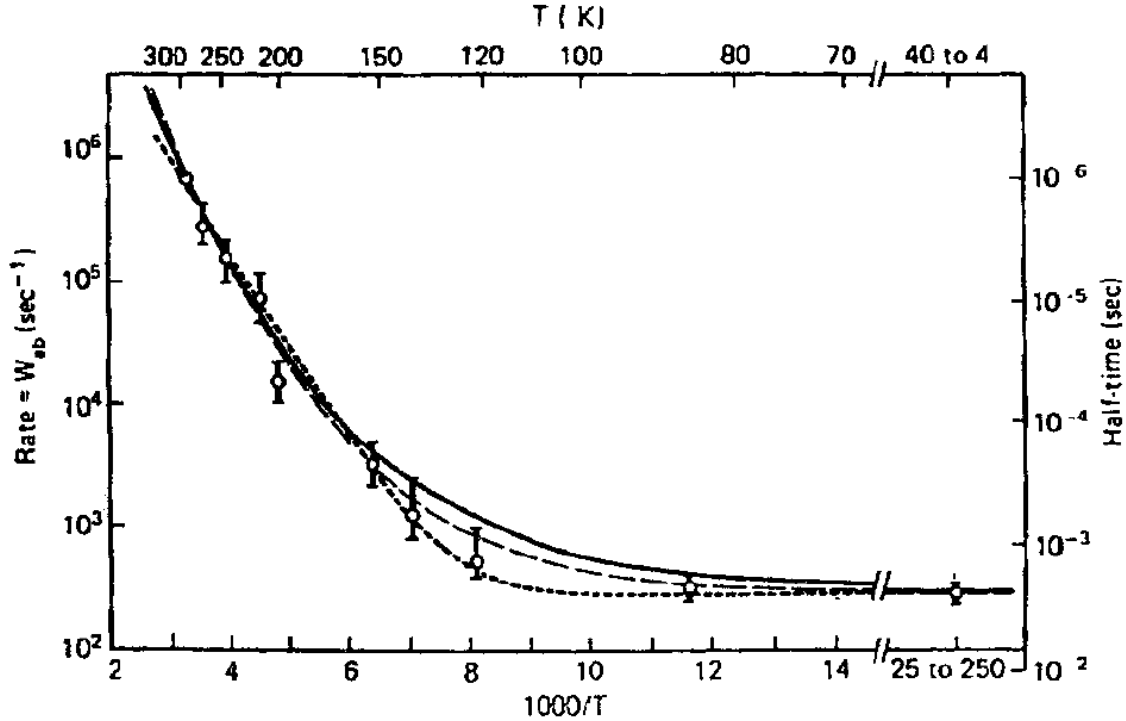


Figure 1.7 Comparison of theories with data on *C. Vinosum* cytochrome oxidation. Data are points; various theoretical models yield the curves. Note the nonvanishing rate constant at low temperature. The line indicated by short dashes is the best fit using the semiclassical equation (equation 1.7) with the following parameters: $|V| = 2.4 \times 10^{-3}$ eV, $\lambda_s = 2.10$ eV, $h\nu = 387$ cm^{-1} , $\Delta G^0 = -0.45$ eV, and $S=43.9$. Reproduced from: DeVault, D. *Quantum Mechanical Tunneling in Biological Systems*; Cambridge University Press: Cambridge, 1984. Copyright 1984 Cambridge University Press.

$\rho(E)$ can be replaced by the Franck-Condon weighted density of states (FCWDS) which is related to the probability that the system reaches the transition state whereupon the donor and acceptor states are isoergic. The following expression ensues:

$$k(E) = \frac{2\pi}{\hbar} |V|^2 \text{FCWDS} \quad (1.6)$$

and the full semi-classical expression for the FCWDS leads to the following

$$k(E) = \frac{2\pi}{\hbar} |V|^2 \frac{1}{\sqrt{4\pi\lambda_0 k_B T}} \sum_{n=0}^{\infty} \frac{e^{-S} S^n}{n!} \exp\left[-\frac{(\lambda_0 + \Delta G^0 + n\hbar\omega)^2}{4\lambda_0 k_B T}\right] \quad (1.7)$$

Where k_B is the Boltzmann constant, T the absolute temperature, λ_o the outer-sphere reorganization energy, ΔG^0 the free energy of charge separation, $\hbar\omega$ the energy spacing of the high frequency mode and S is the Huang Rhys factor given by the ratio of the inner-sphere reorganization energy λ_i to the high frequency energy spacing $\hbar\omega$. Electron transfer is assumed to take place from the lowest vibration manifold of the reactant state. The integer n refers to the vibrational quantum number that the product is formed in.

1.4 Photoinduced Electron Transfer

In order to initiate the electron transfer experiment, it may become necessary to prepare the system in a state that is conducive to charge separation. Some systems require optical absorption, generating an excited state that can undergo electron transfer. The advantage of such systems is the ability to prepare the reactant in a very short time interval by using an ultrafast light pulse. After generation of the reactant state, it is necessary to obtain concentrations of the reactant and product as a function of time in order to determine the kinetics of the electron transfer process. Time-resolved microwave conductivity monitors the concentration of a highly dipolar charge-separated state, with time however the time resolution is poor, typically on the order of a few nanoseconds. Transient absorption is another technique that can be used to generate concentration vs. time data. If the charge-transfer species has an optical absorption that is well separated from the excited state species, then its absorption as a function of time will allow for a concentration vs. time profile to be determined.

Time resolved fluorescence may be used if the initially prepared excited state and/or the charge separated species gives rise to an appreciable fluorescence signature that can be isolated.

For molecules containing both a donor and acceptor group, the fluorescence decay contains contributions from electron transfer as well as other relaxation channels. By monitoring the decay of the excited state in a closely related molecule where the acceptor group has been removed, the rate of relaxation of the excited donor state to the ground state can be determined, and hence the electron transfer rate constant can be calculated. One disadvantage of this technique is the necessity of preparing and measuring the time-resolved fluorescence for a donor-only analog.

1.5 Electron Transfer at an Electrode.

For electron transfer occurring from an electrode to a redox couple located at some distance away from the electrode surface, there must be an overlap between the filled donor electron energy levels in the electrode with the empty acceptor energy levels in the redox couple.

The electron transfer rate constant. As with the unimolecular case, the nonadiabatic electron transfer rate constant k_{et} is given by the *Fermi Golden Rule* expression,

$$k_{\text{et}} = \frac{2\pi}{\hbar} |V|^2 FCWDS \quad (1.8)$$

Equation 1.8 describes the rate of a nonadiabatic transition between two states, with an exchange interaction between the sites of magnitude $|V|$. FCWDS is the Franck-Condon Weighted Density of States and accounts for the impact of nuclear coordinates on the electron transfer rate. When $-\Delta G$ is smaller than the reorganization energy λ (normal region) and high frequency vibrational modes of the donor and acceptor are not a significant part of the reorganization, the FCWDS may be written as

$$FCWDS = \frac{1}{\sqrt{4\pi\lambda k_B T}} \exp\left[-\frac{(\lambda + \Delta G)^2}{4\lambda k_B T}\right] \quad (1.9)$$

The reorganization energy, λ , consists of two components: an inner sphere contribution that is associated with the internal coordinates of the redox species, λ_{in} , and an outer sphere component, λ_{out} , that is dominated by the solvent polarization. For many common redox couples the λ_{out} term is dominant.

Reduction of the redox couple occurs when there is an overlap of the occupied electronic states in the metal with the unoccupied electronic states of the redox couple. By applying an overpotential to the metal electrode, the density of electronic states can be raised in the metal, bringing the Fermi-level of the electrode closer in energy to the unoccupied energy levels of the redox couple acceptor.

For electron transfer at an electrode, equations 1.8 and 1.9 must be generalized to consider the range of electronic states that are available in the solid. For an electron at energy ε in the electrode, the free energy of reaction is given by

$$\Delta G = (\varepsilon_F - \varepsilon) + e\eta \quad (1.10)$$

where η is the overpotential and ε_F is the Fermi level of the electrode. Substitution of eq 1.10 into eq 1.9 generates

$$k_{red}(\varepsilon, \eta) = \frac{2\pi}{\hbar} |V|^2 \frac{1}{\sqrt{4\pi\lambda k_B T}} \exp\left[-\frac{(\lambda + (\varepsilon_F - \varepsilon) + e\eta)^2}{4\lambda k_B T}\right] \quad (1.11)$$

for transfer of an electron from a specific electrode energy state to an electron acceptor.

In the non-adiabatic limit, the rate at which electron transfer occurs from the electrode to the acceptor depends upon the degree of electronic coupling between the filled states in the metal with the unfilled states in the redox couple.

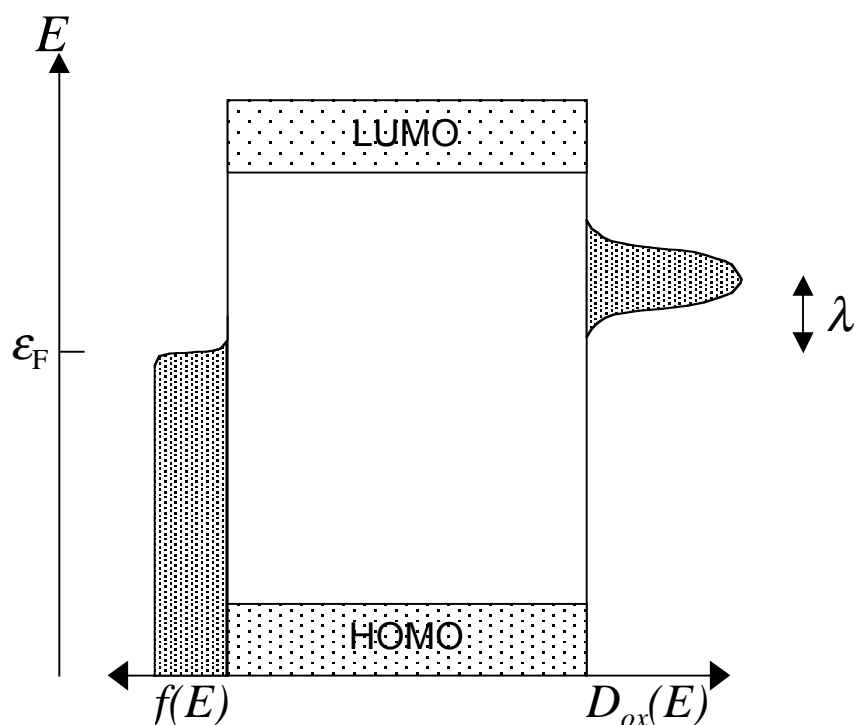


Figure 1.8 Energy diagram for electron transfer from an electrode to a redox couple. $f(E)$ represents the density of donor states in the electrode and $D_{ox}(E)$ represents the density of acceptor states for the redox couple. The HOMO and LUMO levels for a typical alkane spacer are also shown in the middle. For an overpotential $\eta = 0$ V, then center of the gaussian distributed acceptor states lies above the Fermi level of the electrode by the reorganization energy, λ .

The electronic coupling depends upon the orientation and separation of the donor and acceptor moieties, as well as the intervening chemical structure. Although the intervening chemical structure may not allow for a sequential or hopping electron transfer from donor to acceptor, the medium may well promote electronic coupling through a superexchange mechanism, whereby the donor and acceptor wavefunction propagate through the intervening medium, resulting in a much greater electronic coupling compared to the equivalent separation in vacuum.

The rate constant for reduction requires an integration over all energy states of the solid, since electron transfer can in principle occur from any energy level in the donor that is resonant with an empty level on the redox acceptor, so that

$$k_{\text{red}}(\eta) = \frac{2\pi}{\hbar} |V|^2 \frac{1}{\sqrt{4\pi\lambda k_B T}} \int_{-\infty}^{\infty} \rho(\varepsilon) \exp\left[-\left(\frac{(\lambda + (\varepsilon_F - \varepsilon) + e\eta)^2}{4\lambda k_B T}\right)\right] f(\varepsilon) d\varepsilon \quad (1.12)$$

where $\rho(\varepsilon)$ is the density of electronic states of the electrode (often an energy independent average value is used) and $f(\varepsilon)$ is the Fermi-Dirac distribution law

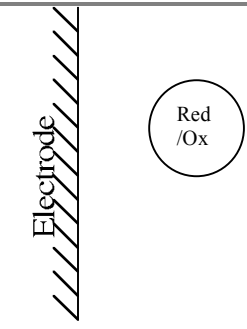
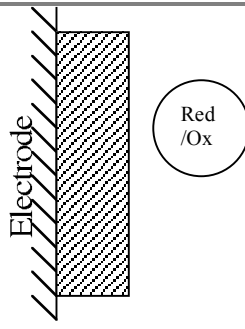
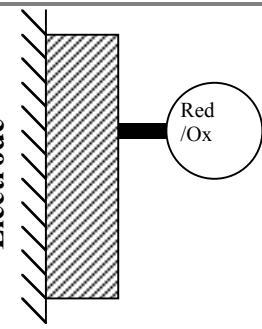
$$f(\varepsilon) = \frac{1}{1 + \exp[(\varepsilon - \varepsilon_F)/k_B T]} \quad (1.13)$$

An expression similar to eq 1.12 can be written for the oxidation current

$$k_{\text{ox}}(\eta) = \frac{2\pi}{\hbar} |V|^2 \frac{1}{\sqrt{4\pi\lambda k_B T}} \int_{-\infty}^{\infty} \rho(\varepsilon) \exp\left[-\left(\frac{(\lambda + (\varepsilon_F - \varepsilon) - e\eta)^2}{4\lambda k_B T}\right)\right] [1 - f(\varepsilon)] d\varepsilon \quad (1.14)$$

Studies of electron transfer at an electrode have typically involved one of three motifs: a bare electrode with a redox couple in solution; a coated electrode with a redox couple in solution; and a coated electrode with a redox couple attached ionically or covalently to the coating.

Table 1.1 The three common electron transfer motifs in electrochemical systems.

		
Type I	Type II	Type III
Freely diffusing No barrier.	Freely diffusing Electrode barrier.	Tethered

Bare electrodes are sensitive to surface contamination which affects the rate at which electron transfer takes place to a redox couple in solution. Because of this electrodes are generally coated in some fashion before the electron transfer experiment takes place. Gold is frequently used for the fabrication of electrochemical electrodes, and has the advantage of forming relatively stable bonds with the sulfur atom of alkanethiols and many other sulfur containing molecules. The surface of a gold electrode is rapidly coated with alkanethiol upon immersion into an ethanolic thiol solution and within a few hours a stable film is formed. A redox couple in solution is now prevented from coming into intimate contact with the electrode surface, and the rate of electron transfer is much slower than with a bare electrode. This is an advantageous occurrence, since rate constants for electrochemical systems are readily measured for a slow transfer.

One problem with coated electrodes is that any imperfection in the coating of the electrode, for example a small area with no coverage (called a pinhole) will lead to the measured electron transfer rate constant being a complicated convolution of the rate constant for transfer through the film and the rate constant for transfer at the pinhole. Rates at pinholes may be many

orders of magnitude faster than through the film, and the measured rate constant will be dominated by this event. The formation of films that are imperfection free (at least to some predefined level) are necessary before rate constants can be reliably correlated to film composition and thickness.

When the redox couple is tethered to the film, the effect of pinholes is effectively muted since the redox couple is no longer free to diffuse and reach the exposed electrode surface. Film defects will still affect electron transfer rates, but to a lesser degree than a freely diffusing redox couple.

One way in which electron transfer rate constants can be measured for redox immobilized species is using cyclic voltammetry. A three electrode setup was used in the studies of electron transfer between gold electrodes and tethered ferrocene self-assembled monolayers (Chapter 6), with a reference electrode (Ag/AgCl), an auxiliary electrode (Pt wire) and a working electrode, consisting of a gold ball electrode with an alkanethiol monolayer containing a terminal ferrocene group to act as the redox couple. The working electrode and the reference electrode are a few mm apart in an aqueous solution consisting of 1.0 M HClO₄. An argon atmosphere is maintained over the electrodes to ensure the elimination of atmospheric oxygen from the solution.

In the cyclic voltammetry experiments, a voltage sweep was typically performed from 0 V to +0.8 V relative to the Ag/AgCl reference. Oxidation and reduction peaks were observed, and at extremely slow voltage scan speeds these lay at the same potential. As the scanning speed was increased, then these peaks moved away from the formal potential, E^0 . For slow electron-transfer rate constants, the bulk of the redox centers will become oxidized or reduced some time after the electrode potential has moved through the formal potential due to a kinetically hindered attainment of thermodynamic equilibrium. This leads to a shift in the peak oxidation or

reduction potential current away from the formal potential. If the rate of electron transfer is fast relative to the speed at which the potential is being scanned, then the peaks will lie much closer to the formal potential since thermodynamic equilibrium is attained much faster.

Electron transfer rate constants can be determined by comparing experimental peak positions with calculations of the curve positions generated by application of equations 1.10-1.14. Full details of this procedure are given in Chapter 6. Figure 1.7 below shows current versus potential calculations at various ratios of k^0 (the electrochemical rate constant for electron transfer at zero overpotential) versus sweep rate, v .

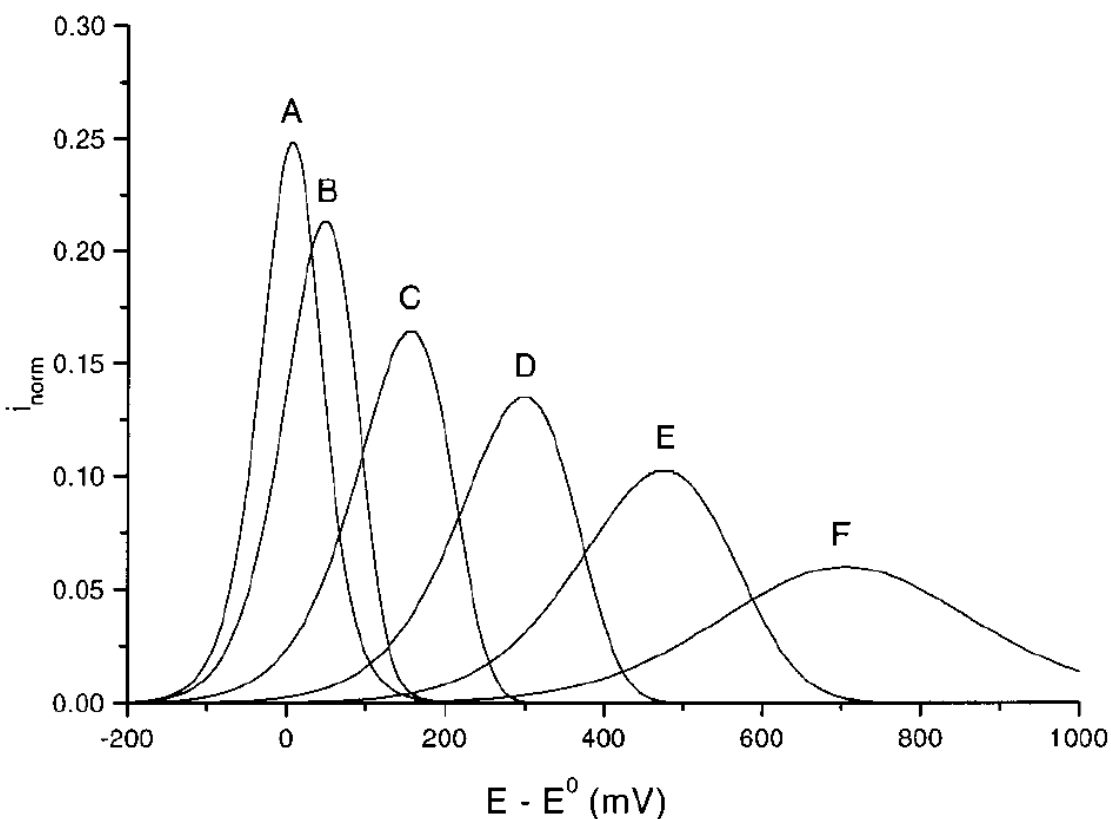


Figure 1.9 Synthetic linear sweep voltammograms were generated for the following $\log(v/k^0)$ parameters: $A = -2.0$, $B = -1.0$, $C = 0$, $D = 1.0$, $E = 2.0$, $F = 3.0$. A value of 5.0 s^{-1} was chosen for k^0 , and λ is 0.8 eV .

1.6 Reorganization Energy

When the reaction driving force is equal to zero in the simple Marcus treatment (equation 1.2) the activation energy takes on a very simple form

$$\Delta G^* = \frac{\lambda}{4} \quad (1.15)$$

The barrier height to electron transfer is exactly one-quarter that of the reorganization energy, λ .

The reorganization energy is related to the need for the reactant's geometry to become distorted from its equilibrium state in order for the system to sample the crossing point of the two diabatic curves of Figure 1.4. The greater the distortion required to approach the crossing point, the greater the reorganization energy. The reorganization energy can be thought of as arising from two distinct contributions: an inner-sphere component, λ_i which arises from a distortion of the normal modes of the reactant molecule about their equilibrium positions, and an outer-sphere reorganization energy, λ_o which arises from polarization changes in the dielectric solvent environment.

The continuum expression for the solvent reorganization energy, λ_o , attending electron transfer between two, initially uncharged, spherical donor and acceptor species is given by equation 1.16,

$$\lambda_o = \frac{e^2}{2} \left(\frac{1}{r_A} + \frac{1}{r_D} - \frac{2}{R_{CC}} \right) \left(\frac{1}{n^2} - \frac{1}{\epsilon_S} \right) \quad (1.16)$$

where r_A and r_D are the effective radii of the acceptor and donor groups, R_{CC} is the center to center charge transfer distance, and $e^2 = 14.4 \text{ eV/\AA}$. The corresponding expression for the free energy change upon electron transfer is given by equation 1.17,

$$\Delta_r G^\circ = E_{\text{OX}} - E_{\text{RED}} - E_{00} - \frac{e^2}{2} \left(\frac{1}{r_A} + \frac{1}{r_D} \right) \left(\frac{1}{\epsilon_{\text{REF}}} - \frac{1}{\epsilon_S} \right) - \frac{e^2}{\epsilon_S R_{\text{CC}}} \quad (1.17)$$

where E_{OX} and E_{RED} are the donor oxidation potential and the acceptor reduction potential, respectively, in a reference solvent (acetonitrile) with static dielectric constant ϵ_{REF} .⁵ E_{00} is the $S_1 - S_0$ energy gap in the solvent of interest, with static dielectric constant ϵ_S .⁶

1.6.1 Continuum Approaches to $\Delta_r G$ and λ_o .

The simplest approach to treating $\Delta_r G$ and λ_o is based on a dielectric continuum model for the solute-solvent interaction.

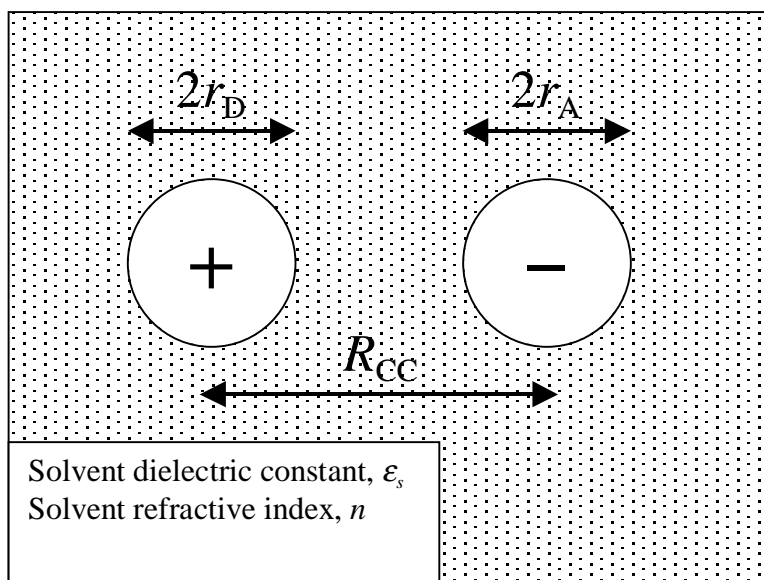


Figure 1.10 The frequently used continuum model used to calculate the reorganization energy assumes that the charge separated state can be approximated by two spheres separated by a distance of R_{cc} immersed in a dielectric continuum with a low frequency dielectric constant of ϵ_s and a high frequency dielectric constant equal to the square of the optical refractive index, n^2 . Equation 1.16 assumes a single positive and negative charge is formed and the radius of the electron donor (cation) is r_D and the acceptor (anion) is r_A .

By modeling the charge separated state as a point dipole μ embedded in a spherical cavity which is further immersed in a dielectric continuum, the continuum reorganization energy λ_o is given by

$$\lambda_{o,\text{cont}} = \frac{\mu^2}{a_o^3} \left(\frac{\varepsilon - 1}{2\varepsilon + 1} - \frac{n^2 - 1}{2n^2 + 1} \right) \quad (1.18)$$

where a_o is the effective cavity radius, ε is the static dielectric constant of the solvent, and n is the refractive index of the solvent. In this same approximation the reaction Gibbs free energy can be written as

$$\Delta_r G = \Delta_{\text{vac}} G - \left[\frac{\mu^2}{a_o^3} \right] \left(\frac{\varepsilon - 1}{2\varepsilon + 1} \right) \quad (1.19)$$

where $\Delta_{\text{vac}} G$ is the reaction Gibbs free energy in the absence of solvation.

Although this continuum treatment of the solute-solvent interaction may be useful in

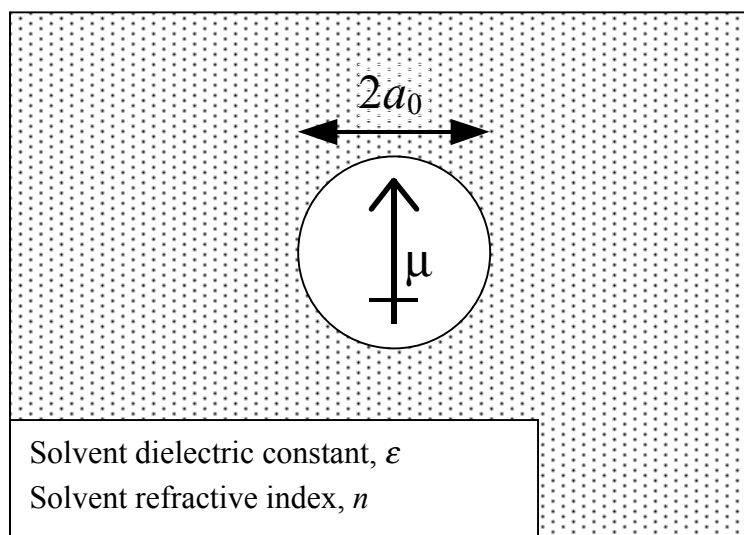


Figure 1.11 Another continuum approach used to calculate the reorganization energy and free energy of reaction is to assume the charge separated state can be modeled as a dipole moment embedded in a spherical cavity of radius a_o which is immersed in a dielectric continuum, with a low frequency dielectric constant of ε_s and a high frequency dielectric constant equal to the square of the optical refractive index, n^2 .

some situations, recent results have shown that a molecular approach provides a superior description, especially in aromatic solvents where quadrupole interactions are important. A number of workers have constructed more elaborate models for the solvent cavity and the medium's dielectric response⁷.

1.6.2 Molecular Approach to $\Delta_r G$ and λ_o :

Molecular based models for solute-solvent interactions are more appropriate than continuum models when weakly polar or nonpolar solvents are employed or when the temperature dependence of the reorganization energy and reaction free energy are needed. Matyushov⁸ has developed a model that treats the solute and solvent molecules as polarizable spheres, with imbedded point dipole moments, and, in the case of solvent, an imbedded point quadrupole moment. The solute dipole moment magnitude μ is given by $\Delta q R_{DA}$, in which Δq is the change in charge and R_{DA} is the charge separation distance. The molecular model treats the reaction free energy as a sum of four components

$$\Delta_r G = \Delta_{\text{vac}} G + \Delta_{\text{dq},i} G^{(1)} + \Delta_{\text{disp}} G + \Delta_i G^{(2)} \quad (1.20)$$

in which $\Delta_{\text{vac}} G$ corresponds to the reaction free energy in a vacuum and the other three terms account for solvation effects. We have shown that the electrostatic and induction terms ($\Delta_{\text{dq},i} G^{(1)}$ and $\Delta_i G^{(2)}$) make the dominant contributions to the solvation free energy and that the dispersion term $\Delta_{\text{disp}} G$ plays a minor part and may be ignored. The reorganization energy was expressed as a sum of three terms

$$\lambda_o = \lambda_p + \lambda_{\text{ind}} + \lambda_{\text{disp}} \quad (1.21)$$

in which λ_p accounts for solvent reorganization arising from electrostatic interactions, λ_{ind} is the contribution from induction forces, and λ_{disp} accounts for dispersion interactions.

One of the main reasons for using a molecular based model rather than the computationally simpler continuum models is that the behavior of the temperature dependence of the continuum models has been shown to be very likely incorrect for certain DBA systems.⁹ The molecular model appears to predict the correct sign for the partial differentials $\frac{\partial \Delta_{\text{rxn}} G}{\partial T}$ and $\frac{\partial \lambda_{\text{out}}}{\partial T}$. For $\Delta_{\text{rxn}} G$, the molecular models are able to reproduce experimental data with sufficient precision by careful adjustment of the various parameters involved, however the absolute value of the reorganization energy is difficult to obtain and typically only the temperature dependence of λ_{out} is used. This may partly be due to the modeling of the solute as a spherical object rather than a more realistic ellipsoid or other such shape.

1.7 Electronic Coupling

The superexchange mechanism, first proposed by McConnell in 1961¹⁰ to explain the electron exchange in α,ω -diphenylalkane anions, is a perturbation treatment for the electronic interaction between molecular subunits. In this treatment the expression for V is given by

$$V = \frac{H_{D1} H_{nA}}{\epsilon_1 - \epsilon_1} \prod_{i=1}^{n-1} \frac{H_{i,i+1}}{\epsilon_i - \epsilon_{i+1}} \quad (1.22)$$

in which n is the number of bridge sites, $H_{i,i+1}$ represents the exchange integral between adjacent bridge sites i and $i+1$, ϵ_i is the energy of bridge site i , H_{D1} is the coupling between the electron donor and the first bridge site, H_{nA} is the coupling between the last bridge site and the electron acceptor, and ϵ_i is the electronic energy at which the electron tunnels from the donor to the acceptor. For identical bridge units, the product in equation 1.22 can be replaced by $(t / \Delta)^{n-1}$

where t is the exchange coupling between adjacent bridge units and Δ is the energy difference between the bridge sites and the tunneling energy. For long bridges, $|V|$ behaves approximately as an exponentially decaying function, so that

$$|V| = |V_0| \exp\left[-\frac{\beta}{2}(n - n_0)\right] \quad ; \quad \frac{\beta}{2} = -\ln\left(\left|\frac{t}{\Delta}\right|\right) \quad (1.23)$$

in which $|V_0|$ would be the coupling in the absence of a bridge and β is the exponential decay parameter (see equation 1.1).

This development of superexchange relies on the nearest-neighbor (tight binding) interactions in order to calculate the electronic coupling through a bridge unit. It has been shown for long bridges that the nearest neighbor coupling is not the dominant coupling mechanism. Indeed, the majority of the interaction arises from pathways (a pathway is a combination of

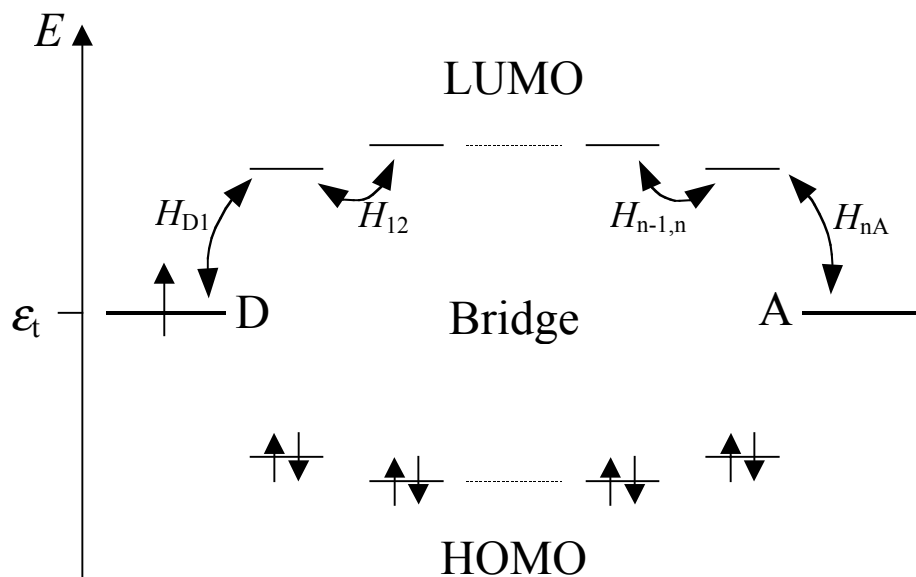


Figure 1.12 The energy diagram for a superexchange interaction given by equation 1.22 is shown. H_{ij} represents the exchange interaction between sites i and j in the system. The coupling pathway shown in the figure using the LUMO levels of the bridge is said to be electron mediated. ϵ_t is the tunneling energy.

exchange interactions that have starting and final points at the donor and acceptor, respectively) that skip over some bonds. If non-nearest-neighbor interactions are considered, many more pathways have to be considered; all of which contribute to the total electronic coupling. It is possible to calculate electronic couplings for all possible routes through a molecule, and the total electronic coupling is equal to the sum of the contributions from each specific pathway.

The contribution to the electronic coupling from a pathway can be either negative or positive and a partial cancellation of contributions from different pathways may occur, destructive interference. Jordan¹¹ and others have discussed the importance of interference for all hydrocarbon systems extensively. Their study gave a distance dependence of $\beta = 0.34$ per methylene as the limiting value ($m > 10$) for hole mediated coupling in molecules of the type: $\text{CH}_2=\text{CH}-(\text{CH}_2)_m-\text{CH}=\text{CH}_2$, whereas bridges of comparable length that contain cyclobutane or norbornane units were shown to have a larger value of β (and smaller electronic coupling). The origin of this difference was shown to lie with the introduction of pathways that destructively interfere for the ring systems.

For the DBA systems studied in this thesis, equation 1.22 can be simplified to consider the case of only one bridging group. For the molecular C-Clamp, A9DCE and related systems, the single bridging group is a solvent molecule. In the pendant U-shaped systems it is a sidechain that is covalently tethered to the U-shaped bridge connecting the donor and acceptor. In this limit, equation 1.22 becomes

$$|V_e| = \frac{H_{DS}H_{SA}}{\Delta_e} \quad (1.24)$$

where Δ_e is the difference in energy between the tunneling D^*SA state and the electron mediated superexchange state $\text{D}^+\text{S}^-\text{A}$. The hole mediated superexchange state, DS^+A^- is not expected to

significantly contribute to the total electronic coupling, $|V|$ from energetic consideration arising from formation of D^+S^-A . This line of reasoning seems to be justified by the strong dependence on the transfer rate when the electron affinity of the solvent bridge (in the C-clamp systems) is varied. The ionization potential of the solvent (which should be related to the stability of the hole-mediated superexchange state) does not seem to have a strong correlation on the overall all magnitude of the electronic coupling extracted from experimental rate constant data.

Stabilization of the electron mediated superexchange state results in a decrease in the denominator of equation 1.24 and hence an increase in $|V_e|$ and a corresponding increase in k_{eT} (assuming $|V_{\text{total}}| \approx |V_e|$). Chapter 7 examines the role of solvent electron affinity for a series of chlorinated aromatic solvents in the C-clamp shaped A9DCE molecule. Chapters 4 and 10 show the dependence of $|V|$ upon the nature of the bridging group when it is covalently tethered, as well as the effect that position of the group has upon $|V|$.

1.8 References.

- (1) Kumar, K.; Tepper, R. J.; Zeng, Y.; Zimmt, M. B. *J. Org. Chem.* **1995**, 60, 4051-4066
- (2) Head, N. J.; Oliver, A. M.; Look, K.; Lokan, N. R.; Jones, G. A.; Paddon-Row, M. N. *Angew. Chem. Int. Ed.* **1999**, 38, 3219.
- (3) a) Marcus, R. A. *J. Chem. Phys.* **1956**, 24, 966; b) Marcus, R. A. *Can. J. Chem.* **1959**, 37, 155; c) Marcus, R. A. *Annu. Rev. Phys. Chem.* **1964**, 15, 155.
- (4) Closs, G. L.; Miller, J. R. *Science* **1988**, 240, 440.
- (5) For the nitroethylene acceptor, $E_{\text{RED}} = -1.29$ V. For the cyclobutenediester, $E_{\text{RED}} = -1.62$ V. The donor $E_{\text{OX}} = 0.87$ V. All potentials measured relative to the Ag/AgCl electrode.
- (6) E_{00} for the S_1 state of the donor varies between 2.98 and 3.04 eV in these solvents. See Kumar, K. Ph.D. Thesis, Brown University, 1995.
- (7) a) Jeon, J.; Kim, H. *J. Phys. Chem. A* **2000**, 104, 9812; b) Zhou, Y.; Griedman, H.; Stell, G. *J. Chem. Phys.* **1989**, 91, 4885.
- (8) Matyushov, D. V.; Voth, G. A. *J. Chem. Phys.* **1999**, 111, 3630.
- (9) Kumar, K.; Kurnikov, I. V.; Beratan, D. N.; Waldeck, D. H.; Zimmt, M. B. *J. Phys. Chem. A* **1998**, 102, 5529.
- (10) McConnell, H. M. *J. Chem. Phys.* **1961**, 35, 508.
- (11) a) Paddon-Row, M. N.; Shephard, M. J.; Jordan, K. D. *J. Phys. Chem.* **1993**, 97, 1743; b) Shephard, M. H.; Paddon-Row, M. N.; Jordan, K. D. *J. Am. Chem. Soc.* **1994**, 116, 5328.

Chapter 2. Solvent-Mediated Electronic Coupling: The Role of Solvent Placement

The role of solvent location in mediating electronic coupling between electron donor and acceptor groups is investigated. The temperature-dependent electron-transfer rate constant in a C-clamp shaped donor-bridge-acceptor (DBA) molecule with a 7-Å donor-to-acceptor separation is used to evaluate the solvent reorganization energy and the electronic interaction between the donor and acceptor sites. By studying the reaction in an homologous series of alkylbenzene solvents, it is demonstrated that the donor-acceptor electronic interaction is greatly reduced in solvents that are too bulky for their aromatic ring to position itself between the donor and acceptor groups. The temperature dependence of the reaction free energy for charge separation, $\Delta_r G$, is directly determined from the experimental data. This allows parametrization of a molecular-based solvation model and provides a means to estimate the outer-sphere reorganization energy and its temperature dependence in aromatic solvents.[§]

2.1 Introduction

Electronic coupling between donor and acceptor sites is a prerequisite for electron-transfer reactions. Covalent bond "mediation" of this coupling is very important for intramolecular electron-transfer reactions, although alternate coupling pathways have been proposed. For example, hydrogen bonds and van der Waals contacts are believed to be important in mediating the electronic coupling for electron-transfer reactions in biomolecules.¹ Recent studies^{2,3,4} have exploited the dependence of bond-mediated coupling magnitudes on the topology of donor-bridge-acceptor (D-B-A) molecules to quantify the relative importance of

[§] Reproduced with permission from Read, I.; Napper, A.; Kaplan, R.; Zimmt, M. B.; Waldeck, D. H.; J. Am. Chem. Soc.; 1999; 121(47); 10976-10986 Copyright 1999 American Chemical Society

coupling pathways involving solvent molecules. Although the latter pathways are usually less important than bond-mediated coupling pathways for electron transfer across linear spacers, pathways involving solvents are expected to be important in intermolecular electron-transfer reactions and for intramolecular electron-transfer reactions involving highly curved spacers.

By studying the kinetics of electron transfer across highly curved donor-bridge-acceptor molecules in strongly polar solvents, it has been possible to demonstrate the participation of solvent in mediating the D-A electronic interaction, a phenomenon referred to as "solvent-mediated superexchange".^{2,3} Detailed analyses of the temperature dependence of the electron-transfer rate constants were used to extract the electronic coupling matrix element, $|V|$, as a function of spacer topology and solvent. These analyses demonstrated a significant enhancement of D-A coupling for the "C-clamp" system **2** in the aromatic solvent benzonitrile, whereas no solvent dependence was found for the "linear" D-B-A molecule **1** (Chart 2.1). Additional evidence for solvent-mediated superexchange in electron transfer across U-shaped intramolecular systems was found by Paddon-Row and co-workers.⁴ Solvent-mediated superexchange coupling in intermolecular electron-transfer reactions has also been identified in fluid solutions by Gould and Farid⁵ and in frozen glasses by Miller.⁶

A deficiency in the earlier studies of **2** is the absence of experimental information that identifies the spatial placement of the solvent molecules most effective at mediating the electronic coupling. Prior theoretical studies indicated that the solvent molecule must lie within the cleft of **2** to produce significant coupling.⁷ Unfortunately, experimental efforts to prove the presence and importance of solvent within the cleft were not successful. As an alternative, this study compares the electronic coupling in solvents that can position an aromatic ring within the cleft interior with those that cannot.

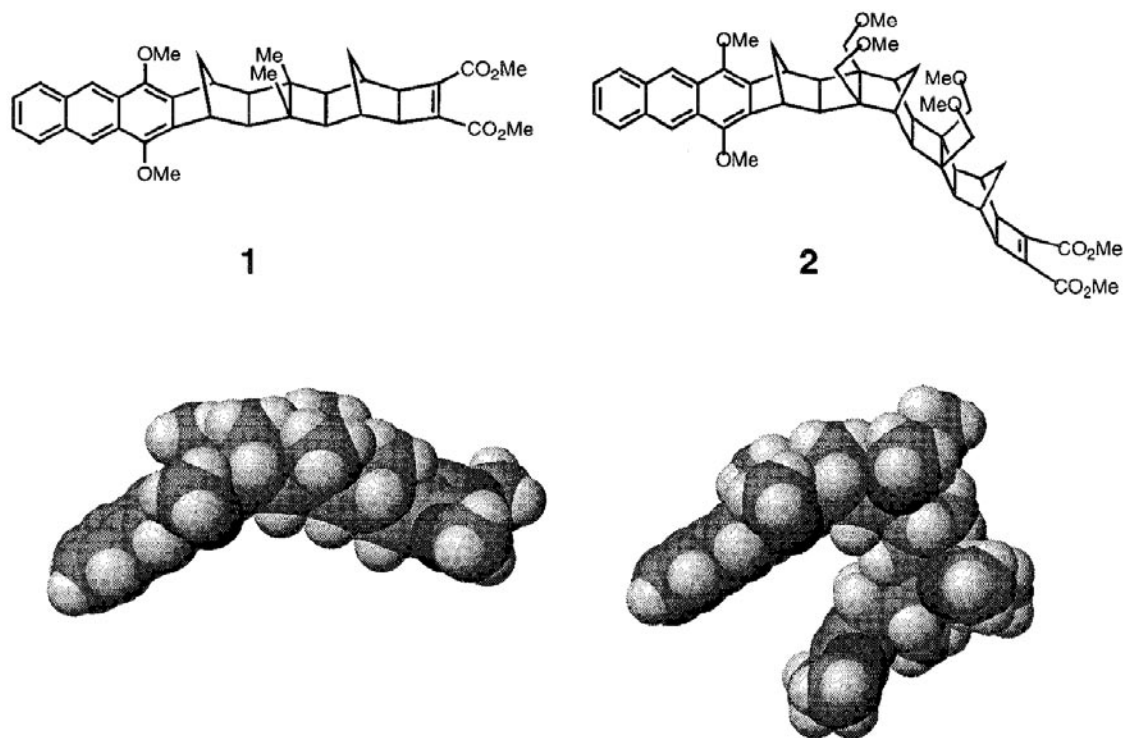


Chart 2.1 Chemical Structures of Donor-Bridge-Acceptor Molecules, A7DCE (1) and A9DCE (2), Are Shown with Their CPK Renderings

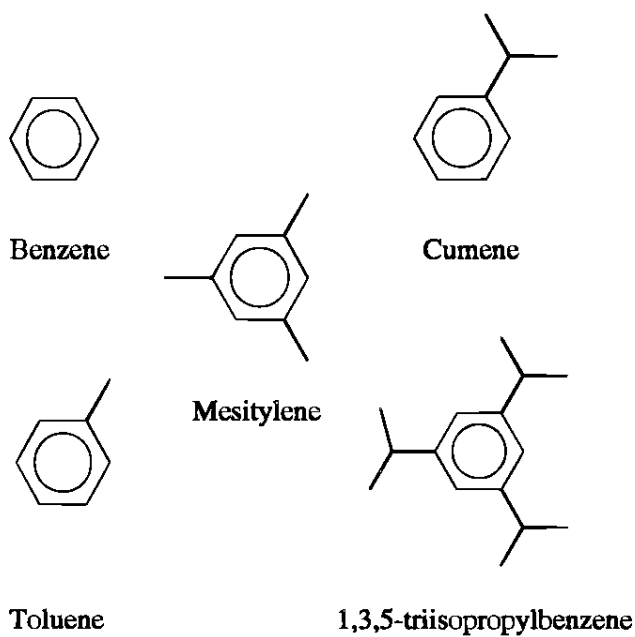


Chart 2.2 Chemical Structures of the Solvents Used in This Work

To this end, electron-transfer rate constants have been determined for **2** in a series of increasingly bulky alkylbenzene solvents (Chart 2.2). Consideration of van der Waals radii and molecular mechanics calculations indicate that benzene and the monoalkylated benzenes can access geometries in which their aromatic core achieves overlap with both the donor and acceptor π -functions of **2**. The steric bulk provided by the isopropyl groups prohibits such simultaneous overlap for 1,3,5-triisopropylbenzene (TIP). The lowest energy conformation of the isopropyl group projects a methyl group above and below the ring plane. The thickness of the molecule is increased in the vicinity of the isopropyl group and this affects the placement of the solvent's aromatic core within the cleft of **2**. Chart 2.3 displays the results of molecular mechanics energy minimizations for **2** with cumene (A) or TIP (B and C). The heavy line connects the 9-position of the anthracene with the acceptor alkene carbon. When the isopropyl group of cumene projects down (Chart 2.3A), the aromatic ring is simultaneously in close proximity to both the anthracene and the alkene acceptor. With TIP, either one isopropyl group (C) or two isopropyl groups (B) must project into the cleft. Although the cleft appears to widen slightly to accommodate this solvent, its aromatic core is significantly further down in the cleft (Chart 2.3B,C) and farther from either the D or A group. If solvent-mediated coupling in **2** requires the solvent's aromatic core to be simultaneously proximate to both the D and A group, the experimentally determined coupling magnitude should decrease with increasing steric bulk of the solvent molecules. This effect has been experimentally observed.

Although the fluorescence decays from **2** in polar solvents^{2,3} exhibited single exponential kinetics, the kinetics observed in these weakly polar aromatic solvents are not single exponential. Instead, they are well fit using biexponential rate expressions.

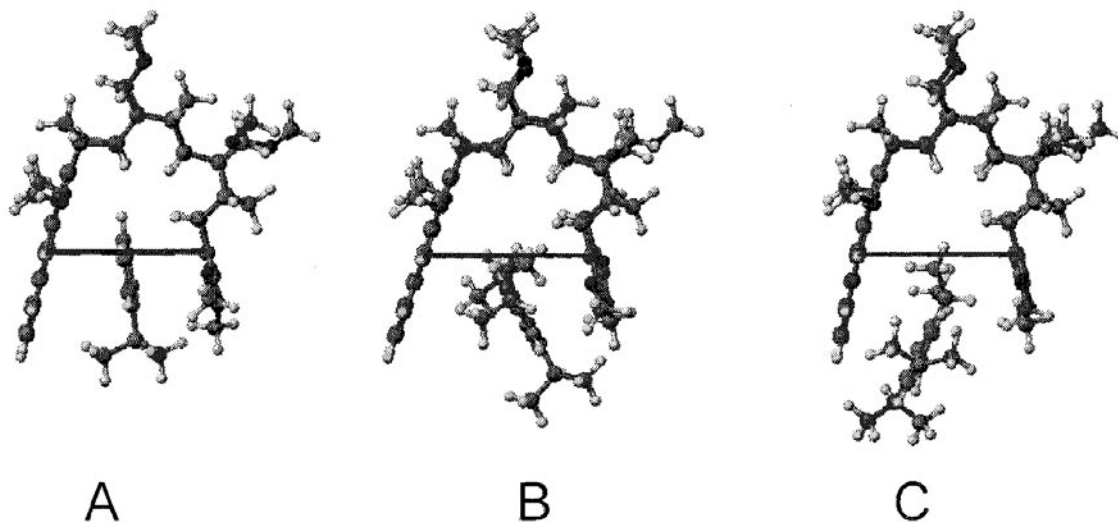


Chart 2.3 Results of Molecular Mechanics Energy Minimizations for **2** with Cumene (A) or TIP (B, C)^a

^a Compound **2** and TIP are displayed as ball and stick renderings. The heavy line connects the anthracene 9 position and the acceptor alkene C.

This feature allows determination of both the forward $k_{\text{for}}(T)$ and reverse $k_{\text{back}}(T)$ electron-transfer rates and, consequently, the free energy of the charge separation reaction, $\Delta_r G(T)$. Direct knowledge of $\Delta_r G(T)$ restricts the number of adjustable parameters in the semiclassical model (eq 2.6) and allows robust conclusions to be drawn concerning the solvent dependence of the electronic coupling. In addition, the experimental $\Delta_r G(T)$ data is used to calibrate a molecular-based model for the solvation energy and the reorganization energy λ_o in weakly polar and nonpolar solvents.⁸ This sophisticated treatment of the outer-sphere reorganization energy produces values that are in reasonable agreement with those extracted from the rate constant data, $k_{\text{ET}}(T)$, assuming temperature independent values of λ_o and the electronic coupling $|V|$.

The paper is organized as follows. Experimental and computational details as well as a general summary of the observations are provided in section 2.2. In section 2.3, the need for temperature-dependent outer-sphere reorganization energy and electronic coupling parameters is

evaluated through analysis of the $k_{ET}(T)$ data with the semiclassical model (eq 2.6) and the experimentally determined $\Delta_r G(T)$. Section 2.4 describes the parametrization of a molecular solvation model using the $\Delta_r G(T)$ data. In section 2.5, the parametrized model is then used to predict the temperature dependence of the outer-sphere reorganization energy and to estimate the electronic coupling. The final section summarizes the findings and draws conclusions.

2.2. Experimental Section

2.2.1 Materials and Equipment.

The preparation of compounds **1** and **2** has been reported elsewhere.⁹ The compounds were stored in a refrigerated desiccator. The optical density of the samples was ~ 0.05 at the excitation wavelength. All solvents were purified in the following manner. First, the solvent was thoroughly washed with concentrated H_2SO_4 until the acid layer remained colorless upon vigorous shaking. Next, the solvent was washed several times with deionized water and dried over $MgSO_4$. Finally, the solvent was fractionally distilled over sodium. In each case, the solvent was freshly distilled for sample preparation. The samples were then freeze-thaw-degassed three times to prevent oxygen quenching of the long lifetime component of the decay law. At higher temperatures, a positive argon (Matheson Inc., 99.99%) pressure was applied to the sample to prevent evaporation of the solvent from the heated section.

The time-correlated single photon counting method was used to measure the fluorescence intensity decays from the locally excited state of the anthracene. The sample was excited by 375-nm radiation from a frequency-doubled 750-nm dye laser pulse. The dye laser pulse train had a repetition rate of ~ 300 kHz and was generated by a cavity-dumped and synchronously

pumped Coherent CR-599 dye laser. The pulse energies were kept below 1 nJ, and the count rates were kept below 4 kHz. All fluorescence measurements were made at the magic angle. Other particulars of the apparatus have been reported elsewhere.¹⁰ The temperature cell was constructed from aluminum and controlled using a NESLAB RTE-110 chiller. Temperature measurements were taken at the sample using a Type-K thermocouple (Fisher-Scientific) accurate to within 0.5 °C.

The fluorescence decays were fit to a sum of two exponential terms using the Marquardt-Levenberg nonlinear least squares algorithm. In each case the decay law was convolved with the instrument response function, measured by scattering from a BaSO₄ colloid, and compared to the observed decay. Fitting to the semiclassical rate equation and the molecular based model calculations of the reorganization energies and reaction free energies were performed using Microsoft Excel 7.0. The FCWDS sum in eq 2.6 converges rapidly and was not evaluated beyond the sixth term.

2.2.2 Kinetic and Thermodynamic Analyses.

In prior studies involving polar solvents,^{2,3} the time evolution of the anthracene's lowest excited state (LE) fluorescence was adequately described by a single-exponential decay law. This indicated irreversible electron transfer to the acceptor; i.e., generation of the charge transfer state (CT). By contrast, in nonpolar solvents, the decay of the LE state is found to exhibit a double exponential decay law.¹¹

Table 2.1 displays lifetime parameters determined at selected temperatures in the alkylated benzene solvents.

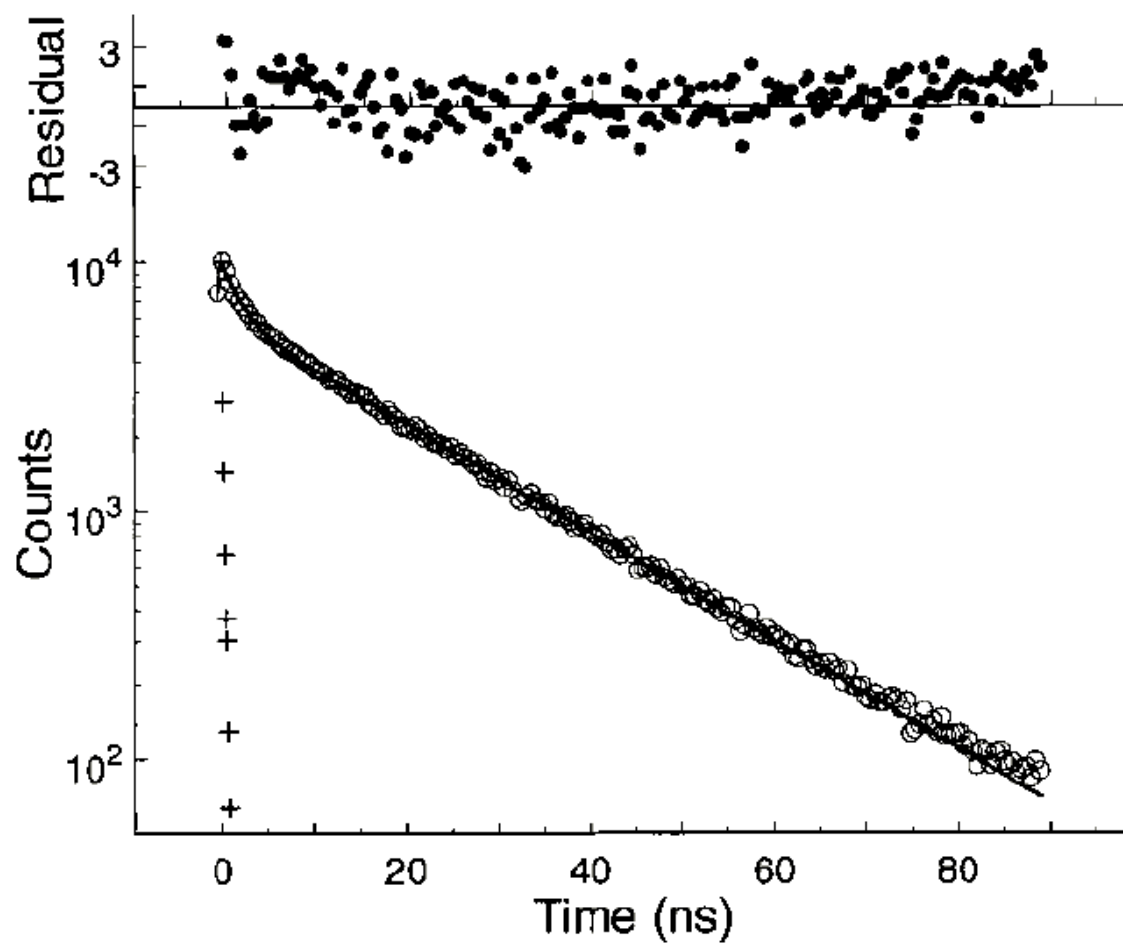


Figure 2.1 A fluorescence decay profile (circles) is shown for A9DCE in mesitylene at 50°C. The instrument function (+) is also shown. The best fit to a double exponential (line) gives $\tau_1 = 0.909$ ns (51.7%); $\tau_2 = 19.3$ ps (48.3%); and a $\chi^2 = 1.5$. The residuals for the fit are also shown.

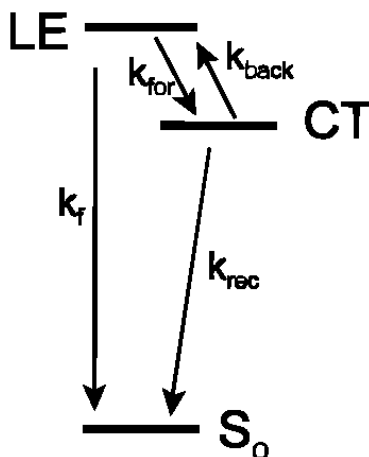


Figure 2.2 This diagram shows the kinetic scheme used to interpret the fluorescence intensity decay from **2** in the alkylated benzene solvents.

Table 2.1 Kinetic Parameters for **2** in Different Solvents as a Function of Solvent Polarity^a

solvent	τ_1 , ps (A_1)	T , K	V , Å ³	ϵ_s	n^2
benzene	325 (99%)	296	148	2.27	2.25
benzene	409 (90%)	342	148	2.19	2.18
toluene	371 (97%)	296	176	2.38	2.24
toluene	463 (69%)	347	176	2.26	2.15
cumene	586 (90%)	296	232	2.38	2.22
cumene	746 (47%)	345	232	2.28	2.13
mesitylene	678 (82%)	296	231	2.27	2.25
mesitylene	909 (52%)	323	231	2.27	2.25
TIP	3260 (68%)	260	397	2.29 ^c	2.26 ^d
TIP ^b	1720 (51%)	283	397	2.27 ^c	2.23

^a The long component time constant is 15–25 ns in each case. ^b TIP is 1,3,5-triisopropylbenzene. ^c The static dielectric constant for triisopropylbenzene could not be found in the literature. The value given here is that of triethylbenzene. ^d Experimentally determined.

For the aromatic solvents other than TIP, increasing the number or size of the alkyl groups on the benzene core, or increasing the sample temperature, generates an increase in the value of the fast component lifetime and a decrease in the fast component amplitude, a_+ . Qualitatively, this suggests that the charge separation rate constant decreases with increasing temperature or with increasing alkyl substitution of the benzene ring. To quantify these variations, the solvent and

temperature dependence of the decay parameters were interpreted using the kinetic scheme illustrated in Figure 2.2, where k_{for} is the forward (charge separation) electron-transfer rate constant (LE \rightarrow CT), k_{back} is the reverse electron-transfer rate constant (CT \rightarrow LE), k_{rec} is the sum of the rate constants for irreversible recombination to lower energy electronic states (CT \rightarrow S₀, T₁) and k_{f} is the observed decay rate of the LE state in the absence of an electron acceptor. With the reasonable assumption that light excitation populates only the locally excited state and that only emission from this state is observed, one obtains a double exponential decay law for the fluorescence $I(t)$ given by

$$I(t) = a_+ \exp(-k_+ t) + (1 - a_+) \exp(-k_- t) \quad (2.1)$$

where a_+ is the fraction of the fluorescence decaying with the fast rate constant k_+ and where k_- is the rate constant of the slow fluorescence decay. These parameters are related to the fundamental molecular rate constants by the following relations:

$$k_{\text{for}} = a_+(k_+ - k_-) + k_- - k_{\text{f}} \quad (2.2)$$

$$k_{\text{back}} = \frac{(k_+ - k_-)^2 - [2(k_{\text{for}} + k_{\text{f}}) - (k_+ + k_-)]^2}{4k_{\text{for}}} \quad (2.3)$$

and

$$k_{\text{rec}} = k_+ + k_- - k_{\text{f}} - k_{\text{for}} - k_{\text{back}} \quad (2.4)$$

The value of k_{f} is obtained from measurements of the donor-bridge compound and is very close to $5 \times 10^7 \text{ s}^{-1}$ in all the solvents at every temperature. The value of k_- (see footnote a to Table 2.1) was found to vary by as much as 50%, depending on the concentration of trace impurities in the solution. Fortunately, the values of k_{for} and k_{back} depend only weakly on the slow rate constant (as it is much smaller than k_+). The scatter in k_- does generate considerable uncertainty

in k_{rec} , however. For this reason only the rate constants k_{for} and k_{back} are compared with the electron-transfer rate theory.

The temperature dependence of the rate constants for the forward (filled symbols) and backward (open symbols) excited-state electron-transfer reactions are plotted in Figure 2.3. Figure 2.3A displays the data for the methyl-substituted benzenes, and Figure 2.3B displays the data for the isopropyl-substituted benzenes. The lines drawn in the graph represent fits to the semiclassical electron-transfer rate equation (vide infra). In the unsubstituted and singly substituted benzene solvents, the charge separation rate constants, k_{for} , exhibit an apparent negative activation energy, whereas the excited-state charge recombination rate constants, k_{back} , exhibit an apparent positive activation energy. In the trisubstituted solvents, the temperature dependence of k_{for} and k_{back} are more complex. In mesitylene, the slope $d(\ln k_{\text{for}})/dT$ becomes increasingly negative with increasing temperature. At low temperatures, k_{back} increases with increasing temperature, but at higher temperatures, k_{back} becomes temperature independent. In triisopropylbenzene, both k_{for} and k_{back} increase with temperature. This observation of apparent positive activation energies for both the charge separation and recombination steps is unique among the five aromatic solvents investigated. The amount of scatter in the TIP data is greater than in the other solvents because the two rate constants for the fluorescence decay are more similar in magnitude, making it more difficult to extract the rate constants reliably. The two decay components are similar because the values of k_{for} and k_{back} are smaller in TIP as compared to the other solvents (Table 2.1). Nonmonotonic and "negative" temperature dependence of electron-transfer rate constants of DBA systems in nonpolar and weakly polar solvents have been reported by other workers.¹¹ These observations may be explained, in part, by consideration of the temperature dependence of the LE \rightarrow CT free energy difference.

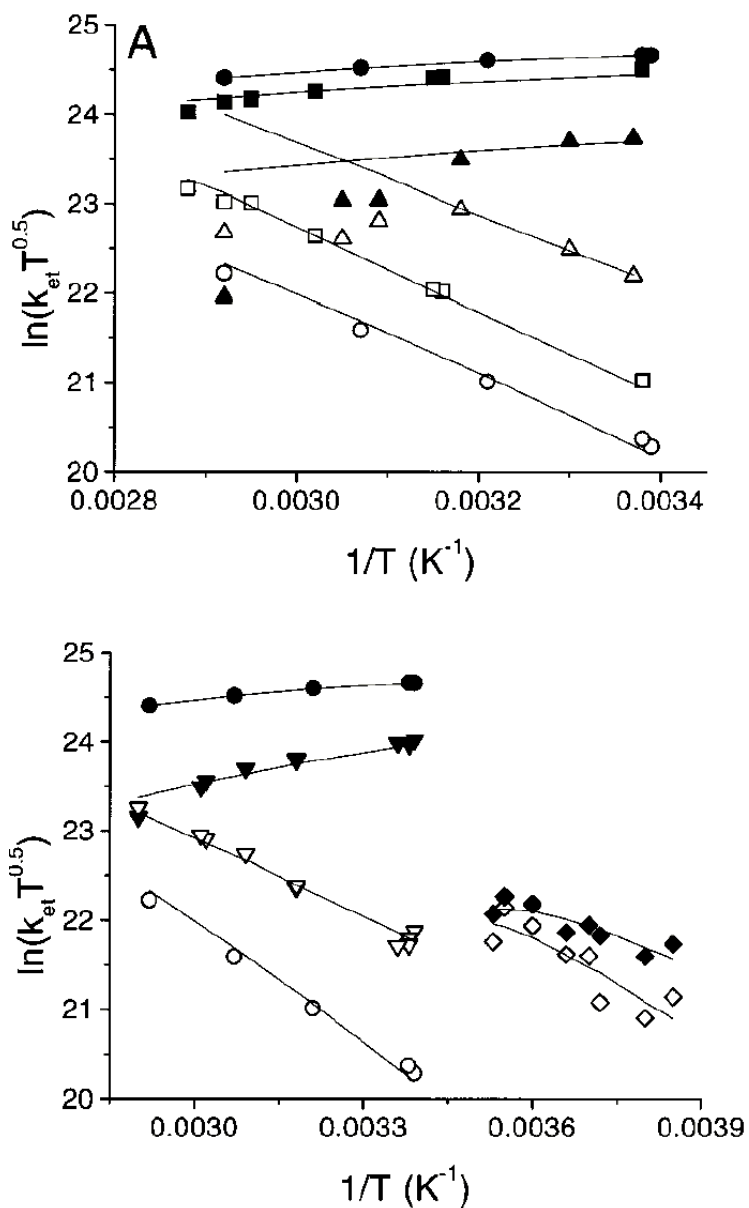


Figure 2.3 The temperature dependence of the forward (filled symbols) and backward (open symbol) electron-transfer rate constants are shown. Panel A shows the data for benzene (●,○), toluene (■,□), and mesitylene (▲,△). Panel B shows the data for benzene (●,○), cumene (▼,▽), and triisopropylbenzene (◆,◇). The lines are fits to the data using the Matyushov model for $\Delta_{\text{r}}G(T)$ and $d\lambda_0(T)/dT$.

The value of $\Delta_r G$ (LE \rightarrow CT) at each temperature was computed from the ratio $k_{\text{for}}/k_{\text{back}}$ (Figure 2.4). In each solvent, $\Delta_r G$ increases with increasing temperature; i.e., the charge transfer state is destabilized upon increasing the temperature. The entropy change upon charge separation, $\Delta_r S$, is quite negative, e.g. -22 and -26 cal/(mol K) in benzene and in cumene, respectively. Continuum models (Born, Onsager)¹² and molecular models of solvation⁸ both predict the negative sign of $\Delta_r S$. However, simple continuum models predict that $\Delta_r G$ in benzene should be more positive than in either toluene or cumene, in contrast to the experimental results. This contradiction is one of numerous examples¹³ that highlight the inability of simple continuum models to predict or rationalize solvation in nonpolar solvents. In an effort to view these results within the framework of a reasonable theory, a molecular model for solvation, developed by Matyushov⁸ for dipolar, polarizable, hard-sphere solvents, is employed. As will be described in section 2.4, this theory reproduces the solvent and temperature variations of $\Delta_r G$ and provides some guidance as to the temperature dependence of the outer-sphere reorganization energy.

2.3 Analyses

A. Kinetic Models. The donor-acceptor electronic coupling for **2** in the aromatic solvents is much smaller than kT and lies in the nonadiabatic, or weak, coupling regime.¹⁴ In this case, the electron-transfer rate constant may be expressed in terms of the Golden Rule formula:

$$k_{\text{ET}} = \frac{2\pi}{\hbar} |V|^2 \text{FCWDS} \quad (2.5)$$

where $|V|$ is the magnitude of the electronic coupling between the donor and acceptor groups and *FCWDS* is the Franck-Condon Weighted Density of States.

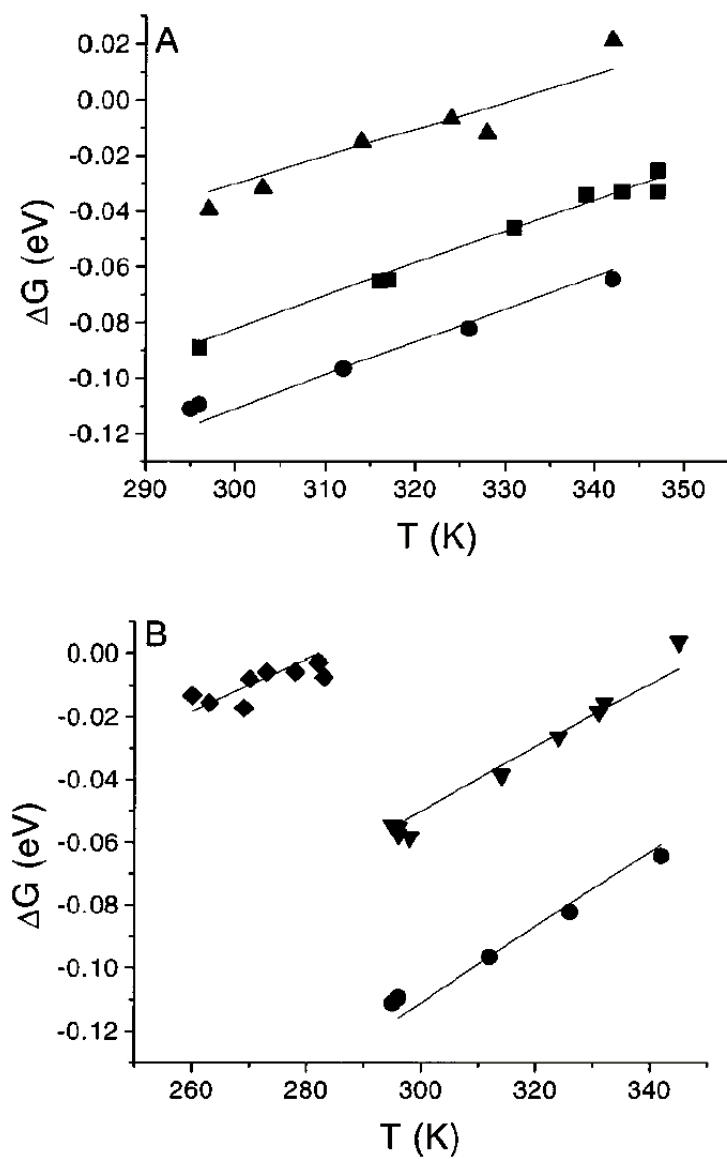


Figure 2.4 The temperature dependence of $\Delta_r G$ for the electron-transfer reaction is shown. Panel A shows the data for benzene (●), toluene (■), and mesitylene (▲). Panel B shows the data for benzene (●), cumene (▼), and triisopropylbenzene (◆).

The *FCWDS* factor accounts for the impact of nuclear coordinates on the electron-transfer rate. As discussed for this DBA system **3** and related ones,^{2,4} a semiclassical expression with a single quantized mode provides an adequate description of the rate constant. In particular,

$$k_{\text{ET}} = \frac{2\pi|V|^2}{\hbar\sqrt{4\lambda_o\pi k_B T}} \sum_{n=0}^{\infty} e^{-S} \left(\frac{S^n}{n!}\right) \exp\left[\frac{-(\Delta_r G + \lambda_o + nh\nu)^2}{4\lambda_o k_B T}\right] \quad (2.6)$$

where k_B is Boltzmann's constant, λ_o is the outer-sphere (or solvent) reorganization energy, ν is the frequency of the effective quantized vibrational mode, $\Delta_r G$ is the reaction free energy, and S is the Huang-Rhys factor defined by

$$S = \frac{\lambda_v}{h\nu} \quad (2.7)$$

in which λ_v is the inner-sphere reorganization energy. The total reorganization energy $\lambda = \lambda_v + \lambda_o$ represents the change in energy if the reactant were to change to the equilibrium configuration of the product without transferring an electron. This model for the rate constant has been widely successful in describing intramolecular electron-transfer processes.^{15,16}

The rate expression in eq 2.6 has five parameters: $\Delta_r G$, λ_v , λ_o , ν , and $|V|$. As noted above, the value of $\Delta_r G$ at each temperature can be obtained directly from the data. The inner-sphere reorganization energy λ_v and the characteristic vibrational frequency ν were previously determined by fitting charge-transfer spectra for a related system (same donor and acceptor units but a shorter bridge unit) and by quantum chemical calculations.³ Those studies found that $\lambda_v = 0.39$ eV and $h\nu = 0.175$ eV were reasonable parameter values. These two quantities reflect the changes in the nuclear arrangement of the anthracene upon oxidation and of the acceptor upon reduction. As such, one expects the two parameters to remain nearly constant with changes in the bridge that are remote from the D or A group, or with changes in the solvent.³ One potential

caveat is raised by the recent computational work of Paddon-Row¹⁷ which suggests that the D-A separation (in vacuo) changes significantly in the Coulomb field of the charge separated state. For **2**, such distortions could result in different $|\Delta_r G|$, λ_v , λ_o , and $|V|$ for the forward and back electron-transfer steps. We have found no particular evidence supporting this behavior in these solvents. Thus, two parameters, $|V|$ and λ_o , remain to be determined from the electron-transfer rate constants and their temperature dependence.

Considerable "parameter coupling" arises between the best fit values of the fitting parameters when analyzing temperature-dependent data. This issue has been discussed at length for these DBA systems in other solvents.³ The availability of the "correct" value of $\Delta_r G$ from the ratio of $k_{\text{for}}/k_{\text{back}}$ at each temperature greatly simplifies the task of extracting accurate values of λ_o and $|V|$. Nevertheless, a parametric relationship exists between the remaining two parameters, λ_o and $|V|$, at each temperature. This relationship is exhibited in Figure 2.5 for benzene, cumene, and triisopropylbenzene at selected temperatures. This figure shows that the value of $|V|$ that is required to reproduce k_{for} varies nonlinearly with the assumed value of the outer-sphere reorganization energy. For these solvents, the parametric relationship varies only slightly with temperature (vide infra). The curves in Figure 2.5 support two limiting conclusions: (1) if λ_o is relatively constant in all three solvents, $|V|$ in benzene and cumene are nearly equal but $|V|$ in TIP is at least three times smaller or (2) if $|V|$ in TIP is the same magnitude as $|V|$ in benzene, λ_o must be ~ 0.1 eV (30-50%) larger in TIP than in benzene. Some combination of these explanations is also possible.

If one makes the conventional assumption that the electronic coupling $|V|$ is temperature independent, it is possible to determine the temperature dependence of the outer-sphere reorganization energy from k_{for} .¹⁸ However, it is possible that solvent-mediated electronic

coupling (in contrast to bond-mediated electronic coupling) is temperature-dependent. Consequently, the analysis of the k_{ET} data proceeds in stages. First, the rate constant data are analyzed with the assumption that $|V|$ is temperature-independent. This allows the apparent temperature dependence of the reorganization energy to be extracted from $k_{\text{for}}(T)$. For the solvents in which λ_0 changes little over a reasonable range of temperatures, the rate constant data can be fit to eq 2.6 with $|V|$ and λ_0 as temperature-independent fitting parameters. Next, a molecular model for solvation is parametrized using the $\Delta_r G(T)$ data. This model is used to predict the temperature dependence of the solvent reorganization energy. The kinetic data are then analyzed using the parametrized model in two ways. Initially, the model is used to predict the $\Delta_r G(T)$ and $d\lambda_0/dT$ values so that $|V|$ and $\lambda_0(295)$ are the adjustable fitting parameters. Finally, the model is more stringently tested by using the predicted $\Delta_r G(T)$ and $\lambda_0(T)$ values with $|V|$ as the only adjustable fitting parameter.

B. Is λ_0 Temperature-Dependent? With values of 0.39 eV for λ_v , 0.175 eV for $h\nu$ and $\Delta_r G(T)$ available from the data, it is possible to obtain $\lambda_0(T)$ if a value for the electronic coupling $|V|$ can be found. As one goal of this study is to learn more about the temperature dependence of λ_0 , we proceed by assuming a reasonable value for $|V|$ and then extract $\lambda_0(T)$ from the data using eq 2.6. Figure 2.6 displays the outer-sphere reorganization energies $\lambda_0(T)$ required to reproduce the $k_{\text{for}}(T)$ data for two different assumed values of the electronic coupling in the different methylbenzene (panel A) and isopropylbenzene (panel B) solvents. As was evident in Figure 2.5, larger values of $|V|$ produce larger values of λ_0 . For both assumed values of $|V|$, the required $\lambda_0(T)$ values in benzene decrease very slightly with temperature.

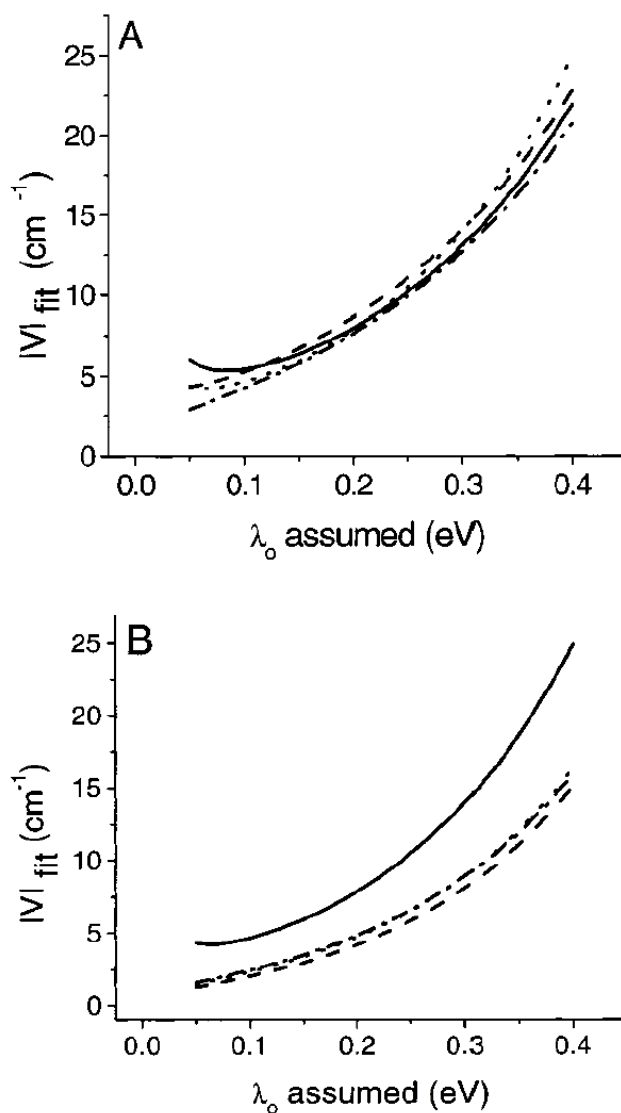


Figure 2.5 This figure illustrates the parameter coupling between $|V|$ and λ_0 . Panel A shows the data for benzene (295 K, solid line), benzene (342 K, dashed line), cumene (270 K, dotted line), cumene (345 K, dash-dot line). Panel B shows the data for cumene (270 K, solid line), triisopropylbenzene (260 K, dashed line), triisopropylbenzene (270 K, dotted line), triisopropylbenzene (283 K, dash-dot line). The 270 and 283 K curves overlap in panel B.

The required $\lambda_0(T)$ values in toluene exhibit a similar magnitude and temperature dependence as the benzene values for the same assumed $|V|$. This result is consistent with the similar electron-transfer rate constants in benzene and toluene, and these solvents' similar properties. Below 320 K, the required λ_0 in mesitylene is within 0.02 eV of that in benzene, for the same $|V|$. However, above 320 K, the λ_0 generated by this analysis rises steeply. In clear contrast to benzene and toluene, some property of mesitylene varies strongly with temperature. Comparing the open symbols ($|V| = 10 \text{ cm}^{-1}$) and the solid symbols ($|V| = 6 \text{ cm}^{-1}$), the absolute value of the reorganization energy is rescaled, but its temperature dependence is not affected. Panel B shows that the required values of λ_0 in cumene are also within 0.02 eV of those for benzene and, as seen in Figure 2.5, appear to increase slightly above 330 K. For the case of $|V| = 6 \text{ cm}^{-1}$, the required λ_0 in TIP is almost double that of benzene and exhibits a steep, negative temperature dependence. Use of a smaller $|V|$ for TIP (open symbols, $|V| = 1 \text{ cm}^{-1}$) produces smaller values of λ_0 and a weaker temperature dependence.

The foregoing analyses indicate that it is reasonable to treat $|V|$ and λ_0 as temperature-independent in benzene, toluene, and cumene. Upon close inspection, either λ_0 decreases slightly or $|V|$ increases slightly with increasing temperature in benzene and toluene. A similar situation appears to exist for mesitylene below 320 K. By contrast, it is not reasonable to treat $|V|$ and λ_0 as temperature-independent in triisopropylbenzene unless the absolute magnitude of $|V|$ is significantly smaller than 6 cm^{-1} . If $|V|$ is 6 cm^{-1} or greater in TIP, then λ_0 must decrease with increasing temperature or $|V|$ must be temperature-dependent. The opposite situation appears to hold in mesitylene above 320 K; either $|V|$ decreases or λ_0 increases sharply with increasing temperature.

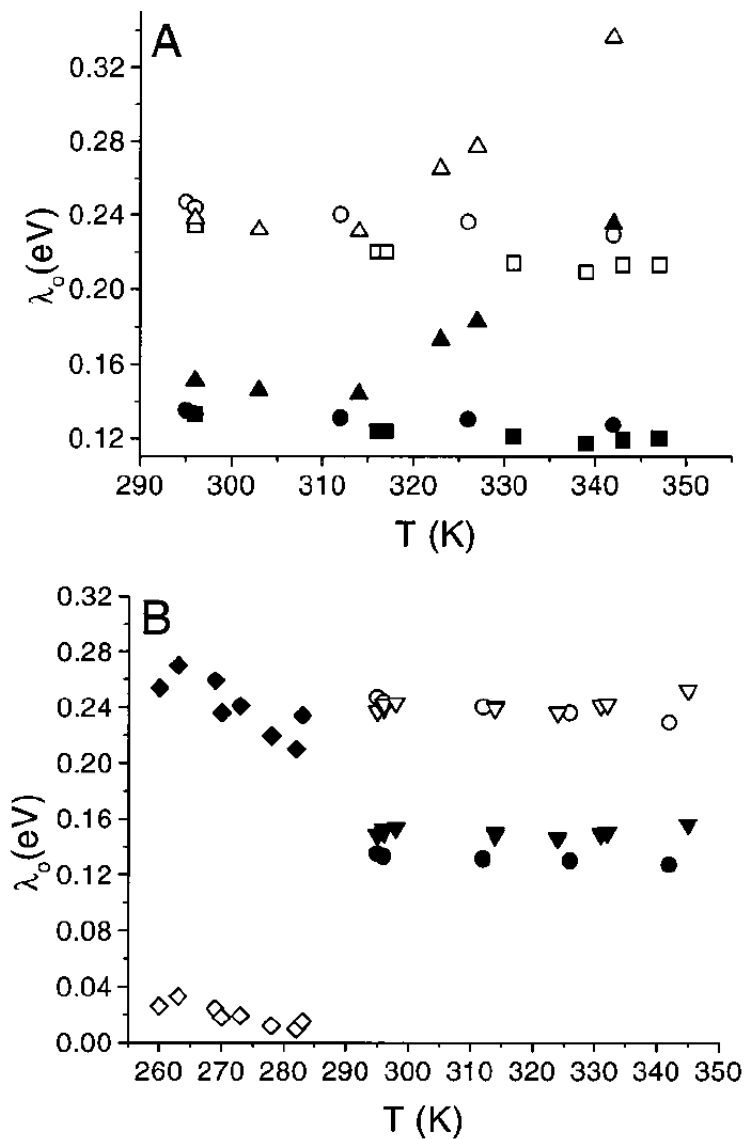


Figure 2.6 The temperature-dependent values of λ_0 that are needed to reproduce the $k_{\text{for}}(T)$. Panel A shows the data for benzene (●,○), toluene (■,□), and mesitylene (▲,△). Panel B shows the data for benzene (●,○), cumene (▼,▽), and triisopropylbenzene (◆,◇). The filled symbols give values of λ_0 for $|V| = 6 \text{ cm}^{-1}$. The open symbols give values of λ_0 for $|V| = 10 \text{ cm}^{-1}$ for all the solvents except TIP where it was set to $|V| = 1 \text{ cm}^{-1}$.

To determine the magnitude and possible temperature dependence of $|V|$ requires a reasonable model for the magnitude and/or temperature dependence of λ_o in these solvents. Continuum models are not able to predict the temperature dependence, let alone the magnitude, of λ_o in these aromatic solvents. To estimate the magnitude and temperature dependence of λ_o , a molecular-based model for the solvation energy and solvent reorganization energy was explored. The analysis and resulting estimates of $|V|$ and λ_o are described in the next section.

2.4 Modeling $\Delta_r G(T)$ and $\lambda_o(T)$

Modeling $\Delta_r G(T)$ and $\lambda_o(T)$ in the alkylbenzenes is expected to be nontrivial because of their nondipolar character. Hence one expects the dispersion and induction forces to play a significant role in the solvation and its temperature dependence.⁸ In addition, the importance of quadrupole and higher order moments should, in principle, be considered. Although theoretical efforts to include such contributions are under development, their implementation remains difficult and their reliability has not been assessed.¹⁹ The description of the solvent dependence of $\Delta_r G(T)$ and $\lambda_o(T)$ used here employs a reference hard-sphere, dipolar polarizable fluid to account for the effects of solvent density variation on the solvation and hence its temperature dependence. The model accounts for both induction and dispersion forces.⁸

Matyushov⁸ writes the reaction free energy $\Delta_r G$ as a sum of three components:

$$\Delta_r G = \Delta G_{\text{vacuum}} + \Delta G_{\text{dipole}} + \Delta G_{\text{dispersion}} \quad (2.8)$$

where ΔG_{vacuum} is the reaction free energy in a vacuum. The ΔG_{dipole} term contains contributions from the dipole-dipole interaction between the solute and solvent and the induction force between the solute dipole and the solvent. This term is given by²⁰

$$\Delta G_{\text{dipole}} = -\frac{\Delta m}{\sigma^3}(m_e' + m_g')P(y, \rho^*, r_0) \quad (2.9)$$

where σ is the hard-sphere diameter of the solvent, ρ^* is the reduced solvent density $\rho\sigma^3$ (ρ is the solvent number density), r_0 is the distance of closest approach between the solute and solvent in reduced units ($r_0 \equiv 0.5 + R_0/\sigma$ where R_0 is the effective radius of the solute molecule - approximated as a sphere), and y is the solvent's zero frequency dipolar density ($y = (4\pi/9kT)\rho m_s^2 + (4\pi/3)\rho\alpha_s$) arising from solvent permanent dipole moments m_s and solvent molecule polarizability α_s . The difference in dipole moment between the solute CT state, m_e , and LE state, m_g , is given by Δm . The solute dipole moments are renormalized as a consequence of the solute polarizability. The slanted prime indicates a renormalized magnitude induced by the solvent's zero frequency dipolar density, y :

$$m' = \frac{m}{\left[1 - \frac{2\alpha_0 P(y, \rho^*, r_0)}{\sigma^3}\right]} \quad (2.10)$$

where α_0 is the solute polarizability. The functions $P(y, \rho^*, r_0)$ are Pade approximants to the dipolar response function of the fluid. Their explicit form is given in Appendix 2.A.

The third term $\Delta G_{\text{dispersion}}$ is the contribution to the free energy from the dispersion interactions between the solute and solvent. It is given by

$$\Delta G_{\text{dispersion}} = \frac{\Delta\gamma'}{\alpha_s} 96\eta\epsilon_{\text{LJ}}^s \left(\frac{\sigma}{\sigma_{0s}}\right)^6 \int_{\sigma_{\text{LJ}}^{0s}}^{\infty} u_1^{0s}(r) g_{0s}^{(0)}(r) r^2 dr \quad (2.11)$$

where η is the solvent-packing fraction of the hard-sphere solvent, $\sigma^{0s} = R_0 + \sigma/2$ is the effective solvent-solute diameter, ϵ_{LJ}^s is the solvent Lennard-Jones energy and $g_{0s}^{(0)}$ is the solute - solvent hard-sphere distribution function. The hard-sphere diameter σ was used for the Lennard-Jones

diameter of the solvent in the Matyushov formulation. The term $u_1^{0s}(r)$ is equal to $u^{0s}(r)\theta(r-\sigma^{0s})$ where $u^{0s}(r)$ is the Lennard-Jones potential function and $\theta(x)$ is the Heaviside function. The term $\Delta\gamma'$ is the change in solute polarizability between the LE and CT states weighted by a ratio of solute and solvent ionization potentials.⁸ Here it was treated as an adjustable solute parameter. These expressions may be evaluated, given the appropriate solute and solvent parameters, and compared to the experimentally determined free energy changes.

Matyushov⁸ also derived an expression for λ_o , the outer-sphere reorganization energy upon electron transfer, which has three sources:

$$\lambda_o = \lambda_{\text{dipole}} + \lambda_{\text{dispersion}} + \lambda_{\text{induction}} \quad (2.12)$$

The dipolar contribution λ_{dipole} is given by

$$\lambda_{\text{dipole}} = \frac{\Delta m}{\sigma^3} [(m_c' - m_g')P(y, \rho^*, r_0) - (m_c^\infty - m_g^\infty)P(y_\infty, \rho^*, r_0)] \quad (2.13)$$

The m^∞ terms reflect solute dipole renormalization by the high-frequency dipolar density that arises from the solvent polarizability. The dispersion contribution to the reorganization energy $\lambda_{\text{dispersion}}$ is given by²⁰

$$\lambda_{\text{dispersion}} = \frac{8\eta}{3}\beta(\epsilon_{\text{LJ}}^s \Delta\gamma')^2 [\int_0^\infty u_1^{0s}(r)^2 g_{0s}^{(0)}(r) r^2 dr - (1 - m_{\text{ss}}(0)) \int_0^\infty u_1^{0s}(r) u_1^{0s}(r + \phi) g_{0s}^{(0)}(r) g_{0s}^{(0)}(r + \phi) r(r + \phi) dr] \quad (2.14)$$

where $m_{\text{ss}}(0) = (1 - \eta)^4 / (1 + 2\eta)^2$ and the phase factor ϕ is given as a function of η in Appendix

2.A. The induction contribution $\lambda_{\text{induction}}$ is given by

$$\lambda_{\text{induction}} = \frac{1}{\eta k_{\text{B}} T} \left(\frac{\Delta m'^2 y_{\infty}}{20\sigma^3} \right)^2 [4(2m_{\infty}^{+}(0) + m_{\infty}^{-}(0)) - 9] \times 9 \int_{r_0}^{\infty} \frac{g_{0s}^{(0)}(r)}{r^{10}} dr \quad (2.15)$$

where

$$m_{\infty}^{+}(0) = \frac{1}{3y_{\infty}} \left(1 - \frac{1}{\epsilon_{\infty}} \right) \quad (2.16a)$$

and

$$m_{\infty}^{-}(0) = \frac{1}{3y_{\infty}} (\epsilon_{\infty} - 1) \quad (2.16b)$$

As with the free-energy expressions, this sum must be evaluated for an appropriate choice of solute and solvent parameters.

Table 2.2 Solvent Parameters Used in the Matyushov Modeling

solvent	m, D^a	$\sigma, \text{\AA}^b$	$\alpha_0, \text{\AA}^3 c$	$\epsilon_{\text{LJ}}, k_{\text{B}}^s$	$\eta(296)$	$d\lambda_o(T)/dT, \text{eV/K}$
benzene	0.01	5.277	10.7	544	0.518	-2.2×10^{-4}
toluene	0.31	5.680	11.8	596	0.543	-6.5×10^{-4}
cumene	0.39	6.286	15.5	662	0.560	-7.2×10^{-4}
mesitylene	0.01	6.400	15.3	862	0.593	-4.5×10^{-4}
TIP ^d	0.01	7.400	30.7	1117	0.534	-1.0×10^{-4}

^a The dipole moments for benzene, mesitylene, and triisopropylbenzene were chosen to be very small but nonzero to facilitate computation. The dipole moments of toluene and cumene were taken from Riddick, J. A.; Bunger, W. B.; Sakano, T.K. *Organic Solvents: Physical Properties and Methods of Purification*; Wiley: New York, NY, 1986.

^b The effective hard-sphere diameters and the Lennard-Jones parameters for the solvents were obtained using the method described by Ben-Amotz, D.; Willis, K. G. *J. Phys. Chem.* **1993**, *97*, 7736. ^c The solvent polarizabilities were taken from the CRC. In each case, they were slightly modified to give a good fit. ^d TIP is 1,3,5-triisopropylbenzene.

Table 2.3 Best Fit Values for $|V|$ and λ_o Using the Experimentally Determined $\Delta_r G(T)$: Method 1

solvent	$ V $, cm^{-1}	λ_o , eV
benzene	5.6	0.12
toluene	5.1	0.10
cumene	5.0	0.12
mesitylene	3.1	0.050
TIP ^a	1.2	0.023

^a TIP is 1,3,5-triisopropylbenzene.

Table 2.4 Best Fit $|V|$ and $\lambda_o(295)$ Using the Matyushov Model for $\Delta_r G(T)$

solvent	method 2 ^a		method 3 ^b	
	$ V $, cm^{-1}	$\lambda_o(295)$, eV	$ V $, cm^{-1}	$\lambda_o(295)$, eV
benzene	5.7	0.124	5.1	0.069
toluene	8.8	0.213	5.7	0.132
cumene	6.6	0.181	4.8	0.129
mesitylene	5.6	0.143	4.2	0.094
TIP ^c	0.7	0.002	1.2	0.027

^a In method 2, $d\lambda_o(T)/dT$ is taken from the Matyushov model. ^b In Method 3, $\lambda_o(T)$ is taken from the Matyushov model. ^c TIP is 1,3,5-triisopropylbenzene.

Equations 2.8 – 2.11 were used to reproduce the experimental values of $\Delta_r G$ and its temperature dependence. Unknown parameters, such as the solute radius, were chosen to achieve the best global fit (in all solvents). The solid lines in Figure 2.4 display the resulting fits to the measured reaction free energies. The effective solute sphere radius was set equal to 5.5 Å. The change in the dipole moment between the LE and CT states was set to 34 D. The vacuum free energy change ΔG_{vacuum} was set to 0.568 eV. The LE state polarizability was set to 100 Å³ and $\Delta\gamma'$ was 2 Å³. The solvent parameters used are reported in Table 2.2. The parameter values were obtained in a standard manner²¹ for each of the solvents. In each case, the polarizability of the solvent was adjusted (by less than 10%) to improve the fit. The temperature-dependent

density, the static dielectric constant and the high-frequency dielectric constant (estimated as n^2) were obtained from the literature.

The parameters determined by fitting $\Delta_r G(T)$ in the various solvents were used to predict the absolute magnitude and the temperature dependence of the reorganization energy $\lambda_o(T)$ in each solvent. The values of $\lambda_o(295)$ predicted by the “calibrated” Matyushov model are all less than 0.15 eV (see Table 2.4, column 5). In toluene and cumene, the two solvents with nonzero dipole moments, the estimated $\lambda_o(295)$ are moderately larger than in benzene and mesitylene. The λ_{dipole} term, eq 2.12, is the source of the larger reorganization energy in toluene and cumene (see Appendix 2.B). Before proceeding to the analysis of the kinetic data, it is important to point out that the parameter set used to fit $\Delta_r G(T)$ is not unique. For example, it is possible to decrease the size of the dipole moment change (Δm) and increase the solute polarizability α_o and still obtain similar quality fits to the data.

2.5 Determination of $|V|$ and λ_o

Values of $|V|$ and λ_o were extracted from the temperature dependent rate constant data using three different procedures. First, the rate data was fit using the experimental $\Delta_r G(T)$ and treating λ_o and $|V|$ as temperature independent, but adjustable, parameters. The results of this “ T -independent” analysis (method 1) are presented in Table 2.3. This procedure is appropriate for the solvents that exhibit a weak temperature dependence of λ_o when a temperature-independent $|V|$ is assumed; i.e., benzene, toluene, and cumene. This condition is also satisfied in mesitylene at low temperatures, and the data in mesitylene at temperatures below 320 K were analyzed in this manner. Use of this method for the triisopropylbenzene data is reasonable only if $|V|$ is

considerably less than 6 cm^{-1} . Given the results of the analysis, an assumption for $|V|$ of 1 cm^{-1} more closely represents the experimental findings (vide infra). In each case the data in Figure 2.3 was well reproduced by this analysis.

According to Table 2.3, the best fit parameter values are consistent with an increase in the electronic coupling when the solvent's aromatic ring is able to position between the donor and acceptor π -functions. The benzene and monosubstituted benzene solvents have similar electronic couplings. In contrast, the electronic coupling in mesitylene, which has three bulky methyl groups equally spaced around the periphery of the ring, is $\sim 40\%$ smaller and the coupling in TIP, which has the greatest steric impediment to entry into the cleft, is 4-5 times smaller than that in benzene. The small $|V|$ is consistent with the assumption of a nearly temperature independent λ_0 (Figure 2.6, vide supra). The best fit values of the reorganization energy provide additional insight into the solvent-solute interaction. The reorganization energy in benzene and the monoalkylated benzenes are similar, whereas the reorganization energy in TIP is smaller. The kinetic model does not account for the presence of the cleft in **2**. None the less, the extracted reorganization energies are strongly influenced by the solvent size. From a molecular perspective, reduced entry of the bulky solvents into the solute cleft would be expected to decrease their ability to stabilize the charge-transfer state and to produce smaller values of λ_0 .

In a second approach, the electronic coupling was determined by fitting the rate data to eq 2.6 using the $\Delta_r G(T)$ and $d\lambda_0/dT$ (Table 2.2) values predicted by the "calibrated" Matyushov model, method 2. In this method, $|V|$ and $\lambda_0(295)$ were the adjustable parameters. The best fit values are reported in Table 2.4 (columns 2 and 3) and the lines displayed in Figure 2.3 represent the result of this fitting procedure. This approach does an excellent job of reproducing both the forward and back electron-transfer data in all five solvents. In contrast to method 1, the electronic

coupling obtained for the monosubstituted benzenes is larger than benzene. The estimated coupling in mesitylene is comparable to the values found for benzene and the monoalkylated benzenes and the coupling in TIP is more than a factor of 5 smaller than the coupling found in benzene. The room temperature reorganization energies $\lambda_o(295)$ obtained in this analysis are between 0.22 and 0.12 eV in all solvents except TIP, for which the reorganization energy was found to be < 0.01 eV. The Matyushov treatment predicts that λ_o should be largest in the slightly dipolar solvents cumene and toluene (vide infra). A dissection of the reorganization energy (see Appendix 2.B) reveals that the dipolar contribution is the source of the larger values in these two solvents. The extracted value of λ_o in TIP is extraordinarily small, but is required to reproduce the observed increase of both the forward and reverse electron-transfer rate constants with increasing temperature. In a final approach, the electronic coupling was determined by fitting the rate data to eq 2.6 using the $\Delta_r G(T)$ and λ_o values predicted by the “calibrated” Matyushov model, method 3. In this method, $|V|$ was the only adjustable parameter. This approach provides a stringent test of the Matyushov model’s ability to predict the solvent reorganization energy in aromatic solvents. The best fit values of $|V|$ are reported in Table 2.4 (column 4) along with the Matyushov model’s predictions of $\lambda_o(295)$ (column 5). With the exception of TIP, the $|V|$ generated by method 3 is as much as 40% smaller than that produced by method 2. Likewise, the $\lambda_o(295)$ value from method 3 is ~ 0.06 eV smaller than that from method 2. For TIP, both $|V|$ and λ_o produced by method 3 are larger. However, as seen in Figure 2.7, method 3 accurately reproduces the kinetic data in toluene, cumene, and mesitylene but fails to reproduce the proper slope of the Arrhenius plots in benzene and TIP. The origin of this failure can be understood by analyzing the temperature dependence of eq 2.6 for the $n = 0$ term.²²

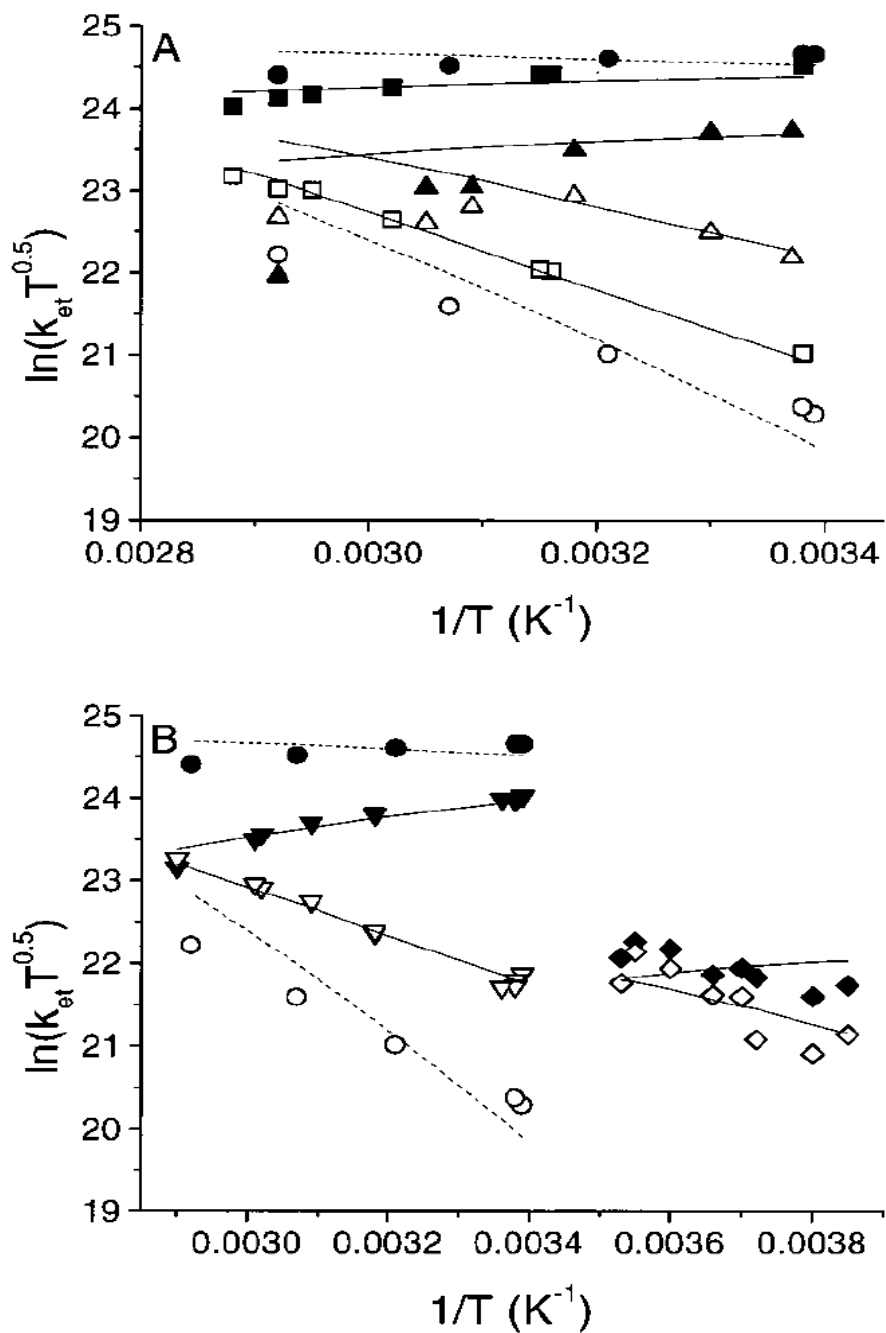


Figure 2.7 The temperature dependence of the forward (filled symbols) and backward (open symbol) electron-transfer rate constants is shown. Panel A shows the data for benzene (●,○), toluene (■,□), and mesitylene (▲,△). Panel B shows the data for benzene (●,○), cumene (▼,▽), and triisopropylbenzene (◆,◇). The lines are fits to the data using the Matyushov model for $\Delta_r G(T)$ and $\lambda_o(T)$. The dashed curves show the fits for benzene and the solid curves are for the other solvents.

Figure 2.8 displays the dependence of the slope of $\ln(k_{\text{for}})$ on the value of $\lambda_o(295)$. For TIP, the observed negative slope ($\bullet\text{-}\bullet$) is reproduced only by values of $\lambda_o(295)$ less than 0.01 eV,²³ whereas the Matyushov value of 0.023 eV produces a weak positive slope, as seen in Figure 2.7. The positive slope of the benzene data ($\diamond\text{-}\diamond$) is reproduced by $\lambda_o(295)$ values greater than 0.1 eV, whereas the Matyushov prediction of 0.048 eV results in a negative slope. Plots analogous to Figure 2.8 for toluene, cumene, and mesitylene predict positive Arrhenius slopes for $\lambda_o(295)$ greater than 0.08 eV. As a result, the fits to the kinetic data and the extracted values of $|V|$ are only moderately affected by the value of $\lambda_o(295)$ in the latter three solvents.

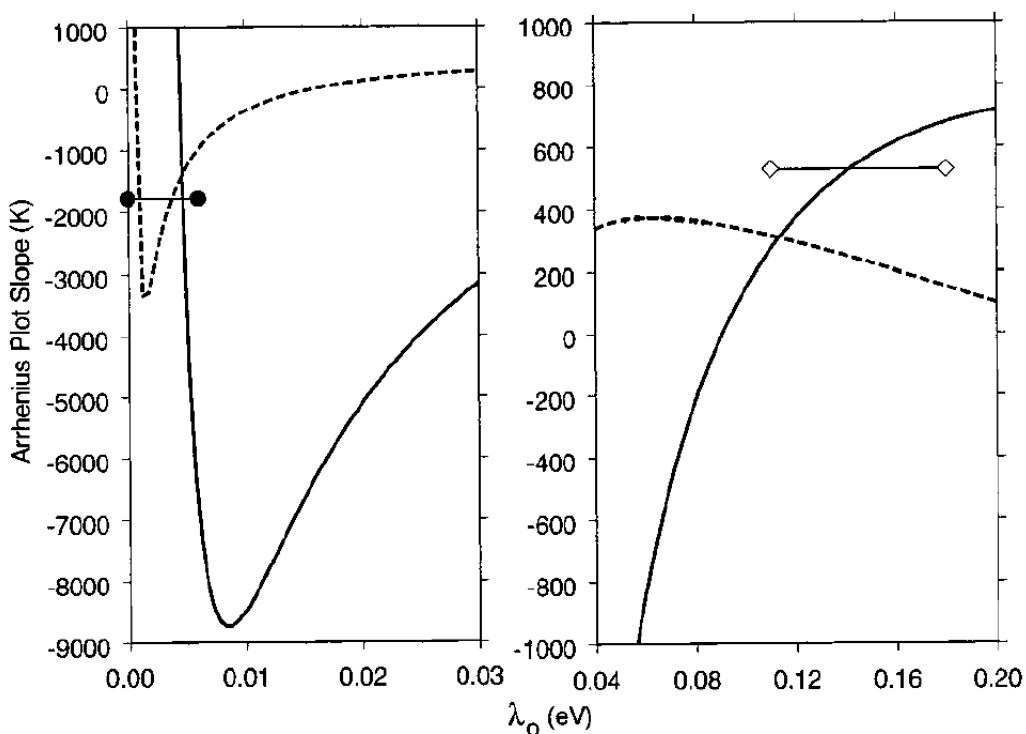


Figure 2.8 The calculated slope of $\ln(k_{\text{for}}(T)/T)$ versus $1/T$ is plotted as a function of λ_o for benzene and TIP. The solid curve is for benzene, and the dashed curve is for TIP. The left panel shows the result for 0-0.03 eV. The horizontal line with circles indicates the experimental slope for TIP. The right panel shows the result for 0.04-0.2 eV. The horizontal line with diamonds indicates the experimental slope for benzene.²⁷

2.6 Discussion and Conclusion

The fluorescence decay of **2** in nonpolar and weakly polar solvents is biexponential. The fast component of the decay involves depopulation of the LE state primarily through establishment of an LE a CT excited-state equilibrium. The slow component arises from irreversible depopulation of the equilibrium mixture to lower energy states.²⁴ Analysis of the biexponential decay law, in conjunction with the intrinsic decay rate constant for the LE state in donor only analogues, enabled reliable determination of three important quantities: the forward electron-transfer rate k_{for} (LE to CT), the backward electrontransfer rate k_{back} (CT to LE), and the charge separation free energy $\Delta_r G$. The data in Figure 2.4 show that the reaction free energy $\Delta_r G(T)$ becomes increasingly endoergic with increasing temperature and with increasing alkyl substitution of the solvents' aromatic core. The destabilization of the charge transfer state with temperature may be understood in terms of decreasing solvent density. A molecular model for the solvent is able to mimic the observed temperature dependence in this series of related solvents.

Among the set of solvents investigated, only toluene and cumene possess permanent dipole moments. The latter are small (< 0.35 D) and, in fact, benzene appears to be more effective at stabilizing the CT state. Benzene's axial quadrupole moment is slightly larger than toluene's^{13a} and, at least from one edge, the unsubstituted benzene ring can get closer to the solute CT state. Although quadrupole contributions to solvation could be significant, the molecular model used here does not include them. The model incorporates the steric/size factor through the solvent's effective hard-sphere diameter, as indicated in Table 2.2. Although the molecular polarizability is larger in the more highly alkylated solvents, their size is also larger, and the $\rho\alpha$ contribution to the dipolar density remains relatively constant in these solvents. It

appears that the differences in the solvation can be attributed to the smaller effective diameter of the less alkylated solvents and changes in the packing fraction η (see Table 2.2 and Appendix 2.B).

The same model and parameters that adequately reproduced $\Delta_r G(T)$ in the different solvents was used to predict the magnitude and temperature dependence of the outer-sphere reorganization energy. The parametrized Matyushov model prediction of the $\lambda_o(295)$ values are all less than 0.15 eV (Table 2.4). For the three nondipolar solvents, increased solvent size (sphere diameter), molecular polarizability, and Lennard-Jones energy reduce the reorganization energy from 0.069 eV in benzene to 0.039 eV in mesitylene and to 0.027 eV in TIP. For the nondipolar solvents, λ_{dipole} makes no contribution to the overall reorganization energy. However, the presence of a small dipole moment in toluene and cumene increases the overall reorganization energy 2-fold in comparison to, the otherwise similar solvent, benzene. As the dipole moment of cumene is 25% larger than that of toluene, one expects the predicted $\lambda_o(295)$ value to be greater for cumene. However, the increased size of cumene reduces the induction contribution $\lambda_{\text{induction}}$ which offsets the increased dipolar contribution λ_{dipole} (Appendix 2.B). As a result, the predicted reorganization energies $\lambda_o(295)$ in these two solvents are quite similar.

The molecular model predicts a weak decrease of λ_o with increasing temperature (Table 2.2) which is corroborated by optical studies of CT emission and absorption bands in benzene²⁵ and other weakly polar solvents.²⁶ The “parametrized” Matyushov model predicts $d\lambda_o/dT$ values (Table 2.2) of about -7×10^{-4} eV/K in the dipolar solvents toluene and cumene and of -1×10^{-4} eV/K in TIP. From a practical standpoint, the parametrized Matyushov model does a reasonable job considering that it does not account for the detailed shape of the molecule. It predicts λ_o values that are remarkably close to those required by the observed k_{ET} temperature dependence

(Figure 2.8) and from a best fit to the data.

With the parametrization of a reasonable model for the temperature dependence of the reaction free energy and the outer-sphere reorganization energy, it was possible to fit the temperature-dependent electron-transfer rate constants to the semiclassical model (eq 2.6) and determine $|V|$. The results from the three analyses of the kinetic data clearly demonstrate that $|V|$ is smaller in an aromatic solvent that is too bulky to effect simultaneous overlap with the π -functions of the donor and acceptor groups. The analyses for the benzene, toluene, and cumene solvents give electronic couplings that are similar ($\sim 6 \text{ cm}^{-1}$). For 1,3,5-triisopropylbenzene, $|V|$ is at least five times smaller than in benzene. The possibility that a smaller value of $|V|$ is obtained as a result of the parametric dependence on the value of λ_0 in eq 2.6 has been evaluated. Figure 2.5 demonstrates that even if an identical value of λ_0 is assumed for this series of solvents, the calculated electronic coupling is at least 3-fold smaller for TIP than for benzene. These experiments emphasize once again the difficulty in interpreting electron-transfer rate constants determined at a single temperature. Without independent characterization of λ_0 and $\Delta_r G$, a single rate measurement can be interpreted to support any number of conclusions.

The variation of $|V|$ with solvent may be rationalized in terms of the effect of the alkyl group steric bulk on the solvent's tendency to enter the cleft of **2** and on the resulting interactions with the D and A groups. For benzene and monosubstituted benzenes, the aromatic core can enter the cleft of **2** with minimal conformational restrictions. The comparable couplings determined for benzene, toluene and cumene suggest similar geometries and probabilities of solvent insertion into the cleft of **2** for all three solvents. For 1,3,5-triisopropylbenzene, the bulky isopropyl groups inhibit entry of the aromatic core into the cleft of **2**, causing a decrease in the electronic coupling by increasing the solvent-to-donor and solvent-to-acceptor distance. It is

possible for an isopropyl group on TIP to insert into the cleft, thus providing a solvent-mediated path for D-A coupling, albeit a less effective one. Mesitylene affords an intermediate value of the coupling. The methyl groups are slightly wider than the aromatic ring. Their presence may decrease the overlap of the ring orbitals with the donor and acceptor groups when mesitylene is located in the cleft. Alternatively, they may limit the available conformations that lead to significant electronic coupling or decrease the time average probability of finding solvent in the cleft. Further studies are required to distinguish these possibilities. The key may lie with the unusual kinetic behavior at higher temperatures in mesitylene.

We have shown that a prerequisite for effective aromatic solvent mediation of electronic coupling is placement of the aromatic core directly between the donor and acceptor groups. One way to hinder a solvent's access into the cleft is to increase its steric bulk. The results of this investigation demonstrate that preventing solvent entry into the cleft significantly reduces the efficacy of solvent-mediated coupling in electron-transfer reactions.

2.7 Appendix 2.A

The dipolar solvent response contains contributions from both solute-solvent and solvent-solvent interactions. Matyushov has shown that

$$P(y, \rho^*, r_o) = \frac{yI_{0s}^{(2)}}{1 + yI_{0s}^{(3)}/I_{0s}^{(2)}}$$

where $I^{(2)}$ and $I^{(3)}$ are the two and three particle solute-solvent integrals approximated by

$$I_{0s}^{(2)} = \frac{1}{r_o^3} + \frac{d(\rho^*)}{r_o^4} + \frac{e(\rho^*)}{r_o^5} + \frac{f(\rho^*)}{r_o^6}$$

$$I_{0s}^{(3)} = \frac{a(\rho^*)}{r_o^3} + \frac{b(\rho^*)}{r_o^4} + \frac{c(\rho^*)}{r_o^5}$$

$$I_{0s}^{(4)} = \frac{1}{r_o^9} + \frac{a(\rho^*)}{r_o^{10}} + \frac{b(\rho^*)}{r_o^{11}} + \frac{c(\rho^*)}{r_o^{12}}$$

The coefficients $a(\rho^*)$, $b(\rho^*)$, $c(\rho^*)$, etc. in the density expansion have been fitted to the calculated dependencies of the solute-solvent integrals and are provided in ref 8a. The explicit form of these integrals is given in ref 8c.

The integrals found in eqs 2.11, 2.14, and 2.15 were evaluated using the Pade form for the integrals. In our calculations,

$$\int_{\sigma_1^0}^{\infty} u_1^{0s}(r) g_{0s}^{(0)}(r) r^2 dr = \left[\frac{I_{0s}^{(4)}}{9} - \frac{I_{0s}^{(2)}}{3} \right]$$

$$9 \int_{r_0}^{\infty} \frac{g_{0s}^{(0)}(r)}{r^{10}} dr = I_{0s}^{(4)}$$

$$\left[\int_0^{\infty} u_1^{0s}(r)^2 g_{0s}^{(0)}(r) r^2 dr - (1 - m_{ss}(0)) \int_0^{\infty} u_1^{0s}(r) u_1^{0s}(r + \phi) g_{0s}^{(0)}(r) g_{0s}^{(0)}(r + \phi) r(r + \phi) dr \right] = I_{0s}^{(4)}$$

The latter integral ignores the contribution from three-body interactions. An effect which becomes increasingly important as the polarity of the solvent increases.

2.8 Appendix 2.B

Table 2.5

T, K	ΔG_{dipole} , eV	$\Delta G_{\text{dispersion}}$, eV	ΔG_{total} , eV	λ_{dipole} , eV	$\lambda_{\text{dispersion}}$, eV	$\lambda_{\text{induction}}$, eV	λ_{total} , eV
benzene							
296	-0.667	-0.018	-0.116	0	0	0.069	0.069
312	-0.648	-0.017	-0.096	0	0	0.065	0.065
326	-0.632	-0.017	-0.080	0	0	0.062	0.062
342	-0.613	-0.016	-0.061	0	0	0.058	0.058
toluene							
296	-0.631	-0.025	-0.087	0.038	0	0.094	0.132
316	-0.608	-0.024	-0.063	0.034	0	0.083	0.118
331	-0.591	-0.024	-0.046	0.032	0	0.076	0.108
339	-0.582	-0.023	-0.037	0.031	0	0.072	0.104
347	-0.573	-0.023	-0.028	0.030	0	0.069	0.099
mesitylene							
297	-0.552	-0.050	-0.033	0	0.001	0.092	0.093
303	-0.547	-0.049	-0.027	0	0.001	0.089	0.090
314	-0.537	-0.048	-0.016	0	0.001	0.084	0.085
324	-0.528	-0.048	-0.007	0	0.001	0.080	0.081
342	-0.512	-0.046	0.011	0	0.001	0.073	0.074
cumene							
296	-0.591	-0.032	-0.054	0.042	0.001	0.086	0.129
314	-0.573	-0.031	-0.036	0.039	0.001	0.076	0.115
324	-0.563	-0.031	-0.025	0.037	0.001	0.070	0.108
331	-0.556	-0.031	-0.018	0.036	0.001	0.067	0.103
345	-0.543	-0.031	-0.005	0.033	0	0.060	0.094
TIP							
260	-0.540	-0.047	-0.018	0	0.001	0.029	0.030
263	-0.538	-0.046	-0.016	0	0.001	0.029	0.030
278	-0.527	-0.046	-0.003	0	0.001	0.027	0.028
282	-0.524	-0.045	0	0	0.001	0.027	0.028

Table 2.5 shows the different contributions to ΔG and λ from the dipolar, induction and dispersion interactions, according to the Matyushov model.

2.9 References

- (1) Onuchic, J. N.; Beratan, D. N. *J. Chem. Phys.* **1990**, *92*, 722.
- (2) (a) Kumar, K.; Lin, Z.; Waldeck, D. H.; Zimmt, M. B. *J. Am. Chem. Soc.* **1996**, *118*, 243. (b) Han, H.; Zimmt, M. B. *J. Am. Chem. Soc.* **1998**, *120*, 8001.
- (3) Kumar, K.; Kurnikov, I. V.; Beratan, D. N.; Waldeck, D. H.; Zimmt, M. B. *J. Phys. Chem. A* **1998**, *102*, 5529.
- (4) (a) Oevering, H.; Paddon-Row, M. N.; Heppener, M.; Oliver, A. M.; Cotsaris, E.; Verhoeven, J. W.; Hush, N. S. *J. Am. Chem. Soc.* **1987**, *109*, 3258. (b) Oliver, A. M.; Craig, D. C.; Paddon-Row, M. N.; Kroon, J.; Verhoeven, J. W. *Chem. Phys. Lett.* **1988**, *150*, 366. (c) Warman, J. M.; Smit, K. J.; de Haas, M. P.; Jonker, S. A.; Paddon-Row, M. N.; Oliver, A. M.; Kroon, J.; Oevering, H.; Verhoeven, J. W. *J. Phys. Chem.* **1991**, *95*, 1979. (d) Lawson, J. M.; Paddon-Row, M. N.; Schuddeboom, W.; Warman, J. M.; Clayton, A. H. A.; Ghiggino, K. P. *J. Phys. Chem.* **1993**, *97*, 13099. (e) Roest, M. R.; Verhoeven, J. W.; Schuddeboom, W.; Warman, J. M.; Lawson, J. M.; Paddon-Row, M. N. *J. Am. Chem. Soc.* **1996**, *118*, 1762. (f) Jolliffe, K. A.; Bell, T. D. M.; Ghiggino, K. P.; Langford, S. J.; Paddon-Row, M. N. *Angew. Chem., Intl. Ed. Engl.* **1998**, *37*, 916.
- (5) Gould, I.; Farid, S. *J. Am. Chem. Soc.* **1994**, *116*, 8176.
- (6) Miller, J. R.; Beitz, J. V. *J. Chem. Phys.* **1981**, *74*, 6746.
- (7) Cave, R. J.; Newton, M. D.; Kumar, K.; Zimmt, M. B. *J. Phys. Chem.* **1995**, *99*, 17501.
- (8) (a) Matyushov, D. V. *Chem. Phys.* **1996**, *211*, 47. (b) Matyushov, D. V.; Schmid, R. *Mol. Phys.* **1995**, *84*, 533. (c) Matyushov, D. V.; Schmid, R. *J. Chem. Phys.* **1995**, *103*, 2034.
- (9) Kumar, K.; Tepper, R. J.; Zeng, Y.; Zimmt, M. B. *J. Org. Chem.* **1995**, *60*, 4051.
- (10) (a) Zeglinski, D. M.; Waldeck, D. H. *J. Phys. Chem.* **1988**, *92*, 692. (b) O'Connor, D. V.; Phillips, D. *Time Correlated Single Photon Counting*; Academic Press: New York, 1984.
- (11) (a) Heitele, H.; Finckh, P.; Weeren, S.; Pöllinger, F.; Michel-Beyerle, M. E. *J. Phys. Chem.* **1989**, *93*, 5173. (b) Kroon, J.; Oevering, H.; Verhoeven, J. W.; Warman, J. M.; Oliver, A. M.; Paddon-Row, M. N. *J. Phys. Chem.* **1993**, *97*, 5065. (c) Asahi, T.; Ohkohchi, M.; Matsusaka, R.; Mataga, N.; Zhang, R. P.; Osuka, A.; Maruyama, K. *J. Am. Chem. Soc.* **1993**, *115*, 5665.
- (12) (a) Marcus, R. A. *Annu. Rev. Phys. Chem.* **1964**, *15*, 155. (b) Marcus, R. A. *J. Chem. Phys.* **1965**, *43*, 679.
- (13) (a) Reynolds, L.; Gardecki, J. A.; Frankland, S. J. V.; Horng, M. L.; Maroncelli, M. *J. Phys.*

Chem. **1996**, *100*, 10337. (b) Gardecki, J.; Horng, M. L.; Papazyan, A.; Maroncelli, M. *J. Mol. Liq.* **1995**, *65*, 49.

(14) Jortner, J. *J. Chem. Phys.* **1976**, *64*, 4860.

(15) (a) Meyer, T. J. *Prog. Inorg. Chem.* **1983**, *30*, 389. (b) Miller, J. R.; Beitz, J. V.; Huddleston, R. K. *J. Am. Chem. Soc.* **1984**, *106*, 5057.

(16) Barbara, P. F.; Meyer, T. J.; Ratner, M. A. *J. Phys. Chem.* **1996**, *100*, 13148.

(17) Shephard, M. H.; Paddon-Row, M. N. *J. Phys. Chem. A* **1999**, *103*, 3347.

(18) (a) Hupp, J. T.; Neyhard, G. A.; Meyer, T. J. *J. Phys. Chem.* **1992**, *96*, 10820. (b) Dong, Y.; Hupp, J. T. *Inorg. Chem.* **1992**, *31*, 3322. (c) Dong, Y.; Hupp, J. T. *J. Am. Chem. Soc.* **1993**, *115*, 6428.

(19) (a) Chitanvis, S. M. *J. Chem. Phys.* **1996**, *104*, 9065. (b) Koga, K.; Tanaka, H.; Zeng, X. C. *J. Phys. Chem.* **1996**, *100*, 16711. (c) Bliznyuk, A. A.; Gready, J. E. *J. Phys. Chem.* **1995**, *99*, 14506. (d) Kim, H. J. *J. Chem. Phys.* **1996**, *105*, 6818. (e) Perng, B.-C.; Newton, M. D.; Raineri, F. O.; Friedman, H. L. *J. Chem. Phys.* **1996**, *104*, 713. (f) Perng, B.-C.; Newton, M. D.; Raineri, F. O.; Friedman, H. L. *J. Chem. Phys.* **1996**, *104*, 7177.

(20) Equations 2.9 and 2.14 given here are a correction of the originally published equations (ref 8). The authors thank Dmitry Matyushov for pointing out the errors.

(21) Ben-Amotz, D.; Herschbach, D. R. *J. Phys. Chem.* **1990**, *94*, 1038.

(22) In these systems, the $n = 0$ terms contribute greater than 95% of the rate calculated using eq 2.6.

(23) The λ_0 value less than 0.003 eV also produces the experimental slope at the indicated temperature; however, use of this λ_0 leads to a 5 order of magnitude reduction in the rate constant over the experimental temperature range, in contrast to the small change that is observed.

(24) In benzene, greater than 20% of the CT state of **2** decays by intersystem crossing to form the anthracene triplet state. Professor J. Goodman (University of Rochester), unpublished results.

(25) Vath, P. A.; Zimmt, M. B. Unpublished results.

(26) (a) Tepper, R. J.; Zimmt, M. B. *Chem. Phys. Lett.* **1995**, *241*, 566. (b) Corte's, J.; Heitele, H.; Jortner, J. *J. Phys. Chem.* **1994**, *98*, 2527.

(27) The calculation of these curves requires values of $\Delta_r G(T)$, $d\Delta_r G(T)/dT$ and $d\lambda_0(T)/dT$. The

$\Delta_r G(T)$ and $d\Delta_r G(T)/dT$ were obtained from the experimental data. The $d\lambda_o(T)/dT$ was evaluated by the Matyushov model.

$$\text{slope} = \left[-\frac{(\Delta G + \lambda)^2}{4\lambda k_B} \right] + \frac{(\Delta G + \lambda)T}{2\lambda k_B} \left(\frac{\partial(\Delta G)}{\partial T} \right) + \frac{T}{k_B} \left[\frac{2\lambda k_B T + 2\lambda(\Delta G + \lambda) - (\Delta G + \lambda)^2}{4\lambda^2} \right] \left(\frac{\partial\lambda}{\partial T} \right)$$

Chapter 3. Electron Transfer in Aromatic Solvents: The Importance of Quadrupolar Interactions

Molecular solvation calculations are performed on a donor-bridge-acceptor (DBA) molecule in polar and nonpolar environments. A strictly dipolar treatment of solvation reproduces experimental values of the reaction free energy, $\Delta_r G$, determined in nondipolar and weakly dipolar aromatic solvents but does not simultaneously predict accurate values of $\Delta_r G$ in highly dipolar solvents. By contrast, a solvation model that includes contributions from solvent dipole and quadrupole moments (*J. Chem. Phys.* **1999**, 111, 3630¹) reproduces $\Delta_r G$ values over a large polarity range. The reliability of the predicted $\Delta_r G$ and solvent reorganization energies, λ_0 , are assessed through fitting experimental rate data. The fits display good agreement with the experimental data and the donor-acceptor electronic couplings derived via these analyses agree with prior determinations. The availability of a model that generates reasonable predictions of $\Delta_r G$ and λ_0 allows a first exploration of the temperature dependence of solvent mediated electronic coupling.[§]

3.1 Introduction

Electron transfer between two chemical species or subunits represents a fundamental theme in many chemical transformations.^{2,3,4} Although the understanding of electron transfer reactions has evolved considerably in the past few decades, the ability to quantify solvent effects on electron transfer rates with simple analytical models has remained elusive. Continuum models are the most widely used approaches to calculation of solvation and solvent

[§] Reproduced with permission from Read, I.; Napper, A.; Zimmt, M. B.; Waldeck, D. H.; *J. Phys. Chem. A.* ; **2000**; 104(41); 9385-9394. Copyright 2000 American Chemical Society

reorganization energies.⁵ This work combines recently obtained^{5b,6a} electron transfer rate data over a range of solvent polarity with new data in 1,2,4-trimethylbenzene to evaluate two recently proposed molecular models for solvation and solvent reorganization energies in electron-transfer reactions.^{1,7} The results demonstrate the importance of including quadrupolar interactions for the interpretation of rate data in nondipolar and weakly dipolar aromatic solvents.

In the past two decades, much of the progress toward understanding electron transfer reactions has been made in characterizing the electronic coupling between the electron donor (D) and acceptor (A) groups, and its dependence on the structural and chemical features of the system under study.³ Donor-bridge-acceptor (DBA) systems figure prominently in these advances because of their ability to control the D/A geometry at which transfer occurs. The electron transfer rate constant's dependence on bridge length, bonding topology, state symmetry, and solvent environment have been characterized.^{3,4} In systems where the D and A groups are widely separated, the (nonadiabatic) transfer is viewed as an electron tunneling event, mediated by the orbitals of the intervening atoms (or molecules). A perturbation treatment of this process, known as "superexchange",⁸ successfully describes the D/A electronic interactions, whether they occur through space,⁹ through covalent bridges,⁴ or through solvent molecules.⁶

Recent studies from our collaboration^{5b,6a,10} focus on understanding electron transfer in highly curved DBA molecules. In these molecules, solvent influences the transfer dynamics through solvation and by mediating the superexchange interaction between the D and A groups. Given tractable theories of solvation and solvent-mediated superexchange, an accurate separation of these two effects is a particular challenge.

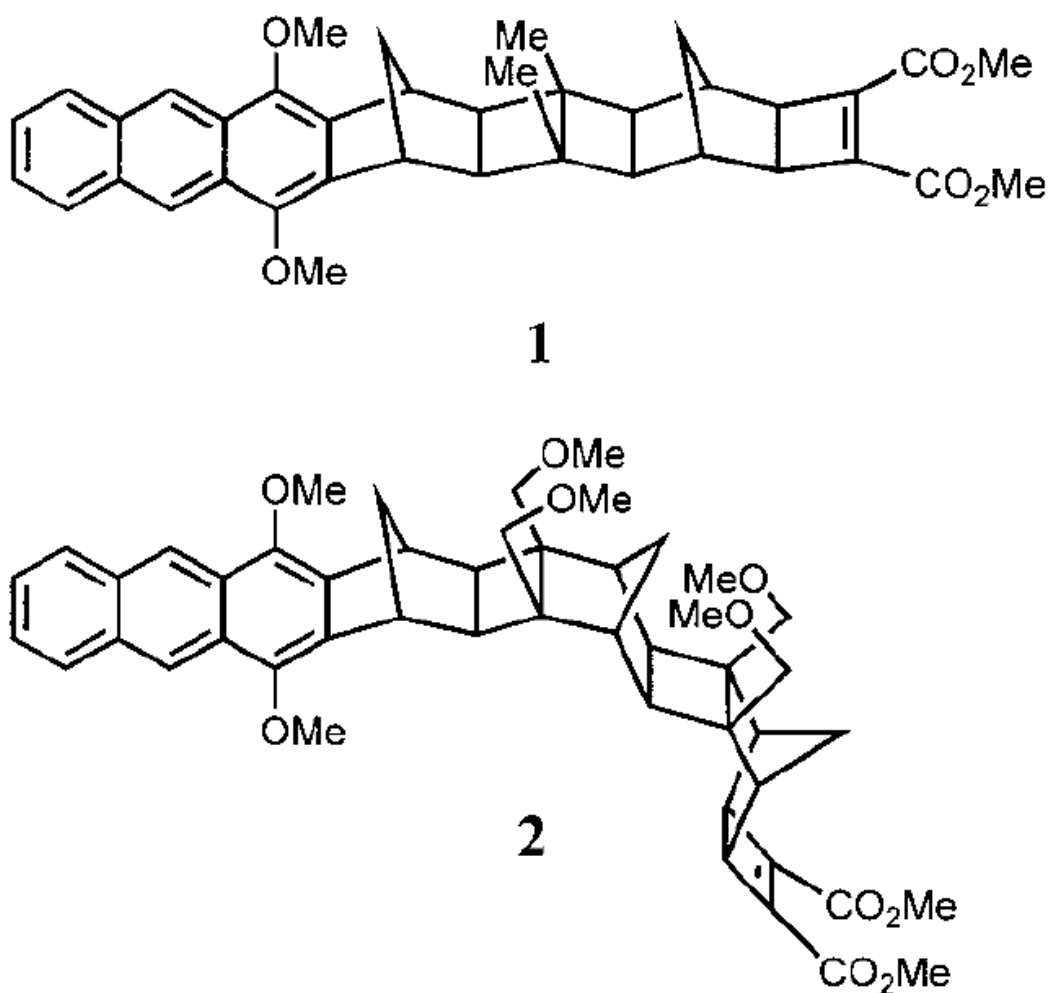


Figure 3.1 Molecular structure of the DBA molecules used in this work.

This study explores the ability of two recent molecular treatments of solvation^{1,7} to reproduce the solvent's influence on the thermodynamics of electron transfer and to allow precise determination of the electronic coupling as a function of solvent and temperature. The DBA structures used in these investigations are shown in Figure 3.1. Each molecule consists of (1) a dimethoxyanthracene unit that acts as the electron donor upon promotion to its lowest singlet excited state, (2) a cyclobutene dicarboxylate derivative that acts as the electron acceptor, and (3)

a rigid, connecting bridge. The dominant source of D/A coupling in **1** is superexchange mediated by the linear bridge.^{5b,10} Thus, the solvent's primary influence on the transfer dynamics in **1** is by way of solvation. The curved bridge in **2** forms a cleft between the donor and acceptor units. The cleft is sufficiently large to accommodate a solvent molecule. The magnitude and solvent dependence of the electron-transfer rate constants in **2** demonstrate that solvents, and in particular aromatic solvents, effectively mediate the required D/A interactions.

The rate constants obtained from these studies are interpreted through the semiclassical expression for the rate constant,¹¹

$$k_{\text{ET}} = \frac{2\pi|V|^2}{\hbar\sqrt{4\lambda_o\pi k_B T}} \sum_{n=0}^{\infty} e^{-S} \left(\frac{S^n}{n!}\right) \exp\left[\frac{-(\Delta_r G + \lambda_o + nh\nu)^2}{4\lambda_o k_B T}\right] \quad (3.1)$$

where $\Delta_r G$ is the reaction free-energy, λ_o is the outer-sphere (solvent) reorganization energy, ν is the frequency of the effective vibrational mode, and S is the Huang-Rhys factor given as the ratio of the inner-sphere reorganization energy, λ_i to $h\nu$. This treatment assumes that the molecule's vibrational modes can be represented using a single effective high-frequency mode. The low-frequency solute and solvent vibrational modes are treated classically. The electronic coupling $|V|$ is typically estimated or calculated. A major focus of this and our previous studies is to extract the coupling magnitude from experimental rate data.

Experimental determination of each parameter ($\Delta_r G$, ν , λ_i , λ_o , $|V|$) in eq 3.1 is desirable, although never achieved. Typically, the effective mode frequency ν and λ_i values are determined through fitting of experimental data (such as charge-transfer spectra¹²) or are calculated quantum chemically. The value of $\Delta_r G$ is often estimated through a combination of experimental redox data and dielectric continuum corrections to the solvation energy. The outer sphere reorganization energy λ_o is usually calculated from continuum solvation theory, or in

some cases may be extracted from charge-transfer spectra. A major problem with the dielectric continuum model is its failure to reproduce solvation and reorganization energies in nondipolar solvents¹³ and its prediction of unreasonable temperature dependencies in highly dipolar solvents.⁷ To date, molecular based models which are applicable in nondipolar or weakly dipolar solvents are unable to predict physically meaningful results in polar environments.¹⁴ A need exists for a model capable of computing free energies and reorganization energies across a large polarity range. Once appropriate values of the four solvation and reorganization parameters are generated, the electronic coupling $|V|$ can be extracted from experimental rate data. The absolute magnitude of the calculated electronic coupling is a strong function of the parameter set used. Nonetheless, comparisons between appropriately chosen systems are robust (see ref 10 for a detailed discussion of this issue).

The reaction free energy, $\Delta_r G$, for charge separation within **2** in aromatic solvents was previously evaluated directly from the rate constants of charge separation ($S_1 \rightarrow CT$) and recombination ($CT \rightarrow S_1$) that interconvert the anthracene excited state (S_1) and the charge transfer state (CT).^{6a} That investigation also demonstrated a very weak temperature dependence of the outer-sphere reorganization energy, λ_o .¹⁵ In conjunction with λ_i and ν values from CT spectra and calculations,¹⁶ it was possible to extract the electronic couplings for **2** in each solvent without the need for calculation of $\Delta_r G$ and λ_o . The experimental $\Delta_r G$ and λ_o were compared to the predictions of a molecular based solvation model that accounted for solvent molecule dipole moment and polarizability.^{6a,14} This model was able to reproduce the experimentally measured $\Delta_r G$ values and predicted a reasonable temperature dependence for λ_o in a variety of alkyl substituted benzene solvents.

This work presents the application of recently developed molecular based solvation models^{1,7} to the thermodynamic and rate data from **2** for a wide range of solvents and as a function of temperature. The more recently developed molecular model accounts for solvent dipole and quadrupole interactions with the solute and incorporates second-order contributions to the solvation chemical potential.^{1,7} This model should provide a more realistic description of $\Delta_r G$ and λ_o as a function of solvent and temperature. This work has two goals. First, it assesses the ability of the solvation models to mimic experimentally measured reaction free energies in nondipolar and weakly dipolar solvents and predict those in highly dipolar solvents. Second, it uses the calculated reorganization energies and reaction free energies to extract the solvent dependence of the electronic coupling $|V|$. The ultimate objective is to generate a thorough understanding of solvent's roles in determining the barrier, which impedes, and the coupling, which promotes, electron transfer.

3.2 Background

3.2.1. Continuum Prediction of $\Delta_r G$ and λ_o .

A crude, but often useful, treatment of the electron-transfer energetics models the solvent as a dielectric continuum. In this treatment, the donor- acceptor moieties are typically represented as individual spheres immersed in the continuum and separated by a distance, R_{cc} . $\Delta_r G$ is calculated using the Rehm-Weller equation,¹⁷

$$\Delta_r G = \Delta_{\text{vac}} G + \frac{e^2}{4\pi\epsilon_o} \left(\frac{1}{2r_d} + \frac{1}{2r_a} - \frac{1}{R_{cc}} \right) \left(\frac{1}{\epsilon} - 1 \right) \quad (3.2)$$

where $\Delta_{\text{vac}}G$ is the free energy of the electron transfer in a vacuum, e is the charge on the electron, and ϵ is the solvent's static dielectric constant. r_d and r_a are the spherical radii of the donor and acceptor. Results from these calculations are used to provide a reference point for the molecular model's predictions. The solvent reorganization energy may also be calculated using continuum theory, by the relation

$$\lambda_o = \frac{e^2}{4\pi\epsilon_o} \left(\frac{1}{2r_d} + \frac{1}{2r_a} - \frac{1}{R_{cc}} \right) \left(\frac{1}{\epsilon_\infty} - \frac{1}{\epsilon} \right) \quad (3.3)$$

where ϵ_∞ is the high-frequency dielectric constant, taken to be the square of the solvent's refractive index.

3.2.2. Molecular Model for $\Delta_r G$.

In earlier work, a dipolar, polarizable hard sphere model for the solvent was used to compute both $\Delta_r G(T)$ and $\lambda_o(T)$ for **2** in weakly dipolar aromatic solvents.^{6a,14} The model treated the solute as a polarizable sphere with different permanent dipole moments for the locally excited and charge transfer states. The model was developed particularly for application to weakly dipolar systems and is expected to fail in highly dipolar solvents since solute-solvent-solvent correlations are neglected. The present investigation uses a more sophisticated treatment of the solute-solvent interactions and compares two separate approaches to the modeling. First, the $\Delta_r G$ values are computed using a revised dipolar, polarizable model.⁷ This treatment includes higher order contributions to the solvation energy, thus providing a more accurate description of solvation in highly dipolar solvents. Second, a solvation model that also explicitly incorporates quadrupolar interactions is used to compute the solvation energies.¹ In both cases, the gas phase

solvent dipole moments are renormalized to account for inductive dipolar and quadrupolar (when relevant) interactions with the surrounding solvent. This renormalization procedure is outlined by Gray and Gubbins.¹⁸

Matyushov calculates $\Delta_r G$ as the sum of four contributions,

$$\Delta_r G = \Delta_{\text{vac}} G + \Delta_{\text{dq,i}} G^{(1)} + \Delta_{\text{disp}} G + \Delta_i G^{(2)} \quad (3.4)$$

where $\Delta_{\text{vac}} G$ is the free energy of the process in a vacuum, $\Delta_{\text{dq,i}} G^{(1)}$ is the contribution from first-order dipole, quadrupole, and induction interactions, $\Delta_{\text{disp}} G$ is the contribution from dispersion interactions and $\Delta_i G^{(2)}$ is the contribution from second-order induction interactions. The $\Delta_{\text{dq,i}} G^{(1)}$ term includes dipole-dipole and dipole-quadrupole interactions between the solute dipole and the solvent electric moments and includes the induction interactions that arise from the polarizability of both the solute and solvent. It is calculated through the relationship

$$\Delta_{\text{dq,i}} G^{(1)} = - \frac{(m_e^2 - m_g^2)}{R_{\text{eff}}^3} f(y_d, y_q) \Psi^P(y_d, y_q) \quad (3.5)$$

where m_e is the solute dipole moment of the charge transfer state, and m_g is the reactant state dipole moment. The function $f(y_d, y_q)$ renormalizes the solute dipole moment to account for its size and polarizability. It is given by

$$f(y_d, y_q) = \left[1 - \frac{2\alpha_0}{R_{\text{eff}}^3} \Psi^P(y_d, y_q) \right]^{-1} \quad (3.6)$$

Here α_0 is the solute polarizability and $\Psi^P(y_d, y_q)$ is referred to as the "polarity response function". R_{eff} represents the effective radius of a spherical dipolar solute. It accounts for the local packing of solvent molecules against the solute sphere and is determined through the

solute-solvent hard sphere pair distribution function $g_{0s}^{(0)}(r)$, namely

$$\frac{1}{R_{\text{eff}}^3} = 3 \int_0^\infty \frac{dr}{r^4} g_{0s}^{(0)}(r) \quad (3.7)$$

Matyushov evaluated the integral numerically and fit it to the following polynomial form; i.e.

$$\frac{1}{R_{\text{eff}}^3} = \frac{I_{0s}^{(2)}}{\sigma^3} \quad (3.8)$$

The form of the $I_{0s}^{(2)}$ is given explicitly in the Appendix. The polarity response function, $\Psi^P(y_d, y_q)$, is written in terms of the reduced dipolar density, y_d , the quadrupolar density, y_q , and the solute-solvent perturbation integrals. The densities are computed using the relations

$$y_d = \frac{4\pi}{9} \frac{\rho}{kT} m'^2 + \frac{4\pi}{3} \rho \alpha \quad (3.9a)$$

$$y_q = \frac{2\pi}{5} \frac{\rho}{\sigma^2 kT} Q^2 \quad (3.9b)$$

where Q is the average quadrupole moment (Table 3.2), m' is the renormalized solvent dipole moment,^{1,7} ρ is the solvent number density, α is the solvent polarizability, and σ is the solvent hard sphere diameter. Matyushov^{1,7} has shown that the perturbation integrals are well represented by a polynomial interpolation and writes $\Psi^P(y_d, y_q)$ as

$$\Psi^P(y_d, y_q) = \frac{\frac{y_d I_{0s}^{(2)} + y_q I_6^{(2)}}{I_{0s}^{(2)}}}{1 + \frac{y_d^2 \kappa_d I_{0s}^{(3)} + y_d y_q \kappa_{dq} I_{DDQ}^{(3)} + y_q^2 \kappa_q I_{DQQ}^{(3)}}{y_d I_{0s}^{(2)} + y_q I_6^{(2)}}} \quad (3.10)$$

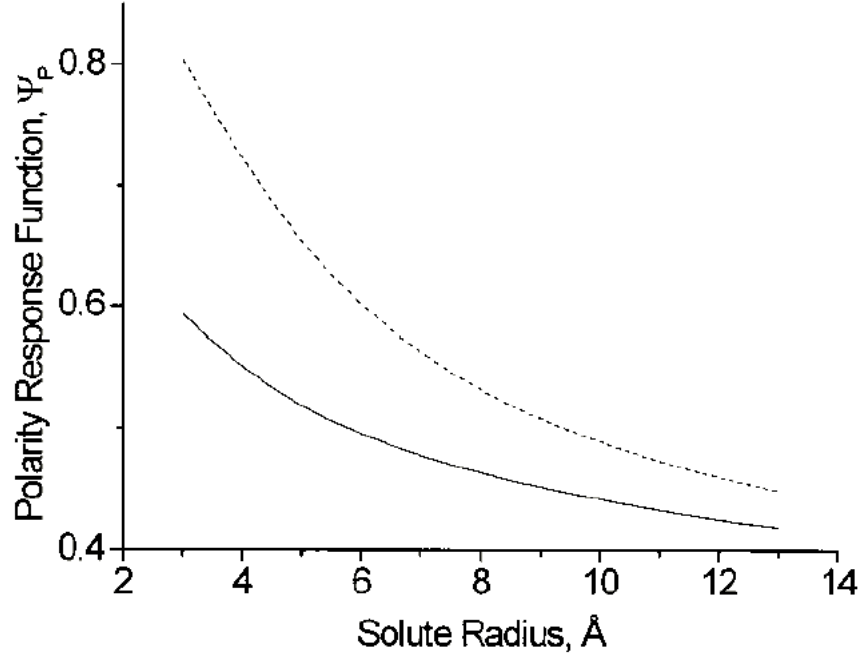


Figure 3.2 Behavior of the polarity response function for the dipole (solid line, $\langle Q \rangle = 0 \text{ D \AA}$) and dipole-quadrupole (dashed line, $\langle Q \rangle = 3 \text{ D \AA}$) models are shown as a function of the solute radius.

The explicit form of the polynomial interpolation for the two- and three-particle perturbation integrals ($I^{(2)}$, $I^{(3)}$) are written in the Appendix.¹⁹ The κ_i parameters correct for saturation of the solvent response that arises from three particle (solute-solvent-solvent) correlations.¹ These factors depend on the ratio of solute-solvent diameters, $d = 2R_o/\sigma$, through the relations,

$$\kappa_d = 1 + \left[\frac{d}{(d+1)} \right]^2 \quad \kappa_q = 2 + \frac{1}{(d^5 + 2)}$$

$$\kappa_{dq} = 2 - \frac{d^5}{(d^5 + 2)}$$

Figure 3.2 shows the dependence of the response function (eq 3.10) on the effective solute radius, R_o , for the dipole model ($Q = 0$, solid line) and the dipole-quadrupole model ($Q = 3.0 \text{ D \AA}$, dashed line). These calculations were performed using constant values for the solvent hard

sphere diameter (5 Å), solvent polarizability (10 Å³), and dipole moment (2 D). The solute polarizability and dipole moment were chosen to be 70 Å³ and 34 D, respectively. In both models, the magnitude of the calculated response function decreases with increasing solute radius. According to eq 3.5, the predicted free energies become more negative as the size of the solute decreases. Figure 3.2 also shows that inclusion of quadrupolar interactions increases the magnitude of the polarity response function. This behavior indicates that quadrupolar interactions are stabilizing, and that their inclusion will require a larger solute radius, relative to the dipolar model, to reproduce a given value of the reaction free energy, $\Delta_r G$.

Second-order induction interactions of the solute dipole with the solvent molecules are accounted for by the $\Delta_r G^{(2)}$ term. These interactions arise from correlations of polarization fluctuations generated by the solvent's induced dipoles.⁷ Matyushov relates these interactions to the solvent polarizability and the high-frequency dielectric constant, ϵ_∞ , and writes,

$$\Delta_r G^{(2)} = -(m_e^4 - m_g^4) f(y_e) \frac{1}{200\pi\rho kT} \frac{(\epsilon_\infty - 1)^2}{(\epsilon_\infty + 2)^2} \times [9 + 8(\epsilon_\infty - 1)^2] I_{0s}^{(4)} \quad (3.11)$$

where the quantity $y_e = (4\pi/3) \rho\alpha$ is the reduced polarizability density of the solvent. The function $f(y_e)$ renormalizes the solute dipole by the polarizability response of the solvent. Its value is calculated using

$$f(y_e) = \left[1 - \frac{2\alpha_0}{R_{\text{eff}}^3} \Psi^P(y_e) \right]^{-1} \quad (3.12)$$

The polarizability response function, $\Psi^P(y_e)$, is given by

$$\Psi^P(y_e) = \frac{y_e}{1 + \kappa_d y_e I_{0s}^{(3)}/I_{0s}^{(2)}} \quad (3.13)$$

Note that eq 3.13 is derived directly from the polarity response function (eq 3.10). When the solvent has no permanent dipole or quadrupole moment, the polarizability response function of the fluid is given by this term.

The dispersion contribution, $\Delta_{\text{disp}}G$, has a relatively small effect on the overall free energy (see Table 3.7). Its value can be calculated from the solvent-solvent Lennard-Jones energy, ϵ_{LJ} , and the solvent hard sphere diameter σ . These parameters were obtained through the additivity method described by Ben-Amotz²⁰ $\Delta_{\text{disp}}G$ is given by

$$\Delta_{\text{disp}}G = -\frac{\Delta\gamma'}{\alpha_s} 8\eta\epsilon_{\text{LJ}}\left(\frac{\sigma}{R_{\text{eff}}}\right)^3 \quad (3.14)$$

where η is the reduced packing density, defined as $(\pi/6)\rho\sigma^3$, and α_s is the solvent polarizability.

The parameter $\Delta\gamma'$ is determined by

$$\Delta\gamma' = \Delta\alpha_o \frac{2I_o}{I_o + I_s} \quad (3.15)$$

where $\Delta\alpha_o$ is the change in polarizability between the locally excited state and the charge transfer state of the solute, I_o is the ionization potential of the solute and I_s is the ionization potential of the solvent. $\Delta\gamma'$ is one of three adjustable parameters determined by a simultaneous fit of the experimental $\Delta_r G$ values measured as a function of temperature in all of the alkylated benzene solvents (The best fit values are reported in Table 3.1). Values for the individual contributions to $\Delta_r G$ are listed in Table 3.7.

3.2.3. Molecular Model for the Reorganization Energy, λ_o .

The same polarizable hard-sphere model¹ is used to compute the reorganization energy

λ_0 . The reorganization energy is written as a sum of three components $\lambda_0 = \lambda_p + \lambda_{\text{ind}} + \lambda_{\text{disp}}$, where λ_p accounts for solvent reorganization arising from the solvent dipole and quadrupole moments, λ_{ind} is the contribution from induction forces and λ_{disp} accounts for the dispersion interactions. An expression for λ_p was derived using the linear response approximation for the chemical potential,¹⁴ so that

$$\lambda_p = \frac{(m_e - m_g)^2}{R_{\text{eff}}^3} [f(y_d, y_q) \Psi^P(y_d, y_q) - f(y_e) \Psi^P(y_e)] \quad (3.16)$$

where $\Psi^P(y_d, y_q)$ is given by eq 3.10 and $\Psi^P(y_e)$ is given by eq 3.13. This contribution accounts for the reequilibration of the solvent's nuclear modes to the newly formed electronic configuration of the charge transfer state. Although the induction forces make a relatively small contribution to the overall reorganization energy in highly polar solvents, in weakly polar systems the dipolar contributions are small and induction interactions are significant. According to ref 7, the induction term can be calculated through,

$$\lambda_{\text{ind}} = \frac{(m_e^2 - m_g^2)^2 f(y_e)^2 (\epsilon_\infty - 1)^2}{kT400\eta\sigma^6 (\epsilon_\infty + 2)^2} \left[3 + \frac{8}{3}(\epsilon_\infty - 1)^2 \right] I_{0s}^{(4)} \quad (3.17)$$

The polynomial form of the two-particle perturbation integral $I_{0s}^{(4)}$, is given in the Appendix. The contribution from the dispersion forces is expected to be small in both dipolar and nondipolar solvents and in most cases these energies can be neglected. However, they can become significant if the solvent diameter and density is large. Matyushov defines $\lambda_{\text{disp}}^{21}$ as a second-order perturbation over the solute-solvent dispersion potential so that

$$\lambda_{\text{disp}} = \frac{\Delta\gamma^2}{\alpha_s^2} \frac{8\eta}{3} \beta \epsilon_{\text{LJ}}^2 J_1(\rho^*, r_{0s}) \quad (3.18)$$

Table 3.1 Best Fit Parameters Used in $\Delta_r G$ Calibrations.

^a Literature values obtained from *CRC Handbook*, 78th ed.; CRC Press: Boca Raton, FL, 1998. ^b TMB is 1,2,4-trimethylbenzene. ^c TIP is 1,3,5-triisopropylbenzene. ^d Literature value could not be found. Value listed is for 1,3,5-tri-*tert*-butylbenzene.

	model		lit. ^a
	dipole	dipole–quadrupole	
solute radius (Å)	6.19	7.25	
$\Delta_{\text{vac}}G$ (eV)	0.326	0.340	
$\Delta\gamma'$ (Å ³)	−9.5	1.7	
	Solvent Polarizability (Å ³)		
benzene	10.3	9.5	10.0
toluene	11.8	10.9	11.8
cumene	15.5	16.3	16.0
mesitylene	15.2	14.8	15.5
TMB ^b	14.6	15.5	
TIP ^c	26.9	31.7	31.8 ^d

The polynomial form of the integral J_1 is given in the Appendix along with the calculated values of λ_o , λ_p , λ_{disp} , and λ_{ind} predicted by the two treatments.²²

3.3 Results and Discussion

3.3.1. Calculation of $\Delta_r G$.

Simulation of the $\Delta_r G$ values using the molecular model requires determination of three parameters: $\Delta_{\text{vac}}G$, the solute radius R_o , and $\Delta\gamma'$. The $\Delta_r G$ values for **2** in every solvent (benzene, toluene, cumene, mesitylene, 1,2,4-trimethylbenzene (TMB), and triisopropylbenzene (TIP)) and temperature were fit, simultaneously, to eq 3.4 using Microsoft Excel 97 on a Pentium based PC. The solvent dipole and quadrupole moments were calculated at the RHF/6-31G**// RHF/6-31G** level of theory using Gaussian 98²³ on a Silicon Graphics Power Indigo workstation (Tables 3.2 and 3.3). The effective quadrupole moment $\langle Q \rangle$ reported in Table 3.3 was used in

the calculations. This effective quadrupole gives exact results for axially symmetric quadrupole tensors and is correct through second order for nonaxially symmetric quadrupole tensors. With the exception of benzonitrile, the quadrupole tensors of the investigated solvents are axially symmetric, or nearly so. The dipole moment of the anthracene excited state was set to 0 D and the dipole moment of the charge separated state was calculated to be 34 D.²⁴ In previous work, the solute polarizability was estimated as 100 Å³, but recent calculations (RHF/6-31+G(d)) suggest that this value is too high and a solute ground-state polarizability of 70 Å³ was used. After initial values of the three parameters were determined, the literature value of the solvent's polarizability was adjusted (<10%) to improve the fits (see Table 3.1). The solvent parameters used in the calculations are given in Tables 3.1-3.3.

Figure 3.3 presents the fits of the two models to the experimental $\Delta_r G$ data, and Table 3.1 presents the parameter set for each fit. It is clear from the plots that both models can reproduce the data in nondipolar solvents but they predict very different $\Delta_r G$ values in highly dipolar solvents.

Table 3.2 Solvent Parameters Used in Matyushov Modeling^a

^a TMB is 1,2,4-trimethylbenzene. TIP is 1,3,5-triisopropylbenzene. ^b The vacuum dipole moment. ^c The hard sphere solvent diameter. ^d The Lennard-Jones energy parameter. ^e The packing fraction at 295 K.

solvent	m^b (D)	σ^c (Å)	ϵ_{LJ}^d (K)	η^e
benzene	0	5.28	544	0.520
toluene	0.29	5.68	603	0.543
cumene	0.25	6.29	679	0.561
mesitylene	0.07	6.40	720	0.593
TMB	0.30	6.31	720	0.579
TIP	0.08	7.40	949	0.552
acetonitrile	4.06	4.14	405	0.425
benzonitrile	4.2	5.68	698	0.562

Table 3.3 Diagonal Quadrupole Moment Tensor Components Used To Compute $\langle Q \rangle$ ^a

^a TMB is 1,2,4-trimethylbenzene. TIP is 1,3,5-triisopropylbenzene. $\langle Q \rangle = \left[\sqrt{\frac{2}{3}} \sum Q_{ii}^2 \right]^{1/2}$.

solvent	Q_{xx} (D Å)	Q_{yy} (D Å)	Q_{zz} (D Å)	$\langle Q \rangle$ (D Å)
benzene	4.146	4.146	-8.288	8.288
toluene	4.122	4.122	-7.893	7.896
cumene	3.624	4.206	-7.830	7.836
mesitylene	3.954	3.519	-7.464	7.467
TIP	2.848	4.835	-7.683	7.770
TMB	4.209	3.088	-7.299	7.326
acetonitrile	-3.369	1.685	1.685	3.369
benzonitrile	-12.61	13.82	-1.214	15.39

In the nitrile solvents the $S_1 \Leftrightarrow CT$ equilibrium was not measurable. As a result a comparison of calculated and experimental $\Delta_r G$ values is not possible. The best fit value of the solute radius in the dipole-quadrupole model, 7.25 Å, is considerably larger than in the dipole analysis, 6.19 Å. This difference is consistent with the larger polarity response function and increased stabilization energy predicted by the model that includes solvent quadrupoles (Figure 3.2). AM1 calculations of **2** indicate that a sphere of ~ 7.0 Å is required to fully encapsulate the solute. This result is consistent with the best fit solute radius found using the dipole-quadrupole model. The best fit $\Delta\gamma'$ was found to be ~ -9.5 Å³ for the dipole model and 1.7 Å³ for the dipole-quadrupole model. In both cases, the small size of $\Delta\gamma'$ suggests similar polarizabilities for the LE and CT states. In the dipole-quadrupole model the dispersion makes a negligible contribution to the reaction free energy. In the dipole model the dispersion term plays a significant role in determining the proper ordering of $\Delta_r G$ with solvent. Quantum chemical calculations of $\Delta_{vac} G$ were performed using the vacuum ionization potentials and electron affinities of the donor-acceptor pair. The results predict that $\Delta_{vac} G$ is $\sim 1.1 \pm 1.0$ eV. The polynomial form of the two-particle perturbation integral $I_{0s}^{(4)}$, is given in the Appendix. The contribution from the dispersion forces is expected to be small in both dipolar and nondipolar solvents and in most cases these energies can be neglected. However, they can become significant if the solvent diameter and density is large. Matyushov defines λ_{disp} as a second-order perturbation over the solute-solvent dispersion potential so that

$$\lambda_{disp} = \frac{\Delta\gamma'^2}{\alpha_s^2} \frac{8\eta}{3} \beta \epsilon_{LJ}^2 J_1(\rho^*, r_{0s}) \quad (3.18)$$

Table 3.1 shows that the best fit value for each model lies within the uncertainty limit of the calculation. Since the values of $\Delta_{\text{vac}}G$ for each model are similar, their absolute magnitude is not expected to effect the overall results. Among the three fit parameters, variation of the solute hard sphere radius, R_o , between the values determined in the two models, exerts the greatest impact on the fitting results. Figure 3.3 shows that both molecular approaches accurately reproduce the observed free energies in nondipolar and weakly dipolar solvents. Because of model specific differences in the best fit solute parameters, the predicted Δ_rG values are strikingly different in the nitrile solvents. The dipolar model predicts a free energy of -1.47 eV in acetonitrile and -1.57 eV in benzonitrile at 300 K, whereas the dipole-quadrupole model predicts a Δ_rG of -0.71 eV in acetonitrile and -0.88 eV in benzonitrile. It is evident that use of the dipole-quadrupole model leads to significantly smaller estimates of the reaction exoergicity in polar solvents. The experimental redox potentials in acetonitrile place the energy of the infinitely separated D^+ and A^- ions -0.51 eV below the energy of the anthracene excited state.¹⁶ Use of continuum models for Coulomb attraction and solvation corrections (eq 3.2) suggest the Δ_rG values are -0.56 eV in acetonitrile and -0.53 eV in benzonitrile (Table 3.4). These comparisons indicate that the dipole model predicts unrealistically negative Δ_rG values in both of the nitrile solvents. The inclusion of quadrupole moments when fitting the data in the nondipolar and weakly dipolar aromatic solvents provides more realistic solute parameters and generates more reasonable Δ_rG values across a wider range of polarity. The dipole-quadrupole model's prediction of a more negative Δ_rG in benzonitrile than in acetonitrile arises from the difference in their quadrupole moments and warrants comment. The model¹ assumes that the dipole moment vector and the principal axis of the quadrupole tensor are collinear, which is incorrect for benzonitrile. Since the quadrupole tensor of benzonitrile is nonaxial, corrections beyond second order may be important.²⁵ As a

result the sum of the two solvation contributions may be less effective than that predicted by the model. For the dipole model, the dipolar density, y_d , is the primary solvent parameter controlling the magnitude of the polarity response function. It accounts for interactions involving the solvent permanent dipole and the solvent polarizability (eq 3.9a).

Table 3.4 Experimental and Calculated $\Delta_r G$ (eV) at 295 K ^a

	expt	model		
		dipole	dipole–quadrupole	continuum
benzene	−0.109	−0.112	−0.115	−0.072
toluene	−0.089	−0.086	−0.083	−0.094
cumene	−0.058	−0.054	−0.051	−0.094
mesitylene	−0.039	−0.033	−0.032	−0.070
TMB	−0.064	−0.062	−0.057	−0.060
TIP ^b	−0.013	−0.020	−0.018	−0.070
acetonitrile		−1.467	−0.713	−0.560
benzonitrile		−1.570	−0.882	−0.530

^a TMB is 1,2,4-trimethylbenzene. TIP is 1,3,5-triisopropylbenzene.

^b Results tabulated at 282 K.

Many of the aromatic solvents employed in this investigation possess small (or zero) permanent dipole moments; thus the stabilization energy from induction forces dominates $\Delta_r G$. Since these interactions are small, the experimental free energies and their temperature dependencies are reproduced by decreasing the solute radius, which enhances the solvent's polarity response function, $\Psi^P(y_d, 0)$. Although the required, best fit solute radius is clearly too small, one obtains a reasonable fit to the data in a similar set of solvents, such as the alkylbenzenes. However, in those solvents where the polarity response function is dominated by permanent dipole moments, as in acetonitrile and benzonitrile, the small cavity radius predicts unrealistically large solvation energies.

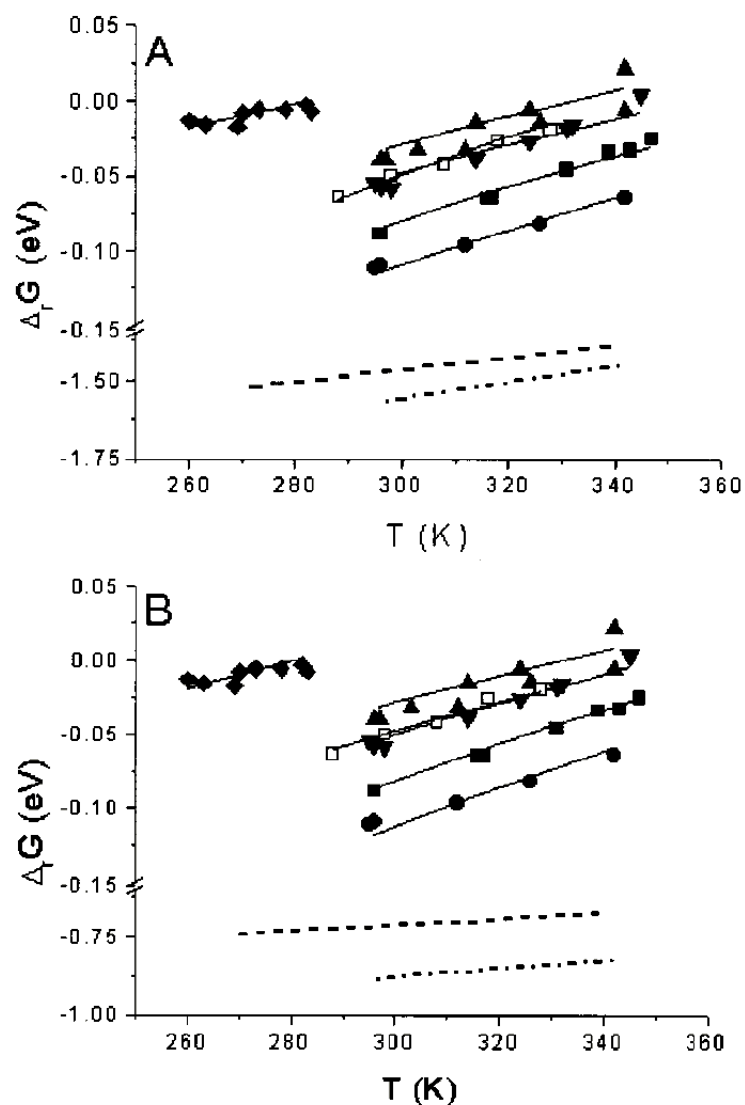


Figure 3.3 The lines show the temperature-dependent free energies calculated using the dipole model in panel A and the dipole-quadrupole model in Panel B. The solid lines show the predicted free energies in alkylbenzenes, the dashed line shows the predicted free energy in acetonitrile and the dashed-dotted line shows the predicted free energy in benzonitrile. Experimental data is shown for benzene (●), toluene (■), cumene(▼), mesitylene (▲), TMB (□) and TIP (◆). Note that the y-axis is broken in both plots.

The small differences between the predicted $\Delta_r G$ values in acetonitrile and benzonitrile result from their different polarizabilities.

Inclusion of quadrupole solvation provides a more realistic description of the intermolecular forces experienced by the solute in aromatic solvents. The best fit solute radius is larger than that found with the dipole model and is in reasonable agreement with the molecule's van der Waals radius. The $\Delta_r G$ values calculated using the dipole-quadrupole model are shown in Figure 3.3B. (The dipole-quadrupole polarity response function (eq 3.10) includes both y_d and y_q .) For the nondipolar and weakly dipolar aromatic solvents, y_q and y_d are comparable, so that one observes a large increase in the stabilization energy for the quadrupole model compared to the dipole model. This produces a 1.1 Å increase in the best fit solute radius compared to the dipole only model. As a result, the $\Delta_r G$ values in the nitrile solvents are markedly different from those calculated when the quadrupole terms are not included (see Table 3.4). This change reflects the decreased solvation provided by the dipole density for larger R_o values. Because the quadrupolar density makes only a small contribution to the polarity response function in acetonitrile, the $\Delta_r G$ value is largely determined by dipole interactions.

The results show that the dipole-quadrupole model can predict reasonable $\Delta_r G$ values across a wide range of polarity. For comparison, calculations of $\Delta_r G$ using continuum theory are presented in Table 3.4. The results show that these solvents can be divided into three groups: nondipolar (benzene, mesitylene, TIP), weakly dipolar (toluene, cumene), and highly dipolar (acetonitrile, benzonitrile). In each group, the continuum estimates are identical: -0.07 (nondipolar), -0.094 (weakly dipolar), and \sim -0.54 (highly dipolar). As expected, these results do not agree with experiment. The value of $\Delta_r G$ in the alkylated benzene solvents are determined primarily by the size of the solvent molecules (an observation consistent with the solvents ability

to pack against the solute). For the nitrile solvents, exact experimental data is not available, but because the quadrupole moment of acetonitrile is significantly smaller than benzonitrile, one expects different $\Delta_r G$ values in these two solvents. In addition, the continuum model overestimates the stabilization energy of the weakly dipolar solvents toluene and cumene. These findings confirm the inability of the continuum model to reproduce the experimentally determined $\Delta_r G$ values.

3.3.2. Calculation of the Reorganization Energy.

Table 3.7 presents the calculated λ_o values from both models and list the individual contributions to the reorganization energy as a function of temperature. Although the calculated λ_o are physically reasonable, it is difficult to assess their accuracy as very little experimental data is available for λ_o . In the nondipolar and weakly dipolar solvents, the dipole only model predicts λ_{ind} to be the dominant contributor to the overall reorganization energy. In contrast, when the quadrupole moments are included, λ_p is the dominant term in every solvent. This result can be understood in terms of the dipole and quadrupole densities. In the dipole model, dipolar and polarization interactions contribute to the polarity response function of the fluid. For a nondipolar solvent, $\Psi^P(y_d, 0)$ and $f(y_d, 0)$ reduce to $\Psi^P(y_e)$ and $f(y_e)$, respectively. The two terms in eq 3.16 cancel and λ_p is zero. If the solvent molecule possesses a dipole moment, the dipolar density increases to a value greater than the polarizability density, y_e . In highly polar solvent, e.g., nitriles, the dipole contribution dominates. In the dipole-quadrupole model, λ_p contains an additional contribution from the quadrupole density, y_q . Because the quadrupole density exceeds the polarizability density in every solvent, λ_p always makes the dominant contribution to the

overall reorganization energy. The best fit solute radius is larger when quadrupole moments are included in the data fitting; thus contributions from induction forces are reduced compared to those in the dipole model. Both the dipole and dipole-quadrupole models suggest that λ_o decreases with increasing temperature in all solvents. This prediction agrees with experimental results.^{7,26} By contrast, the continuum model predicts that λ_o increases with temperature in highly dipolar solvents.

Dispersion interactions make negligible contributions to λ_o in highly dipolar solvents but increase in importance as the polarity of the solvent decreases. According to eq 3.18, λ_{disp} depends quadratically on the Lennard-Jones energy ϵ_{LJ} (the magnitude of which is correlated to the size and number of substituents on the aromatic ring²⁰) and the reduced packing density, η . The dipole model predicts significant λ_{disp} values in the nondipolar aromatic systems because of the increased contribution from the perturbation integral, J_1 . This contribution is less significant for larger values of R_o . As a result, the dipole-quadrupole model predicts negligible values for λ_{disp} in every solvent.

3.3.3. Fitting the Rate Constants.

With values for λ_i , ν , λ_o , and $\Delta_r G$, it is possible to fit the experimentally determined electron-transfer rate data to the semiclassical rate equation and to determine the electronic coupling, $|V|$. As discussed elsewhere for **2**,¹⁰ λ_i was taken to be 0.39 eV and ν was taken to be 1410 cm^{-1} . The rate constants were fit using the results from both the dipole and the dipole-quadrupole model. As found previously,^{6a} attempts to reproduce the observed rate constants using the λ_o predicted by the models and a constant $|V|$ were not entirely successful. The solid lines in Figure 3.4 show the predicted temperature dependence of the electron-transfer rate

constants in the nitrile solvents. These curves were obtained using the $\Delta_r G$ and λ_o derived from the dipole-quadrupole model and a temperature independent value of $|V|$. Clearly, the fits are poor. The dashed lines represent fits in which $|V|$ and $\lambda_o(295\text{ K})$ are treated as adjustable parameters. The temperature dependence of the reorganization energy was predicted by the dipole- quadrupole model. These fits are excellent and predict electronic couplings of 27 cm^{-1} in acetonitrile and 93 cm^{-1} in benzonitrile. These values agree well with those found from an earlier continuum treatment,^{5b} but are 4-5-fold larger than values predicted using an alternate ion pair solvation model.¹⁰

Two different approaches were taken to fit the data in the alkylated aromatic solvents. In the first approach, the $\Delta_r G$ and $d\lambda_o/dT$ were taken from the model. Both $|V|$ (assumed temperature independent) and $\lambda_o(295\text{ K})$ were allowed to vary in each solvent. The fits to the rate constant data for the alkylated benzene solvents are shown as a function of temperature in Figure 3.5 for the dipole model (panel A) and the dipole- quadrupole model (panel B). In every case, the sum of eq 3.1 was evaluated through the sixth term. The best fit parameters obtained from each method are summarized in Table 3.5. In the second approach, it was assumed that the $\Delta_r G$ and λ_o values predicted by the dipole-quadrupole model are accurate and the electronic coupling was treated as both solvent and temperature dependent. The results of this analysis are shown in Figure 3.6.

In the first approach, fitting the rate constant data (Figures 3.4 and 3.5) provides values for the electronic coupling and the room temperature reorganization energy as a function of solvent (see Table 3.5). The electronic coupling decreases monotonically as the alkyl substitution on the phenyl ring increases for both models.

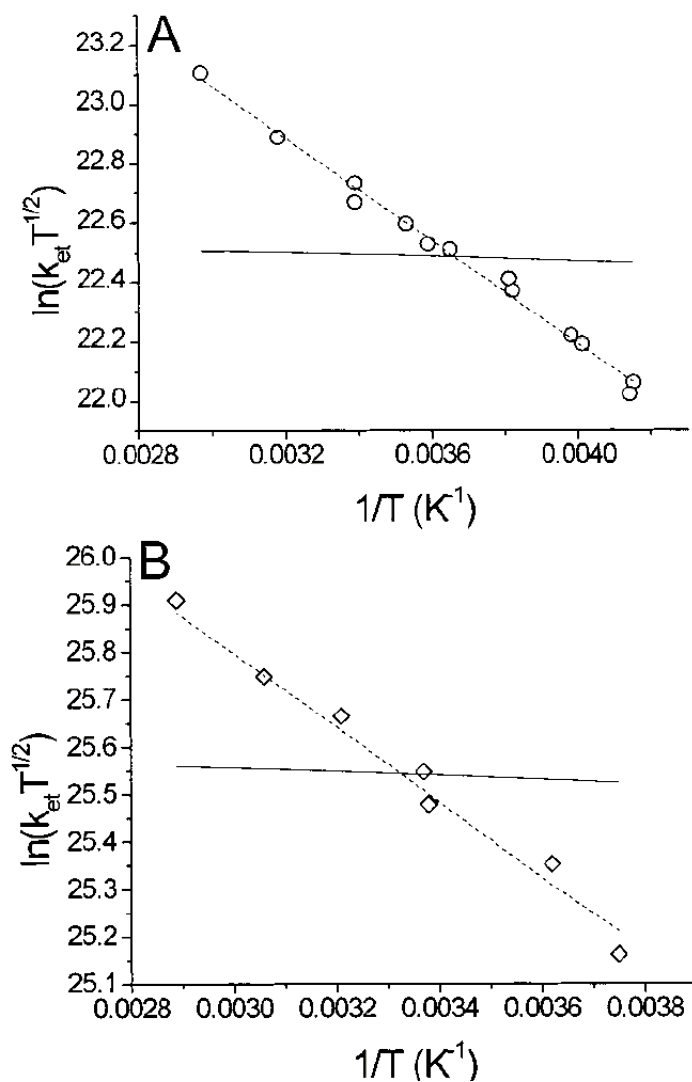


Figure 3.4 Experimental rate data is shown for acetonitrile (O, Panel A) and benzonitrile (\diamond , Panel B). The solid lines represent fits using the free energy and reorganization energy calculated using the dipole-quadrupole model. The dashed lines represent the calculated rate constants when the free energies and the temperature dependence of λ_0 was calculated using the dipole-quadrupole model but λ_0 (295 K) was varied.

As discussed elsewhere,^{6a} this trend results from increased steric bulk of the solvent molecules inhibiting access of the aromatic core to the molecular cleft between the donor and acceptor groups. This results in decreased through solvent coupling. The magnitudes of the coupling elements are slightly different from those reported earlier. In cumene and mesitylene, a decreased quality of the fitted curves is observed. There are several possible explanations for the effect. First, the temperature dependence of λ_0 calculated by the molecular models may be too steep. The fits to the data using a constant λ_0 are significantly better than those shown here. However, this explanation cannot explain the particularly steep decrease of the rate constant in mesitylene with increasing temperature.

Table 3.5 Regression Estimates of the Electronic Couplings and Reorganization Energies Obtained Using the Matyushov Solvation Model ^a

solvent	model			
	dipole		dipole–quadrupole	
	$ V $ (cm ⁻¹)	$\lambda_0(295)$ (eV)	$ V $ (cm ⁻¹)	$\lambda_0(295)$ (eV)
benzene	9.47	0.239	10.1	0.258
toluene	8.84	0.220	8.93	0.217
cumene	6.70	0.180	6.33	0.167
mesitylene	6.12	0.152	5.91	0.144
TMB	7.99	0.189	6.98	0.162
TIP	1.03	0.001	1.09	0.009
acetonitrile	31.6	2.51	27.7	1.49
benzonitrile	116.7	2.60	92.7	1.67

^a TMB is 1,2,4-trimethylbenzene. TIP is 1,3,5-triisopropylbenzene.

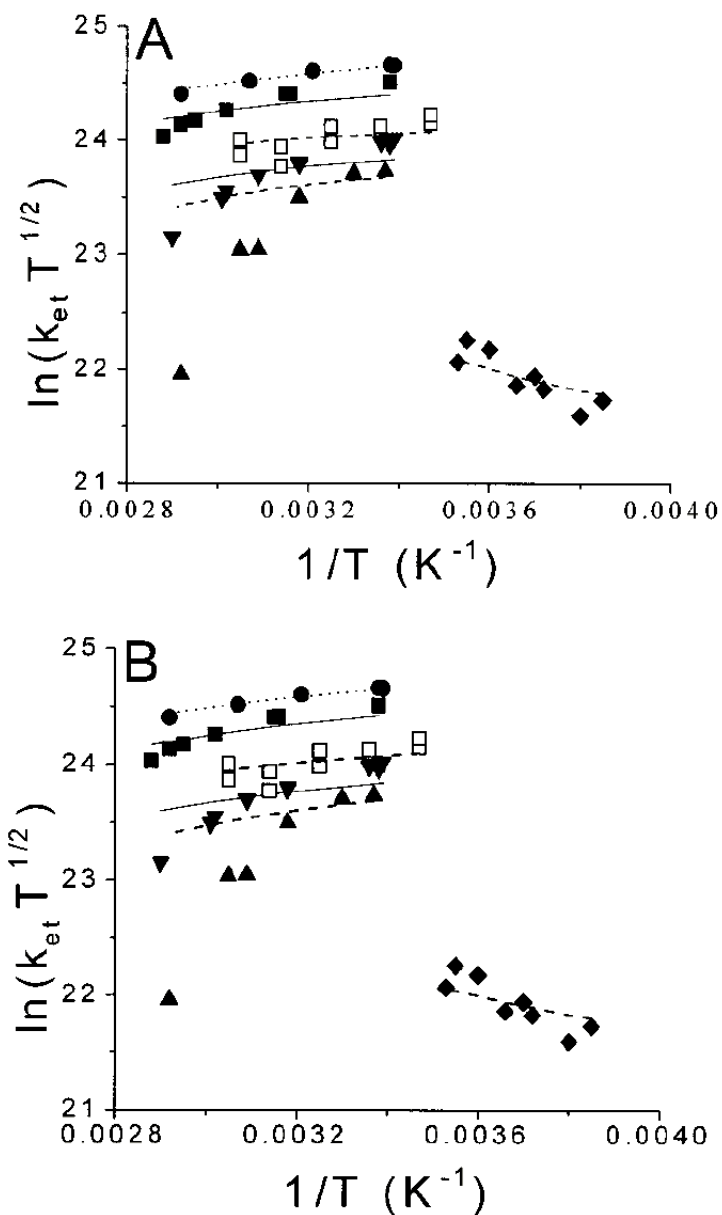


Figure 3.5 Experimental rate data (k_{et}) are shown for benzene (●), toluene (■), cumene(▼), mesitylene(▲), TMB (□), and TIP (◆). Panel A shows the fits using the free energy and temperature dependence of the outer sphere reorganization energy predicted by the dipole model. Panel B shows the fits using the energies predicted by the dipole- quadrupole model. The dotted curve shows the fit for the benzene data, the solid curve shows the fits for the singly substituted benzenes (toluene and cumene), and the dashed curves show the fits for the triply substituted benzenes (mesitylene, 1,2,4-trimethylbenzene, TIP). In each case, the electronic coupling and reorganization energy at 295 K were fitting parameters.

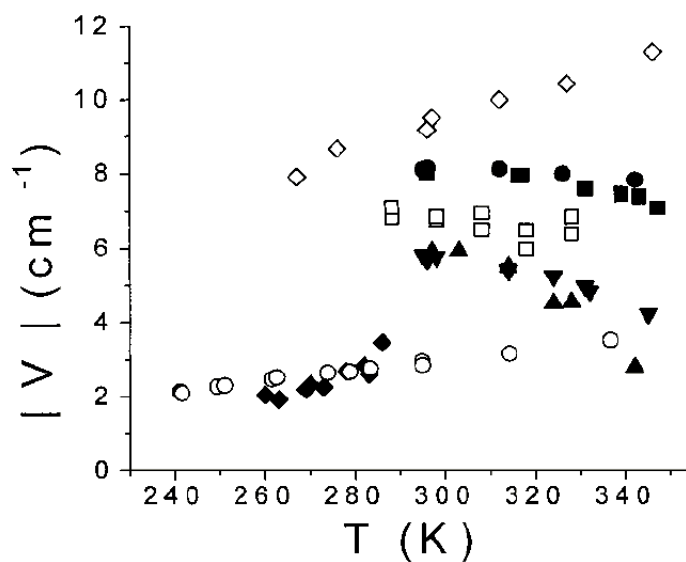


Figure 3.6 Temperature-dependent electronic couplings are shown. These values are calculated from eq 3.1 using the absolute $\Delta_r G$ and λ_0 values from the dipole-quadrupole model. Data are shown for benzene (●), toluene (■), cumene (▼), mesitylene (▲), TMB (□), TIP (◆), acetonitrile (○), and benzonitrile (◇).

Second, both models predict a quasi-linear temperature dependence for λ_0 which may not be accurate in these solvent systems. If the equilibrium between solvent bound and solvent unbound "clefts" changes significantly through this temperature range, nonlinear changes in λ_0 and $|V|$ with temperature would be expected. We are currently exploring the origin of these steep drops in rate with temperature in the bulkier aromatic solvents.

The second approach to fitting the rate data hypothesizes that the electronic coupling is temperature dependent. In this approach, the values of $\Delta_r G$ and λ_0 predicted by the dipole-quadrupole model (see Table 3.7) were used, and the value of $|V|$ at each temperature was derived from the experimental rate constants. Figure 3.6 shows a plot of the electronic couplings as a function of temperature. It is clear from the plot that solvents in which an aromatic core can access the cleft display the largest electronic couplings. In the nondipolar and weakly dipolar aromatic solvents (other than TIP), the coupling displays a systematic but small decrease as the temperature increases (resulting in a predicted decrease of rate by 10-60% over a 40 to 50 K temperature range). To speculate, this behavior could indicate a shift in the distribution of solvent-bound and solvent-unbound DBA "clefts" in solution. With increasing temperature, the population of unbound "clefts" increases and the ensemble averaged value of the electronic coupling decreases because the solvent-unbound structure lacks the through solvent coupling pathway. This trend is correlated to solvent size and is most apparent in cumene and mesitylene. The triisopropyl solvent exhibits the opposite behavior; i.e., the coupling increases as the temperature increases. Previously, it was demonstrated that this solvent experiences a large energy barrier to placement of its aromatic core within the cleft, between the D and A groups. Higher temperatures may increase the probability of placing the solvent's aromatic core between the D and A groups. In the polar solvents, the coupling increases with temperature also,

enhancing the rate constant by 1.5-3-fold. While this approach to fitting the rate data provides stimulating conjecture into the temperature dependence of the electronic coupling, the observed changes may result from systematic errors in the determination of $\Delta_r G$ and/or λ_0 . More experimental work is necessary before a reliable conclusion can be reached.

3.4 Conclusions

Measurement of $\Delta_r G$ and rate constants for electron transfer in highly dipolar, weakly dipolar and nondipolar solvents were used to evaluate two molecular models of solvation. The analysis shows that quadrupolar interactions must be included when computing solvation energies in nondipolar and weakly dipolar aromatic solvents. The quadrupole model was shown to accurately reproduce experimental free energy data and to make reasonable predictions of these energies in the polar solvents acetonitrile and benzonitrile. The analysis shows that λ_{disp} is inconsequential and may be ignored. In addition, the quadrupole model was able to produce physically reasonable values of λ_0 . Two separate approaches were used to fit the experimental rate constants. First, the calculated temperature dependence of λ_0 was used, and the electronic coupling and λ_0 at 295 K were treated as adjustable parameters. The electronic couplings obtained from these fits are in good agreement with those values found previously. The extent of the solvent mediated superexchange mechanism was found to decrease significantly with an increase in the number and size of alkyl groups attached to the benzene core. In the second approach, the calculated $\Delta_r G$ and λ_0 values were used to determine the electronic coupling at each temperature. The results show a steep decrease with increasing temperature of the D/A coupling in mesitylene and a less dramatic change in the other solvents that readily fit between

the D and A groups. Molecular association could be the source of the decreased coupling at higher temperatures but further experimental work is necessary to determine this conclusively.

The Matyushov dipole-quadrupole solvation model is able to accurately reproduce and, in some cases predict, free energies in solvents ranging from nondipolar to highly dipolar. The model requires the vacuum free energy difference, $\Delta_{\text{vac}}G$, the difference in polarizability between the solute neutral and CT states, $\Delta\gamma'$, and an effective solute radius, R_{eff} . Calculations of these parameters may pose a significant problem, especially for large solutes. In addition, the use of the point dipole approximation for the charge redistribution in longer distance charge-transfer systems may be a limitation.²⁷ To conclude, the dipole-quadrupole model reproduces experimental rate data and provides insight into the solvent and temperature dependence of donor-acceptor electronic couplings.

3.5 Acknowledgment.

This work was supported in part by the National Science Foundation (Grants CHE-9708351 (M.B.Z.) and CHE-941693 (D.H.W.)) We acknowledge numerous discussions with Dr. Dmitry Matyushov (University of Utah) and Prof. K. D. Jordan (University of Pittsburgh).

3.6 Appendix: Polynomial Forms of the Perturbation Integrals

$$I_{0s}^{(2)} = \frac{1}{r_0^3} + \frac{a(\rho^*)}{r_0^4} + \frac{b(\rho^*)}{r_0^5} + \frac{c(\rho^*)}{r_0^6}$$

$$I_6^{(2)} = \frac{a(\rho^*)}{r_0^5} + \frac{b(\rho^*)}{r_0^6} + \frac{c(\rho^*)}{r_0^7} + \frac{d(\rho^*)}{r_0^8}$$

$$I_{0s}^{(3)} = \frac{a(\rho^*)}{r_0^3} + \frac{b(\rho^*)}{r_0^4} + \frac{c(\rho^*)}{r_0^6}$$

$$I_{0s}^{(4)} = \frac{1}{r_0^9} + \frac{a(\rho^*)}{r_0^{10}} + \frac{b(\rho^*)}{r_0^{11}} + \frac{c(\rho^*)}{r_0^{12}}$$

$$I_{\text{DQQ}}^{(3)} = \frac{a(\rho^*)}{r_0^6} + \frac{b(\rho^*)}{r_0^7} + \frac{c(\rho^*)}{r_0^8} + \frac{d(\rho^*)}{r_0^9}$$

$$I_{\text{DDQ}}^{(3)} = \frac{a(\rho^*)}{r_0^5} + \frac{b(\rho^*)}{r_0^6} + \frac{c(\rho^*)}{r_0^7} + \frac{d(\rho^*)}{r_0^8}$$

$$J_1 = \frac{a(\rho^*)}{r_0^9} + \frac{b(\rho^*)}{r_0^{10}} + \frac{c(\rho^*)}{r_0^{11}}$$

In each case, r_0 is the reduced solute-solvent distance of closest approach, $r_0 = R_0/\sigma + 0.5$, and the functions $a(\rho^*)$, $b(\rho^*)$, etc. are fit to third-order polynomials over the reduced density, $\rho^* \equiv \rho\sigma^3$ such that

$$a(\rho^*) = a_0 + a_1\rho^* + a_2\rho^{*2} + a_3\rho^{*3}$$

These coefficients are listed in Table 3.6.

Table 3.6 Values of the Coefficients for the Polynomial Forms

i	$I_{0s}^{(2)}$			$I_{0s}^{(3)}$			$I_6^{(2)}$				$I_{0s}^{(4)}$		
	a_i	b_i	c_i	a_i	b_i	c_i	a_i	b_i	c_i	d_i	a_i	b_i	c_i
0	0.000	0.000	0.000	1.000	-0.563	0.031	1.000	0.000	0.000	0.000	0.000	0.000	0.000
1	1.935	-1.675	0.439	0.602	0.255	-0.256	0.586	1.062	-0.970	0.241	3.212	-2.580	0.608
2	-0.972	2.183	-1.051	-0.381	0.848	-0.263	-1.390	4.608	-4.134	1.194	2.862	-4.349	1.564
3	0.398	-0.831	0.465	-0.061	-0.107	0.098	0.776	-2.964	3.798	-1.393	-0.695	3.066	-1.447

i	$I_{\text{DQQ}}^{(3)}$				$I_{\text{DDQ}}^{(3)}$				J_1		
	a_i	b_i	c_i	d_i	a_i	b_i	c_i	d_i	a_i	b_i	c_i
0	0.208	0.000	-0.078	0.008	0.800	-0.500	0.000	0.031	0.774	0.021	1.140
1	0.936	-1.629	10.350	-6.712	0.365	1.652	-1.510	0.044	0.412	0.445	0.739
2	0.330	0.509	-20.530	13.990	-0.656	4.779	-7.378	3.770	0.885	0.372	0.751
3	-0.216	1.005	10.300	-7.512	0.179	-2.297	5.087	-2.928	0.565	0.361	0.410

Table 3.7 Individual Contributions to $\Delta_r G$ and λ_o (All Values in eV) ^a

Dipole Model Values for ΔG and λ ($\Delta_{vac}G = 0.326$)									Dipole-Quadrupole Model Values for ΔG and λ ($\Delta_{vac}G = 0.340$)								
T (K)	$\Delta_{dq_i}G^{(1)}$	$\Delta_iG^{(2)}$	$\Delta_{disp}G$	Δ_rG	λ_p	λ_{ind}	λ_{disp}	λ_o	T (K)	$\Delta_{dq_i}G^{(1)}$	$\Delta_iG^{(2)}$	$\Delta_{disp}G$	Δ_rG	λ_p	λ_{ind}	λ_{disp}	λ_o
Benzene																	
296	-0.407	-0.095	0.064	-0.112	0.000	0.095	0.003	0.099	296	-0.415	-0.031	-0.008	-0.115	0.163	0.031	0.000	0.194
312	-0.397	-0.086	0.062	-0.095	0.000	0.086	0.003	0.089	312	-0.399	-0.028	-0.008	-0.096	0.153	0.028	0.000	0.181
326	-0.388	-0.079	0.061	-0.081	0.000	0.079	0.003	0.082	326	-0.386	-0.026	-0.008	-0.080	0.144	0.026	0.000	0.170
342	-0.378	-0.072	0.059	-0.065	0.000	0.072	0.002	0.074	342	-0.371	-0.024	-0.008	-0.063	0.136	0.024	0.000	0.159
Toluene																	
296	-0.404	-0.097	0.089	-0.086	0.021	0.097	0.005	0.123	296	-0.379	-0.033	-0.012	-0.083	0.139	0.033	0.000	0.171
316	-0.391	-0.084	0.086	-0.063	0.019	0.084	0.005	0.108	316	-0.361	-0.028	-0.011	-0.061	0.127	0.028	0.000	0.156
331	-0.382	-0.076	0.084	-0.048	0.018	0.076	0.004	0.098	331	-0.348	-0.026	-0.011	-0.045	0.120	0.026	0.000	0.145
339	-0.377	-0.072	0.083	-0.040	0.017	0.072	0.004	0.093	339	-0.342	-0.024	-0.011	-0.037	0.116	0.024	0.000	0.140
347	-0.372	-0.068	0.082	-0.032	0.016	0.068	0.004	0.089	347	-0.335	-0.023	-0.011	-0.030	0.112	0.023	0.000	0.135
Cumene																	
296	-0.372	-0.097	0.088	-0.054	0.011	0.097	0.008	0.115	296	-0.347	-0.034	-0.010	-0.051	0.094	0.034	0.000	0.128
314	-0.362	-0.084	0.086	-0.035	0.010	0.084	0.007	0.101	314	-0.334	-0.030	-0.010	-0.034	0.087	0.030	0.000	0.117
324	-0.357	-0.078	0.084	-0.025	0.009	0.078	0.007	0.094	324	-0.328	-0.028	-0.010	-0.025	0.083	0.028	0.000	0.111
331	-0.354	-0.074	0.084	-0.018	0.009	0.074	0.006	0.090	331	-0.323	-0.026	-0.010	-0.019	0.081	0.026	0.000	0.107
345	-0.347	-0.067	0.082	-0.006	0.008	0.067	0.006	0.081	345	-0.314	-0.024	-0.010	-0.008	0.076	0.024	0.000	0.100
TMB																	
288	-0.382	-0.111	0.105	-0.062	0.026	0.111	0.011	0.148	288	-0.346	-0.039	-0.012	-0.057	0.094	0.039	0.000	0.134
298	-0.376	-0.104	0.103	-0.051	0.025	0.104	0.011	0.139	298	-0.339	-0.037	-0.012	-0.048	0.091	0.037	0.000	0.128
308	-0.370	-0.097	0.102	-0.040	0.023	0.097	0.010	0.131	308	-0.333	-0.034	-0.012	-0.040	0.088	0.034	0.000	0.123
318	-0.364	-0.091	0.100	-0.029	0.022	0.091	0.009	0.123	318	-0.328	-0.032	-0.012	-0.032	0.086	0.032	0.000	0.118
328	-0.359	-0.086	0.099	-0.020	0.021	0.086	0.009	0.116	328	-0.322	-0.030	-0.012	-0.024	0.083	0.030	0.000	0.113
Mesitylene																	
297	-0.365	-0.101	0.107	-0.033	0.001	0.101	0.011	0.114	297	-0.322	-0.036	-0.014	-0.032	0.081	0.036	0.000	0.117
303	-0.361	-0.097	0.106	-0.027	0.001	0.097	0.011	0.109	303	-0.318	-0.034	-0.013	-0.026	0.079	0.034	0.000	0.114
314	-0.356	-0.091	0.104	-0.016	0.001	0.091	0.010	0.102	314	-0.313	-0.032	-0.013	-0.016	0.075	0.032	0.000	0.107
324	-0.350	-0.085	0.103	-0.007	0.001	0.085	0.010	0.096	324	-0.304	-0.030	-0.013	-0.007	0.072	0.030	0.000	0.102
342	-0.341	-0.076	0.100	0.009	0.001	0.076	0.009	0.085	342	-0.293	-0.027	-0.013	0.008	0.067	0.027	0.000	0.094
TIP																	
260	-0.326	-0.117	0.097	-0.020	0.001	0.117	0.015	0.133	260	-0.303	-0.044	-0.010	-0.018	0.048	0.044	0.000	0.092
263	-0.325	-0.115	0.097	-0.017	0.001	0.115	0.014	0.130	263	-0.301	-0.044	-0.010	-0.016	0.047	0.044	0.000	0.091
278	-0.319	-0.104	0.095	-0.002	0.001	0.104	0.013	0.118	278	-0.294	-0.039	-0.010	-0.003	0.044	0.039	0.000	0.083
282	-0.317	-0.101	0.094	0.002	0.001	0.101	0.013	0.115	282	-0.292	-0.038	-0.010	0.000	0.043	0.038	0.000	0.081
Acetonitrile																	
250	-1.906	-0.038	0.051	-1.567	1.544	0.038	0.002	1.583	250	-1.083	-0.012	-0.006	-0.761	0.848	0.012	0.000	0.859
270	-1.868	-0.033	0.049	-1.526	1.517	0.033	0.001	1.552	270	-1.065	-0.010	-0.006	-0.741	0.837	0.010	0.000	0.847
300	-1.813	-0.027	0.046	-1.467	1.478	0.027	0.001	1.506	300	-1.039	-0.008	-0.006	-0.713	0.821	0.008	0.000	0.829
320	-1.776	-0.023	0.045	-1.429	1.452	0.023	0.001	1.477	320	-1.021	-0.007	-0.005	-0.694	0.810	0.007	0.000	0.817
340	-1.740	-0.020	0.043	-1.391	1.427	0.020	0.001	1.448	340	-1.004	-0.006	-0.005	-0.676	0.799	0.006	0.000	0.806
Benzonitrile																	
296	-1.864	-0.121	0.089	-1.570	1.444	0.121	0.007	1.572	296	-1.170	-0.041	-0.011	-0.882	0.892	0.041	0.000	0.933
312	-1.832	-0.109	0.088	-1.527	1.419	0.109	0.006	1.534	312	-1.154	-0.037	-0.011	-0.862	0.881	0.037	0.000	0.917
324	-1.807	-0.101	0.086	-1.496	1.400	0.101	0.006	1.507	324	-1.143	-0.034	-0.011	-0.847	0.872	0.034	0.000	0.906
342	-1.770	-0.090	0.084	-1.450	1.371	0.090	0.005	1.467	342	-1.125	-0.030	-0.010	-0.826	0.860	0.030	0.000	0.890

^a TMB is 1,2,4-trimethylbenzene; TIP is 1,3,5-triisopropylbenzene.

3.7 References.

- (1) Matyushov, D. V.; Voth, G. A. *J. Chem. Phys.* **1999**, 111, 3630. The formulation used in this manuscript includes solvent polarizability. We thank Dr. D. Matyushov for providing access to this form of the model.
- (2) (a) Electron Transfer - From Isolated Molecules to Biomolecules. *Adv. Chem. Phys.*, Jortner, J., Bixon, M., Eds., (Wiley: NY **1999**) (b) Barbara, P. F.; Meyer, T. J.; Ratner, M. A. *J. Phys. Chem.* **1996**, 100, 13148. (c) Newton, M. D. *Chem. Rev.* **1991**, 91, 767. (d) Closs, G. L.; Miller, J. R. *Science* **1988**, 240, 440. (e) Marcus, R. A.; Sutin, N. *Biochimica et Biophysica Acta* **1985**, 811, 265.
- (3) (a) Newton, M. D. *Adv. Chem. Phys.* **1999**, 106, 303. (b) Gray, H. B.; Winkler, J. R. *Annu. Rev. Biochem.* **1996**, 65, 537. (c) Closs, G. L.; Calcaterra, L. T.; Green, N. J.; Penfield, K. W.; Miller, J. R. *J. Phys. Chem.* **1986**, 90, 3673; (d) Jordan, K. D.; Paddon-Row, M. N. *Chem. Rev.* **1992**, 92, 395.
- (4) (a) Nitzan, A.; Mujica, V.; Davis, W. B.; Wasielewski, M. R.; Ratner, M. A. *J. Phys. Chem.* **1997**, 101, 6158. (b) Häberle, T.; Hirsch, J.; Pöllinger, F.; Heitele, H.; Michel-Beyerle, M. E.; Anders, C.; Döhling, A.; Krieger, C.; Rückemann, A.; Staab, H. A. *J. Phys. Chem.* **1996**, 100, 18269. (c) Heitele, H.; Pöllinger, F.; Häberle, T.; Michel-Beyerle, M. E.; Staab, H. A. *J. Phys. Chem.* **1994**, 98, 7402. (d) Liu, J.; Schmidt, J. A.; Bolton, J. R. *J. Phys. Chem.* **1991**, 95, 6924. (e) Ratner, M. A. *J. Phys. Chem.* **1990**, 94, 4877. (e) Larsson, S. *Chem. Phys. Lett.* **1982**, 90, 136. (f) Helms, A.; Heiler, D.; McLendon, G. *J. Am. Chem. Soc.* **1991**, 113, 4325.
- (5) (a) Liang, N.; Miller, J. R.; Closs, G. L. *J. Am. Chem. Soc.* **1989**, 111, 8740. (b) Kumar, K.; Lin, Z.; Waldeck, D. H.; Zimmt, M. B. *J. Am. Chem. Soc.* **1996**, 118, 243. (c) Kroon, J.; Oevering, H.; Verhoeven, J. W.; Warman, J. M.; Oliver, A. M.; Paddon-Row, M. N. *J. Phys. Chem.* **1993**, 97, 5065. (d) Wasielewski, M. R.; Gaines, G. L. III.; O'Neill, M. P.; Svec, W. A.; Niemczyk, M. P.; Prodi, L.; Gosztola, D. in 'Dynamics and Mechanisms of Photoinduced Electron Transfer and Related Phenomena,' Mataga, N., Okada, T., Masuhara, H., Eds., Elsevier, **1992**; p 87.
- (6) (a) Read, I.; Napper, A.; Kaplan, R.; Zimmt, M. B.; Waldeck, D. H. *J. Am. Chem. Soc.* **1999**, 121, 10976. (b) Han, H.; Zimmt, M. B. *J. Am. Chem. Soc.* **1998**, 120, 8001. (c) Roest, M. R.; Verhoeven, J. W.; Schuddeboom, W.; Warman, J. M.; Lawson, J. M.; Paddon-Row, M. N. *J. Am. Chem. Soc.* **1996**, 118, 1762.
- (7) Vath, P.; Zimmt, M. B.; Matyushov, D. V.; Voth, G. A. *J. Phys. Chem. B* **1999**, 103, 9130.
- (8) McConnell, H. M. *J. Chem. Phys.* **1961**, 35, 508.
- (9) Gosztola, D.; Wang, B.; Wasielewski, M. R. *J. Photochem. Photobio. A* **1996**, 102, 71.

(10) Kumar, K.; Kurnikov, I. V.; Beratan, D. N.; Waldeck, D. H.; Zimmt, M. B. *J. Phys. Chem. A*. **1998**, 102, 5529.

(11) Jortner, J. *J. Chem. Phys.* **1976**, 64, 4860.

(12) (a) Marcus, R. A. *J. Phys. Chem.* **1989**, 93, 3078. (b) Lilichenko, M.; Tittelbach-Helmrich, D.; Verhoeven, J. W.; Gould, I. R.; Myers, A. B. *J. Chem. Phys.* **1998**, 109, 10958. (c) Gould, I. R.; Noukakis, D.; Goodman, J. L.; Young, R. H.; Farid, S. *J. Am. Chem. Soc.* **1993**, 115, 3830.

(13) Reynolds, L.; Frankland, S. J. V.; Horng, M. L.; Maroncelli, M. *J. Phys. Chem.* **1996**, 100, 10337.

(14) Matyushov, D. V. *Chem. Phys.* **1996**, 211, 47.

(15) Given the experimental rate constants, free energies, and the previous predictions of λ_i and ν , it was possible to compute the temperature dependence of λ_o at three values of the electronic coupling (ref 6a). The results gave nearly constant values of λ_o in every solvent but mesitylene. The origin of this temperature dependence in mesitylene is under investigation.

(16) Zeng, Y.; Zimmt, M. B. *J. Phys. Chem.* **1992**, 96, 8395.

(17) Rehm, D.; Weller, A. *Z. Phys. Chem. (Munich)* **1970**, 69, 183.

(18) Gubbins, K. E.; Joslin, C. G.; Gray, C. G. *Mol. Phys.* **1985**, 54, 1117.

(19) (a) Matyushov, D. V.; Schmid, R. *J. Chem. Phys.* **1996**, 105, 4729. This reference reports an erroneous value for the c_3 coefficient in the $I_{0s}^{(2)}$ polynomial form. Its value should be + 0.0983. See b) Matyushov, D. V.; Ladanyi, B. M. *J. Chem. Phys.* **1999**, 110, 994.

(20) Ben-Amotz, D.; Willis, K. G. *J. Phys. Chem.* **1993**, 97, 7736.

(21) Matyushov, personal communication.

(22) The values for the integral J_1 were provided by Dr Matyushov and fit to the polynomial form in the Appendix.

(23) Frisch, M. J.; Trucks, G. W.; Schlegel, H. B.; Scuseria, G. E.; Robb, M. A.; Cheeseman, J. R.; Zakrzewski, V. G.; Montgomery, J. A., Jr.; Stratmann, R. E.; Burant, J. C.; Dapprich, S.; Millam, J. M.; Daniels, A. D.; Kudin, K. N.; Strain, M. C.; Farkas, O.; Tomasi, J.; Barone, V.; Cossi, M.; Cammi, R.; Mennucci, B.; Pomelli, C.; Adamo, C.; Clifford, S.; Ochterski, J.; Petersson, G. A.; Ayala, P. Y.; Cui, Q.; Morokuma, K.; Malick, D. K.; Rabuck, A. D.; Raghavachari, K.; Foresman, J. B.; Cioslowski, J.; Ortiz, J. V.; Stefanov, B. B.; Liu, G.; Liashenko, A.; Piskorz, P.; Komaromi, I.; Gomperts, R.; Martin, R. L.; Fox, D. J.; Keith, T.; Al-Laham, M. A.; Peng, C. Y.; Nanayakkara, A.; Gonzalez, C.; Challacombe, M.; Gill, P. M. W.;

Johnson, B. G.; Chen, W.; Wong, M. W.; Andres, J. L.; Head-Gordon, M.; Replogle, E. S.; Pople, J. A. Gaussian 98, revision A.4; Gaussian, Inc.: Pittsburgh, PA, 1998.

(24) The dipole moment of the charge transfer state was calculated assuming a point charge separation of 7.1 Å.

(25) Gubbins, K. E.; Gray, C. G.; Machado, J. R. S. *Mol. Phys.* **1981**, 42, 817.

(26) (a) Vath, P.; Zimmt, M. B. *J. Phys. Chem. A* **2000**, 104, 2626. (b) Cortés, J.; Heitele, H.; Jortner, J. *J. Phys. Chem.* **1994**, 98, 2527.

(27) Zimmt, M. B. Unpublished results.

Chapter 4. An Unequivocal Demonstration of the Importance of Nonbonded Contacts in the Electronic Coupling between Electron Donor and Acceptor Units of Donor-Bridge-Acceptor Molecules

Because of their ubiquity, electron transfer (ET) reactions have received considerable attention over the past few decades. The current view of a superexchange mechanism to treat the electronic interaction for electron-transfer processes in the nonadiabatic limit has been quite successful. Although it is widely believed that covalent linkages between donor and acceptor units provide the dominant pathway for this mechanism,¹ recent work suggests that other pathways involving hydrogen-bonded linkages^{2,3} and non-bonded interactions^{4,5} can be important. This work assesses the importance of nonbonded contacts by comparing three different unimolecular ET systems that differ by the juxtaposition of a pendant group between the electron donor and acceptor units. This design provides an avenue to quantify the importance of an aromatic moiety's placement on the electron-transfer rate. The work presents unequivocal evidence that electronic coupling through nonbonded moieties can compete effectively with covalent linkages, when the mediating moiety lies between the electron donor and acceptor groups.[§]

This study utilizes a U-shaped donor-bridge-acceptor (DBA) dyad in which a pendant moiety (P) is placed between the electron donor and acceptor units by a covalent linkage to the bridge (see the cartoon in Chart 4.1). Through systematic change of the pendant molecular unit

[§] Reproduced with permission from Napper, A. M.; Read, I.; Waldeck, D. H.; Head, N. J.; Oliver, A. M.; Paddon-Row, M. N.; *J. Am. Chem. Soc.*; **2000**; 122(21); 5220-5221. Copyright 2000 American Chemical Society

it is possible to demonstrate its importance to the ET and the role of its placement on the efficiency of ET. This approach has several advantages over earlier approaches. First, the moiety that mediates the superexchange interaction (solvent molecule in earlier studies^{4,5}) is clearly located between the donor and acceptor groups. Second, the nature of P can be changed, and a homologous series of DBA molecules can be studied in a single solvent, thereby minimizing any differences in the reaction free energy and outer sphere reorganization energy that may result from solvation changes. These systems also promise an ability to change the geometry of the mediating unit and to investigate how its nuclear dynamics impact the ET.

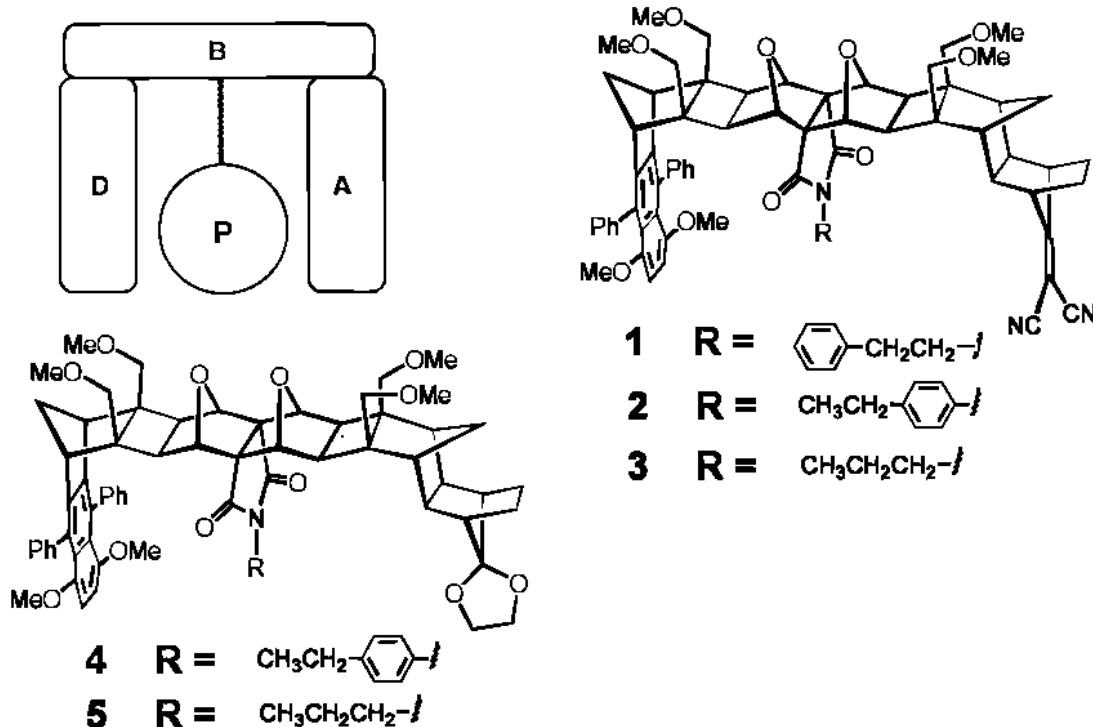


Chart 4.1 Chemical structures of the molecules studied in this paper.

The ET rates of **1-3** in Chart 4.1 were studied in three different solvents (acetonitrile, dichloromethane, and tetrahydrofuran) as a function of temperature. The general synthetic strategy for these molecules and the specific synthesis of **3** has been reported elsewhere.⁶ The

molecules in Chart 4.1 have the same electron donor unit, 1,4-dimethoxy-5,8-diphenylnaphthalene. Molecules **1**, **2**, and **3** have a 1,1-dicyanovinyl (DCV) acceptor unit, and ET occurs when the naphthalene moiety is electronically excited by 300 nm light. These donor and acceptor units have been used for intramolecular ET studies in the past.^{1c} Molecules **4** and **5** have a 1,3-dioxolane unit in place of the DCV acceptor. These molecules do not undergo ET and are used as experimental controls. A comparison of the ET rate constant for **1**, **2**, and **3** provides information on the effectiveness of an aromatic ring for mediating the electronic coupling in the ET, as compared to that of an alkyl unit, and addresses the importance of its placement. The ET rate constant was determined by subtracting the excited-state relaxation rate of the control molecules (**4** and **5**) from that of the ET molecules (**1**, **2**, and **3**).

The ET rate constants as a function of temperature are shown in Figure 4.1 for compounds **1**, **2**, and **3**. In each solvent studied the ET rate for **2** is significantly faster than that found for the other compounds. The larger ET rate constant for **2** compared to **3** demonstrates the benefit of placing an aromatic unit between the electron donor and acceptor rather than an alkyl unit. The larger ET rate constant for **2** compared to that for **1** demonstrates the importance of the aromatic unit's placement between the donor and acceptor groups. Molecular modeling calculations of the molecular geometries of **1** and **2** show that the phenyl ring in compound **2** is in the "line-of-sight" between the donor and acceptor groups (see Figure 4.2), whereas the phenyl ring in compound **1** is shifted down from the line-of-sight position.⁷ The very similar rates for **3** and **1** corroborate this conclusion. In short, the propyl **3** and 2-phenylethyl **1** pendant units are similar with respect to their influence on the ET, but the p-ethylphenyl unit in **2** is markedly different. These comparisons imply enhanced tunneling when the phenyl ring is in line-of-sight.

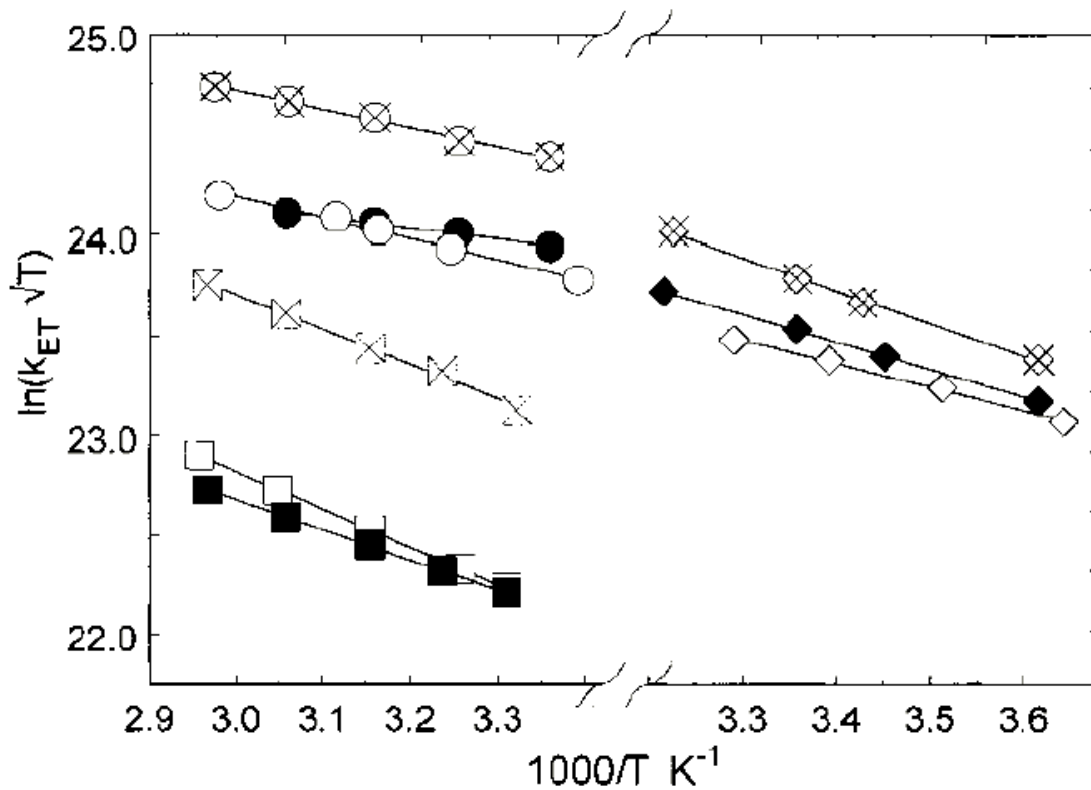


Figure 4.1 These plots show the temperature dependence of the ET rate constant k_{ET} in three solvents: acetonitrile (squares), dichloromethane (diamonds), and tetrahydrofuran (circles). The filled symbols represent the data for **1**, the open symbols with an x represent the data for **2**, and the open symbols represent the data for **3**. The lines are linear regression fits to the data.

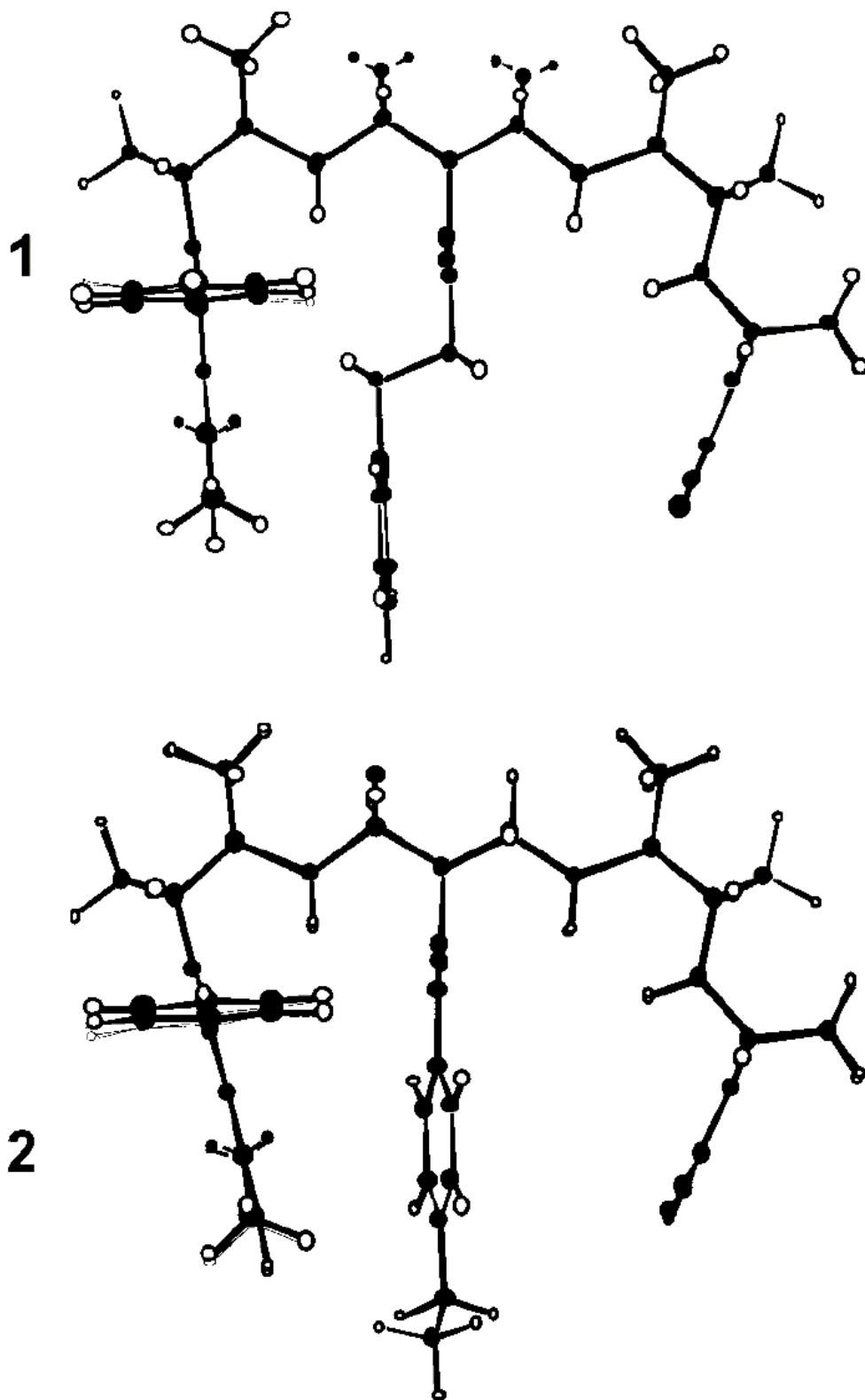


Figure 4.2 This figure shows ball-and-stick renderings of MM2 optimized structures of the DBA molecules **1** and **2**. The phenyl ring of the pendant group in **2** is on the line-of-sight between the donor and acceptor units.

In each solvent system, the ET rate displays a temperature dependence. A fit of the data provides activation energies between 2 and 4 kcal/mol. The similarity of the activation suggests that the Franck-Condon terms (the reaction free energy $\Delta_r G$ and the reorganization energies λ) are similar for the three compounds. The ET activation energies for **1-3** display a solvent dependence, decreasing by a factor of ~ 2 , upon changing the solvent from acetonitrile to tetrahydrofuran. If the Franck-Condon factors are not changing for the compounds in a single solvent, the difference in the rate constants reflects a change in the electronic coupling $|V|$. This logic is supported by the very similar rates that are observed for **1** and **3** in each of the different solvents. From an analysis of the temperature dependence in each solvent and assuming that the reorganization energy in a given solvent is the same for each of the molecules **1-3**, it is possible to extract reliable relative electronic couplings. Table 4.1 presents the relative electronic couplings in acetonitrile. The results reveal that the coupling in **2** is 2.5 times larger than in **3** and 30% larger than in **1**. Similar differences in the electronic couplings are found in tetrahydrofuran and CH_2Cl_2 .

Table 4.1 Comparison of Rate Constants k_{ET} and Relative Electronic Couplings $|V_{\text{rel}}|$ in Acetonitrile Solvent at 300 K.

^a The electronic couplings are compared to the value for **3**

compd	1	2	3	6	7	8
k_{ET} (ns^{-1})	0.25	0.64	0.245	0.16	30.	2.2
$ V_{\text{rel}} ^a$	1.9	2.4	1			

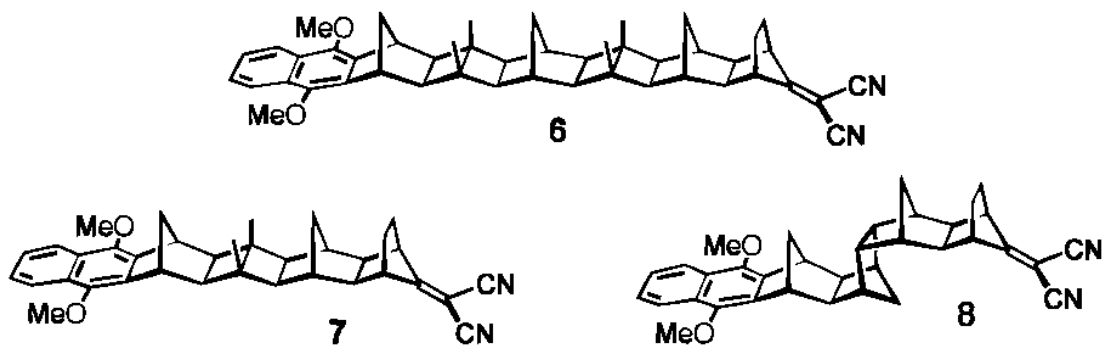


Chart 4.2 Chemical Structures of Linear Bridged Donor-Bridge-Acceptor Molecules Previously Studied.^{1a}

Comparison of these rate constants with those from earlier studies supports the conclusion that ET in **1-3** is occurring through the pendant group and not through the covalent bonds of the bridge (see Table 4.1). In all three dyads, **1-3**, the bridge is 12 bonds long and has two cisoid kinks. The rate constants for **1-3** are all larger than that for the all-trans 12-bond DMN-DCV (see **6** of Chart 4.2) for the same solvents.^{1a} This comparison becomes more significant when one realizes that ET through an all-trans bridge is much faster than that through a bridge having two cisoid kinks.⁸ For example, the ET rate constant for the all-trans **7** is up to 14 times larger than that for **8**, which has two cisoid links.⁸ These considerations suggest that the propyl chain in **3** mediates ET more efficiently than does its 12-bond, double-kinked, covalent bridge! A caveat to these comparisons is that the $\Delta_r G$ and λ could be changing, because of the smaller donor- acceptor separation in **1-3** (9.0 - 9.9 Å), compared to that in **6** (~ 14 Å). Initial investigations indicate that the free energies in these systems are similar,⁹ however more studies are required to better quantify these considerations.

A comparison of ET rates in the different DBA molecules **1**, **2**, and **3** demonstrates the importance of the molecular functionality that lies between the donor and acceptor units, even

though it does not covalently link them. By changing the pendant unit that lies between the electron donor and acceptor, it has been possible to explore how its nature and its placement impact the ET rate. A more quantitative study of these systems and their electronic coupling is underway. Nonbonded contacts are ubiquitous in chemical and biological systems, and it will be interesting to investigate a wider range of systems. In particular, we are currently synthesizing variants of **2**, in which the ethyl substituent of the phenyl ring is replaced by groups having different electronegativities, to delineate how the donor-acceptor electronic coupling depends on the electronic properties of the pendant aromatic group.

4.1 References.

- (1) (a) Oevering, H.; Paddon-Row, M. N.; Heppener, H.; Oliver, A. M.; Cotsaris, E.; Verhoeven, J. W.; Hush, N. S. *J. Am. Chem. Soc.* **1987**, 109, 3258. (b) Closs, G. L.; Miller, J. R. *Science* **1988**, 240, 440-447. (c) Paddon-Row, M. N. *Acc. Chem. Res.* **1994**, 27, 18.
- (2) (a) Berman, A.; Izraeli, E. S.; Levanon, H.; Wang B.; Sessler, J. L. *J. Am. Chem. Soc.* **1995**, 117, 8252. (b) Roberts, J. A.; Kirby, J. P.; Nocera, D. G. *J. Am. Chem. Soc.* **1995**, 117, 8051. (c) de Rege, P. J. F.; Williams, S. A.; Therien, M. J. *Science* **1995**, 269, 1409. (d) LeCours, S. M.; Philips, C. M.; DePaula, J. C.; Therien, M. J.; *J. Am. Chem. Soc.* **1997**, 119, 12578. (e) Turro, C.; Chang, C. K.; Leroi, G. E.; Cukier, R. I.; Nocera, D. G. *J. Am. Chem. Soc.* **1992**, 114, 4013. (f) Arimura, T.; Brown, C. T.; Springs, S. L.; Sessler, J. L. *Chem. Commun.* **1996**, 2293.
- (3) (a) Beratan, D. N.; Onuchic, J. N. Protein Electron Transfer; Bendall, D. S., Ed.; BIOS Scientific Publishers Ltd.: Oxford, **1996**; p 23. (b) Nocek, J. M.; Zhou, J. S.; De Forest, S.; Priyadarshy, S.; Beratan, D. N.; Onuchic, J. N.; Hoffman, B. M. *Chem. Rev.* **1996**, 96, 2459.
- (4) (a) Kumar, K.; Lin, Z.; Waldeck, D. H.; Zimmt, M. B. *J. Am. Chem. Soc.* **1996**, 118, 243. (b) Gu, Y.; Kumar, K.; Lin, Z.; Read, I.; Zimmt, M. B.; Waldeck, D. H. *J. Photochem. Photobiol. A* **1997**, 105, 189. (c) Kumar, K.; Kurnikov, I.; Beratan, D.; Waldeck, D. H.; Zimmt, M. B.; *J. Phys. Chem. B* **1998**, 102, 5394. (d) Read, I.; Napper, A.; Kaplan, R.; Zimmt, M. B.; Waldeck, D. H. *J. Am. Chem. Soc.* **1999**, 121, 10976.
- (5) (a) Oliver, A. M.; Craig, D. C.; Paddon-Row, M. N.; Kroon, J.; Verhoeven, J. W. *Chem. Phys. Lett.* **1988**, 150, 366. (b) Lawson, J. M.; Paddon-Row, M. N.; Schuddeboom, W.; Warman, J. M.; Clayton, A. H.; Ghiggino, K. P. *J. Phys. Chem.* **1993**, 97, 13099. (c) Roest, M. R.; Lawson, J. M.; Paddon-Row, M. N.; Verhoeven, J. W. *Chem. Phys. Lett.* **1994**, 230, 536. (d) Roest, M. R.; Verhoeven, J. W.; Schuddeboom, W.; Warman, J. M.; Lawson, J. M.; Paddon-Row, M. N. *J. Am. Chem. Soc.* **1996**, 118, 1762. (e) Verhoeven, J. W.; Koeberg, M.; Roest, M. R.; Paddon-Row, M. N.; Lawson, J. M. In Biological Electron-Transfer Chains: Genetics, Composition and Mode of Operation; Canters, G. W., Vijgenboom, E., Eds.; Kluwer: Dordrecht, **1998**; pp 51-61. (f) Jolliffe, K. A.; Bell, T. D. M.; Ghiggino, K. P.; Langford, S. J.; Paddon-Row, M. N. *Angew. Chem., Int. Ed.* **1998**, 37, 916.
- (6) Head, N. J.; Oliver, A. M.; Look, K.; Lokan, N. R.; Jones, G. A.; Paddon-Row, M. N. *Angew. Chem., Int. Ed.* **1999**, 38, 3219.
- (7) The images in Figure 4.2 were calculated at the MM2 level. More sophisticated geometry calculations are underway. Preliminary calculations on **2** at the HF 3-21G level indicate that the phenyl ring is located on a line of sight between the donor and acceptor, but it is twisted ($\sim 70^\circ$) from the plane of the imide ring.
- (8) Oliver, A. M.; Craig, D. C.; Paddon-Row, M. N.; Kroon, J.; Verhoeven, J. W. *Chem. Phys. Lett.* **1988**, 150, 366.

(9) The oxidation potential of the dimethoxynaphthalene in **6** is 0.1 eV smaller than dimethoxydiphenylnaphthalene group in **1** to **3**, and the ground to locally excited-state energy of **6** is 0.2 eV larger than in **1** to **3**, implying about 0.3 eV more driving force for the reaction. However, the Coulomb stabilization of the charge transfer state in **6** is about 0.2 eV smaller than in **1** to **3**. This suggests that the reaction free energies will be close to one another, within 0.1 to 0.2 eV.

Chapter 5. Solvent Mediated Coupling Across 1 nm: Not a π Bond in Sight

Significant electronic coupling between donor (D) and acceptor (A) moieties is a prerequisite for rapid electron transfer.¹ A variety of "rigid" media are known to effect coupling between widely separated D and A units.² Recent reports show that fluid solvents also provide electronic coupling for highly curved D-bridge-A molecules.³ Significant solvent-mediated coupling (SMC) has been reported in cases where (i) the covalent bridge (B) connecting the D and A provides little coupling (e.g. long bridges with non-trans σ -bond units^{3,4} or symmetry-forbidden DBA topology⁵), (ii) the through solvent "path" from D to A is relatively short (<14 Å), and (iii) the solvent is aromatic or contains a high density of π bonds (e.g nitriles).^{3,6} For electron transfer involving excited donors, we reported⁶ a correlation between SMC magnitude, $|V|$, and solvent vertical electron affinity, EA_V .⁷ Only solvents with π bonds were investigated. Transfer rate constants in saturated solvents were too small to measure for the curved DBA molecules that rely on SMC. The absence of transfer "across" saturated solvents is puzzling given numerous examples of through σ -bond coupling in other systems.^{1,2} Herein, we report that saturated halocarbon solvents ($CH_{4-n}X_n$) produce D*/A couplings across 1 nm that are as large or larger than the coupling provided by any π bond containing solvent explored to date. The largest rate constants and couplings are found in brominated or chlorinated solvents with $EA_V \sim 0$. The results demonstrate that EA_V strongly influences SMC magnitudes, whether or not the solvent contains π bonds.[§]

[§] Reproduced with permission from Kaplan, R. W.; Napper, A. M.; Waldeck, D. H.; Zimmt, M. B.; *J. Am. Chem. Soc.* ; **2000**; 122(48); 12039-12040. Copyright 2000 American Chemical Society

Table 5.1 ϵ_S , n_D , EA_V , and k_{CS} for **1** and **2** and k_{DB} at 295 K

^a Mottola, H. A.; Freiser, H. *Talanta* **1967**, 14, 864.

solvent	ϵ_S^{15}	n_D^{15}	EA_V^7	$k_{CS(1)}/ns^{-1}$	$k_{CS(2)}/ns^{-1}$	k_{DB}/ns^{-1}
Et ₂ O	4.3	1.353		0.011	2.2	0.036
CH ₃ CN	37.5	1.346	-2.8	0.047	6.2	0.022
THF	7.6	1.405		0.054	7.3	0.032
CH ₂ Cl ₂	8.9	1.421	-1.2	0.39	16.	0.025
PhCH ₂ CN	18.7	1.521	-1.0	0.46	16.	0.032
CHCl ₃	4.9	1.443	-0.35	1.0	25.	0.039
PhCN	25.2	1.526	0.2	1.2	24.	0.033
CH ₂ BrCl	8.0 ^a	1.483		1.2	35.	0.050
CH ₂ Br ₂	7.4	1.555	-0.2	2.6	50	0.21

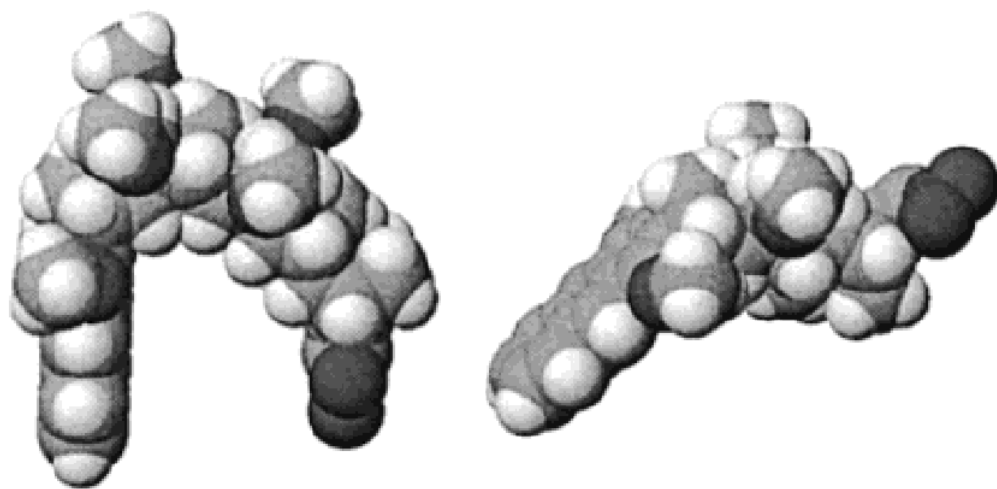


Chart 5.1 Electron Transfer Molecules: **1** (left) and **2** (right)

Charge separation (CS) rate constants, k_{CS} , in the C-shaped and linear DBA molecules, **1** and **2**, were determined from time-resolved fluorescence decays.⁸ In both molecules, the donor is the lowest singlet excited state of the dimethoxyanthracene group and the acceptor is a nitroethylene group. The CS distance is 10.0 Å in **1** and 12.2 Å in **2**.⁹ The rate constants at 295 K (Table 5.1) exhibit interesting solvent dependence. Changing from the least to the most polar solvent (Et₂O → CH₃CN) produces comparable percentage increases of k_{CS} in **1** and **2**. By contrast, changing from CH₃CN to CHCl₃ or PhCN increases the rate 4-fold for **2** but increases the rate 21- to 26-fold for **1**. k_{CS} values for **1** are fastest in electron deficient aromatic and halocarbon solvents. In the latter, k_{CS} increases with an increase in the number of halogens and upon replacement of chlorine by bromine. These trends are not the result of heavy atom induced intersystem crossing or electron transfer to the solvent because the reported k_{CS} values account for the donor's intrinsic decay rate constant (k_{DB}) in each solvent and at each temperature.¹⁰ k_{CS} for **2** also increase as one proceeds down the list of solvents in Table 5.1; however, the increase is significantly greater (up to 10-fold) for **1**. Semiclassical electron transfer theories express the transfer rate constant as the product of $|V|^2$ and the Franck-Condon weighted density of states (FCWDS).¹¹ It is not possible to determine $|V|$ and the FCWDS from k_{CS} at a single temperature. Values of $|V|$ (D*/A) and λ_S (295 K) for **1** and **2** can be determined by fitting the k_{CS} data as a function of temperature to the semiclassical rate expression.^{11,12} The variation of λ_S and ΔG with temperature must be modeled.¹² Continuum models predict reasonable values of λ_S at room temperature but generate erroneous temperature dependence, particularly in polar solvents.¹³ Instead, the temperature dependence of λ_S was evaluated using Matyushov's dipolar, polarizable hard-sphere model.¹⁴ This model combines reorientation, λ_P , and translation, λ_D , reorganization contributions to produce λ_S . The ratio λ_P/λ_D at 295 K and the temperature dependence of λ_S

were determined according to Matyushov.^{12,14} The temperature dependence of λ_p was calculated by using the Pekar factor.¹⁵ As implemented here, the model predicts $\lambda_S(T)/\lambda_S(295\text{ K})$ so that $\lambda_S(295\text{ K})$ scales λ_S at all temperatures.¹⁶ The solvent and temperature dependence of ΔG was calculated according to Weller.¹⁷

Table 5.2 Regression Values of $|V|$ and $\lambda_S(295\text{ K})$ [$\lambda_S(295\text{ K})$ Predicted by a Two Sphere Continuum Model, for the Same Range of Radii, Are Also Shown]

^a The range of values obtained for different r_A values is indicated by the number following the \pm symbol.

DBA	solvent	$ V $ (cm ⁻¹) ^a	λ_S (eV) ^a	$\lambda_{\text{continuum}}$ (eV) ^a
1	CH ₃ CN	3.6 ± 0.1	1.45 ± 0.01	1.09 ± 0.07
1	CH ₂ Cl ₂	4.4 ± 0.4	0.99 ± 0.01	0.79 ± 0.05
1	PhCH ₂ CN	5.2 ± 0.1	1.17 ± 0.01	0.78 ± 0.05
1	CHCl ₃	6.7 ± 1.3	0.75 ± 0.02	0.57 ± 0.04
1	PhCN	6.8 ± 0.1	1.13 ± 0.01	0.81 ± 0.05
1	CH ₂ Br ₂	13.5 ± 1.5	0.99 ± 0.01	0.59 ± 0.04
2	Et ₂ O	20 ± 6	0.79 ± 0.03	0.75 ± 0.04
2	CH ₃ CN	18 ± 1	1.20 ± 0.01	1.23 ± 0.07
2	PhCN	20 ± 1	0.96 ± 0.01	0.91 ± 0.05

D and A radii are needed to calculate ΔG and λ_S as a function of solvent and temperature. The radii influence the calculated *FCWDS* most significantly in weakly polar solvents. Radii of 4.5 Å were used for this D and an alkene-diester A.^{5b,12} The nitroethylene acceptor contains fewer atoms, suggesting a smaller value of the radius, r_A . To assist evaluation of r_A , k_{CS} for **2** was determined in cyclohexane, Bu₂O, Pr₂O, and Et₂O. Negligible transfer was detected in C₆H₁₂.¹⁸ Weller's model predicts $\Delta G_{CS} < 0.06$ eV in C₆H₁₂ for $r_A > 4.3$ Å. Measurable k_{CS} is expected for $\Delta G_{CS} < 0.06$ eV,¹⁹ thus ΔG_{CS} must be more positive in C₆H₁₂ and r_A must be

smaller than 4.3 Å. The volume of the neutral acceptor group²⁰ corresponds to a radius of 3.3 Å. The appropriate Born radius for an anion is typically larger than the neutral radius.²¹ To explore the influence of r_A on the analysis, $\lambda_S(295\text{ K})$ and $|V|$ for **2** were extracted from $k_{CS}(T)$ data in CH₃CN, PhCN, and Et₂O. Table 5.2 lists the means and range of values from analyses using $r_A = 3.5, 3.7, 3.9, \text{ and } 4.1\text{ Å}$. $|V|$ in Et₂O is most sensitive to the value of r_A ($\pm 30\%$ of the mean). The $|V|$ for **2** appear constant in three solvents of very different polarity and ability to mediate coupling.^{6,12} A constant, through bond $|V|$ is expected^{2c,6,12} for a DBA with an all σ -trans bridge. Its observation for **2** indicates the temperature dependence of the *FCWDS* is reasonably modeled.^{6,12,13} Fixing $r_A = 3.7\text{ Å}$ yields $|V| = 20 \pm 2\text{ cm}^{-1}$ for **2** in all three solvents.²²

In contrast to **2**, the $|V|$ obtained by fitting $k_{CS}(T)$ data from **1** vary substantially with solvent (Table 5.2). The largest $|V|$ for **1**, in CH₂Br₂, is nearly as large as the coupling provided by the covalent bridge of **2**. The $|V|$ in the next two most effective solvents, CHCl₃ and PhCN, are half as large.²³ These three solvents have the most positive EA_V (Table 5.1). Two of these three solvents lack π bonds entirely.²⁴ The smallest $|V|$ for **1** are found in solvents with the most negative EA_V .²²

Compared to **2**, the bridge in **1** contains one bend and four more σ -bonds. If only bond mediated coupling is active, $|V|$ (**1**) should be less than $0.07 \times |V|$ (**2**) = 1.4 cm^{-1} .²⁵ The D, B, and A groups of **1** constitute the walls of a molecular cleft that is wide enough ($\sim 7\text{ Å}$ between the "walls") to entrain solvent molecules. These may act as a "second" bridge for the purpose of coupling. For SMC involving unfilled orbitals of a single solvent within the cleft, $|V|$ may be approximated as $\beta_{D^*S}\beta_{SA}/\Delta$, where the β are D^*S and SA exchange integrals and Δ is the vertical energy gap between the CS transition state and the superexchange state, D^+S^-A .²⁶ The vertical energy gap is smallest for solvents with the lowest energy, unfilled orbitals (most positive EA_V).

Thus, the EA_V in the halogenated methanes and PhCN enhance SMC relative to the other solvents. At this point, it is premature to ascribe $|V|$ (**1**) in CH_3CN as primarily solvent or bridge mediated.

The EA_V allow coarse grouping of Δ (and SMC) for the solvents.²⁷ Within each group, the dependence of $|V|$ on EA_V is not monotonic (e.g., in PhCN, $CHCl_3$, and CH_2Br_2). SMC magnitudes are affected by the D*/S and S/A exchange integrals.²⁶ These integrals depend on solvent shape, placement, orientation and on the atomic coefficients of the active molecular orbitals, presumably the LUMO for the most positive EA_V solvents. The LUMO coefficients of PhCN are largest at C_1 and C_4 with smaller values at C_2 , C_3 , and CN. For a single PhCN to span the cleft requires specific solvent placement and orientation; with C_4 proximate to D(A) and CN proximate to A(D). The σ^* LUMO's of $CH_{4-n}X_n$ have large coefficients on the halogen and carbon atoms.²⁸ The halomethanes readily access orientations that span the cleft of **1** and place the solvent LUMO (on a Cl or Br) nearly in van der Waals contact with the D and A.²⁹ This should produce a larger percentage of SMC competent, “in-cleft” solvent configurations, particularly for the largest solvent, $CHCl_3$.³⁰ Even though $1/\Delta$ is smaller for $CHCl_3$ and CH_2Br_2 than for PhCN, larger values of $\beta_{D^*S}\beta_{SA}$ in a larger fraction of solvent configurations are likely responsible for the observed order of couplings.³¹ The low energy and spatially expansive LUMO of the halomethanes give rise to substantial solvent mediated electronic coupling on the 1 nm length scale.

5.1 References.

- (1) Newton, M. *Adv. Chem. Phys.* **1999**, 106 (Pt. 1), 303.
- (2) (a) Winkler, J. R.; Di Bilio, A. J.; Farrow, N. A.; Richards, J. H.; Gray, H. B. *Pure Appl. Chem.* **1999**, 71, 1753. (b) Grinstaff, M. W. *Angew. Chem., Int. Ed.*, **1999**, 38, 3629. (c) Paddon-Row: M. N. *Acc. Chem. Res.* **1994**, 27, 18.
- (3) (a) Lawson, J. M.; Paddon-Row: M. N.; Schuddeboom, W.; Warman, J. M.; Clayton, A. H. A.; Ghiggino, K. P. *J. Phys. Chem.* **1993**, 97, 13099. (b) Kumar, K.; Lin, Z.; Waldeck, D. H.; Zimmt, M. B. *J. Am. Chem. Soc.* **1996**, 118, 243.
- (4) Oliver, A. M.; Craig, D. C.; Paddon-Row: M. N.; Kroon, J.; Verhoeven, J. W. *Chem. Phys. Lett.* **1988**, 150, 366.
- (5) (a) Oevering, H.; Verhoeven, J. W.; Paddon-Row: M. N.; Warman, J. M. *Tetrahedron* **1988**, 45, 4751. (b) Zeng, Y.; Zimmt, M. B. *J. Am. Chem. Soc.* **1991**, 113, 5107. (c) Williams, R. M.; Koeberg, M.; Lawson, J. M.; An, Y. Z.; Rubin, Y.; Paddon-Row: M. N.; Verhoeven, J. W. *J. Org. Chem.* **1996**, 61, 5055.
- (6) Han, H.; Zimmt, M. B. *J. Am. Chem. Soc.* **1998**, 120, 8001.
- (7) Jordan, K. D.; Burrow, P. D. *Chem. Rev.* **1987**, 87, 557.
- (8) Both 1 and 2 contain 2% of an impurity whose fluorescence lifetime is the same as that of a donor only (DB) model compound.
- (9) CS distance determined using the Generalized Mulliken Hush method; Cave, R. J.; Newton, M. D. *Chem. Phys. Lett.* **1996**, 249, 15.
- (10) $k_{CS} = k_{DBA} - k_{DB}$. The nitroethylene is replaced by a carbonyl in DB.
- (11) Jortner, J. *J. Chem. Phys.*, **1976**, 64, 4860.
- (12) For details, see Kumar, K.; Kurnikov, I. V.; Beratan, D. N.; Waldeck, D. H.; Zimmt, M. B. *J. Phys. Chem. A* **1998**, 102, 5529.
- (13) Vath, P.; Zimmt, M. B.; Matyushov, D. V.; Voth, G. A. *J. Phys. Chem. B* **1999**, 103, 9130.
- (14) (a) Matyushov, D. V. *Chem. Phys.* **1993**, 174, 199. (b) Matyushov, D. V. *Mol. Phys.* **1993**, 115, 3830.
- (15) (a) Marcus, Y. *Ion Solvation*; Wiley: Chichester, **1985**; pp 136-138. (b) Yaws, C. L. *Chemical Properties Handbook*; McGraw-Hill, New York, **1991**.

-
- (16) See ref 12 for a study of the influence of different $\lambda_S(T)$ models.
- (17) Knibbe, H.; Rehm, D.; Weller, A. *Ber. Bunsen-Ges. Phys. Chem.* **1969**, 73, 839.
- (18) k_{CS} in Bu₂O and Pr₂O are 23 and 50 x 10⁷ s⁻¹.
- (19) Read, I.; Napper, A.; Kaplan, R.; Zimmt, M. B.; Waldeck, D. H. *J. Am. Chem. Soc.* **1999**, 121, 10976.
- (20) Volume of nitro, olefin and bridgehead CH groups determined with CAChe for Windows, 2.1, Oxford Molecular Group, OR, 1996.
- (21) (a) Latimer, W. M.; Pitzer, K. S.; Slansky, C. M. *J. Chem. Phys.* **1939**, 7, 108. (b) Rashin, A. A.; Honig, B. *ibid.*, **1985**, 89, 5588.
- (22) The $|V|$ for **1** in PhCN, PhCH₂CN and for **2** are half as large as the $|V|$ determined for the same DB's with a dicyanoethylene acceptor.⁶ AM1 estimates of the internal reorganization energy, λ_V , are 0.39 eV for the D/A pair in **1** and **2** and $\lambda_V = 0.30$ eV for the same D with a dicyanoalkene A. The 2-fold difference in $|V|$ for the DB with the different A's is eliminated by altering each λ_V by < 0.13 eV. Errors in the AM1 derived λ_V are a likely source of the difference. The GMH method yields the same $|V|$ for **2** with either A.⁹
- (23) λ_S for **1** are 0.2 to 0.4 eV larger than the continuum estimates. Analyses of $k_{CS}(295\text{ K})$ using $\lambda_{\text{continuum}}$ yield $|V|$ in PhCN, CHCl₃ and CH₂Br₂ that are 3.0, 3.4 and 4.1-fold bigger than $|V|$ in CH₃CN. The solvent dependence of $|V|$ is robust to the model used for λ_S .
- (24) Enhanced k_{CS} in D*BA containing halogenated cyclopropanes was reported recently: Tsue, H.; Imahori, H.; Kaneda, T.; Tanaka, Y.; Okada, T.; Tamaki, K.; Sakata, Y. *J. Am. Chem. Soc.* **2000**, 122, 2279.
- (25) (a) $|V|$ decreases ~ 40% with each bond in these spacers.^{2c} An *s-cis* units reduce $|V|$ more than 2-fold.²⁶ (b) Oliver, A. M.; Craig, D. C.; Paddon-Row, M. N.; Kroon, J.; Verhoeven, J. W. *Chem. Phys. Lett.* **1988**, 150, 366.
- (26) McConnell, H. M. *J. Chem. Phys.* **1961**, 35, 508.
- (27) For the S₁ energy and E_{OX} of this anthracene D, the “good” solvents have EA_V > -0.4 eV.; the poor solvents have EA_V < -2 eV.
- (28) Modelli, A.; Scagnolari, F.; Distefano, G.; Jones, D.; Guerra, M. *J. Chem. Phys.* **1992**, 96, 2061.
- (29) The halogen center to center distance plus twice the van der Waals radius is 6.6 Å for CH₂Cl₂ and CHCl₃ and 7.1 Å for CH₂Br₂.

(30) By this argument, CCl₄ should provide an even larger $|V|$ for **1**. D* transfers an electron to CCl₄. This illustrates the energetic proximity of D*S and D⁺S⁻ for near zero EA_V solvents.

(31) The importance of solvent “spanning” the cleft for effective coupling was recently noted. See ref 19 and Lokan, N. R.; Paddon-Row, M. N.; Koeberg, M.; Verhoeven, J. W. *J. Am. Chem. Soc.* **2000**, 122, 5075.

Chapter 6. The Nature of Electronic Coupling between Ferrocene and Gold through Alkanethiolate Monolayers on Electrodes. The Importance of Chain Composition, Interchain Coupling, and Quantum Interference.

Cyclic voltammetry was used to measure electron transfer rate constants of self-assembled mixed-monolayers on gold electrodes formed by coadsorption of a redox-active ferrocene-based alkanethiol [$(\eta^5\text{C}_5\text{H}_5)\text{Fe}(\eta^5\text{C}_5\text{H}_4)\text{CO}_2(\text{CH}_2)_5\text{X}(\text{CH}_2)_6\text{SH}$, where $X = -\text{CH}_2-$ or $-\text{O}-$] and a diluent alkanethiol [$\text{CH}_3(\text{CH}_2)_4\text{Y}(\text{CH}_2)_6\text{SH}$, where $Y = -\text{CH}_2-$ or $-\text{O}-$]. The replacement of a methylene link by an ether link in the redox-active component leads to a significant reduction in the rate of electron transfer and results from a decrease in the electronic coupling through the chain. The corresponding replacement in the diluent leads to a smaller, but measurable, decrease in rate constant – suggesting that intermolecular electronic coupling pathways also contribute to the electron transfer.[§]

6.1 Introduction

Electron transfer at interfaces is an area of great fundamental and practical importance. The creation of nanometer scale electronic materials is a new technology that relies on such processes. Understanding and controlling charge transport through organic films of nanometer thickness is of fundamental importance to this area of research and others (such as sensor technologies, anti-corrosion films, etc.). Knowledge of how chemical composition and chemical structure impact electron transfer between a solid substrate and a redox active molecule is central to the development of these applied areas of research. Recent studies show how

[§] Reproduced with permission from Napper, A. M.; Liu, H.; Waldeck, D. H.; *J. Phys. Chem. B.* ; 2001; 105(32); 7699-7707. Copyright 2001 American Chemical Society

phenomenological factors affect electron transfer at interfaces, for example the solvent reorganization energy^{1,2}, the density of electronic states in the metal^{3,4}, and electronic coupling between the electrode and the redox couple^{5,6}. This study explores systems for which the electronic coupling changes because of the chemical constitution of the organic film, which constitutes the tunneling barrier.

The development of self-assembly methods for the construction of monolayer films on electrode surfaces provides a means to control and manipulate the interfacial characteristics⁷. This technology has been exploited to investigate fundamental issues of electron transfer between an electrode and a redox couple, either covalently attached or freely diffusing in solution^{8,9}. When such films are composed of saturated molecules (most commonly alkanethiols), the film acts as a barrier to electron transfer from the electrode to a redox couple placed in solution. Through chemical synthesis the thickness of such films can be controlled to a precision of Ångströms. Numerous studies have investigated the thickness dependence of the electron transfer rate constant^{8,9,10} and find it to be well described by an exponential decay law

$$k_{\text{eT}} \propto \exp(-\beta L) \quad (6.1)$$

where β is an empirical parameter and L is the film thickness. For insulating films on metal electrodes, β is typically of the order of 1 \AA^{-1} . Other systems, for example alkane films on InP¹¹ and films comprised of conjugated molecules¹², display weaker distance dependencies. Other studies have addressed the influence of temperature¹³, solution composition¹⁴, pressure¹⁵, film heterogeneity¹⁶ and double layer structure¹⁴ on the transfer rate.

The perspective used to describe electron transfer through insulating films has been based on insights gained from studies of intramolecular and intermolecular electron transfer. For electron donor and electron acceptor units that interact weakly (the nonadiabatic limit), a

superexchange mechanism^{17, 18, 19} for the electronic coupling may be used successfully with molecular systems however its applicability to electron transmission through films is not well-established. The view that ‘through-bond’ superexchange coupling is dominant when it is a possible mechanism suggests that the electron transfer should be sensitive to the properties of the linking molecule (e.g., the alkane chain) such as its composition, connectivity, and geometry. In addition, it suggests that electron transfer through noncovalent interactions, which are present in the monolayer film, will be of minor importance. This view stands in contrast to the simple solid-state view of ‘line-of-sight’ tunneling through an effective one-dimensional barrier. At a higher level of treatment these two views should be merged since the characteristics of the barrier, e.g., its dimensionality and shape, are determined by the intramolecular and intermolecular properties of the film constituents. The current study investigates the importance of chain composition and interchain interactions (i.e., electronic coupling through nonbonded contacts) on the electron transfer rate constant for fully saturated chains.

The importance of film composition on the electron transfer rate is of current interest, in particular for building conductive links between electrodes (‘molecular wires’) and for better insulating electrodes from one another. Miller and coworkers²⁰ studied the rate of electron transfer between a gold electrode and a freely diffusing redox couple in solution ($\text{Fe}(\text{CN})_6^{3-/4-}$ and $\text{Os}^{\text{III}}(\text{bipy})_3$) through self-assembled monolayers consisting of $\text{HO}(\text{CH}_2)_n\text{X}(\text{CH}_2)_m\text{SH}$, in which X denotes an ether, olefin or alkyne function. All three chemical modifications resulted in a decrease in the rate constant compared to the hydrocarbon parent ($X = \text{CH}_2$), by a factor of *ca.* 2. This result was interpreted to arise from a decrease in the electronic coupling across the monolayer. In contrast, Creager²¹ has reported that an *n*-alkylcarboxamide linked ferrocene moiety has the same rate constant as an all *n*-alkane linked ferrocene. Finally, these results are

distinct from studies of films comprised of fully conjugated molecules for which the conductivity is high.^{12,22}

Because of film compactness, interchain interactions can play a role in the electron transfer process.^{23,24,25} Majda and coworkers²³ examined interchain electronic interactions by changing the tilt angle that thioalkanes make on the surface of a hanging drop mercury electrode. Upon tilting, the films retained their passivating character (indicating the absence of defects) but displayed an increase in tunneling current ($\text{Fe}(\text{CN})_6^{3-} / \text{Fe}(\text{CN})_6^{4-}$ is the redox couple) as the tilt angle was increased. For a dodecanethiol film they found that the current increased with tilt angle and were able to quantify this change by considering two parallel coupling pathways: one through the covalent linkages of an individual alkane chain and the other involving an interchain ‘hop’ along with the through-bond pathway [see reference 23b]. Although it represents a significantly weaker dependence than that found by changing the number of methylene units in the alkane chain, their result indicates an increase in electronic coupling $|V|$ as a result of enhanced chain-to-chain interaction. The authors estimated that chain-to-chain coupling was about five times smaller than through-chain coupling for alkylthiol monolayers. Finklea²⁴ examined monolayers containing the electroactive $\text{HS}(\text{CH}_2)_n\text{C}(\text{O})\text{NHCH}_2\text{pyRu}(\text{NH}_3)_5^{2+/3+}$ and a diluent $\text{HS}(\text{CH}_2)_m\text{COOH}$. This comprehensive investigation characterized both the reorganization energy, λ , and the standard rate constant, k° for systems in which $m = n$ (matched) and $n > m$ (exposed). The matched systems displayed β values of 0.97 ± 0.03 per methylene, and the exposed systems displayed β values of 0.83 ± 0.03 per methylene – in reasonable agreement with other studies. For the systems in which $n < m$ (buried), β was significantly smaller, 0.16 ± 0.02 . This large decrease in β suggests a strong effect of interchain coupling on the electron transfer.

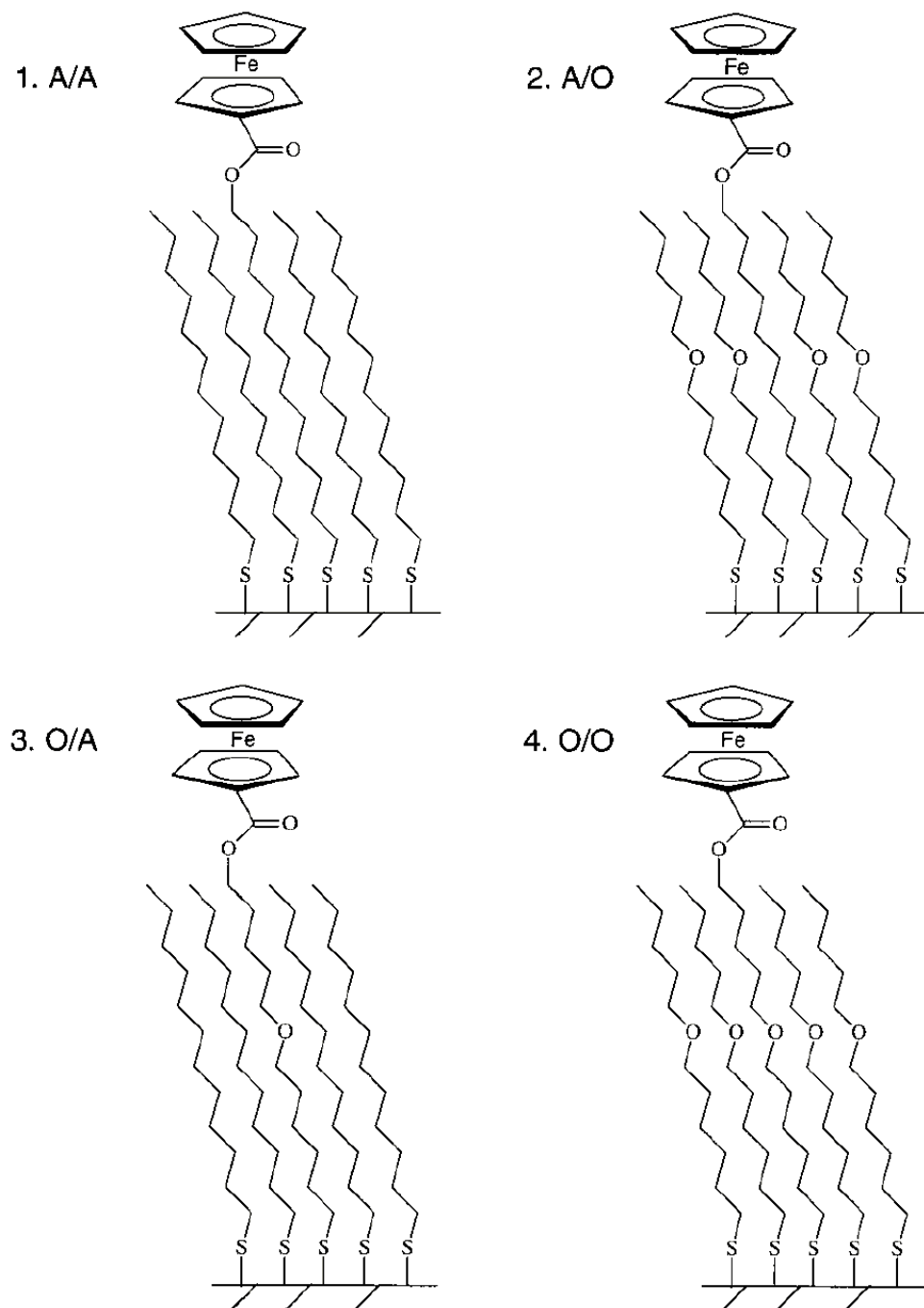


Figure 6.1 Schematic illustration of the four systems studied.

They suggest that this strong effect arises from the ability of the neighboring chains to form intermolecular hydrogen bonds between the terminal carboxylic acid group and the ruthenium redox couple. This result is in reasonable agreement with the recent work of Sek et al.²⁵ in which an increase in electron transfer rate is associated with internal hydrogen bonding between amide groups in the monolayer.

This study demonstrates the importance of chain composition and interchain effects for electron transfer in the four systems drawn in Figure 6.1. The rate constant for electron transfer to a ferrocene moiety that is tethered to an ether spacer is found to be four to five times smaller than that through a pure alkane chain. This reduction is found in films comprised of both an alkane diluent and an ether diluent, thereby muting possible concerns about subtle changes in the reorganization energy, or effective dielectric constant of the film. In addition, the comparison of electron transfer rates with a given electroactive system in differing diluent molecules indicates that interchain interactions have a less than 50% effect on the electron transfer rate constant.

6.2 Experimental

6.2.1 Reagents.

Dodecanethiol (98+%, Aldrich), Perchloric Acid (70%, Mallinckrodt), Ethanol (200 proof, Pharmco Products, inc.), and Gold wire (99.99+%, 250 μ m dia., Goodfellow) were used as received. Water for preparing electrolyte solutions and rinsing of electrodes was purified using a Barnstead-Nanopure system and was 18 M Ω -cm. Thiourea (99%), potassium hydroxide, ferrocenecarboxylic acid (97%), 1,6-dibromohexane (98%), 1,5-pentanediol (99%), *N,N'*-dicyclohexylcarbodiimide (DCC), 4-(dimethylamino)pyridine (DMAP), sodium hydride (95%), 1-pentanol, and 12-bromo-1-dodecanol were purchased from Aldrich.

6.2.2 Electrode Fabrication.

Gold wire was heated in a natural gas / O₂ flame to form a ball ca. 0.5 mm in radius. The exposed wire was sealed in a soft-glass capillary tube. The gold ball was re-heated in the flame until glowing and then cooled in a stream of Ar gas. The electrode was immediately placed into an ethanol solution of 1 mM total thiol concentration. Typically a 9:1 molar ratio of diluent to electroactive thiol comprised the deposition solution. Deposition time was typically 48 h following which the electrode was rinsed with copious quantities of absolute ethanol, followed by 18 MΩ-cm water. A brief (20 s) immersion in 40 °C 1 M HClO₄, prior to use in the electrochemical cell was found to improve the quality of the measured voltammograms.

6.2.3 Synthesis of CH₃(CH₂)₄O(CH₂)₆SH.

1-Pentanol (2.190 g, 24.84 mmol) was reacted with 95% NaH (0.753 g, 29.8 mmol) in dry tetrahydrofuran for 15 minutes. 1,6-dibromohexane (18.15 g, 74.55 mmol) was added, and the mixture was refluxed for three hours. After filtering the NaBr solid, the solvent was removed under vacuum. Br(CH₂)₆O(CH₂)₄CH₃ was obtained by column chromatography (silica gel, hexane and dichloromethane, 1:1). 7-oxo-1-dodecyl mercaptan was prepared by converting the bromide to the mercaptan by treatment with thiourea followed by base hydrolysis and column chromatographic purification. ¹H NMR (300 MHz) CDCl₃: 3.399 (t, *J* = 6.75 Hz, 4H); 2.532 (q, *J* = 7.35 Hz, 2H); 1.605 (m, 4H); 1.422 - 1.265 (broad, 11H); 0.908 (t, *J* = 6.12 Hz, 3H).

6.2.4 Synthesis of (η⁵C₅H₅)Fe(η⁵C₅H₄)CO₂(CH₂)₁₂SH.

12-(Ferrocenylcarbonyloxy)dodecyl bromide was prepared as follows: DCC (0.9335 g, 4.52 mmol) was added to a concentrated solution of ferrocenecarboxylic acid (0.9541 g, 4.15 mmol), 12-bromo-1-dodecanol (1.0 g, 3.7 mmol) and DMAP (50.7 mg, 0.415 mmol) in

dichloromethane at 0 °C. After 1 h the solution was allowed to warm to room temperature and was stirred overnight. After removal of the precipitated dicyclohexylurea (DCU) by filtration, the product was recovered by extraction with CH₂Cl₂. After washing the CH₂Cl₂ extracts twice with dilute HCl solution and water, it was dried over magnesium sulfate and evaporated under reduced pressure. The product was dissolved in methylene chloride and chromatographed on silica gel with methylene chloride. The bromide (a brown solid, 1.55 g) was obtained by evaporation under reduced pressure. ¹H NMR (300 MHz) CDCl₃: δ 4.814 (t, *J* = 1.86 Hz, 2H); 4.395 (t, *J* = 1.85 Hz, 2H); 4.216 (t, *J* = 6.6 Hz, 2H); 4.206 (s, 5H); 3.412 (t, *J* = 6.84 Hz, 2H); 1.857 (m, 2H), 1.730 (m, 2H); 1.42 (m, 4H); 1.398-1.297 (broad, 12H). A portion of this bromide (0.551 g, 1.15 mmol) and thiourea (0.263 g, 3.45 mmol) were added to 25 mL of absolute ethanol and the resulting solution was stirred and refluxed under argon overnight. After removal of solvent under vacuum, 25 mL of an aqueous solution of potassium hydroxide (0.193 g, 3.45 mmol) was added, and the mixture was refluxed for 4 h under argon and then cooled down to room temperature. The resulting solution was extracted with three 50 mL portions of methylene chloride, and the combined extract was washed with dilute HCl solution and water, respectively. The extract was dried with anhydrous magnesium sulfate. The solution was concentrated under vacuum and chromatographed on silica gel with methylene chloride. The first yellow band contained the desired 12-(ferrocenylcarbonyloxy)dodecane thiol product (0.26 g, a brown solid), and a second yellow band contained the corresponding disulfide. ¹H NMR (300 MHz) CDCl₃: δ 4.812 (t, *J* = 1.86 Hz, 2H); 4.393 (t, *J* = 1.85 Hz, 2H); 4.214 (t, *J* = 6.6 Hz, 2H); 4.205 (s, 5H); 2.525 (q, *J* = 7.380 Hz, 2H); 1.707 (m, 2H), 1.609 (m, 2H); 1.435-1.288 (broad, 17H).

6.2.5 Synthesis of $(\eta^5\text{C}_5\text{H}_5)\text{Fe}(\eta^5\text{C}_5\text{H}_4)\text{CO}_2(\text{CH}_2)_5\text{O}(\text{CH}_2)_6\text{SH}$.

A starting material, $\text{HO}(\text{CH}_2)_5\text{O}(\text{CH}_2)_6\text{Br}$ (12-bromo-6-oxo-1-dodecanol), was prepared by a procedure analogous to that used for $\text{CH}_3(\text{CH}_2)_4\text{O}(\text{CH}_2)_6\text{Br}$. ^1H NMR (300 MHz) CDCl_3 : δ 3.622 (t, $J=5.88$ Hz, 2H); 3.407 (m, 6H); 1.649 (m, 2H); 1.552 (m, 8H); 1.405 (m, 4H). 12-(Ferrocenylcarbonyloxy)-7-oxo-1-dodecyl mercaptan was prepared by a method analogous to that described above for the 12-(ferrocenylcarbonyloxy)dodecane thiol. ^1H NMR (300 MHz) CDCl_3 : δ 4.802 (t, $J=1.91$ Hz, 2H); 4.384 (t, $J=1.91$ Hz, 2H), 4.217 (t, $J=6.54$ Hz, 2H); 4.196 (s, 5H); 3.437 (t, $J=4.85$ Hz, 2H); 3.404 (t, $J=5.00$ Hz, 2H); 2.518 (q, $J=7.38$ Hz, 2H); 1.752 (m, 2H); 1.613 (m, 8H); 1.386 (m, 5H).

6.2.6 Electrochemical Measurements.

Cyclic voltammetry was performed using an EG&G PAR-283 potentiostat controlled by a PC running ver. 4.30 of PAR's M270 software and a GPIB board. All measurements were performed at room temperature in a 1.0 M HClO_4 aqueous electrolyte solution. The counter electrode was a platinum spiral and potentials were referenced against a Ag/AgCl reference electrode from BAS. The uncompensated resistance was measured to be less than 10 Ω , leading to a maximum error of 10 mV at the highest scan rate. This corresponds to 3% of the peak separation observed at the same scan rate. The iR drop was less than 1 mV for most scan rates. In addition to these measurements, the sweep rate data was analyzed for systematic trends in the extracted rate constant at different sweep rates. All of the data used here was independent of any systematic change, indicating that iR drop is not important for these measurements²⁶.

6.3 Background

6.3.1 The Electron Transfer Rate Constant.

In the nonadiabatic limit, the electron transfer rate constant k_{eT} is given by the *Fermi Golden Rule* expression,

$$k_{eT} = \frac{2\pi}{\hbar} |V|^2 FCWDS \quad (6.2)$$

Equation 6.2 describes the rate of a nonadiabatic transition between two states, with an exchange interaction between the sites of magnitude $|V|$. *FCWDS* is the Franck-Condon Weighted Density of States and accounts for the impact of nuclear coordinates on the electron transfer rate. When $-\Delta G$ is smaller than the reorganization energy λ of the reaction (normal region) and high frequency vibrational modes of the donor and acceptor are not a significant part of the reorganization, the FCWDS may be written as

$$FCWDS = \frac{1}{\sqrt{4\pi\lambda k_B T}} \exp\left[-\frac{(\lambda + \Delta G)^2}{4\lambda k_B T}\right] \quad (6.3)$$

The reorganization energy, λ , consists of two components: an inner sphere contribution that is associated with the internal coordinates of the redox species, λ_{in} , and an outer sphere component, λ_{out} , that is dominated by the solvent polarization. For the ferrocene/ferrocenium redox couple, which is discussed here, a frequently used approximation is to consider only the dominant λ_{out} term. When the internal reorganization energy is important, a semi-classical expression for the rate constant should be used – however this level of sophistication is not needed for this study. See reference 27 for a more detailed discussion of this model.

For electron transfer at an electrode, eqs 6.2 and 6.3 must be generalized to consider the range of electronic states that are available in the solid. For an electron at energy ε in the electrode, the free energy of reaction is given by

$$\Delta G = (\varepsilon_F - \varepsilon) + e\eta \quad (6.4)$$

where η is the overpotential and ε_F is the Fermi level of the electrode. Substitution of eq 6.4 into eq 6.3 generates

$$k_{\text{red}}(\varepsilon, \eta) = \frac{2\pi}{\hbar} |V|^2 \frac{1}{\sqrt{4\pi\lambda k_B T}} \exp\left[-\frac{(\lambda + (\varepsilon_F - \varepsilon) + e\eta)^2}{4\lambda k_B T}\right] \quad (6.5)$$

for transfer of an electron from a specific electrode energy state to an electron acceptor. The rate constant for reduction requires an integration over all energy states of the solid, so that

$$k_{\text{red}}(\eta) = \frac{2\pi}{\hbar} |V|^2 \frac{1}{\sqrt{4\pi\lambda k_B T}} \int_{-\infty}^{\infty} \rho(\varepsilon) \exp\left[-\left(\frac{(\lambda + (\varepsilon_F - \varepsilon) + e\eta)^2}{4\lambda k_B T}\right)\right] f(\varepsilon) d\varepsilon \quad (6.6)$$

where $\rho(\varepsilon)$ is the density of electronic states of the electrode (often an energy independent average value is used) and $f(\varepsilon)$ is the Fermi-Dirac distribution law

$$f(\varepsilon) = \frac{1}{1 + \exp[(\varepsilon - \varepsilon_F)/k_B T]} \quad (6.7)$$

An expression similar to eq 6.6 can be written for the oxidation current

$$k_{\text{ox}}(\eta) = \frac{2\pi}{\hbar} |V|^2 \frac{1}{\sqrt{4\pi\lambda k_B T}} \int_{-\infty}^{\infty} \rho(\varepsilon) \exp\left[-\left(\frac{(\lambda + (\varepsilon_F - \varepsilon) - e\eta)^2}{4\lambda k_B T}\right)\right] [1 - f(\varepsilon)] d\varepsilon \quad (6.8)$$

6.3.2 Obtaining Rate Constants from Voltammograms.

The electron transfer rate constants were obtained by measuring the peak shift as a function of scan rate in cyclic voltammetry experiments.²⁸ Working curves of $\log(\text{scan rate})$ vs. peak position were generated for specific values of λ and T by a Microsoft QuickBasic routine which numerically integrated the relevant equations. These working curves were used to fit the experimental data and obtain the standard rate constant k° , the rate constant at zero overpotential.

Equations 6.6 and 6.8 were modified to calculate synthetic cyclic voltammograms. In particular, the electronic density of states in the metal was approximated as being constant over the energy regime that contributes significantly to the measured current. In this case eqs 6.6 and 6.8 become

$$k_{\text{red},\eta} = \mu\rho k_B T \int_{-\infty}^{\infty} \frac{\exp\left[-(x - (\lambda + \eta)/k_B T)^2 (k_B T/4\lambda)\right]}{1 + \exp(x)} dx \quad (6.9)$$

$$k_{\text{ox},\eta} = \mu\rho k_B T \int_{-\infty}^{\infty} \frac{\exp\left[-(x - (\lambda - \eta)/k_B T)^2 (k_B T/4\lambda)\right]}{1 + \exp(x)} dx \quad (6.10)$$

in which ρ is the effective density of electronic states in the metal electrode, x is $(\epsilon - \epsilon_F)/kT$, and

$\mu = \frac{|V|^2}{h} \sqrt{\frac{4\pi^3}{\lambda k_B T}}$. The integrals were evaluated numerically, from -9 to +9 V at a step size of 1

mV using Simpson's rule.

The measured current i_{meas} in the voltammetric experiment is directly related to the reduction and oxidation rate constants.²⁸ The linear sweep voltammograms were generated by application of eqs 6.11 and 6.12, using a potential step size of 0.5 mV. The dimensionless current i_{norm} may be written as

$$i_{\text{norm}} = \frac{\Delta f}{\Delta E / (RT/F)} = \left(\frac{RT/F}{\Delta E} \right) (f_{\text{target}} - f_o) (1 - \exp[-(k_{\text{red}} - k_{\text{ox}})\Delta t]) \quad (6.11)$$

$$f_{\text{target}} = \frac{1}{1 + \exp(-EF/RT)} \quad (6.12)$$

in which Δt is the time interval over which the potential is applied ($\Delta t = \Delta E / \nu$), ν is the sweep rate, ΔE the potential step size, and f_o is the fraction of oxidized species initially present in the time interval over which the potential step is applied.

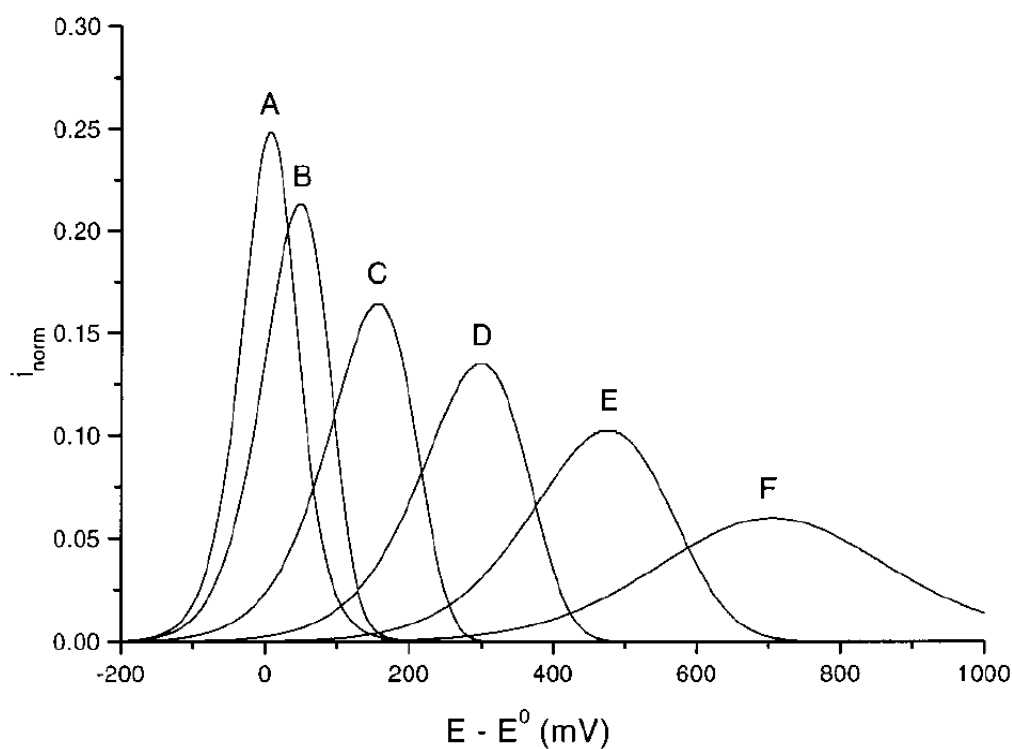


Figure 6.2 Synthetic linear sweep voltammograms were generated for the following $\log(\nu / k^{\circ})$ parameters: **A** = -2.0, **B** = -1.0, **C** = 0, **D** = 1.0, **E** = 2.0, **F** = 3.0. A value of 5.0 s^{-1} was chosen for k° , and λ is 0.8 eV.

Working curves of $\log(\nu / k)$ vs. peak position ($E_p - E^{\circ}$) were generated and used to fit the experimental data. For a fixed standard rate constant, Figure 6.2 demonstrates the increasing

deviation of the curve maxima from the fully reversible value of E° . This change arises from the inability of the electron transfer event to keep up with the rapidly scanning sweep rate. Note the broadening of the curve and the decrease in peak height at higher values of $\log(v/k)$. At low sweep rates, the curve width at half height is equal to the thermodynamic value of 90.6 mV (at 298 K). $k_{\text{ox},0}$ and $k_{\text{red},0}$ were set to 5 s^{-1} in the simulation, by alteration of the prefactor $\mu\rho k_{\text{B}}T$ in eqs 6.9 and 6.10.

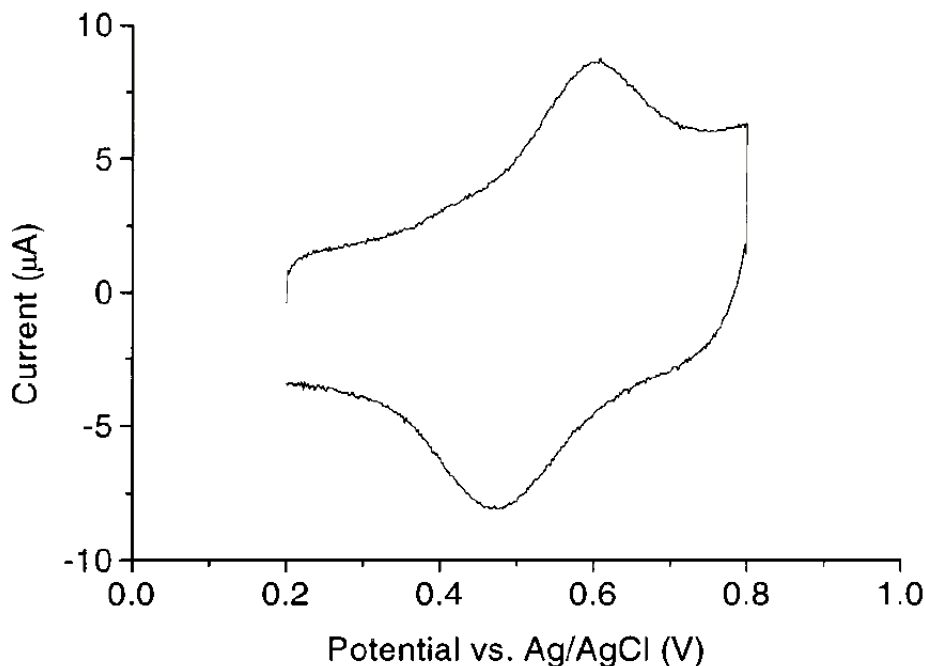


Figure 6.3 This figure shows a typical cyclic voltammogram for the O/A system, at a scan rate of 3200 mV/s. The supporting electrolyte is 1.0 M HClO_4 , and the surface coverage of electroactive thiols is about 10%.

6.4 Results

The quality of the electroactive SAMs was assessed by three factors: peak widths at low scan rate, peak separations at low scan rates, and fractional ferrocene coverage. Typically, the peak widths were between 90 and 110 mV for the slowest scan rates. For an ideal system at

thermodynamic equilibrium, the peak width is expected to be 91 mV.⁸ Figure 6.3 shows a voltammogram for an ether-linked ferrocene in an alkane diluent at an intermediate scan rate. As the scan rate is lowered the peak separation decreases toward zero, indicating reversibility. Surface coverage of the ferrocene was estimated from the integrated charge of the ferrocene / ferrocenium species and the electrode's physical surface area, which was estimated by measuring the diameter of the gold balls with calipers. Typical ferrocene coverages were between 5 and 15%.

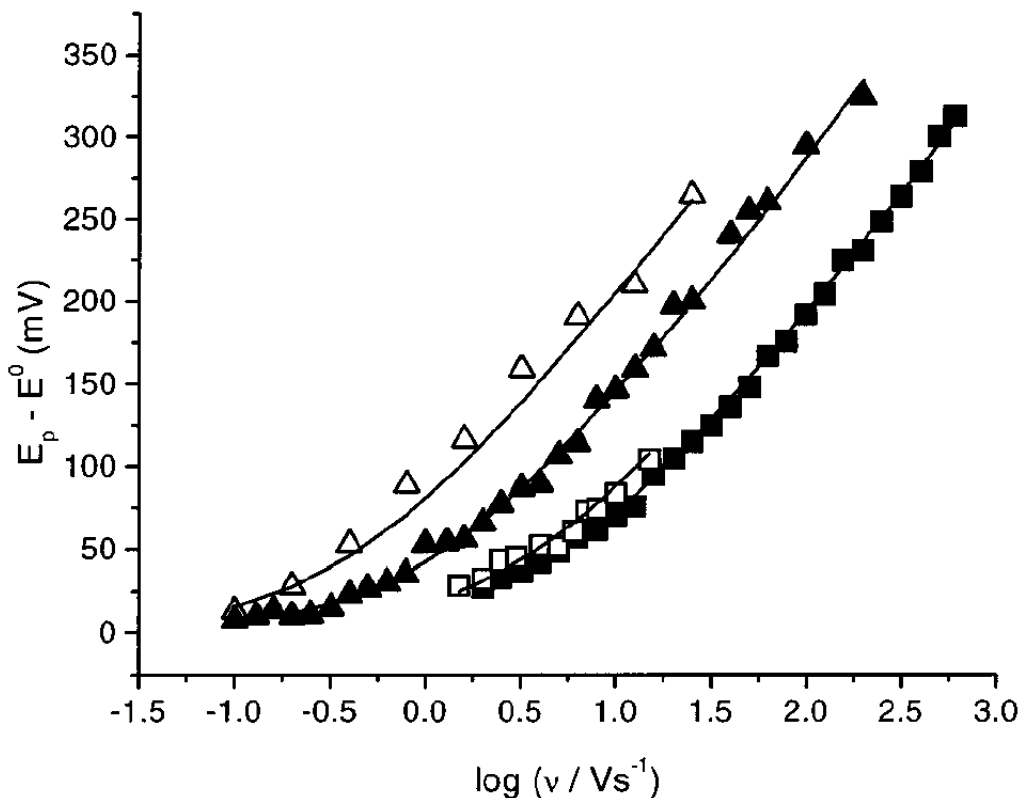


Figure 6.4 Plot of anodic ($E_p - E^0$) vs. \log (sweep rate) for all four systems studied. The solid lines are the best fit to the data points using the Marcus model described in the text. λ is taken to be 0.8 eV and $T = 298$ K. The data points are from a specific run, and the calculated k^0 is 52.8 s^{-1} for A/A (filled squares), 37.3 s^{-1} for A/O (open squares), 12.2 s^{-1} for O/A (filled triangles), and 4.4 s^{-1} for O/O (open triangles).

Figure 6.4 presents plots of the anodic peak potential minus the formal potential for each of the four systems. The more rapid increase in the peak separation for the ether-linked ferrocene (open triangles are ether diluent and the filled triangles are for alkane diluent) as compared to the alkane-linked ferrocene (open squares are for the ether diluent and the filled squares are for the alkane diluent) is clearly evident. In each case a best fit of the rate constant to the model (eqs 6.9 - 6.12) is shown by a solid line and found to characterize the rate constant's dependence on scan rate. The standard rate constant, k° , values that are obtained from these fits are reported in Table 6.1.

Table 6.1 Kinetic Data for the Four Model Systems^a

electroactive thiol	diluent thiol	rate constant (s ⁻¹)	E° (mV vs Ag/AgCl)	number of determinations
alkane	alkane	55.0 ± 9.1	522 ± 13	10
alkane	ether	35 ± 12	532 ± 31	6
ether	alkane	12 ± 3	534 ± 13	3
ether	ether	8.4 ± 2.5	516 ± 32	7

^a The reported errors represent ±1 standard deviation.

Previous measurements of k° are available for the alkane tethered system in an alkanethiol diluent and agree well with the value reported here. The rate constant value for the twelve carbon chain was obtained by Chidsey^{7c,10b} using chronoamperometry. They report a k° value of 0.625 s⁻¹ for electron transfer through a hexadecane chain,²⁹ and they report a chain length decay parameter, β , of 1.11 per methylene unit.^{10b} Using these values one estimates a k° value of 53 s⁻¹ for electron transfer through a dodecanethiol chain at 298K. Carter et al.³⁰ have also measured k° for this ferrocene system, and they extrapolate their low temperature data to obtain a rate

constant of 35.5 s^{-1} at 273 K and $\eta = 0$. The system studied here was measured at larger temperatures (ca. 295 K) and are expected to be somewhat faster than those at 273 K. Further extrapolation of Carter's rate data from 273 K to 295 K gives a k° value of 67 s^{-1} . Both of these previous measurements (53 s^{-1} and 67 s^{-1}) are in good agreement with the best fit rate of 55 s^{-1} reported here.

Figure 6.5 illustrates how the assumed λ affects the quality of the data fitting. The solid line represents a fit to $k^\circ = 52.8 \text{ s}^{-1}$ and $\lambda = 0.8 \text{ eV}$. The dashed lines represent fits with $k^\circ = 52.8 \text{ s}^{-1}$ and $\lambda = 0.6$ or 1.0 eV . A 25% change in λ does not seem to compromise the quality of fit significantly. Presumably any small difference in λ between the four systems does not significantly alter the calculated rate constants. On the other hand it is not possible to use these data to distinguish any possible variations in λ between the four systems.

Spectroscopic studies by Miller and coworkers²⁰ on ether-linked alkanethiols revealed no perceptible change in the tilt angle of the chain molecules and a small (ca. 10%) twist angle with respect to the alkane films. Hence structural differences between layer types are expected to be small. The most significant effect on λ is expected to arise from a dipole in the ether-linked chains, which cause a change in the effective dielectric constant of the film, compared to the alkane layers. It is for this reason that control experiments were performed with both alkane and ether linked diluent films (see Table 6.1). For the four systems, the effective dielectric constant of the layer should be smallest for the all alkane system, somewhat larger for the ether-linked ferrocene (10%) embedded in the all alkane (90%) diluent, significantly larger for the alkane

tethered ferrocene (10%) embedded in the ether-linked diluent (90%), and largest for the all ether-linked system. The rate constants do not follow this trend.

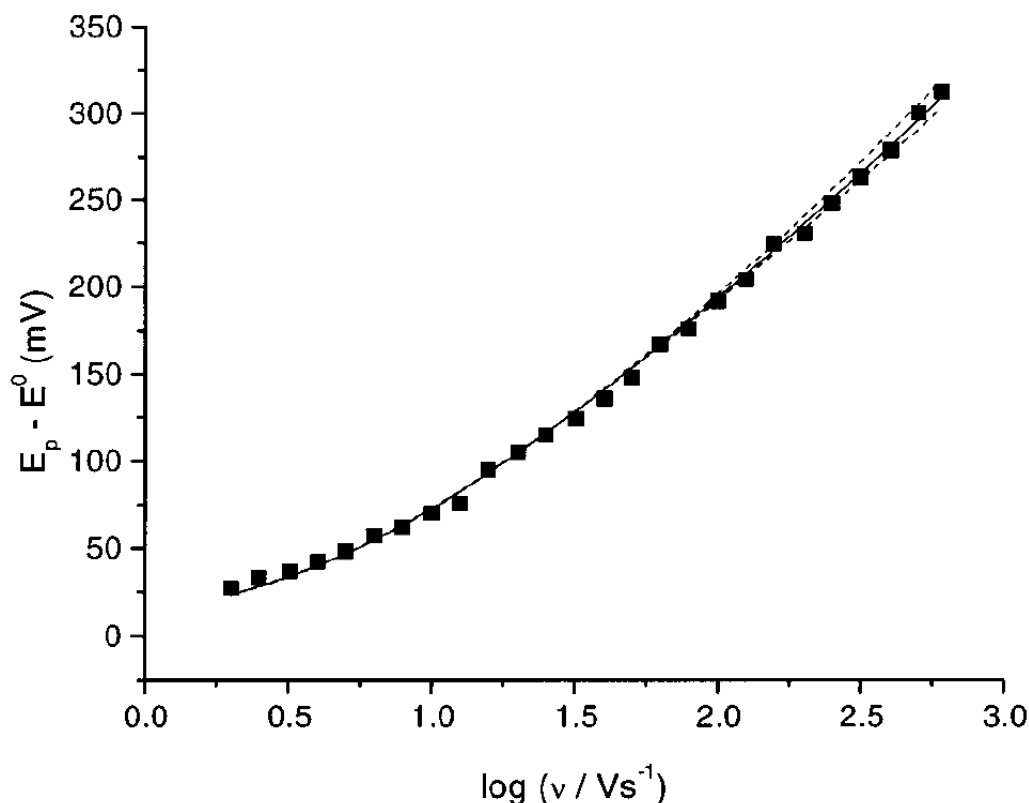


Figure 6.5 This figure shows fits to the peak separation data for A/A using different values of the reorganization energy. The dotted lines show the fits of the rate data to reorganization energies of 0.6 and 1.0 eV at a fixed rate constant of 52.8 s^{-1} .

The experimental rate constants are provided in Table 6.1. The introduction of an ether linkage into the electroactive thiol chain has a dramatic effect upon the rate constant, causing a reduction of 4.2 ± 0.1 times for the ether diluent to 4.6 ± 0.1 times for the alkane diluent. This observation is consistent with ‘through-bond’ electronic coupling of the ferrocene / ferrocenium with the electrode. A similar reduction in rate constant is found for both the ether and the alkane

diluent and suggests that changes in the reorganization energy that one might find upon replacing the methylene in the alkane with an oxygen atom (the ether) is not the origin of this affect. A comparison of the same electroactive tether in the two different diluents (ether and alkane) reveals a much smaller, but still quite visible, change in the rate constant. For both electroactive species the electron transfer rate constant is smaller in the ether diluent and by a similar amount (0.30 ± 0.27 and 0.36 ± 0.24 reductions), even though the absolute rate constants differ by a factor of four to five for the two types of electroactive tethers.

6.5 Discussion

The superexchange mechanism, first proposed by McConnell in 1961³¹ to explain the electron exchange in α,ω -diphenylalkane anions, is a perturbation treatment for the electronic interaction between molecular subunits. In this treatment the expression for V is given by

$$V = \frac{H_{D1}H_{nA}}{\epsilon_t - \epsilon_1} \prod_{i=1}^{n-1} \frac{H_{i,i+1}}{\epsilon_t - \epsilon_{i+1}} \quad (6.13)$$

in which n is the number of bridge sites, $H_{i,i+1}$ represents the exchange integral between adjacent bridge sites, ϵ_i is the energy of bridge site i , H_{D1} is the coupling between the electron donor and the first bridge site, H_{nA} is the coupling between the last bridge site and the electron acceptor, and ϵ_t is the electronic energy at which the electron tunnels from the donor to the acceptor. For identical bridge units, the product in eq 6.13 can be replaced by $(t / \Delta)^{n-1}$ where t is the exchange coupling between adjacent bridge units and Δ is the energy difference between the bridge sites and the tunneling energy. For long bridges, $|V|$ behaves approximately as an exponentially decaying function, so that

$$|V| = |V_0| \exp\left[-\frac{\beta}{2}(n - n_0)\right] \quad ; \quad \frac{\beta}{2} = -\ln\left(\frac{t}{\Delta}\right) \quad (6.14)$$

in which $|V_0|$ would be the coupling in the absence of a bridge and β is the exponential decay parameter (see eq 6.1). Replacement of one of the bridging methylene units by an oxygen atom introduces two different exchange integrals (t for the methylene and t' for the ether link) in eq 6.13 and modifies the denominator accordingly (Δ for the methylene site and Δ' for the oxygen site).

This development of superexchange relies on the nearest-neighbor (tight binding) interactions in order to calculate the electronic coupling through a bridge unit. It has been shown for long bridges that the nearest neighbor coupling is not the dominant coupling mechanism. Indeed, the majority of the interaction arises from pathways (a pathway is a combination of exchange interactions that have starting and final points at the donor and acceptor, respectively) that skip over some bonds. If non-nearest-neighbor interactions are considered, many more pathways have to be considered; all of which contribute to the total electronic coupling. It is possible to calculate electronic couplings for all possible routes through a molecule, and the total electronic coupling is equal to the sum of the contributions from each specific pathway. The contribution to the electronic coupling from a pathway can be either negative or positive and a partial cancellation of contributions from different pathways may occur, destructive interference. Jordan³² and others have discussed the importance of interference for all hydrocarbon systems extensively. Their study³⁶ gave a distance dependence of $\beta = 0.34$ per methylene as the limiting value ($m > 10$) for hole mediated coupling in molecules of the type: $\text{CH}_2=\text{CH}-(\text{CH}_2)_m-\text{CH}=\text{CH}_2$, whereas bridges of comparable length that contain cyclobutane or norbornane units were shown³⁶ to have a larger value of β (and smaller electronic coupling). The origin of this difference was shown to lie with the introduction of pathways that destructively interfere for the ring systems.

The electronic coupling was calculated for two symmetric, model compounds: $\bullet\text{CH}_2(\text{CH}_2)_{11}\text{CH}_2\bullet$ and $\bullet\text{CH}_2(\text{CH}_2)_5\text{O}(\text{CH}_2)_5\text{CH}_2\bullet$. Previous work has shown that the neutral diradical calculation can be used to identify both the radical cation coupling (expected to be dominated by a hole mediated mechanism) and the radical anion coupling (expected to be dominated by an electron mediated mechanism) when combined with Koopmans theorem approximation.^{34,35} The radical cation coupling was obtained by analyzing the α -spin bonding and antibonding orbitals (as well as the two lone pairs on the oxygen) to determine the splitting in the ionization potential of the diradical, and the radical anion coupling was obtained by analyzing the β -spin bonding and antibonding orbitals to determine the splitting in the electron affinity of the diradical. The geometry of the triplet diradical was optimized at the UHF/3-21G level of theory using Gaussian 98.³³ Previous studies show that this level of theory gives reasonable results for the electronic coupling.^{34,35,36} The canonical molecular orbitals obtained from the calculation were transformed into the Natural Bond Orbital^{33b} (NBO) basis in order to analyze the differences found for the coupling between these systems.

The electronic couplings for the radical cation and anion were obtained in two different ways.

- (1) Splitting of the α -HOMO and HOMO-1 levels in the full unrestricted Hartree-Fock molecular orbital analysis corresponds to $2|V|$ for the radical cation species. Both hole- and electron-transfer processes contribute to the Donor / Acceptor electronic coupling, however it is often the case that the hole-transfer process dominates in the radical cation analysis.³⁴ The splitting of the β -LUMO and LUMO+1 orbitals corresponds to $2|V|$ for the radical anion (see Table 6.2). This approach utilizes Koopmans approximation.

Table 6.2 Electronic couplings for the radical cation and anion determined from electronic structure calculations.

	$\bullet\text{CH}_2(\text{CH}_2)_{11}\text{CH}_2\bullet$	$\bullet\text{CH}_2(\text{CH}_2)_5\text{O}(\text{CH}_2)_5\text{CH}_2\bullet$
$ V _{\text{cation}}^a$	340	200
$ V _{\text{anion}}^a$	70	76
$ V _{\text{cation}}(\sigma \text{ manifold})^b$	160	86
$ V _{\text{cation}}(\sigma^* \text{ manifold})^b$	1.2	1.4
$ V _{\text{cation}}(\text{full})^b$	340	200
$ V _{\text{anion}}(\sigma^* \text{ manifold})^b$	36	39

^a Determined from energy splittings of HOMO or LUMO levels.

^b Determined from diagonalization of modified NBO Fock matrix.

(2) The delocalized canonical SCF molecular orbitals (MOs) obtained from method (1) were transformed into the Natural Bond Orbitals basis, defined by Weinhold.³⁷ These orbitals can be divided into “occupied”, corresponding to core orbitals, σ bonds, π bonds, and lone pairs, and “unoccupied” orbitals, corresponding to σ^* and π^* antibonding orbitals and extra-valence-shell orbitals (Rydbergs). Elements from the full Fock matrix, corresponding to the terminal radical lobes and the σ and σ^* bridge orbitals, were extracted and used to form a reduced Fock matrix. This reduced matrix was analyzed to obtain the electronic coupling for the radical cation from the splitting in the α HOMO levels and for the radical anion from the splitting in the β LUMO levels.³⁸

The results of these analyses are presented in Table 6.2. The molecular orbital calculation shows similar electronic couplings for the two compounds in the case of the radical anion. Significantly different couplings are found for the radical cations of the two model compounds, and the alkane compound is larger than that of the ether linked compound, in agreement with the experimental

observation. The NBO analysis is also presented in Table 6.2, and it was performed in order to display the couplings associated with different orbital types. These calculations show that the larger electronic coupling for the radical cation has its origin in the σ bonding manifold of the alkane chain. Pathways that include both the σ and σ^* manifold also contribute significantly and these results will be presented elsewhere.³⁹ This observation suggests that the electronic coupling for these model systems is dominated by hole mediated processes.

Equation 6.2 predicts that the rate constant is proportional to the square of the electronic coupling matrix element. Assuming that the Franck-Condon Weighted Density of States is similar for both systems, the ratio of experimental rate constants can be used to determine the relative ratio of electronic couplings in the alkane and ether linked systems. The average ratio of rate constants is 4.4 ± 0.2 , so presumably the ratio of $V_{\text{alkane}} / V_{\text{ether}}$ should be equal to the square root of this quotient, or 2.1. For the radical cation, the couplings obtained from diagonalizing the reduced NBO Fock matrix (see Table 6.2) give a ratio of 1.8 and that found from the direct MO calculation give a ratio of 1.7. The theoretical values are in reasonable agreement with experiment, which seems to confirm the validity of the model compounds being used to draw conclusions about the ferrocene tethered systems.

In order to further explore the origin of the difference in electronic coupling for the radical cations of the alkane and ether chains, a detailed pathway analysis was performed. Pathways through the σ manifold were used since the coupling through the σ^* manifold was found to be so much weaker. A program was written that calculated all possible (forward hopping) pathways through the two model compounds using the NBOs corresponding to bridge CC σ orbitals.

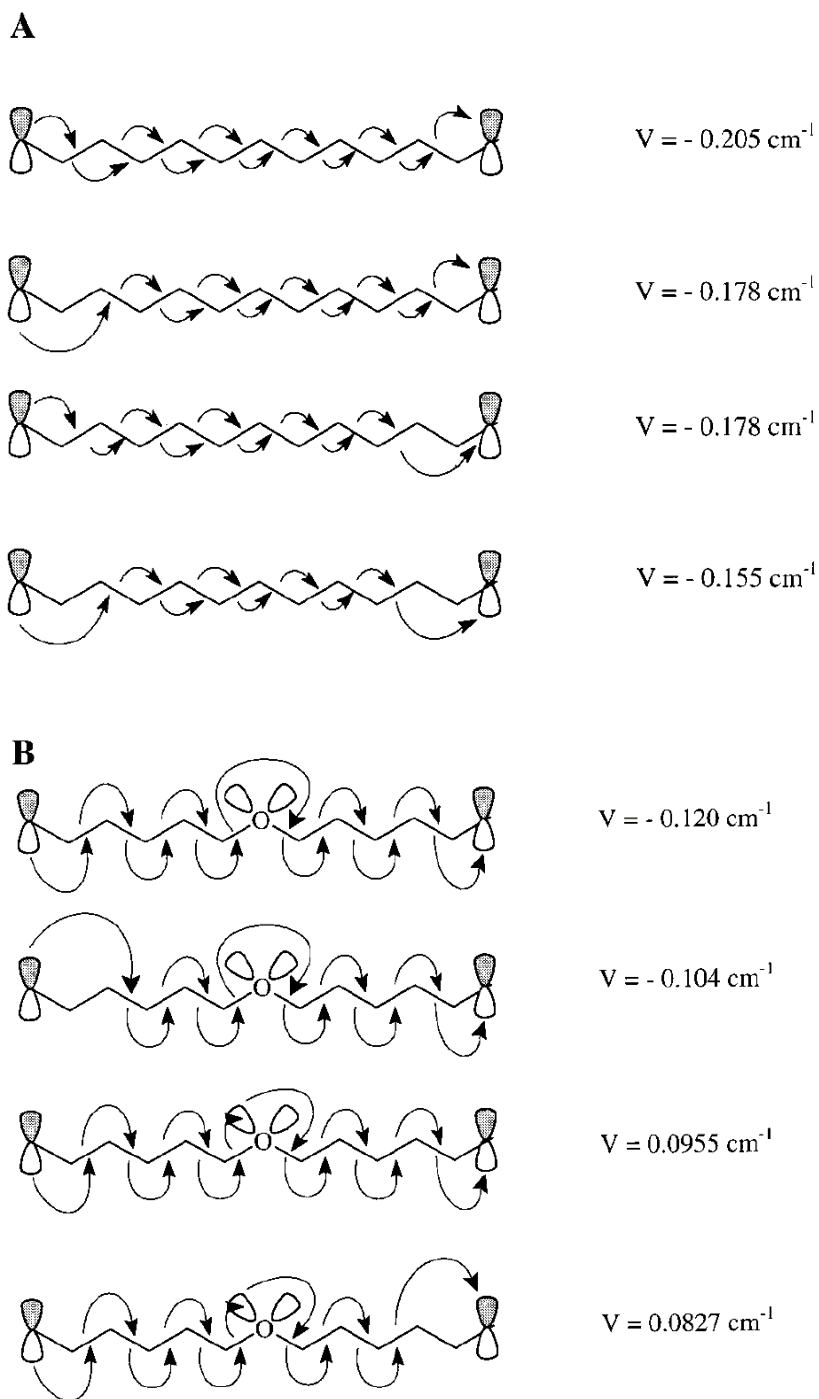
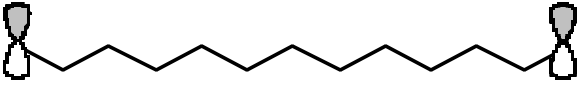
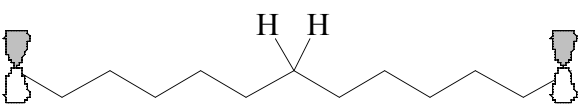
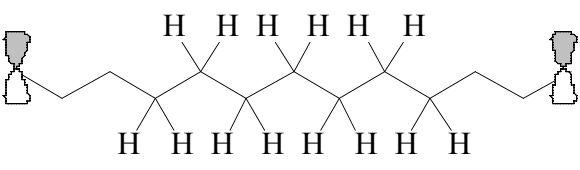
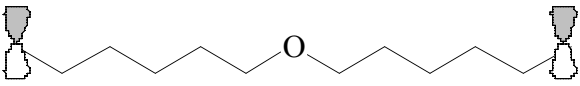
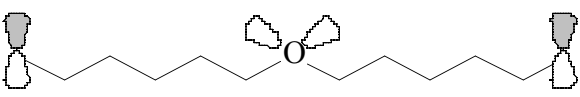
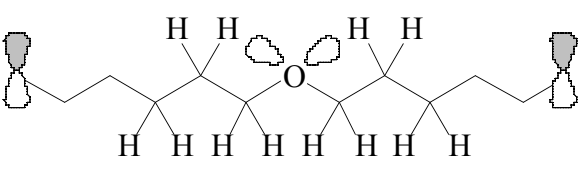


Figure 6.6 Panel A shows the four dominant pathways for the all methylene diradical model compound, along with the contribution each one makes to the electronic coupling. Panel B shows the four dominant pathways for the ether linked diradical model compound, along with the contribution each one makes to the electronic coupling. The diagrams are intended to reflect the molecules connectivity, not its stereochemistry.

Table 6.3 NBO Pathway Decomposition of the Electronic Coupling through Part of the Bonding Orbital Manifold for Two-Model Diradicals

System	$V_{\text{total}}(\text{cm}^{-1})$	$V_{+}(\text{cm}^{-1})$	$V_{-}(\text{cm}^{-1})$
	-43 cm^{-1}	0 cm^{-1}	-43 cm^{-1}
	-37 cm^{-1}	17 cm^{-1}	-54 cm^{-1}
	-16 cm^{-1}	1633 cm^{-1}	-1649 cm^{-1}
	-27 cm^{-1}	0 cm^{-1}	-27 cm^{-1}
	-25 cm^{-1}	12 cm^{-1}	-37 cm^{-1}
	-11 cm^{-1}	950 cm^{-1}	-961 cm^{-1}

This analysis could be limited to the carbon (and oxygen) backbone or extended to include the lone pair electrons on the oxygen and the C-H bonds. Figure 6.6 shows the four backbone pathways that contribute the greatest to the overall electronic coupling for each species. Similar to the findings of others, no single pathway is found to dominate the coupling.³⁴⁻³⁶ It is clear from these figures and the coupling magnitudes that the nearest neighbor pathway is no more significant than pathways that involve non-nearest neighbor couplings. For the ether linkages, some pathways have a positive signed coupling and some have a negative signed coupling. Because the total coupling is a sum over all of the pathways, the terms of opposite sign partially cancel, leading to a decrease in the overall electronic coupling. In contrast, all of the pathways for the alkane system have the same sign. When the lone pair orbitals on the oxygen are removed from the pathway analysis, all of the pathways through the ether-linked backbone have the same sign for the coupling; i.e., no destructive interference is evident.

Table 6.3 presents these results for some particular subsets of pathways and provides information on both positive and negative contributions to the electronic coupling for the radical cation of both systems. Comparison of the results in Table 6.3 with those in Table 6.2 show that the backbone pathways (CC and CO bonds) only account for 10% to 20% of the total coupling, however. The pathway analyses reveal that the CH σ orbitals introduce many new coupling pathways but with both positive and negative sign so that they largely cancel out. This result is in qualitative agreement with earlier studies for intramolecular electron transfer system, which showed that the efficiency of pure methylene chains in mediating the electron transfer process is superior to that of saturated ring systems. The small size of the couplings found for the pathway analysis may lie with the exclusion of the ‘retracing’ pathways (only forward hops are presented here). This issue is under investigation. The large number of pathways, the

importance of non-nearest neighbor coupling, and the considerable destructive interference between pathways make it difficult to identify local effects through a brute force analysis of pathways. For this reason a different tack was taken to address the impact of the ether substitution.

Table 6.4 Effect of Oxygen Parameters on the Electronic Coupling through the Bonding Orbital Manifold for Two Model Diradicals.

modification	$E_{CO} = E_{CC}$ $ V _{\text{NBO}} (\text{cm}^{-1})$	E_{CO} unmodified $ V _{\text{NBO}} (\text{cm}^{-1})$
none	1120	120
$t' = t$	1660	140
$t'' = t$	170	73
$t' = t'' = t$	200	81

^a The corresponding coupling through the CC backbone of the alkane chain is 240 cm^{-1} . The calculations in this table do not include lone pair orbitals on the oxygen and CH bonding orbitals. The exchange couplings and energies are defined as



Table 6.4 presents couplings computed for the ether chain in the NBO basis (through the σ manifold) with different modifications of the exchange coupling and site energy at the oxygen of the chain. This calculation was performed for the backbone bonding orbitals (CC and CO) and does not include the lone pair orbitals of the oxygen. The couplings are shown for the situation in which the C-O self-energy is artificially set equal to that of the C-C and for the situation in

which they are kept different. A comparison of these columns shows the impact of the site energy on the electronic coupling. The actual electronic coupling (120 cm^{-1}) is a factor of two smaller than that for the all alkane chain (240 cm^{-1}). If the site energies are arbitrarily adjusted to be the same value then the total electronic coupling is found to rise by five times over that of the alkane chain. The primary contribution to this increase results from the enhanced exchange coupling between the two CO bond orbitals in the chain, relative to the CC bond case. Decreasing these couplings (t'') to the value of a C-C bond (t) decreases the overall coupling to 170 cm^{-1} which is smaller than that found for the alkane chain. Adjustment of the site energy, the CO to CO coupling (t''), and the nearest-neighbor CC to CO coupling (t') to the values found for the all carbon chain in the NBO basis generates a total coupling of 200 cm^{-1} which is still significantly smaller than the 240 cm^{-1} coupling found for the alkane chain in the same basis. The 40 cm^{-1} difference represents exchange coupling differences for non-nearest neighbor couplings that involve the CO bonds.

The importance of non-nearest neighbor interactions in the electronic coupling suggest that interchain coupling could be important in electron tunneling through compact monolayer films. In particular, a non-nearest neighbor coupling between chains is not necessarily any smaller than that between two orbitals on the same chain. However, the experimental rate data show that the through bond interaction is stronger than the inter-chain interaction for the ferrocene tethered systems studied here. This may reflect the better defined geometry between orbital sites on a chain, as opposed to those between chains. Some evidence for interchain effects can be found for the rates dependence on the chemical composition of the diluent chains. A reduction of approximately one-third is found upon going from an alkane diluent to an ether containing diluent, and both pairs A/A & A/O and O/A & O/O show a similar reduction in rate

constant going from alkane to ether linked diluents. Disentangling the effects of interchain coupling from changes in the effective dielectric constant remains a challenge. It is reasonable to expect that the intermolecular interactions will be more important for systems in which the redox couple is not covalently linked to the insulating film.

6.6 Conclusions

The replacement of a single methylene group by an ether link in the electroactive thiol causes a marked decrease in rate constant. This result arises from a decrease in electronic coupling between the gold surface and ferrocene redox couple. Quantum chemical calculations support this conclusion. An NBO analysis shows that the decrease in coupling arises from both exchange interaction and energetic changes in the ether-linked molecule. A local (nearest neighbor) view of the superexchange coupling was not adequate to explain the results; non-nearest neighbor interactions and destructive interference are important components of the overall coupling. Also, the introduction of an ether linkage in the diluent thiols led to the observation of a reduced rate constant. This latter result is suggestive of the importance of intermolecular interactions when determining the electronic coupling through compact films.

6.7 Acknowledgements

This research was supported by the U.S. Dept. of Energy, Division of Chemical Sciences (Grant #DE-FG02-89ER14062). We would like to thank Prof. K. D. Jordan and Prof. D. N. Beratan for useful discussions during this study.

6.8 References

- (1) Liu, Yi-Ping; Newton, M. D. *J. Phys. Chem.* **1994**, *98*, 7162-7169.
- (2) Newton, M. D. *J. Electroanal. Chem.* **1997**, *438*, 3-10.
- (3) Gosavi, Shachi; Marcus, R. A. *J. Phys. Chem. B*; **2000**, *104*, 2067-2072.
- (4) a) Forster, R. J.; Loughman, P.; Keyes, T. E. *J. Am. Chem. Soc.* **2000**, *122*, 11948-11955; b) Finklea, H. O.; Yoon, K.; Chamberlain, E.; Allen, J.; Haddox, R. *J. Phys. Chem. B* **2001**, ASAP.
- (5) Marcus, R. A.; Hsu, Chao-Ping *J. Chem. Phys.* **1997**, *106*, 584-598.
- (6) Hsu, Chao-Ping *J. Electroanal. Chem.* **1997**, *438*, 27-35.
- (7) a) A. Ulman *Characterization of Organic Thin Films*; Butterworth-Heinemann: Stoneham MA, **1995**. ; b) Ulman A. *An Introduction to Ultrathin Organic Films: From Langmuir- Blodgett to Self-Assembly*; Academic: Boston, **1991**; c) Dubois, L. H.; Nuzzo, R. G., *Ann. Rev. Phys. Chem.* **1992**, *43*,437.
- (8) Finklea, H. O. in *Electroanalytical Chemistry*, Bard, A. J., Rubinstein, I., Eds.; Marcel Dekker: New York, **1996**; Vol. 19, pp 109-335.
- (9) a) Chidsey, C. E. D *Science* **1991**, *251*, 919; b) Chidsey, C. E. D.; Bertozzi, C. R.; Putvinski, T. M.; Muijsce, A. M. *J. Am. Chem. Soc.* **1990**, *112*, 4301.
- (10) a) Weber, K.; Hockett, L.; Creager, S. *J. Phys. Chem. B* **1997**, *101*, 8286; b) Smalley, J. F.; Feldberg, S. W.; Chidsey, C. E. D.; Linford, M.R.; Newton, M. D.; Liu, Y. P. *J. Phys. Chem.* **1995**, *99*, 13141; c) Finklea, H. O.; Hanshew, D. D. *J. Am. Chem. Soc.* **1992**, *114*, 3174; d) Guo, L. H.; Facci, J. S.; McLendon, G. *J. Phys. Chem.* **1995**, *99*, 8458.
- (11) a) Gu, Y.; Waldeck, D. H. *J. Phys. Chem. B* **1998**, *102*, 9015; b) *ibid*, **1996**, *100*, 9573.
- (12) a) Creager, S.; Yu, C. J.; Bamdad, C.; O'Connor, S.; Maclean, T.; Lam, E.; Chong, Y.; Olsen, G. T.; Luo, J.; Gozin, M.; Kayyem, J. F. *J. Am. Chem. Soc.* **1999**, *121*, 1059; b) Sachs, S. B.; Dudek, S. P.; Hsung, R. P.; Sita, L. R.; Smalley, J. F.; Newton, M. D.; Feldberg, S. W.; Chidsey, C. E. D. *J. Am. Chem. Soc.* **1997**, *119*, 10563.
- (13) a) Finklea, H. O.; Ravenscroft, M. S. *Israel J. Chem.* **1997**, *37*, 179; b) Finklea, H. O.; Ravenscroft, M. S.; Snider, D. A. *Langmuir* **1993**, *9*, 223; c) Curtin, L. S.; Peck, S. R.; Tender, L. M.; Murray, R. W.; Rowe, G. K.; Creager, S. E. *Anal. Chem.* **1993**, *65*, 386; d) Richardson, J. N.; Peck, S. R.; Curtin, L. S.; Tender, L. M.; Terrill, R. H.; Carter, M. T.; Murray, R. W.; Rowe, G. K.; Creager, S. E. *J. Phys. Chem.* **1995**, *99*, 766.
- (14) a) Creager, S. E.; Rowe, G. K. *J. Electroanal. Chem.* **1997**, *420*, 291; b) Redpenning, J.; Flood, J. M. *Langmuir* **1996**, *12*, 508; c) Rowe, G. K.; Creager, S. E. *J. Phys. Chem.* **1994**, *98*,

5500; d) Creager, S. E.; Weber, K. *Langmuir* **1993**, *9*, 844; e) Fawcett, W. R. *J. Electroanal. Chem.* **1994**, *378*, 117.

(15) Cruanes, M. T.; Drickamer, H. G.; Faulkner, L. R. *Langmuir* **1995**, *11*, 4089.

(16) a) Carter, M. T.; Rowe, G. K.; Richardson, J. N.; Tender, L. M.; Terrill, R. H.; Murray, R. W. *J. Am. Chem. Soc.* **1995**, *117*, 2896; b) Richardson, J. N.; Rowe, G. K.; Carter, M. T.; Tender, L. M.; Curtin, S. C.; Peck, S. R.; Murray, R. W. *Electrochim. Acta.* **1995**, *40*, 1331; c) Rowe, G. K.; Carter, M. T.; Richardson, J. N.; Murray, R. W. *Langmuir* **1995**, *11*, 1797.

(17) a) Kumar, K.; Kurnikov, I. V.; Beratan, D. N.; Waldeck, D. H.; Zimmt, M. B. *J. Phys. Chem. A*, **1998**, *102*, 5529-5541; b) Kumar, K.; Lin, Z.; Waldeck, D. H.; Zimmt, M. B. *J. Am. Chem. Soc.* **1996**, *118*, 243-244.

(18) Ratner, M. A. *J. Phys. Chem.* **1990**, *94*, 4877-4883.

(19) Newton, M. D. *Chem. Rev.* **1991**, *91*, 767-792.

(20) a) Cheng, J.; Sàghi-Szabó, G.; Tossel, J. A.; Miller, C. J. *J. Am. Chem. Soc.* **1996**, *118*, 680-684; b) Sinniah, K.; Cheng, J.; Terrettaz, S.; Reutt-Robey, J. E.; Miller, C. J. *J. Phys. Chem.* **1995**, *99*, 14500.

(21) Sumner, J. J.; Weber, K. S.; Hockett, L. A.; Creager, S. E. *J. Phys. Chem B* **2000**, *104*, 7449.

(22) a) Kergueris, C.; Bourgoïn, J. P.; Palacin, S. *Nanotechnology* **1999**, *10*, 8; b) Kergueris, C.; Bourgoïn, J. P.; Palacin, S.; Esteve, D.; Urbina, C.; Magoga, M.; Joachim, C. *Phys. Rev. B* **1999**, *59*, 12505; c) Tian, W.; Datta, S.; Hong, S.; Reifengerger, R.; Henderson, J. I.; Kubiak, C. P. *J. Chem. Phys.* **1998**, *109*, 2874; d) Samanta, M. P.; Tian, W.; Datta, S.; Henderson, J. I.; Kubiak, C. P. *Phys. Rev. B* **1996**, *95*, R7626.

(23) a) Slowinski, K.; Chamberlain, R. V.; Majda, M.; Bilewicz, R. *J. Am. Chem. Soc.* **1996**, *118*, 4709; b) Slowinski, K.; Chamberlain, R. V.; Miller, C. J.; Majda, M. *J. Am. Chem. Soc.* **1997**, *119*, 11910-11919.

(24) Finklea, H. O.; Liu, L.; Ravenscroft, M. S.; Punturi, S. *J. Phys. Chem.* **1996**, *100*, 18852.

(25) Sek, S.; Misicka, A.; Bilewicz, R. *J. Phys. Chem. B* **2000**, *104*, 5399-5402.

(26) Richardson, J. N.; Rowe, G. K.; Carter, M. T.; Tender, L. M.; Curtin, L. S.; Peck, S. R.; Murray, R. W., *Electrochim. Acta* **1995**, *40*, 1331-1338.

(27) Barbara, P.F.; Meyer, T. J.; Ratner, M. A. *J. Phys. Chem.* **1996**, *100*, 13148-13168.

(28) a) Tender, L.; Carter, M. T.; Murray, R. W. *Anal. Chem.* **1994**, *66*, 3173; b) Weber, K.; Creager, S. E. *Anal. Chem.* **1994**, *66*, 3166; c) Honeychurch, M. J. *Langmuir* **1999**, *15*, 5158.

(29) In the Chidsey report, the definition used for k^0 corresponds to $k_f + k_b$ at $E = E^{0'}$; see eq 3 in reference 9a. Here the more common definition of $k^0 = k_f = k_b$ for $\alpha = 0.5$ and $E = E^{0'}$ is used. Hence, the 1.25 s^{-1} value that was reported in 9a corresponds to 0.625 s^{-1} for the current definition of k^0 .

(30) Carter, M. T.; Rowe, G. K.; Richardson, J. N.; Tender, L. M.; Terrill, R. H.; Murray, R. W. *J. Am. Chem. Soc.* **1995**, *117*, 2896-2899.

(31) McConnell, H. M. *J. Chem. Phys.* **1961**, *35*, 508.

(32) a) Paddon-Row, M. N.; Shephard, M. J.; Jordan, K. D. *J. Phys. Chem.* **1993**, *97*, 1743; b) Shephard, M. H.; Paddon-Row, M. N.; Jordan, K. D. *J. Am. Chem. Soc.* **1994**, *116*, 5328.

(33) a) Gaussian 98, Revision A.9, M. J. Frisch, G. W. Trucks, H. B. Schlegel, G. E. Scuseria, M. A. Robb, J. R. Cheeseman, V. G. Zakrzewski, J. A. Montgomery, Jr., R. E. Stratmann, J. C. Burant, S. Dapprich, J. M. Millam, A. D. Daniels, K. N. Kudin, M. C. Strain, O. Farkas, J. Tomasi, V. Barone, M. Cossi, R. Cammi, B. Mennucci, C. Pomelli, C. Adamo, S. Clifford, J. Ochterski, G. A. Petersson, P. Y. Ayala, Q. Cui, K. Morokuma, D. K. Malick, A. D. Rabuck, K. Raghavachari, J. B. Foresman, J. Cioslowski, J. V. Ortiz, A. G. Baboul, B. B. Stefanov, G. Liu, A. Liashenko, P. Piskorz, I. Komaromi, R. Gomperts, R. L. Martin, D. J. Fox, T. Keith, M. A. Al-Laham, C. Y. Peng, A. Nanayakkara, M. Challacombe, P. M. W. Gill, B. Johnson, W. Chen, M. W. Wong, J. L. Andres, C. Gonzalez, M. Head-Gordon, E. S. Replogle, and J. A. Pople, Gaussian, Inc., Pittsburgh PA, **1998**; b) NBO Version 3.1, E. D. Glendening, A. E. Reed, J. E. Carpenter, and F. Weinhold.

(34) a) Liang, C.; Newton, M. D. *J. Phys. Chem.* **1992**, *96*, 2855-2866; b) Liang, C.; Newton, M. D. *J. Phys. Chem.* **1993**, *97*, 3199-3211.

(35) a) Naleway, C. A.; Curtiss, L. A.; Miller, J. R. *J. Phys. Chem.* **1991**, *95*, 8434-8437; b) Naleway, C. A.; Curtiss, L. A.; Miller, J. R. *J. Phys. Chem.* **1993**, *97*, 4050-4058; c) Curtiss, L. A.; Naleway, C. A.; Miller, J. R. *Chem. Phys.* **1993**, *176*, 387-405

(36) a) Jordan K. D.; Paddon-Row, M. N.; "Electron Transfer Calculations", in *Encyclopedia of Comp. Chem.*, ed., P.V.R. Schleyer, **1998**, *2*, 826; b) Jordan, K. D.; Nachtigallova, D.; Paddon-Row, M. N. in *Modern Electronic Structure Theory and Applications in Organic Chemistry*, ed. E.R. Davidson, World Scientific: Singapore, **1997**, 257.

(37) a) Reed, A. E.; Curtiss, L. A.; Weinhold, F. *Chem. Rev.* **1988**, *88*, 899; b) Reed, A. E.; Weinhold, F. *J. Chem. Phys.* **1985**, *83*, 1736.

(38) A detailed description of how to perform this analysis can be found elsewhere.³⁶ As a reference point for the pathway calculations, we provide some details here. All Fock matrix elements involving Rydberg and core electrons were set to zero. Additionally, the terms involving antibonding orbitals (for the radical cation) or bonding orbitals (for the radical anion) on

the bridging atoms were zeroed out, however this was found to have a negligible effect upon the overall electronic coupling. This latter finding indicates that the coupling mechanism for radical cations is dominated by hole-mediated superexchange and that for radical anions is dominated by electron-mediated superexchange (at least in these systems). The resulting NBO fock matrix was diagonalised, and the energy splitting associated with the α HOMO and HOMO-1 levels and β LUMO and LUMO+1 was taken as being equal to $2|V|$ for the radical cation and anion respectively.

(39) A. M. Napper, H. Yamamoto, H. Liu and D. H. Waldeck, ACS Conference Proceedings submitted.

Chapter 7. Solvent Mediated Superexchange in a C-Clamp Shaped Donor-Bridge-Acceptor Molecule: The Correlation between Solvent Electron Affinity and Electronic Coupling

7.1 Introduction

Electron-transfer reactions remain of fundamental and practical importance. The understanding of how energetic factors, such as reorganization energy and reaction free energy, impact reaction rates is well established; however, our ability to model or calculate these properties remains limited.^{1,2} For electron transfer reactions in the nonadiabatic limit, the transfer process is well described by an electron tunneling mechanism. In this scenario, rearrangement of the surrounding medium, consisting of both intramolecular (innersphere) and intermolecular (outersphere) nuclear motions, allows exploration of those parts of phase space where the initial and final electronic states are in resonance. Electron transfer occurs in this crossing region, although the system may pass through it many times before the transfer event.³ The electronic coupling matrix element $|V|$ is a measure of the interaction energy between the initial and final electronic states in the crossing region and is directly related to the electron-transfer rate constant.⁴ This study explores how the electronic coupling, or electron tunneling, between an electron donor and electron acceptor depends on the electronic structure of an intervening molecule. A correlation between the electronic coupling and the electron affinity of the intervening molecule is identified.[§]

This study uses molecule **1** which contains an electron donor (D) and electron acceptor (A) that are joined together by a “rigid” saturated bridge (a DBA molecule).⁵

[§] Reproduced with permission from Napper, A. M.; Read, I.; Kaplan, R.; Zimmt, M. B.; Waldeck, D. H.; *J. Phys. Chem. A.*; **2002**; 106(21); 5288-5296. Copyright 2002 American Chemical Society

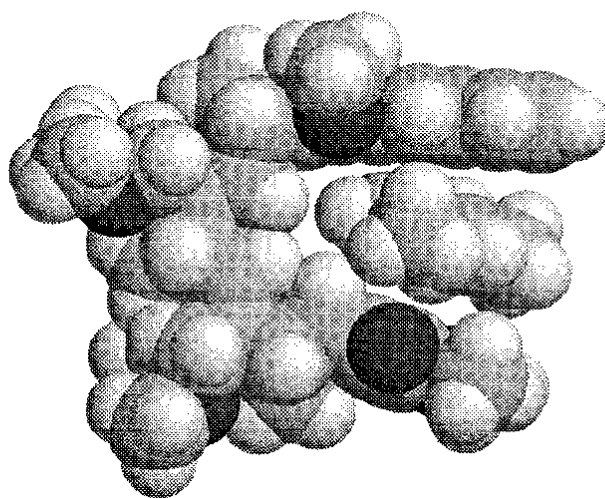
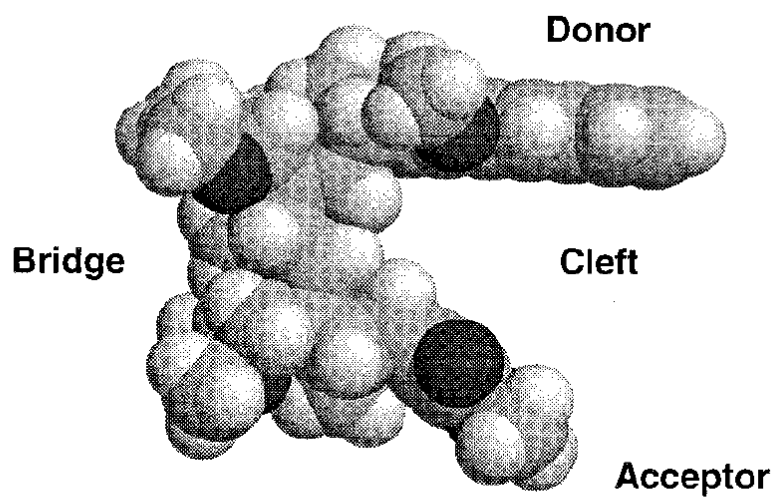
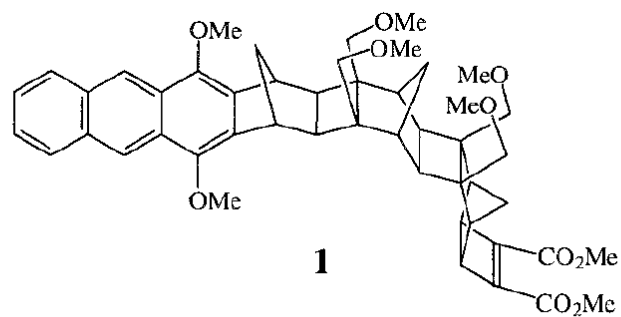


Chart 7.1 Line Structure and Space-filling Representations of **1**. In the bottom part, a space-filling model with 1,2,4-trimethylbenzene in the cleft of **1** is shown.

Chart 7.1 provides a space filling, CPK rendering of **1** that illustrates the vacant “cleft” which lies directly between the donor and acceptor groups. For a molecule of this topology, electron tunneling through the cleft occurs in addition to tunneling mediated by the covalent linkages of the bridge. Previous work^{2,6} has shown that the presence of a solvent molecule within the cleft enhances the rate of tunneling as compared to that through the bridge. The simultaneous interaction of the solvent, e.g., 1,2,4-trimethylbenzene (Chart 7.1), with the donor and acceptor groups is believed to cause the enhancement. An earlier study found that increasing the size of alkyl substituents on aromatic solvents reduces the electronic coupling magnitude because bulky alkyl groups, such as isopropyl, impede access of the solvents’ aromatic core to the cleft of **1**. In contrast, the current work explores how the electronic coupling depends on the *electronic* characteristics of the substituted benzene, rather than on its steric bulk.

In the nonadiabatic limit, Fermi’s Golden Rule can be used to calculate the electron-transfer rate constant, k_{et}

$$k_{\text{et}} = \frac{2\pi}{\hbar} |V|^2 \text{FCWDS} \quad (7.1)$$

$|V|$ is the donor/acceptor electronic coupling, and FCWDS is the Franck-Condon weighted density of states, which accounts for the nuclear rearrangement that must precede the electron tunneling event. Among solvents that provide similar FCWDS factors, the donor-acceptor electronic coupling will determine the relative magnitudes of the transfer rate constants. Molecules that lie between the donor and acceptor can enhance the electronic coupling through interaction of their molecular orbitals with those of the donor and acceptor. When the electronic coupling is weak enough, it can be calculated using a perturbation theory approach, known as superexchange.⁷ The superexchange mechanism predicts a dependence of the electronic coupling on the energy of electronic states that mediate the electron’s (or a hole’s) movement

from donor to acceptor. Previous studies have suggested that electron mediated superexchange is more important than hole mediated superexchange for the transfer of an electron from the locally excited state of **1**.⁸ For a single site between the donor and acceptor (see Figure 7.2), the superexchange expression for an electron-mediated process is given by

$$|V| = \frac{H_{D^*S}H_{SA}}{E_{D^+S^-A} - E_{D^*SA}} \quad (7.2)$$

where H_{D^*S} and H_{SA} are the donor/solvent and solvent/acceptor exchange integrals, respectively. E_{D^*SA} and $E_{D^+S^-A}$ represent the energies of the transition state and the vertically displaced superexchange state (D^+S^-A). By using solvents with differing vertical electron affinities (EA_v), it should be possible to manipulate the size of the denominator in eq 7.2 and tune $|V|$. In particular, solvents that are more favorable toward electron attachment (more positive values of EA_v) are predicted to stabilize the superexchange state D^+S^-A and enhance the total electronic coupling, $|V|$.

Previous studies of solvent mediated superexchange with **1** identified a significantly larger value of the electronic coupling for benzonitrile in the cleft than for benzene or alkylbenzenes. The current study explores how the solvent molecule's electronic character affects the size of the superexchange coupling. The earlier data in benzonitrile and alkylbenzene solvents showed that methyl substitution of the aromatic ring reduced the electronic coupling slightly. By contrast, those studies showed that multiple isopropyl groups on a benzene kept its aromatic core out of the cleft of **1**. The current study compares the coupling provided by methyl-substituted aromatic solvents with correspondingly substituted chloro aromatic solvents (see Chart 7.2). The similar size of methyl and chloro groups should produce similar steric effects, thus allowing the electronic effects to be identified (the new feature of this study). Two pairs of

solvents (pair 1: *meta*-chlorotoluene/*meta*-dichlorobenzene; pair 2: 2,5-dichlorotoluene/1,2,4-trimethylbenzene) are investigated. The solvents in each pair have significantly different electron affinity, but have similar sizes, shapes, and electrostatic properties (see Table 7.2) and should give rise to similar FCWDS terms. The *meta*-chlorotoluene/*meta*-dichlorobenzene pair was chosen because it is moderately polar, and the 2,5-dichlorotoluene/1,2,4-trimethylbenzene pair was chosen because it is weakly polar and should allow an accurate determination of the reaction free energies. To the extent that the FCWDS factors are the same for each solvent pair, a direct comparison of the electron transfer rate constants can be ascribed directly to variation of the coupling magnitude,⁹ and the correlation between $|V|$ and solvent electron affinity may then be analyzed.

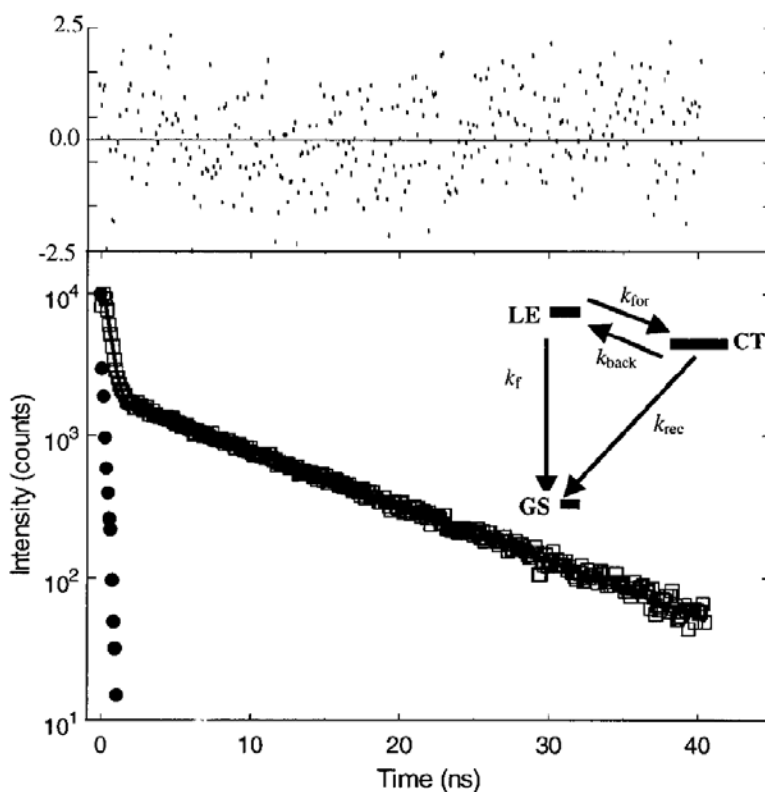


Figure 7.1 A fluorescence decay profile is shown for **1** in 2,5-dichlorotoluene at 338 K. The best fit parameters are 311 ps (90%), 11.15 ns (10%) and a χ^2 of 1.14. The top graph plots the residuals for the best-fit decay law (thick line through data points). For clarity, only every tenth data point is plotted here. The inset shows the level kinetics used to interpret these data.

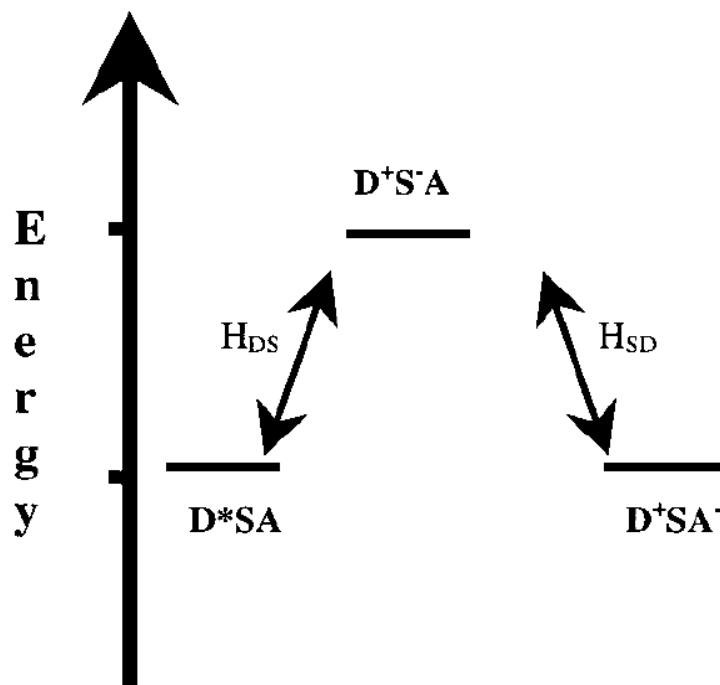


Figure 7.2 This diagram illustrates the energy level scheme that is used in the superexchange model to calculate $|V|$.

This work proceeds by measuring the electron-transfer rates as a function of temperature in each of the solvents. Extracting the electronic coupling from the data requires an accurate modeling of the FCWDS in each solvent as a function of temperature. Use of different FCWDS models yields different estimates of the coupling, but *relative* coupling magnitudes in different solvents are robust to changes in the FCWDS model [these affects have been discussed elsewhere¹⁰]. The results are analyzed using two different models for the FCWDS: a dielectric continuum treatment and a molecular based treatment. The molecular treatment is the same as that used previously to describe the temperature-dependent electron-transfer rate constant and reaction free energy in a series of alkyl-substituted benzenes.⁶ This study extends the application of this model to the more polar chlorobenzene solvents and benzonitrile, identifying its limitations for characterizing the reaction free energy, solvent reorganization energy and their temperature dependencies. A

dielectric continuum treatment is also used to model the FCWDS. This model is expected to provide reasonable estimates in the polar solvents and act as a point of reference for the molecular treatment. Combining these models for $\Delta_r G$ with previous results for the internal reorganization energy parameters, allows the solvent dependent reorganization energy $\lambda_o(T)$ and the electronic coupling magnitude $|V|$ to be determined from the temperature dependence of the rate constant. The correlation of $|V|$ with the solvent's electronic character could then be analyzed.

Table 7.1 Reaction Free Energies $\Delta_r G$, Reorganization Energies λ_o , and FCWDS Are Given at $T = 295$ K for the Electron Transfer Reaction Using Different Models^a

solvent ^c	continuum ^b			molecular			from $k(T)$ data	
	$\Delta_r G$, eV	λ_o , eV	FCWDS, eV ⁻¹	$\Delta_r G$, eV	λ_o , eV	FCWDS, eV ⁻¹	$\Delta_r G$, eV	λ_o , eV
mesitylene	-0.19	0.0038	50	-0.044	0.06	6.7	-0.039	0.03
toluene	-0.20	0.016	30	-0.090	0.09	6.8	-0.089	0.09
benzene	-0.19	0.0045	47	-0.11	0.10	6.3	-0.11	0.10
TMB	-0.20	0.013	31	-0.054	0.07	3.7	-0.057	0.09
DCT	-0.26	0.053	15	-0.10	0.15	0.053	-0.10	0.15
DCB	-0.35	0.14	13	-0.28	0.32	0.25		0.60 ± 0.08
MCT	-0.35	0.14	13	-0.31	0.36	2.8		0.39 ± 0.03
CB	-0.32	0.14	13	-0.32	0.33	1.5		0.47 ± 0.04
benzonitrile	-0.47	0.28	12	-0.52	0.52	0.084		1.06 ± 0.05

^a The error estimates in the polar solvents represent the effect of different models for the reaction free energy's temperature dependence. See text for details. ^b The solute parameters used in both calculations are 8.51 Å for the cavity radius, 34 D for the CT state dipole moment, and 0.08 eV for the gas-phase driving force. Relevant solvent parameters are reported in Table 7.2. ^c Solvent abbreviations correspond to the structures in Chart 7.2.

7.2 Background

The single-mode semiclassical expression for the FCWDS models interactions with the solvent classically and treats solute vibrations using a single effective high-frequency, quantum mechanical, mode.^{1b,11} The rate constant expression is

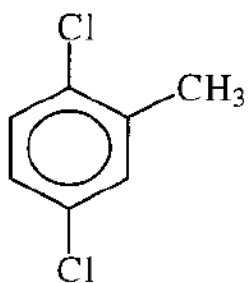
$$k_{\text{ct}} = \frac{4\pi^2}{h} |V|^2 \frac{1}{\sqrt{4\lambda_o \pi k_B T}} \sum_{n=0}^{\infty} \exp(-S) \left(\frac{S^n}{n!}\right) \times \exp\left[-\frac{(\Delta_r G + \lambda_o + nh\nu)^2}{4\lambda_o k_B T}\right] \quad (7.3)$$

This equation has five parameters: $\Delta_r G$ (the change in reaction Gibbs free energy), λ_o (low frequency-primarily solvent reorganization energy), λ_i (high frequency-primarily solute reorganization energy), ν (the effective frequency of the quantum mechanical mode), and $|V|$ (donor/acceptor electronic coupling). S (the Huang-Rhys factor) is defined as

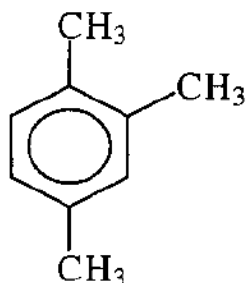
$$S = \frac{\lambda_i}{h\nu} \quad (7.4)$$

Of these five parameters, λ_i and ν can be estimated from analysis of charge-transfer absorption and emission spectra.^{10,11} Typically, $\Delta_r G$ and λ_o are estimated using a theoretical model. In this study, $\Delta_r G$ was determined experimentally in the weakly dipolar solvents, where its magnitude was within 0.1 eV of zero, and was modeled in the more polar solvents of the series. The molecular model employed (vide infra) provides $\Delta_r G$ values that are in reasonable agreement with the experimental values from the weakly polar solvents and with predictions of a dielectric continuum model for the highly polar solvents. Once reliable values of $\Delta_r G$, λ_i , and ν have been obtained, the electronic coupling matrix element $|V|$ and the solvent reorganization energy $\lambda_o(T)$ can be extracted from analysis of the temperature-dependent rate constant by way of eq 7.3.

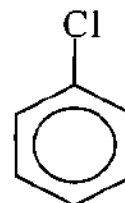
Chart 7.2 Molecular Structures for the Five Solvents in This Study^a



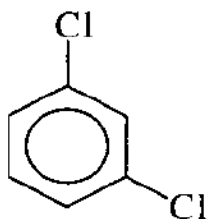
DCT
2,5-Dichlorotoluene



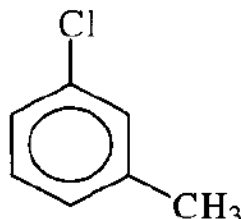
TMB
1,2,4-Trimethylbenzene



CB
Chlorobenzene



DCB
m-Dichlorobenzene



MCT
m-Chlorotoluene

^a Their abbreviations are included for easy reference.

7.2.1 Continuum Approaches to $\Delta_r G$ and λ_o .

The simplest means of estimating $\Delta_r G$ and λ_o is to use a dielectric continuum model for the solute-solvent interaction. Such treatments have been used successfully to describe the solvent reorganization energy and reaction free energy for electron transfer in polar solvents. The continuum model used here treats the charge-separated state as a point dipole μ embedded in a spherical cavity that is immersed in a dielectric continuum. This description of the solute shape and electrostatic character is the same as that used in the molecular model and allows a direct comparison between the two treatments. The continuum reorganization energy λ_o is given by

$$\lambda_{o,\text{cont}} = \frac{\mu^2}{a_0^3} \left(\frac{\epsilon - 1}{2\epsilon + 1} - \frac{n^2 - 1}{2n^2 + 1} \right) \quad (7.5)$$

where a_0 is the effective cavity radius, ϵ is the static dielectric constant of the solvent, and n is the refractive index of the solvent. In this same approximation the reaction Gibbs free energy can be written as

$$\Delta_r G = \Delta_{\text{vac}} G - \left[\frac{\mu^2}{a_0^3} \right] \left(\frac{\epsilon - 1}{2\epsilon + 1} \right) \quad (7.6)$$

where $\Delta_{\text{vac}} G$ is the reaction Gibbs free energy in the absence of solvation. Although this continuum treatment of the solutesolvent interaction is useful in some situations, recent results² have shown that a molecular approach provides more accurate values of $\Delta_r G$ and λ_o for weakly dipolar solvents and especially for aromatic solvents where quadrupole interactions are important. A number of workers have constructed more elaborate models for the solvent cavity^{10,12} and the medium's dielectric response.¹³ As a point of reference, the spherical cavity

dielectric continuum model is used to predict values for λ_o (outer sphere reorganization energy), $\Delta_r G$, and the FCWDS for the solvents studied here, see Table 7.1.

7.2.2 Molecular Approach to $\Delta_r G$ and λ_o .

Previous work showed⁶ that a molecular description of solute-solvent interactions was important for accurately characterizing the reorganization energy, the reaction free energy, and their temperature dependencies in aromatic solvents. Matyushov¹⁴ has developed a model that treats the solute and solvent molecules as polarizable spheres, with imbedded point dipole moments, and, in the case of solvent, an imbedded point quadrupole moment. The solute dipole moment magnitude μ is given by $\Delta q R_{DA}$, in which Δq is the charge transferred from the donor to the acceptor and R_{DA} is the charge separation distance. This model was successfully used to simulate the solvent and temperature dependencies of the reaction free energy for **1** in a series of six alkylbenzene solvents using only four parameters to represent the solute.² The molecular model treats the reaction free energy as a sum of four components

$$\Delta_r G = \Delta_{\text{vac}} G + \Delta_{\text{dq},i} G^{(1)} + \Delta_{\text{disp}} G + \Delta_i G^{(2)} \quad (7.7)$$

in which $\Delta_{\text{vac}} G$ corresponds to the reaction free energy in a vacuum and the other three terms account for solvation effects. This earlier study showed that the electrostatic and induction terms ($\Delta_{\text{dq},i} G^{(1)}$ and $\Delta_i G^{(2)}$) make the dominant contributions to the solvation free energy and that the dispersion term $\Delta_{\text{disp}} G$ plays a minor part and may be ignored. The reorganization energy was expressed as a sum of three terms

$$\lambda_o = \lambda_p + \lambda_{\text{ind}} + \lambda_{\text{disp}} \quad (7.8)$$

in which λ_p accounts for solvent reorganization arising from electrostatic interactions, λ_{ind} is the contribution from induction forces, and λ_{disp} accounts for dispersion interactions. A more detailed description of this model and its application to **1** may be found elsewhere.²

7.2.3 Internal Reorganization Parameters.

The internal reorganization energy λ_i and the effective frequency ν significantly influence the quantitative data analysis, but do not have a significant solvent dependence. Although the absolute value of the electronic couplings that are extracted from the measured electron-transfer rates depend on the values used for the internal reorganization parameters, the relative coupling magnitudes for **1** in different solvents do not depend on the values used for the internal reorganization parameters. The correlation between parameters in this system is discussed at length elsewhere.¹⁰ The value used for λ_i is 0.39 eV and that used for ν is 1412 cm^{-1} . These are the same values that were used in previous studies^{2,6} and were obtained through a combination of quantum chemical calculations and the analysis of charge-transfer spectra.

7.2.4 Kinetic Analysis.

Photoexcitation of the anthracene donor moiety creates a locally excited state that is slightly higher in energy than the charge separated state. Figure 7.1 shows the level kinetics scheme that is used to describe the decay of the locally excited (LE) state prepared by the light pulse. In highly dipolar solvents where k_{back} is small, the fluorescence decay of the locally excited state is single exponential with a decay constant that is the sum of the forward electron-transfer rate constant k_{for} and the intrinsic fluorescence decay rate constant of the chromophore.

By measuring the deactivation of the locally excited state (k_f) in an analogue of **1** that has no electron acceptor, it is possible to extract the electron transfer rate constant. This procedure can be used to assess any contributions from the external heavy atom effect or exciplex formation with chlorinated aromatic solvents and quantitatively account for them. The fluorescence decay rate of the donor only compound does not change in any significant way with the chlorine content of the solvent (see the Supporting Information and ref 8). To reiterate, the analysis assumes that the difference in fluorescence decay between the locally excited state of **1** and a donor only control compound in the same solvent arises from the electron transfer deactivation channel in **1**.

In weakly dipolar solvents the fluorescence decay law becomes double exponential because k_{back} is no longer small. In this case the analysis must account for the excited-state equilibrium and provides the three rate constants: k_{for} , k_{back} , and k_{rec} [see footnote 15 for details of this analysis]. The Gibbs free energy of the forward reaction is obtained from the ratio of the forward and back rate constants via

$$\Delta_r G = -RT \ln(k_{\text{for}}/k_{\text{back}}) \quad (7.9)$$

It is empirically found that $\Delta_r G$ values ≥ -0.1 eV can be reliably determined. More negative values have a small amplitude of the second decay component, which causes large uncertainty in the determination of k_{back} and of $\Delta_r G$.

7.3 Experimental Section

Solutions of **1** were prepared with an optical density of ca. 0.05 at the laser excitation wavelength, 375 nm. The preparation of **1** was reported elsewhere.¹⁶ Chlorobenzene (99.9+%,

HPLC grade), *m*-chlorotoluene (98%), *m*-dichlorobenzene (98%), 1,2,4-trimethylbenzene (98%), and 2,5-dichlorotoluene (98%) were purchased from Aldrich. The chlorinated solvents were dried over CaCl₂ for 2 days, filtered, and then fractionally distilled using a vigreux column. The purified fractions were used immediately in all the experiments. 1,2,4-trimethylbenzene was dried with anhydrous magnesium sulfate, filtered, and then refluxed over sodium for 2 days. The solution was then fractionally distilled using a vigreux column, and the purified fraction was immediately used to prepare the sample. Each solution was freeze-pump-thawed a minimum of three times. The samples were back-filled with Ar to reduce evaporation at the higher experimental temperatures.

Excitation of the sample was performed at 375 nm by the frequency-doubled cavity-dumped output of a Coherent CR-599-01 dye laser using LDS750 (Exciton) dye, which was pumped by a modelocked Coherent Antares Nd:YAG. The dye laser pulse train had a repetition rate of ca. 300 kHz. Pulse energies were kept below 1 nJ, and the count rates were kept below 3 kHz. All fluorescence measurements were made at the magic angle. Other specifics of the apparatus have been reported elsewhere.¹⁷ The temperature cell was fabricated out of aluminum and was controlled by a NESLAB RTE-110 chiller. Temperatures were measured using a Type-K thermocouple (Fisher-Scientific), accurate to within 0.1 °C.

The fluorescence decays were fit to a sum of two exponentials using the Marquardt-Levenberg nonlinear least squares algorithm. Instrument response functions were measured using a sample of colloidal BaSO₄ in glycerol. Figure 7.1 shows a fluorescence decay from **1** in 2,5-dichlorotoluene at 338 K, the best fit to a sum of two-exponential and the fitting residuals.

Fitting to the semiclassical equation (eq 7.3) was performed using Microsoft Excel 2000. The FCWDS sum rapidly converges for the solvents in this study, and was not evaluated past the

sixth term.

7.4 Results and Discussion

Fluorescence decay profiles of **1** and its donor only analogue were measured in the five aromatic solvents shown in Chart 7.2. The rate data is provided in the Supplemental Information. The lifetimes obtained for the donor only compound in each solvent do not differ greatly and do not display a significant temperature dependence. The donor only compound's fluorescence lifetimes were not significantly different from lifetimes measured in previous studies,¹⁸ muting possible concerns about the chlorinated aromatic solvents affecting the intrinsic photophysics of the dimethoxyanthracene moiety. The fluorescence decays from **1** in the different solvents were analyzed using the kinetic scheme in Figure 7.1. The decay profiles in 1,2,4-trimethylbenzene and 2,5-dichlorotoluene, the pair of solvents with the smallest dipole moments, had a significant long time constant component, which allowed an accurate determination of k_{back} and $\Delta_r G$. Although a second decay component could be identified in the more polar chlorinated solvents, a single exponential dominated the decay profiles, making it too difficult to reliably determine k_{back} and, hence, $\Delta_r G$. The amplitude of the long lifetime component correlated with the size of the solvent dipole moment, in accordance with its critical role in determining the solvation of the charge separated state. The present analysis is limited to the behavior of the forward rate constants, because they could be reliably determined for all of the solvents.

The charge separation rate constant for **1** in 2,5-dichlorotoluene is larger than that in 1,2,4-trimethylbenzene at all temperatures investigated (see Figure 7.4). The rate constant ratio varied from 1.5 at 295 K to 2.2 at 328 K. Determination of the relative electronic coupling

magnitudes in these two solvents requires estimation of the FCWDS. Before proceeding with quantitative modeling of the reaction free energy $\Delta_r G(T)$ and the outer sphere reorganization energy $\lambda_o(T)$ by way of a molecular solvation model, it is useful to consider the predictions of a simple dielectric continuum model. The dielectric continuum treatment was used to predict the FCWDS terms at 295 K for each of the solvent pairs, 1,2,4-trimethylbenzene/2,5-dichlorotoluene and *m*-dichlorobenzene/*m*-chlorotoluene, see Table 7.1.¹⁹ The continuum model estimate of the FCWDS factor in 2,5-dichlorotoluene is half of its value in 1,2,4-trimethylbenzene. Accordingly, the ratio of the square of the electronic coupling magnitudes is 3, via eq 7.3. This indicates that the electronic coupling for **1** in 2,5-dichlorotoluene is 75% larger than that in 1,2,4-trimethylbenzene. It is important to realize that the continuum model prediction for the FCWDS in this weakly polar pair of solvents may not be reliable; e.g., quadrupole contributions to the solvation could be quite different for the two solvents. For the *m*-dichlorobenzene/*m*-chlorotoluene pair, the charge separation rate constant of **1** in *m*-dichlorobenzene is larger than that of *m*-chlorotoluene at all temperatures (see Figure 7.4). At 295K the *m*-dichlorobenzene rate constant is 1.3 times larger. The continuum model predicts that the FCWDS for **1** in *m*-dichlorobenzene is the same as in *m*-chlorotoluene, so that the ratio of the squares of the electronic coupling terms is 1.3. This ratio gives an electronic coupling for **1** in *m*-dichlorobenzene that is about 15% larger than that in *m*-chlorotoluene. This analysis suggests that the difference in the electron transfer rate constants between the structurally similar solvents can be attributed, at least in part, to differences in the $|V|$. In addition, the continuum treatment provides a reference point for the molecular model described below.

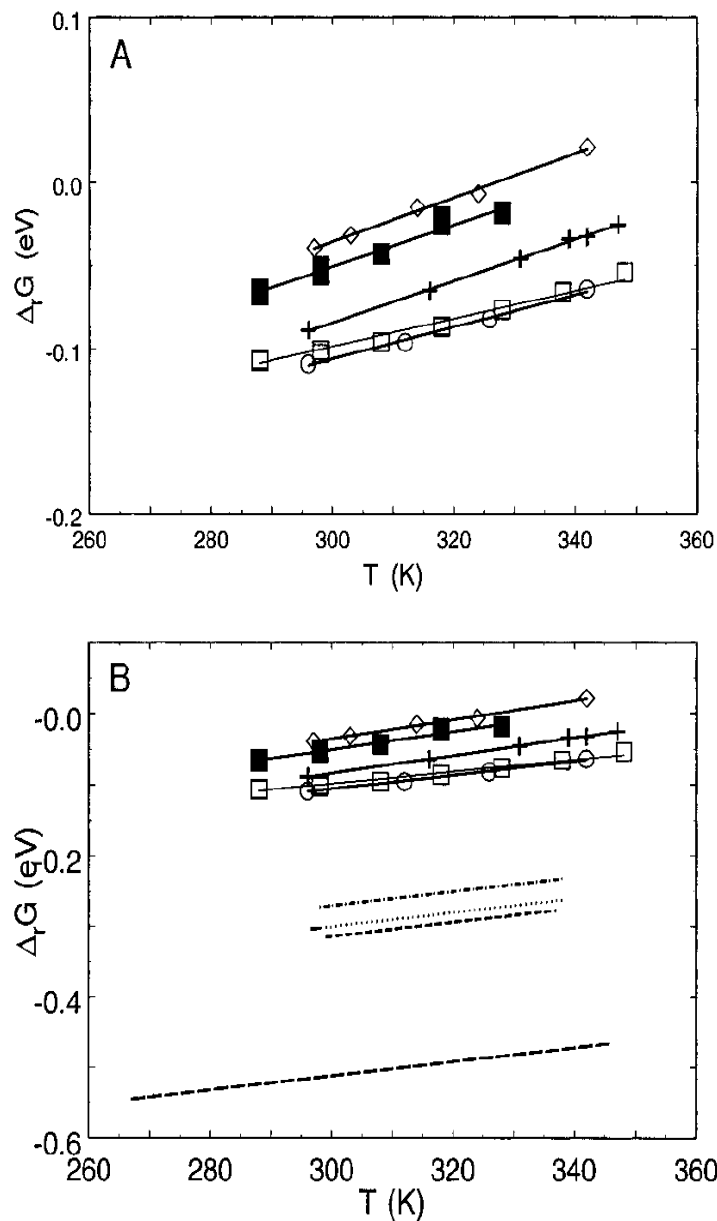


Figure 7.3 The experimental $\Delta_r G$ data for 2,5-dichlorotoluene (open squares), 1,2,4-trimethylbenzene (filled squares), toluene (+), benzene (open circle), and mesitylene (open diamonds) are shown here. Panel A shows an expanded view of the data for which experimental $\Delta_r G$ data are available. The best fit predictions from the molecular model are shown as solid lines for each data set (see text for details). Panel B shows the predicted free energies for all the solvents. The long dashed curve is the prediction for benzonitrile, the short dashed curve is the prediction for chlorobenzene, the dotted curve is the prediction for *m*-chlorotoluene, and the dashed-dotted curve is the prediction for *m*-dichlorobenzene.

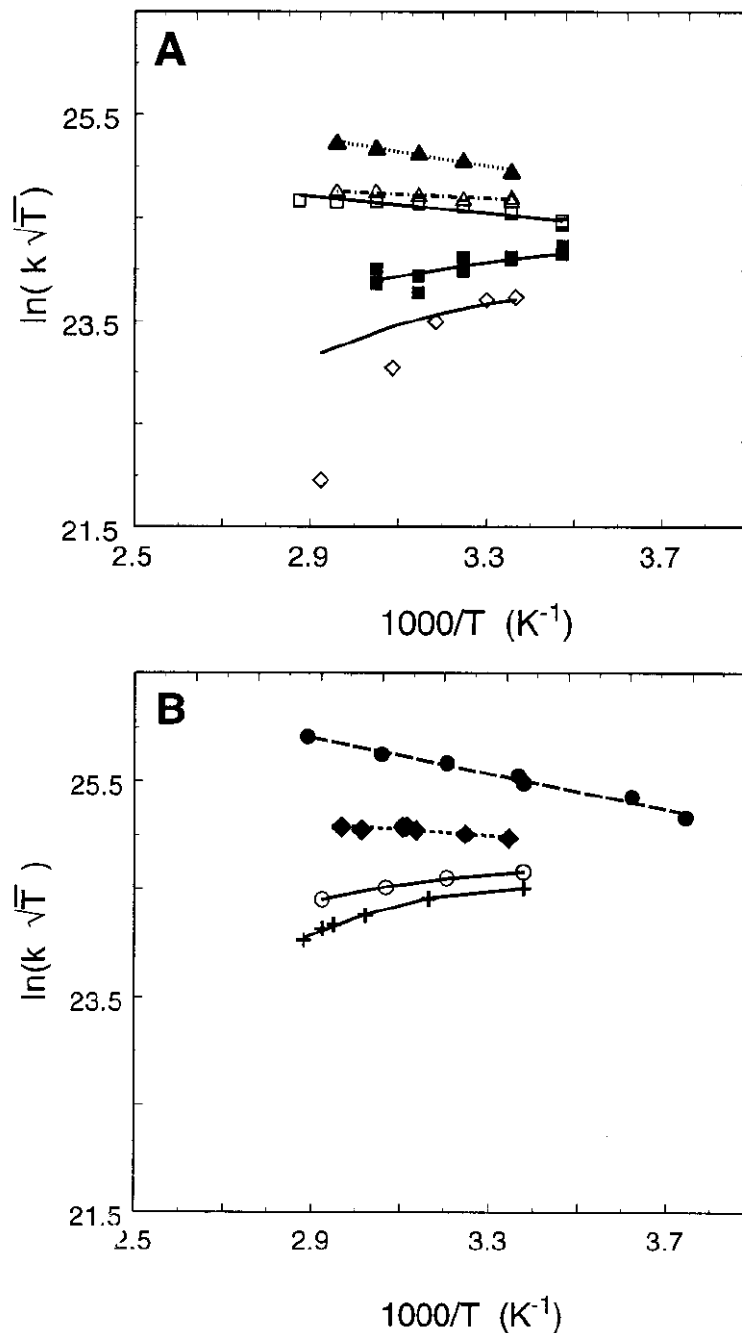


Figure 7.4 The temperature-dependent rate data are fit to the semiclassical expression in each of the solvents. The data are plotted in two panels for clarity, however the axis scales are identical. Part A plots the data for *m*-dichlorobenzene (filled triangles), *m*-chlorotoluene (open triangles), 2,5-dichlorotoluene (open squares), 1,2,4-trimethylbenzene (filled squares), and mesitylene (open diamonds). Part B plots the data for benzonitrile (filled circles), chlorobenzene (filled diamonds), benzene (open circles), and toluene (+). The lines represent best fit curves using the semiclassical equation (see Figure 7.3 for convention on line type).

7.4.1 Molecular Model.

Quantitative modeling of the reaction free energy and the reorganization energy was performed with a molecular model that accounts for solvent dipole, polarizability and quadrupole interactions.^{2,14} The solvent molecule parameters needed for the model are reported in Table 7.2. An earlier study demonstrated that this model accurately reproduces the magnitudes and temperature dependence of the reaction free energy in a homologous series of alkylbenzenes. The model has four parameters for the solute. For **1** in the alkylbenzene solvents, these parameters were a cavity radius of 7.25 Å, a charge separated state dipole moment of 34 D, a solute molecular polarizability of 70 Å³ and a vacuum reaction free energy, $\Delta_{\text{vac}}G$, of 0.34 eV.² Use of these parameters to calculate Δ_rG in 2,5-dichlorotoluene generates a value that is 0.15 eV too exoergic. One can adjust the four solute parameters in an effort to improve the agreement between the experimental and calculated Δ_rG values. However, it was not possible to produce an accurate fit of the free energy data in all the solvents as a function of temperature. It was possible to fit Δ_rG at 295 K from 2,5-dichlorotoluene and from all of the alkylbenzene solvents. The parameters needed to accurately describe the data at 295 K were a cavity radius of 8.51 Å, a dipole moment of 34 D, a solute polarizability of 100 Å³, and a $\Delta_{\text{vac}}G$ of 0.08 eV. The calculated solvent dependence of the free energy data is most sensitive to the cavity radius. The larger radius used for the fit at 295 K reduces the size of the electrostatic solvation and predicts a temperature dependence for the free energy that is much smaller than the experimentally observed dependence (e.g., the model predicts a free energy change for **1** in 2,5-dichlorotoluene of 0.025 eV from 295 to 347 K, whereas the observed change is 0.049 eV).

Figure 7.3 shows the reaction free energies for the solvents reported here as a function of temperature. It was found empirically that the average temperature dependence of the reaction

free energy in the alkylbenzene and dichlorotoluene solvents is about 1 meV/K. The solid lines in the figure show a linear fit to the reaction free energy's temperature dependence. The observed temperature dependencies are 0.83 meV/K for 2,5-dichlorotoluene, 1.1 meV/K for 1,2,4-trimethylbenzene, 0.96 meV/K for benzene, 1.2 meV/K for toluene, and 1.3 meV/K for mesitylene. The quality of the fit is evident in Figure 7.3A, which expands the free energy scale about the experimental values found in the weakly dipolar solvents. The average of these slopes is 1.1 meV/K. Because the reaction free energy is not available in the more polar solvents and a physical model is not available to guide the change in temperature dependence through the different solvent systems studied here, an empirical value of 1 meV/K was used in these solvents (vide infra).

Figure 7.3B shows the data of Figure 7.3A along with the reaction free energies that are predicted using the molecular solvation model and the new parameter set for **1** in chlorobenzene, *m*-chlorotoluene, *m*-dichlorobenzene, and benzonitrile. $\Delta_r G$ in these solvents is too negative to be determined experimentally from the fluorescence decays. The molecular model predictions of the free energies at 295 K can be compared with the continuum model predictions (see Table 7.1). For the more polar solvents, i.e., for solvents with $\epsilon_s \geq 5$, the largest deviation between the two sets of predicted values occurs for *m*-dichlorobenzene and represents a 20% difference, 0.07 eV in magnitude. The continuum model and molecular model predictions deviate much more significantly in the nondipolar and weakly dipolar solvents, where the dielectric continuum treatment is expected to fail. The dielectric continuum model performs reasonably well for **1** in more polar solvents, as discussed previously for the electron transfer of **1** in acetonitrile and benzonitrile.¹⁰ This agreement between the continuum model and the molecular model in the polar solvents and between the experimental measurements and the molecular model in the

weakly dipolar solvents supports the reliability of the molecular model's $\Delta_r G$ prediction at 295 K.

The electronic coupling magnitude can be determined from the rate data and eq 7.3 provided accurate values of the solvent reorganization energy and its temperature dependence are available. The failure of the molecular model, with the new parameter set, to reproduce the temperature dependence of $\Delta_r G$ in this set of solvents requires use of an alternate method (vide infra) to evaluate λ_s and its temperature dependence. The results of the analysis are sensitive to the value used for the temperature derivative of $\Delta_r G$. To estimate the uncertainty in the derived values of the reorganization energy and the electronic coupling, three different values of $d(\Delta_r G)/dT$ were used for solvents in which this quantity was not directly measured; benzonitrile, 1,3-dichlorobenzene, chlorobenzene, and 3-chlorotoluene. Because the temperature dependencies of the reaction free energy in the nonpolar and weakly polar solvents are clustered near 1 meV/K, this value was used as the best estimate. This is the value used for preparation of the plots shown in Figures 7.3 through 7.6. To estimate the error in this value for the reaction free energy's temperature dependence, an upper bound was obtained by using a slope of 2 meV/K and a lower bound was obtained by using the predicted slope from the continuum model.²⁰ Independent fits to the data were performed with these estimates and used to determine the upper and lower bounds on the solvent reorganization energy and the electronic coupling (see Tables 7.1 and 7.3).²¹

Given the difficulty in using the molecular model to quantitatively reproduce the temperature dependence of the reaction free energies, the model was not employed to make predictions of the solvent reorganization energies, for which no direct experimental data is

available. Nonetheless, it was possible to evaluate the temperature-dependent reorganization energy and the electronic coupling from the rate data using eq 7.3 and the available information.

Table 7.2 This Data Provides Physical Parameters of the Solvents Used in This Study

solvent	n_D^a	ϵ^a	IP, eV ^b	EA _v , eV ^c	μ , D ^d	$\langle Q \rangle$, D Å ^d	α , Å ^{3e}	σ , Å	ϵ_{LJ} , K	η
mesitylene	1.50	2.27	8.4	-1.03	0.07	7.4	17.0	6.26	870	0.556
toluene	1.49	2.38	8.8	-1.11	0.29	7.8	12.4	5.66	704	0.538
benzene	1.50	2.28	9.2	-1.12	0.00	8.2	10	5.27	614	0.518
TMB	1.50	2.38	8.4-8.6	-1.07	0.30	7.3	17.0	6.26	865	0.562
DCT	1.55	3.01	8.8	-0.31	0.57	14	17.0	6.36	972	0.630
DCB	1.55	5.02	9.1	-0.31	2.03	10	13.2	5.97	882	0.587
MCT	1.52	5.55	8.7	-0.75	2.34	7.8	13.2	6.01	838	0.579
CB	1.52	5.62	9.1	-0.75	2.15	8.4	11.5	5.62	748	0.552
benzonitrile	1.53	25.9	9.7	0.24	4.85	15.2	12.5	5.69	741	0.565

[§] See Chart 7.2 for solvent abbreviations. ^a Data were obtained from Landolt-Bornstein. The value for DCT was estimated using the Debye formula and the vacuum dipole moment. ^b NIST Webbook at webbook.nist.gov. ^c Electron Affinities were obtained from ref 22. ^d The dipole moment and quadrupole moments were calculated at the RHF/6-31G**//RHF/6-31G** level using Gaussian 98. ^e Polarizabilities were obtained from the literature (*CRC Handbook*, 78th ed.; CRC Press: Boca Raton, FL, 1998), but optimized, by <10%, for a best fit of the $\Delta_r G(295\text{ K})$ data. ^f The hard sphere diameter, α and the Lennard-Jones energy parameter ϵ_{LJ} were obtained from the literature.²⁸ ^g The reduced packing density, $\eta = \pi\rho\sigma^3/6$, was determined using literature values of the density (*CRC Handbook* (vide supra)).

The temperature-dependent reorganization energy was determined from the temperature dependence of the rate data through the slope of the plot in Figure 7.4. The derivative, $(\partial \ln(k_{\text{et}}xT) / \partial(1/T))$, was evaluated analytically from eq 7.3 and was fit to the temperature-dependent slope to determine the solvent reorganization energy at each temperature (vide infra). Figure 7.5 shows the temperature dependent solvent reorganization energies obtained from this analysis, and Table 7.1 presents values for the reorganization energies at 295 K. A comparison of the 295 K reorganization energies with those predicted by the continuum model and the molecular model can be made from Table 7.1. In the nondipolar solvents the molecular model and the experimentally derived reorganization energies are in good agreement, whereas the continuum model predicts a reorganization energy that is much too small. The latter result is

expected since the continuum model does not account for solvent quadrupoles, which are significant contributors to solvation, in these solvents. In the polar solvents, the predictions of both models deviate strongly from the experimentally derived values. Among the chlorinated solvents, the continuum model predicts that the reorganization energies in chlorobenzene, *m*-dichlorobenzene, and *m*-chlorotoluene (the three solvents with >2 D dipole moments) are comparable and are 3-fold larger than the reorganization energy in 2,5-dichlorotoluene ($\mu = 0.57$ D).

Table 7.3 The Best Fit $|V|$, the Electron Affinity EA, and the Ionization Potential IP

solvent ^a	$ V $, cm ⁻¹	IP, ^b eV	EA, ^c eV
mesitylene	2.8	8.4	-1.03
toluene	4.7	8.8	-1.11
benzene	5.3	9.2	-1.12
TMB	4.6	8.4–8.6	-1.07
DCT	9.6	8.8	-0.31
DCB	22 ± 8	9.1	-0.31
MCT	7.3 ± 1	8.7	-0.75
CB	11 ± 2	9.1	-0.75
benzonitrile	55 ± 13	9.7	0.24

^a Solvent abbreviations correspond to the structures in Chart 2.

^b The ionization potentials are taken from the NIST Webbook at webbook.nist.gov. ^c The electron affinities are taken from ref 27. The error estimates in the polar solvents represent the effect of different models for the reaction free energy's temperature dependence. See text for details.

^a Solvent abbreviations correspond to the structures in Chart 7.2. ^b The ionization potentials are taken from the NIST Webbook at webbook.nist.gov. ^c The electron affinities are taken from ref 27. The error estimates in the polar solvents represent the effect of different models for the reaction free energy's temperature dependence. See text for details.

The molecular model predictions of λ_0 are two to 3-fold larger than the continuum predictions.

The molecular model also predicts that λ_0 values among the first three solvents (chlorobenzene, *m*-dichlorobenzene and *m*-chlorotoluene) are comparable and are roughly 2-fold larger than

those for 2,5-dichlorotoluene. The experimentally derived values of λ_0 are roughly 66% larger than the values obtained from the molecular model and show similar grouping by solvent, albeit with considerably more scatter. The temperature dependence of the experimental reorganization energies are weak, Figure 7.5, a finding that is consistent with the weak dependence predicted by the molecular model.²³

Figure 7.4 presents the rate constant data for the five solvents in Chart 2 and also previously published data in benzene, toluene, mesitylene, and benzonitrile. The solid curves correspond to a best fit to these data by the semiclassical expression, eq 7.3, using the reaction free energies (vide supra) and the internal reorganization energies found previously for **1**.¹⁰ The data were fit in a two step process that decoupled the electronic coupling parameter $|V|$, assumed to be temperature independent, from the temperature-dependent reorganization energy $\lambda_0(T)$. In the first step, the temperature-dependent slope was fit to obtain the reorganization energy, as described above. In the second step, the temperature-dependent reorganization energies were input to eq 7.3 and the $|V|$ parameter was adjusted to fit the data. The best fit curves are displayed in Figure 7.4. The best fit $|V|$ values are reported in Table 7.3.

The rate constants in Figure 7.4 are reproduced accurately by the semiclassical expression for all the solvents except mesitylene. In the latter case the rate constant displays an anomalous decline at higher temperatures. This feature of the kinetics will be discussed elsewhere.²⁴ The rate constants in the alkylbenzene solvents appear to lie near the peak of the Marcus curve (see λ_0 in Table 7.1 and $\Delta_r G$ in Figure 7.3), whereas the rate constant in the more polar solvents clearly lie in the normal region. The electronic couplings obtained from these fits are presented in Table 7.3 with the solvent molecules' electron affinity and ionization potential.

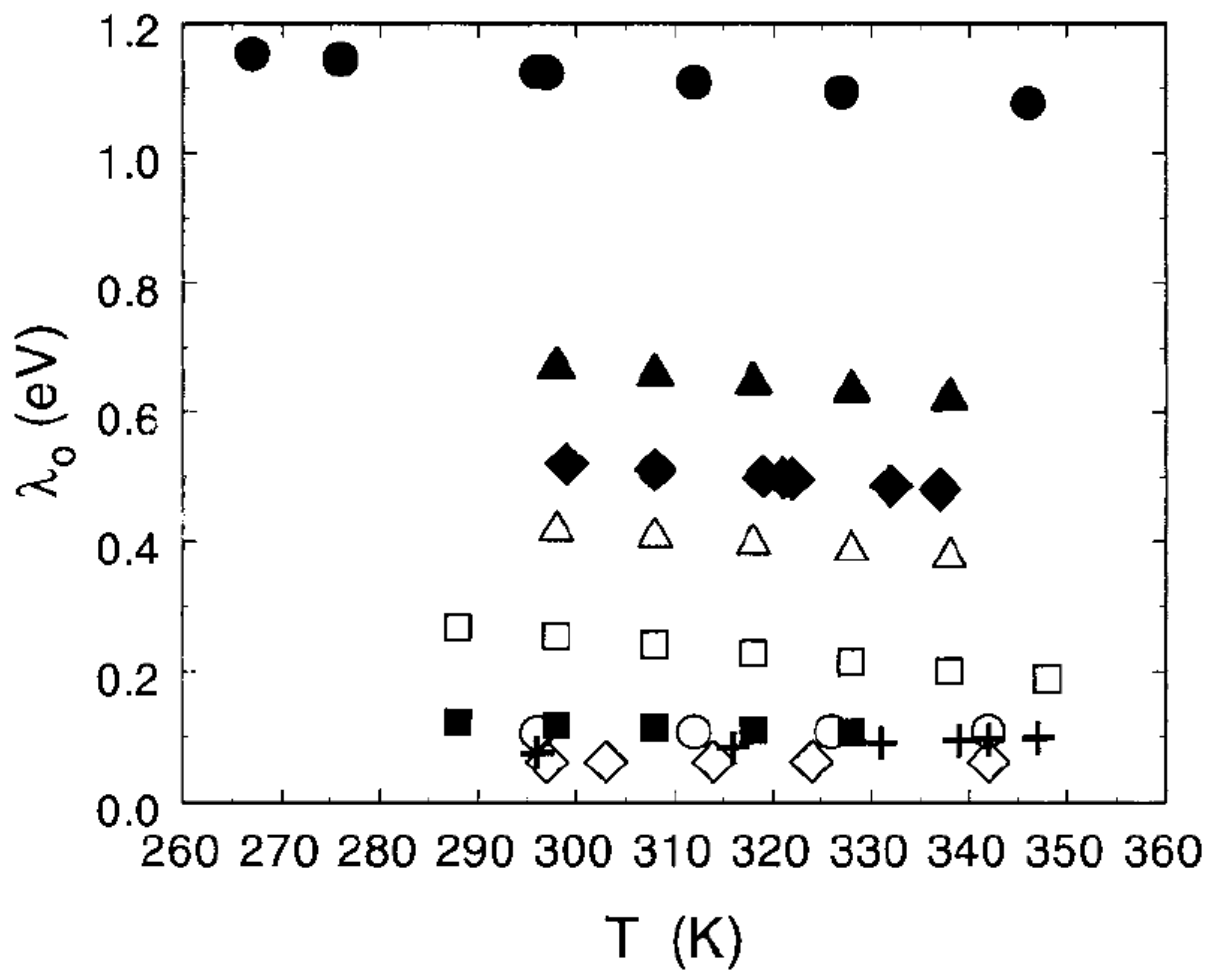


Figure 7.5 The temperature-dependent reorganization energies, predicted by the molecular-based model, are presented here for each of the solvents. The symbol convention is the same as that in Figure 7.4.

The value for the electronic coupling of 2,5-dichlorotoluene is two times larger than that for the similarly shaped 1,2,4-trimethylbenzene, and the electronic coupling for *m*-dichlorobenzene is three times larger than that of the structurally similar *m*-chlorotoluene. These results are in qualitative agreement with the conclusions drawn from the continuum treatment; however, the magnitudes of the electronic coupling changes are larger in magnitude. The electronic couplings reported for the alkylbenzenes and benzonitrile are smaller than the values reported previously.⁶ This difference arises from the different reorganization energy values used in the different analyses and reflects the sensitivity of the electronic coupling magnitude to quantitative details of the modeling.

A comparison of the electronic coupling values to the reported ionization potentials of the solvent molecules indicates no apparent correlation or dependence. A comparison of the electronic coupling magnitudes with the vertical electron affinities of the solvent molecules displays a correlation: see Figure 7.6. Equation 7.2 predicts that a plot of $1/|V|$ versus $(E_{D+S-A} - E_{D*BA})$ should be linear. The vertical electron affinity of the solvent molecule, which is hypothesized to be proportional to the difference in energy between the transition state and the mediating superexchange state,²⁵ is used as a measure of this energy gap in Figure 7.6. As expected from the superexchange treatment, the graph shows a general correlation between $-EA$ and $1/|V|$. This correlation shows that solvents with more positive electron affinities (more readily accept an electron) have a larger $|V|$ than solvents with more negative electron affinities (less readily accept an electron). The value of the electronic coupling is also dependent on the solvent size and this adds a degree of scatter to the plot. The plot shows that the bulkier, trisubstituted solvents (open squares) generate a smaller electronic coupling than smaller solvents (filled circles) of a comparable electron affinity.

Presumably, the more highly substituted solvents are less effective at mediating electron transfer because of their reduced ability to access geometries that have good electronic wave function overlap with the donor and acceptor moieties, described by the exchange terms in eq 7.2. The reasonable correlation between $-EA$ and $1/|V|$ indicates that electron mediated superexchange involving solvent is the dominant source of coupling in this system.

The line in Figure 7.6 represents a linear fit to the couplings in all the solvents that are not triply substituted; i.e., filled circles. The slope of this line (1123 eV^{-2}) can be used to estimate the geometric mean of the two exchange couplings H_{D^*S} and H_{AS} ; , $\beta \equiv \sqrt{H_{D^*S}H_{AS}} = 0.030 \text{ eV}$ or 240 cm^{-1} . This value is 3-6 times smaller than couplings found for cyanoanthracene-alkylbenzene contact ion pairs formed by excitation of charge transfer complexes.²⁷ Coulomb attraction between the ions presumably reduces the separation and enhances the exchange coupling in the contact ion pairs. The estimate of β for **1** with aromatic solvents is only about fifteen percent larger than the β found for solvents spanning the wider, 10 \AA cleft of a related C-shaped molecule.^{8a} The smaller cleft for **1** would be expected to support more extensive, simultaneous interactions between the donor, “cleft resident” solvent, and the acceptor and, therefore, to produce an even larger mean value of β . A difference of the electronic symmetry in the active orbitals on the donor and acceptor may act to reduce the effective mean β for **1**, as compared to the previously studied case.²⁸

7.5 Summary and Conclusions

A molecular model that describes the reaction free energy and solvent reorganization energy in alkylbenzene solvents was extended to electron-transfer studies in chlorinated benzene solvents. The previous calibration of this model for solute molecule **1** resulted in reaction free

energies in the chlorinated solvents that were more negative than observed experimentally. The model was parametrized to characterize the reaction free energy at 295 K for the alkylbenzenes and dichlorotoluene. In particular, the cavity radius of the solute was increased in order to not overestimate the amount of solvation in dichlorotoluene. This procedure predicted a temperature dependence for the reaction free energy that was weaker than that observed experimentally. For the nonpolar and weakly polar solvents the temperature dependent reaction free energy was determined empirically. Although the molecular model successfully replicates the solvation provided by a homologous series of solvents; e.g., the alkylbenzenes, it fails to extrapolate well to a broader range of solvents.

To obtain an accurate modeling for the reaction free energy through the range of solvents studied here, the molecular model was fit to the experimental data in nonpolar solvents at 295 K. The reaction free energies that this model predicts in the more polar solvents are in good agreement with the values predicted by the dielectric continuum model. The temperature dependence of the reaction free energy in the polar solvents was treated as linear. Three different values of the slope ($d\Delta_r G/dT$) were used in order to span a reasonable range of values. With the reaction free energy in hand, the temperature-dependent rate data was used to obtain the solvent reorganization energy and the electronic coupling magnitude. The analysis generated solvent reorganization energies that were larger than those predicted by the molecular model and the dielectric continuum model. The electronic couplings found for the aromatic solvents correlated with the vertical electron affinities of the solvent molecules; *more positive* electron affinities produce a *larger* electronic coupling for **1** than solvents with less positive electron affinities. This observation is consistent with a superexchange mechanism that predicts an increase in the electronic coupling when the energy separation between the electron-transfer

transition state (D^*SA) and the superexchange state (D^+S^-A) is reduced. This energy separation should be smaller in solvents with more positive electron affinities. The poor correlation of $1/|V|$ with solvent ionization potential indicates that the electronic coupling is dominated by electron mediated pathways rather than hole-mediated pathways. These data also show that more highly substituted aromatic solvents are less effective at mediating electron transfer in **1** than sparsely substituted solvents of similar electron affinity. This decreased efficiency is rationalized as an inability of the solvent to enter the cleft, and/or its decreased ability to access favorable orientations once inside the cleft.

7.6 References.

(1) (a) Jortner, J., Bixon, M., Eds. Electron Transfer-From Isolated Molecules to Biomolecules. In *Advances in Chemical Physics*; Wiley: New York, 1999. (b) Barbara, P. F.; Meyer, T. J.; Ratner, M. A. *J. Phys. Chem.* **1996**, *100*, 13148.

(2) Read, I.; Napper, A.; Zimmt, M. B.; Waldeck, D. H. *J. Phys. Chem. A* **2000**, *104*, 9385.

(3) (a) Newton, M. D. *Chem. Rev.* **1991**, *91*, 767; (b) Jordan, K. D.; Paddon-Row, M. N. *Chem. Rev.* **1992**, *92*, 395.

(4) (a) Nitzan, A. *J. Phys. Chem. A* **2001**, ASAP. (b) Segal, D.; Nitzan, A.; Ratner, M.; Davis, W. B. *J. Phys. Chem. B* **2000**, *104*, 2790; (c) Nitzan, A.; Jortner, J.; Wilkie, J.; Burin, A. L.; Ratner, M. A. *J. Phys. Chem. B* **2000**, *104*, 5661.

(5) The word “rigid” is used to indicate that the bridge has only one (not multiple) minimum energy conformation.

(6) (a) Read, I.; Napper, A.; Kaplan, R.; Zimmt, M. B.; Waldeck, D. H. *J. Am. Chem. Soc.* **1999**, *121*, 10976; (b) Kumar, K.; Lin, Z.; Waldeck, D. H.; Zimmt, M. B. *J. Am. Chem. Soc.* **1996**, *118*, 243.

(7) (a) McConnell, H. M. *J. Chem. Phys.* **1961**, *35*, 508. (b) Newton, M. D. *Chem. Rev.* **1991**, *91*, 767. (c) Ratner, M. A. *J. Phys. Chem.* **1990**, *94*, 4877.

(8) (a) Kaplan, R.; Napper, A. M.; Waldeck, D. H.; Zimmt, M. B. *J. Phys. Chem. A* **2002**, *106*, 1917. (b) Kaplan, R. W.; Napper, A. M.; Waldeck, D. H.; Zimmt, M. B. *J. Am. Chem. Soc.* **2000**, *122*, 12039.

(9) If the FCWDS for each solvent pair is constant, then an increase in rate constant for the solvent pair may be linked to an enhanced electronic coupling, since

$$\frac{k_1}{k_2} = \frac{\frac{2\pi}{\hbar}|V_1|^2\text{FCWDS}_1}{\frac{2\pi}{\hbar}|V_2|^2\text{FCWDS}_2} = \frac{|V_1|^2}{|V_2|^2}$$

A qualitative analysis of this sort in a broad range of solvents is reported elsewhere.⁸ These comparisons provide good evidence that the electronic coupling is correlated to the solvent molecule's electron affinity, so that an electron mediated superexchange mechanism is operative for **1**'s photoinduced electron transfer.

(10) Kumar, K.; Kurnikov, I. V.; Beratan, D. N.; Waldeck, D. H.; Zimmt, M. B. *J. Phys. Chem. A* **1998**, *102*, 5529.

(11) (a) Marcus, R. A. *J. Phys. Chem.* **1989**, *93*, 3078. (b) Zeng, Y.; Zimmt, M. B. *J. Phys. Chem.* **1992**, *96*, 8395.

(12) (a) Brunschwig, B. S.; Ehrenson, S.; Sutin, N. *J. Phys. Chem.* **1986**, *90*, 3657. (b) Barzykin, A. V.; Tachiya, M. *Chem. Phys. Lett.* **1998**, *285*, 150.

(13) (a) Jeon, J.; Kim, H. J. *J. Phys. Chem. A* **2000**, *104*, 9812. (b) Zhou, Y.; Griedman, H.; Stell, G. *J. Chem. Phys.* **1989**, *91*, 4885.

(14) Matyushov, D. V.; Voth, G. A. *J. Chem. Phys.* **1999**, *111*, 3630.

(15) The fluorescence decay of **1** in 1,2,4-trimethylbenzene is fit to the biexponential form: $I(t) = a_+e^{-k_+t} + (1 - a_+)e^{-k_-t}$. The forward electron transfer rate constant k_{for} is obtained from $k_{\text{for}} = a_+(k_+ - k_-) - k_f + k_-$, and the reverse electron-transfer rate constant k_{back} is obtained from $k_{\text{back}} = [(k_+ - k_-)^2 - (2k_f + 2k_{\text{for}} - k_+ - k_-)^2]/4k_{\text{for}}$. k_f , the donor only decay rate constant, is equated to the rate constant measured for the donor only analogue in the same solvent and temperature.

(16) Details concerning the preparation of the DBA compound have been reported elsewhere. (a) Kumar, K.; Tepper, R. J.; Zeng, Y.; Zimmt, M. B. *J. Org. Chem.* **1995**, *60*, 4051. (b) Kaplan, R. Ph. D. Thesis, Brown University, Providence, RI, 2001.

(17) (a) Zeglinski, D. M.; Waldeck, D. H. *J. Phys. Chem.* **1988**, *92*, 692. (b) O'Connor, D. V.; Phillips, D. *Time Correlated Single Photon Counting*; Academic Press: New York, 1984.

(18) Kaplan, R. W.; Napper, A.; Zimmt, M. B.; Waldeck, D. H. *J. Am. Chem. Soc.* **2000**, *122*, 12039.

(19) The parameters in the continuum calculation (cavity radius, vacuum free energy difference and dipole moment change) were chosen to match the parameters in the molecular treatment. This choice allowed a direct comparison between the two models.

(20) The slopes found via the continuum model were 0.30 meV/K for 1,3-dichlorobenzene, 0.40 meV/K for chlorobenzene, 0.40 meV/K for chlorotoluene, and 0.12 meV/K for benzonitrile. Previous work (Vath, P.; Zimmt, M. B. *J. Phys. Chem. A* **2000**, *104*, 2626) showed that the continuum model underestimates the temperature dependence of the reaction free energy.

(21) (a) With a temperature dependence of 2 meV/K for Δ_rG , one finds $\lambda_0 = 0.44$ eV and $|V| = 9.6$ cm⁻¹ in chlorobenzene, $\lambda_0 = 0.53$ eV and $|V| = 16.6$ cm⁻¹ in dichlorobenzene, $\lambda_0 = 0.37$ eV and $|V| = 6.9$ cm⁻¹ in *meta*-chlorotoluene, and $\lambda_0 = 1.0$ eV and $|V| = 42$ cm⁻¹ in benzonitrile. (b) With the continuum model's temperature dependence for Δ_rG (see ref 20), one finds $\lambda_0 = 0.51$ eV and $|V| = 12$ cm⁻¹ in chlorobenzene, $\lambda_0 = 0.68$ eV and $|V| = 31$ cm⁻¹ in dichlorobenzene, $\lambda_0 = 0.42$ eV, and $|V| = 8.1$ cm⁻¹ in *meta*-chlorotoluene, and $\lambda_0 = 1.1$ eV and $|V| = 65$ cm⁻¹ in benzonitrile.

(22) (a) Matyushov, D. V.; Schmid, R. *J. Chem. Phys.* **1996**, *104*, 8627. (b) Ben-Amotz, D.; Willis, K. G. *J. Phys. Chem.* **1993**, *97*, 7736.

(23) The apparent, slight increase of the solvent reorganization energy with temperature (Figure

7.5) does not agree with the slight decrease observed in experiments²⁰ or predicted by modern solvation theory.¹⁴ This slight difference is likely a result of the assumed temperature independence of the electronic coupling. See ref 24.

(24) Napper, A. M.; Read, I.; Waldeck, D. H.; Kaplan, R. W.; Zimmt, M. B. *J. Phys. Chem. A.*; 2002; *106*(18); 4784-4793.

(25) For the situation in which the solvent mediated pathway dominates the other contributions to the electronic coupling magnitude, the superexchange state is depicted by D^+S^-A (for a reaction “mechanism” of $D^*SA \rightarrow D^+S^-A \rightarrow D^+SA^-$). Between the different solvent systems being studied, the major change in energetics of the superexchange state will arise from the energetics of S^- . The solvent dependence of the donor’s ionization potential is assumed to be small. Hence, the electron affinity of the solvent gauges the change in energetics.

(26) (a) Jordan, K. D.; Michejda, J. A.; Burrow, P. D. *J. Am. Chem. Soc.* **1976**, *98*, 7189. (b) Burrow, P. D.; Modeli, A.; Jordan, K. D. *Chem. Phys. Lett.* **1986**, *132*, 441. (c) Burrow, P. D.; Howard, A. E.; Johnston, A. R.; Jordan, K. D. *J. Phys. Chem.* **1992**, *96*, 7570 and references therein.

(27) Gould, I. R.; Young, R. H.; Mueller, L. J.; Albrecht, A. C.; Farid, S. *J. Am. Chem. Soc.* **1994**, *116*, 8188.

(28) Cave, R. J.; Newton, M. D.; Kumar, K.; Zimmt, M. B. *J. Phys. Chem.* **1995**, *99*, 17501.

Chapter 8 The Role Played by Orbital Energetics in Solvent Mediated Electronic Coupling

Electron transfer rates are measured for three supramolecular species, which contain an electron donor, electron acceptor and rigid connecting bridge. Two of the species are linear and the third species is C-shaped. The latter topology produces a 10 Å wide, solvent accessible gap between the donor and acceptor units. This molecular design allows the dependence of the electron transfer rate on the solvent's electronic character to be evaluated. The results display a strong correlation between the energy of the solvent's lowest unoccupied molecular orbital and the magnitude of solvent mediated electronic coupling in systems with electronically excited donors. The variation of the electronic coupling with solvent modulates transfer rate constants by more than an order of magnitude.[§]

8.1 Introduction

For many long distance electron transfer systems, the factors controlling transfer dynamics are sufficiently understood to permit reasonable interpretation of rate constants. Within semi-classical formulations, non-adiabatic electron transfer rate constants are expressed as the product of a Franck Condon weighted density of states (*fcwds*), which determines the probability that the system attains the transition state geometry, and an electron tunneling probability, which characterizes the primary electronic event (see eq 8.1).¹ The *fcwds* and activation barriers may be estimated with models that account for molecular shape, changes in charge distributions, and the relevant properties of the medium (solvent). The tunneling

[§] Reproduced with permission from Kaplan, R.; Napper, A. M.; Waldeck, D. H.; Zimmt, M. B.; *J. Phys. Chem. A.*; **2002**; 106(10); 1917-1925. Copyright 2002 American Chemical Society

probability is determined by the electronic coupling $|V|$ between the electron donor (D) and acceptor (A) groups in the transition state geometry and depends on the molecular and medium structures. Depending on the complexity of the medium between the D and A groups, $|V|$ may be predicted using a variety of empirical or theoretical methods.² Numerous investigations have delineated the dependence of the D / A electronic coupling on the structure of the medium and have found good agreement between experimental and theoretical results. Still, novel means of effecting and modulating D / A electronic coupling are of considerable interest. Recent studies report that solvent molecules may contribute sizeable D / A electronic coupling under specific circumstances.³⁻⁶ In particular, solvent mediated coupling contributions are significant when (1) coupling mediated by covalent connections (the bridge) between a D and an A group is ineffective, (2) solvent molecules readily access the space directly between the D and A groups and make van der Waals contact with both groups, and (3) the electronic properties of the solvent are conducive to electronic coupling.

Non-adiabatic electron transfer rate constants provide a means to probe the D/A electronic coupling and identify correlations between molecular structure and D/A coupling magnitudes. Extracting this information from rate data requires independent determination of *fcwds* contributions, however. In our prior investigations of solvent mediated coupling, the temperature dependence of the electron transfer rate data was analyzed to separate *fcwds* and electronic coupling contributions.³⁻⁵ Various models were employed to predict the temperature dependence of the outer sphere reorganization energy λ_o and the reaction free energy $\Delta_r G$. Each model produced a slightly different relationship between the estimated FCWDS, its temperature dependence, and solvent properties. (Note: for clarity, reference to the actual *fcwds* will be indicated by italicized, lower case letters. Calculated FCWDS will be indicated by capitalized,

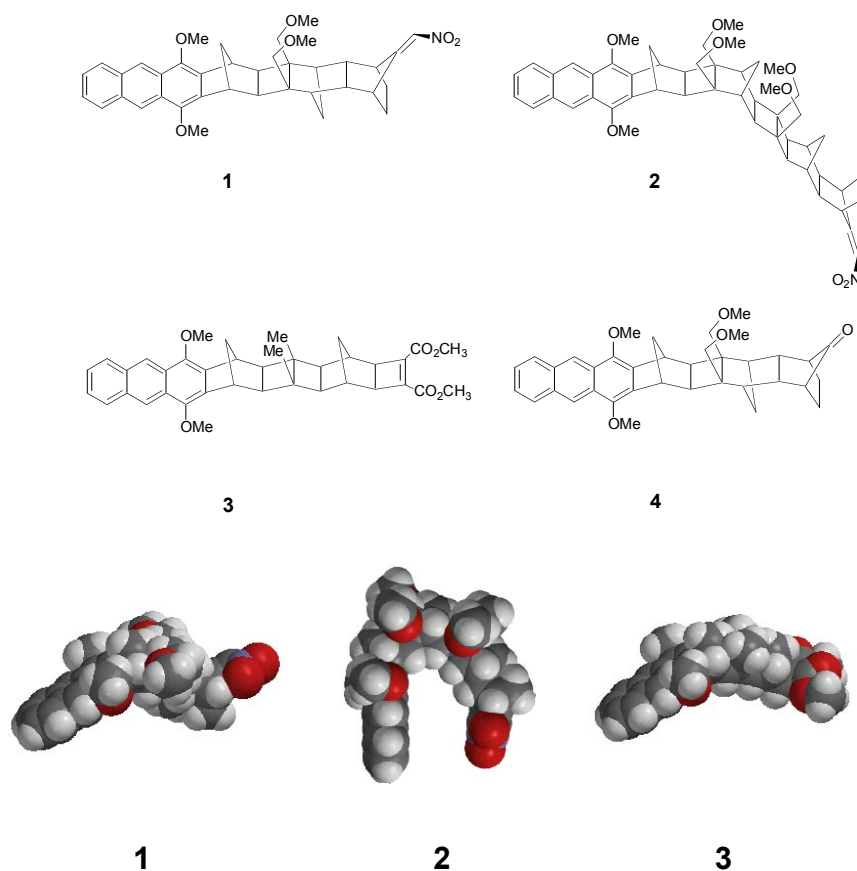
normal type.) Use of molecular solvation models⁷ to calculate the FCWDS temperature dependence resulted in solvent independent values of $|V|$ for linear DBA molecules; e.g., compounds **1** and **3** in Scheme 8.1. By contrast, strongly solvent dependent values of $|V|$ were obtained for highly curved DBA molecules, in which the D and A groups are cofacial and separated by a gap of 7 to 10 Å. Initial characterization of the relationship between coupling magnitude and solvent structure was obtained in this manner.^{3,4} Two significant impediments frustrate this approach to delineating structure - coupling correlations. First, the molecular solvation model requires accurate values of numerous solvent properties, both molecular and bulk, in order to calculate the FCWDS temperature dependence.⁷ These parameters are available for a limited number of solvents, thus proscribing the model's general use. Second, the method of analyzing $k_{eT}(T)$ data presumes that $|V|$ is temperature independent. This assumption is reasonable in systems where "rigid" covalent bridges propagate the electronic coupling. Its validity is less certain in situations where solvent - substrate interactions mediate the coupling. If $|V|$ varies significantly with temperature,⁸ this variation will be incorporated into the *fcwds* analysis and will generate incorrect values for the *fcwds* and $|V|$.

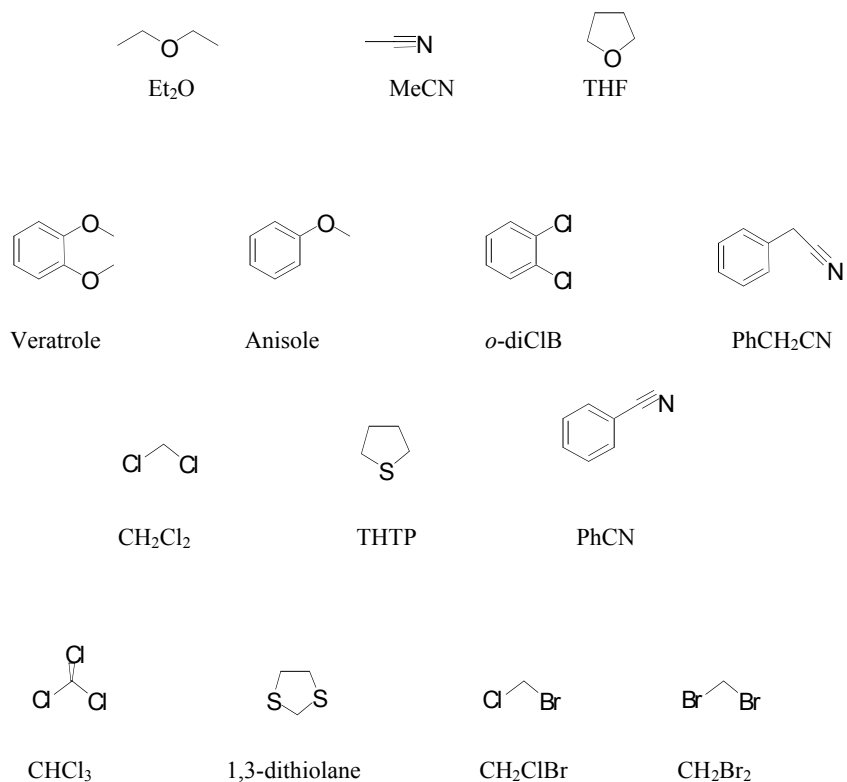
An alternative procedure for the analysis of electron transfer rates is employed in this manuscript.⁹ Room temperature electron transfer data from two linear and one C-shaped molecule are reported in fourteen solvents. The charge transfer distances in these molecules range from 10 to 12.4 Å. Despite differences in bridge topology, acceptor structure, and driving force among the three molecules, the rate constant data indicate qualitative similarities in the solvent dependence of the electron transfer rates. The origin of this similarity is investigated using continuum models. This similarity is exploited to probe the dependence of solvent mediated coupling on the solvent molecule's electronic structure.

Table 8.1 Electron Transfer and Donor Only Decay Rate Constants for **1** - **4** in fourteen solvents.

Solvent	$k_{eT}(1) / 10^7 \text{ s}^{-1}$	$k_{eT}(2) / 10^7 \text{ s}^{-1}$	$k_{eT}(3) / 10^7 \text{ s}^{-1}$	$k_{SI}(4) / 10^7 \text{ s}^{-1}$
Ethyl Ether	220 ^a	1.1 ^a	2.0 ^b	3.6 ^a
Acetonitrile	620 ^a	4.7 ^a	2.6 ^{b,c}	2.2 ^a
Tetrahydrofuran	730 ^a	5.4 ^a	5.8 ^b	3.2 ^a
Veratrole	960 ^d	10.0 ^d	15.2 ^d	4.8 ^d
Anisole	1160 ^d	18.0 ^d	13.9 ^d	4.1 ^d
o-dichlorobenzene	1380 ^d	69.3 ^d	20. ^d	4.1 ^d
PhCH ₂ CN	1560 ^a	46.0 ^a	15. ^d	3.2 ^a
CH ₂ Cl ₂	1600 ^a	39.0 ^a	6.8 ^d	2.5 ^a
Tetrahydrothiophene	1650 ^d	20.0 ^d	15.8 ^d	4.0 ^d
PhCN	2400 ^a	120. ^a	15. ^c	3.3 ^a
CHCl ₃	2500 ^a	100. ^a	26.3 ^d	3.9 ^a
1,3-dithiolane	2660 ^d	62.6 ^d	32. ^d	4.7 ^d
CH ₂ ClBr	3500 ^a	120. ^a	14.4 ^d	5.0 ^a
CH ₂ Br ₂	5000 ^a	260. ^a	23.4 ^d	20.7 ^a

a) Data reported in Reference 3c. b) Data reported in Reference 10. c) Data reported in References 3a and 5. d) Data reported here for the first time.

**Scheme 8.1** Line structures of molecules **1** - **4**, and CPK structures of **1** - **3**.



Scheme 8.2 Molecular structures of the solvents and their abbreviations.

8.2 Experimental Details

Excited state lifetimes of molecules¹¹ **1** – **4** (Scheme 8.1) were determined using picosecond photon counting and nanosecond time resolved fluorescence methods.³⁻⁵ Sample optical densities at the excitation wavelength (370 or 398 nm) were < 0.15, corresponding to concentrations less than 40 μ M. Samples were freeze-thaw-degassed for a minimum of four cycles, and then transferred in vacuo, via a side arm, to optical quality 1 cm pathlength cells. The sample temperature was equilibrated to 295 ± 1 K prior to data acquisition. Solvents were dried over Na, CaH or CaSO₄ and distilled prior to use. The structures of the solvents and their abbreviations are presented in Scheme 8.2. The excited state lifetime τ_4 of the donor only

compound **4** was used to determine the intrinsic lifetime of the 1,4-dimethoxyanthracene chromophore in each solvent. Electron transfer rate constants were determined for each compound, X, using the relationship $k_{\text{eT}}(\text{X}) = 1/\tau_{\text{X}} - 1/\tau_4$. Rate constants are listed in Table 8.1.

8.3 Results and Analysis

Structures of the four molecules investigated are shown in Scheme 8.1. Each of the molecules contains a 1,4-dimethoxyanthracene chromophore, which serves as the electron donor when in its lowest energy singlet excited state. The electron acceptor in molecules **1** and **2** is a nitroethylene group and is a cyclobutenediester in molecule **3**. Molecule **4** does not have an electron acceptor. It serves as the donor only reference for determination of the electron transfer rate constants. Space-filling CPK renderings of **1-3** are shown at the bottom of Scheme 8.1. The bridges in molecules **1** and **3** span seven σ -bonds in an all *trans* configuration and lie in the line of sight between the D and A groups. The charge transfer distances, R_{CC} , are 12.4 and 11.5 Å, respectively.^{12,13} The bridge in molecule **2** spans 11 σ -bonds and incorporates one *s-cis* link. The D and A groups extend from the same face of the bridge, yielding a C-shaped structure. The 10.0 Å gap between the cofacial D and A groups is not obstructed by the bridge and may be occupied by solvent molecules.

Table 8.1 lists electron transfer rate constants for molecules **1 – 3** and the excited donor decay rate constant ($k_{\text{S1}} = 1/\tau_4$) in fourteen solvents (Scheme 8.2). The solvents are ordered by ascending rate constant determined for molecule **1**. The electron transfer rate constants for molecules **2** and **3** exhibit a solvent ordering that is similar to that of **1**, but with some important differences. The transfer rate constants vary by factors of 23, 240 and 16 from the slowest

solvent (ethyl ether) to the fastest solvent for **1** (CH₂Br₂), **2** (CH₂Br₂), and **3** (1,3-dithiolane), respectively. Within the group of five solvents yielding the slowest rate constants for **1** (ethyl ether, acetonitrile, THF, veratrole, anisole), the transfer rate constants for **2** and **3** increase, but remain within a factor of two of each other. However, in seven of the nine other solvents, the transfer rate constants for the C-shaped DBA molecule, **2**, are from three to eleven times larger than for the linear DBA, **3**. The rate data in Table 8.1 raise two questions. What factors produce the different ordering of solvents, as gauged by electron transfer rate constants, for the three DBA molecules? What is the origin of the greater sensitivity to solvent for the transfer rates in molecule **2** as compared to molecules **1** and **3**?

8.4 Calibrating the FCWDS

Within semi-classical electron transfer theory,¹ non-adiabatic rate constants k_{eT} are calculated as the product of the *fcwds* and the square of the donor-acceptor electronic coupling matrix element, $|V|^2$;

$$k_{eT} = \frac{2\pi}{\hbar} |V|^2 \text{fcwds} \quad (8.1)$$

Experimental rate constant data may be used to examine the solvent dependence of $|V|$, provided the FCWDS can be calculated accurately. Alternatively, rate data can be used to probe the solvent dependence of the *fcwds* if $|V|$ is constant. The bridge in **1** is comprised of an all *trans* arrangement of σ -bonds and is positioned directly between the D and A groups. In addition, at their points of contact with the bridge, the D and A LUMO's of **1** exhibit the same symmetry with respect to the bridge's mirror plane symmetry element. These factors conspire to make the σ -bonded bridge the only significant source of D/A coupling in **1**, hence $|V(\mathbf{1})|$ should be solvent

independent.¹⁴ The variation of electron transfer rates observed for **1** (Table 8.1) arises from the solvent dependence of the *fcwds*. The reaction free energy, $\Delta_r G$, and the solvent reorganization energy, λ_0 , are the solvent dependent quantities contributing to the *fcwds*. The rate data from **1** can be used to test the accuracy of solvation models' predictions of FCWDS as a function of solvent and to identify whether specific solvation effects are present.

Table 8.2 Solvent Properties

Solvent	n_D ^a	ϵ_s ^b	Pekar	LUMO (eV)	$ V(2) $ (cm ⁻¹)
Ethyl Ether	1.353	4.3	0.32	6.46	0.9
Acetonitrile	1.344	37.5	0.53	5.77	1.1
Tetrahydrofuran	1.407	7.6	0.37	6.21	1.1
Veratrole	1.533	4.4	0.20	4.01	1.3
Anisole	1.516	4.3	0.20	3.93	1.6
<i>o</i> -dichlorobenzene	1.551	9.9	0.31	3.20	2.8
PhCH ₂ CN	1.523	18.7	0.38	3.43	2.2
CH ₂ Cl ₂	1.424	8.9	0.38	4.19	2.0
Tetrahydrothiophene	1.504	7.	0.30	5.30	1.4
PhCN	1.528	25.2	0.39	2.44	2.8
CHCl ₃	1.446	4.9	0.27	3.29	2.5
1,3-dithiolane	1.599	-	-	4.08	1.9
CH ₂ ClBr	1.483	8.	0.33	3.55	2.4
CH ₂ Br ₂	1.541	7.	0.28	3.20	2.9

- n_D values obtained from the Aldrich Handbook of Fine Chemicals and Laboratory Equipment, 2000-2001.
- ϵ_s values obtained from Table 6.3 in Ref. 39a and from Ref. 38b.

Continuum models provide convenient, albeit simplistic, prescriptions for calculation of $\Delta_r G$ and λ_0 from the solvent dielectric constant, ϵ_s , and the refractive index, n_D (see Table 8.2 for these, and other, solvent properties). These formulas offer insight as to the variations of driving force and λ_0 with solvent. When used with the semi-classical rate equation, continuum models often predict trends of rate constant versus solvent that are qualitatively similar to experimental

observations.¹⁵ This success stands in sharp contrast to these (continuum) models' erroneous predictions of the temperature dependence of $\Delta_r G$ and λ_o .¹⁶ Simple continuum models account for solvent dipole reorientation but fail to account for density contributions to the solvent response. Density contributions to $\Delta_r G$ and λ_o vary more sharply with temperature than solvent reorientation contributions and must be accounted for when investigating rates as a function of temperature.¹⁷ The objective of this investigation is to understand the solvent dependence of transfer rate constants, preferably without introducing complexities related to any temperature dependence of the *fcwds* or $|V|$. For these reasons, the accuracy of a simple continuum model's prediction of the FCWDS variation with solvent is compared to the observed solvent dependence of the transfer rates for **1** and **3**.

The continuum expression for the solvent reorganization energy, λ_o , attending electron transfer between two, initially uncharged, spherical donor and acceptor species is given by Equation 8.2,

$$\lambda_o = \frac{e^2}{2} \left(\frac{1}{r_A} + \frac{1}{r_D} - \frac{2}{R_{CC}} \right) \left(\frac{1}{n_D^2} - \frac{1}{\epsilon_S} \right) \quad (8.2)$$

where r_A and r_D are the effective radii of the acceptor and donor groups, R_{CC} is the center to center charge transfer distance, and $e^2 = 14.4 \text{ eV/\AA}$. The corresponding expression for the free energy change upon electron transfer is given by Equation 8.3,

$$\Delta_r G = E_{OX} - E_{RED} - E_{00} - \frac{e^2}{2} \left(\frac{1}{r_A} + \frac{1}{r_D} \right) \left(\frac{1}{\epsilon_{REF}} - \frac{1}{\epsilon_S} \right) - \frac{e^2}{\epsilon_S R_{CC}} \quad (8.3)$$

where E_{OX} and E_{RED} are the donor oxidation potential and the acceptor reduction potential, respectively, in a reference solvent (acetonitrile) with static dielectric constant ϵ_{REF} .¹⁸ E_{00} is the $S_1 - S_0$ energy gap in the solvent of interest, with static dielectric constant ϵ_S .¹⁹ Values of 4.5 Å, 3.7 Å and 3.9 Å were previously established^{3c,5} for the effective radii of the anthracene donor, the

nitroethylene acceptor and the cyclobutenediester acceptor, respectively, by reproducing λ_o and Δ_rG values calculated using a finite difference Poisson Boltzman model²⁰ that takes into account the details of each molecule's shape and the charge distributions of the reduced and oxidized acceptors and donors. Charge transfer distances, R_{CC} , were calculated using the Generalized Mulliken Hush method.¹³ The value of Δ_rG and λ_o for each DBA structure in each solvent was used to calculate the FCWDS within a single quantized mode, semi-classical model (Equation 8.4).

$$\text{FCWDS} = (4\pi\lambda_o k_B T)^{-1/2} \sum_{n=0}^{\infty} \left(\frac{e^{-S} S^n}{n!} \right) \exp\left[-(\lambda_o + \Delta_rG + nh\nu)^2 / 4\lambda_o k_B T\right]; S = \lambda_v / h\nu \quad (8.4)$$

A quantized mode energy spacing, $h\nu$, of 0.175 eV was used for each DBA molecule. Previous estimates of the quantized mode reorganization energy (λ_v) were used: 0.30 eV for **1** and **2** and 0.39 eV for **3**.^{3c,5} These values are assumed to be solvent independent. Their choice does not influence either the solvent dependence or the relative magnitudes determined for $|V|$ in **1** and **2**.

A plot of the calculated FCWDS versus the experimental electron transfer rate constants for **1** is displayed in Figure 8.1A. If the continuum derived FCWDS calculations are correct and $|V|$ is solvent independent, the plotted points should lie on a line with a slope equal to $\frac{\hbar}{2\pi |V|^2}$ and an intercept equal to zero. For seven of the eight non-aromatic solvents (solid circles), the calculated FCWDS and the experimental rate constants exhibit a reasonably linear correlation with an intercept that is close to zero. The slope of a linear regression fit to these seven points yields $|V| = 25 \text{ cm}^{-1}$. A previous analysis of the temperature dependence of the rate constant, $k_{eT}(T)$, in ethyl ether, acetonitrile and benzonitrile yielded a value of $|V|=19 \pm 2 \text{ cm}^{-1}$ for the D/A coupling in **1**.^{3c} The values of $|V|$ from these independent analyses are in reasonable agreement.

For **1**, the continuum based FCWDS values appear to be consistent with the experimental rate constants in most of the non-aromatic solvents. The points for the six aromatic solvents and THTP are scattered and fall substantially above the regression line for the non-aromatic solvents. In these solvents, the calculated FCWDS are considerably larger than the actual *fcwds*, which are indicated by the position along the experimental transfer rate constant axis. Figure 8.1B shows an analogous plot for **3**.

The linearity of the data in non-aromatic solvents is evident in this system also (with the exception of CHCl_3). A linear regression fit of the rate data from the non-aromatic solvents, excluding CHCl_3 , yields $|V(\mathbf{3})| = 4.9 \text{ cm}^{-1}$. As with **1** the calculated FCWDS values in aromatic solvents are anomalous but not uniformly higher than those for the non-aromatic solvents. Previous investigations^{4b,21} have shown that in weakly dipolar solvents, quadrupole moments play a significant role in determining $\Delta_r G$ and λ_o . The simple continuum model used here does not account for solvent quadrupole interactions. Thus, the poor correlation between the continuum derived FCWDS calculations and the experimental rate constants in the aromatic solvents is not surprising. Numerous groups are working to develop solvation theories that incorporate quadrupole contributions.^{7a,22}

Rate data from **1** and **3** may be of use in benchmarking these theories. For the purposes of this investigation, Figure 8.1 demonstrates that continuum expressions for $\Delta_r G$ and λ_o generate reasonable estimates of the FCWDS for **1** and **3** in some, but not in all, solvents of interest.

The accuracy of FCWDS calculations for **2** is likely to exhibit a similar dependence on solvent type as observed for **1**.

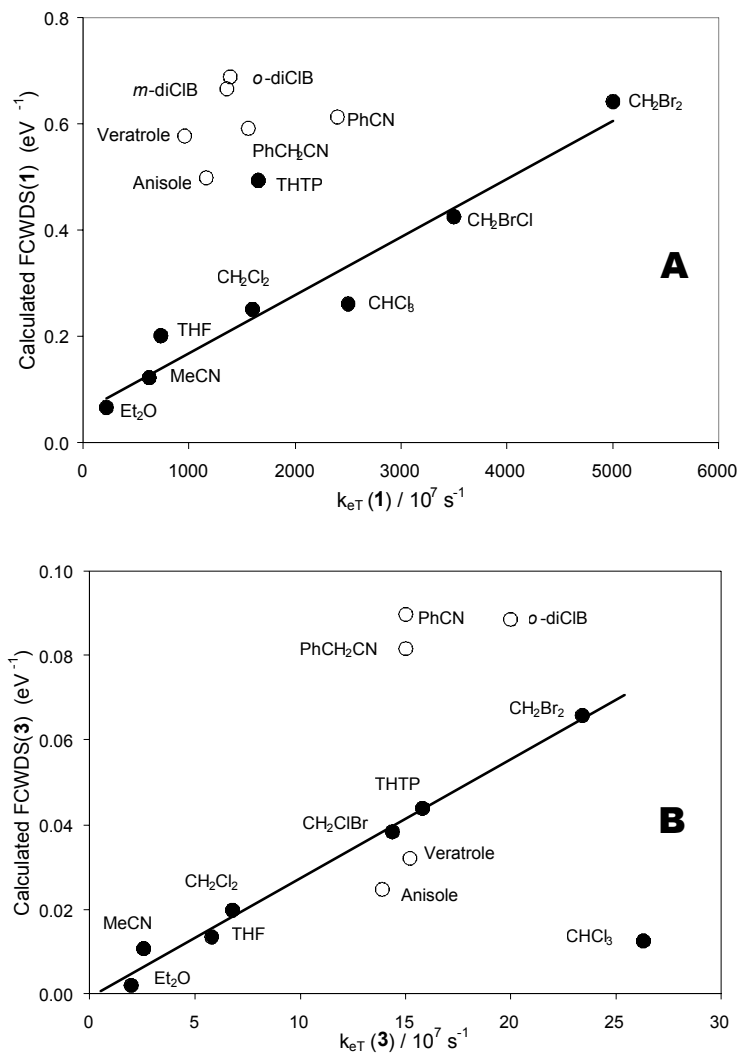


Figure 8.1 Panel A shows a plot of the Franck Condon Weighted Density of States (FCWDS) calculated for **1** at 295 K using continuum models for $\Delta_r G$ and λ_0 vs. the experimental transfer rate constants of **1**. Panel B shows a similar plot for **3**. For both panels, the filled circles indicate non-aromatic solvents and the empty circles indicate aromatic solvents. Points for 1,3-dithiolane are not included as ϵ_s of this solvent is unavailable.

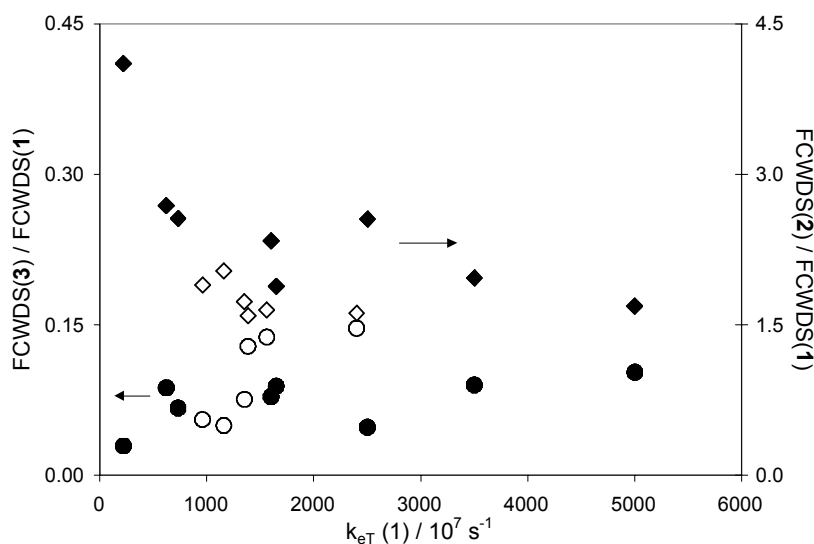


Figure 8.2 Plots of calculated continuum FCWDS ratios at 295 K for **3** : **1** (circles, left axis) and **2** : **1** (diamonds, right axis) versus the experimental transfer rate constants for **1**. Filled symbols indicate non-aromatic solvents; empty symbols indicate aromatic solvents.

As the objective of this study is to determine the solvent dependence of $|N|$ in **2**, an approach is required that generates accurate estimates of the $fcwds$ in all solvents. Since **1** and **2** contain identical D and A groups and comparable charge transfer distances, the solvent dependence of the actual $fcwds$ from **1** might be used to predict the solvent dependent $fcwds$ for **2**. This approach will be successful if the $fcwds$ for **1** and **2** vary proportionally with solvent. Figure 8.2 (diamonds) displays ratios of the continuum derived FCWDS estimates, $FCWDS(2) / FCWDS(1)$, versus the observed rate constants for **1**. The experimental rates from **1** are used as the x-axis to reflect the change of the actual $fcwds(1)$ with solvent.²³ For the non-aromatic solvents (filled diamonds), with the exception of ethyl ether, the FCWDS ratio varies from 1.7 to 2.7 with an average value of 2.2 ± 0.4 . The predicted FCWDS ratio is slightly smaller for the non-aromatic solvents that provide the fastest rate constants for **1**. Interestingly, the anomalous FCWDS values found for **1** in aromatic solvents (Figure 8.1) are not manifest when rate ratios

are plotted (Figure 8.2, open diamonds). Continuum models predict relative magnitudes of the FCWDS for **2** and **1** that are reasonably close to the mean value (to within $\sim 30\%$ for all the solvents). Near constancy of the actual *fcwds* ratio for **1** and **2** would provide a simple means to evaluate the solvent dependence of the coupling in **2** (vide infra). However, this prediction cannot be directly verified if $|V|$ for **2** is solvent dependent. For this reason, the accuracy of continuum derived FCWDS ratios will be tested by comparing the solvent dependent FCWDS ratios and rate ratios for **3** and **1**.

As for **1**, the all *trans* σ -bridge of **3** is the dominant source of D/A coupling and $|V(\mathbf{3})|$ should be solvent independent.^{3a,5} The charge transfer distance in **3**, $R_{CC} = 11.5 \text{ \AA}$, is intermediate between that of **1** and **2**. The shape and charge distributions of the reduced acceptors in **1** and **3** are very different. As a result, the variations of $\Delta_r G$ and λ_o with solvent should be dissimilar for **1** and **3**. In addition, the acceptor in **3** affords a substantially smaller driving force for charge separation (by 0.3 eV in MeCN) than does the acceptor in **1**. Given the substantial differences in structure and driving force, comparison of the FCWDS ratios and rate constant ratios for **1** and **3** should constitute a critical test of the continuum model's predictions. Figure 8.2 shows the continuum derived FCWDS ratio, $\text{FCWDS}(\mathbf{3}) / \text{FCWDS}(\mathbf{1})$, (circles) plotted versus the solvent dependent transfer rates of **1** (open circles indicate aromatic solvents; filled circles indicate non-aromatic solvents). The predicted ratios are largely independent of solvent, although a slight increase in ratio with increasing transfer rate for **1** may be present. For the non-aromatic solvents, the FCWDS ratios range between 0.029 and 0.10, with an average of 0.074 ± 0.023 .²⁴ This plot indicates that the continuum model predicts comparable scaling of the FCWDS with solvent for **1** and **3** despite the significant differences in the acceptor structures and

the driving force for electron transfer in these two DBA molecules. The crucial question is whether the kinetic data for **1** and **3** indicate comparable scaling of the *fcwds* with solvent?

8.5 Experimental Rate Ratios (3:1) for Linear Systems

Figure 8.3 displays the experimental rate constant ratio, $k_{eT}(\mathbf{3}) / k_{eT}(\mathbf{1})$ (circles) plotted versus the rate constants for **1**. The continuum model prediction that $FCWDS(\mathbf{3}) / FCWDS(\mathbf{1})$ does not vary significantly with solvent appears to be supported by the rate constant data. For the non-aromatic solvents (filled circles), the rate ratio is relatively constant. Upon more critical inspection, the rate ratio decreases slightly with increasing rate of **1**, in contrast to the slight increase predicted by the FCWDS calculations. The scatter in both plots precludes interpreting this difference. The average value of the rate ratio in the non-aromatic solvents is 0.0074 ± 0.0031 .

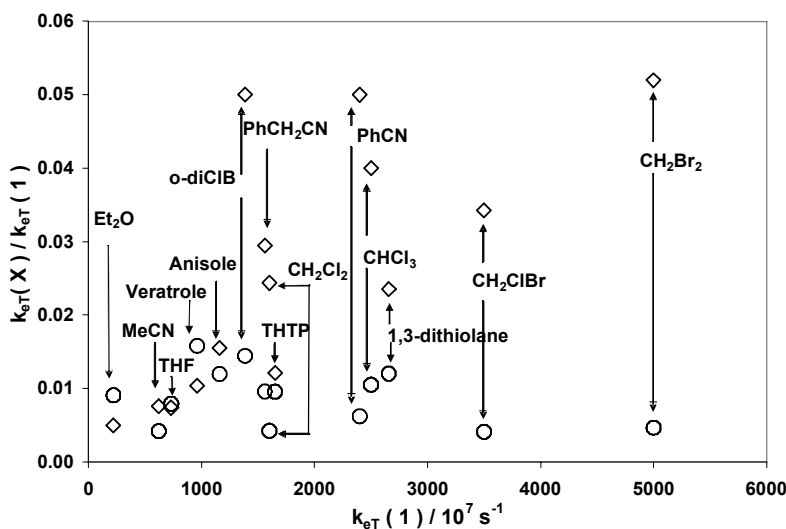


Figure 8.3 Plots of experimental rate constant ratios $k_{eT}(X) : k_{eT}(\mathbf{1})$ versus the experimental transfer rate constants of **1**. $X = \mathbf{3}$ (circles) and $X = \mathbf{2}$ (diamonds). The solvent corresponding to each pair of points is indicated.

For all fourteen solvents, the experimental rate ratio is 0.0089 ± 0.0039 . Among solvents with common structural features, the rate ratio exhibits greatly reduced scatter. For example, despite large variations of the transfer rate constants for the three dihalomethane solvents, the rate ratio remains remarkably constant; $\langle k_{\text{eT}}(\mathbf{3}) / k_{\text{eT}}(\mathbf{1}) \rangle = 0.0043 \pm 0.003$. In acetonitrile, which also has three heavy (non-hydrogen) atoms, $k_{\text{eT}}(\mathbf{3}) / k_{\text{eT}}(\mathbf{1})$ equals 0.0042. These values differ substantially from the average value of $k_{\text{eT}}(\mathbf{3}) / k_{\text{eT}}(\mathbf{1})$ (0.0097 ± 0.0017) in the four, non-aromatic ether and thioether solvents: ethyl ether, THF, tetrahydrothiophene (THTP) and 1,3-dithiolane. The clustering of rate ratios, apparently correlated to the number of heavy atoms in each solvent, may reflect the influence of solvent size on solvation of the different size acceptor groups in **1** and **3** (vide infra). Given that the continuum predictions of the FCWDS (Figures 8.1 and 8.2, open symbols) are suspect for aromatic solvents, it is encouraging that the experimental rate ratios in the aromatic solvents (Figure 8.3, open circles) are similar to those in the non-aromatic solvents. Still, the five aromatic solvents display the greatest scatter and the largest values of the rate ratio. Values range 2.5 fold, from 0.0060 in benzonitrile to 0.016 in veratrole, with an average $k_{\text{eT}}(\mathbf{3}) / k_{\text{eT}}(\mathbf{1})$ of 0.012 ± 0.004 . Overall, the small variation of the experimental rate ratios for **3** and **1** with solvent is in accord with the continuum derived FCWDS predictions.

The accuracy of D/A electronic coupling magnitudes derived from rate ratio analyses using calculated FCWDS ratios may be evaluated using **3**, because $|V(\mathbf{3})|$ is solvent independent and can be independently determined using Figure 8.1B. The D/A coupling for **3** in non-aromatic solvents may be extracted from rate constant ratios using the calculated FCWDS ratios for the non-aromatic solvents and equation 8.5.

$$|V(\mathbf{3})| = |V(\mathbf{1})| \times \sqrt{\frac{k_{\text{et}}(\mathbf{3}) / \text{FCWDS}(\mathbf{3})}{k_{\text{et}}(\mathbf{1}) / \text{FCWDS}(\mathbf{1})}} \quad (8.5)$$

With the reasonable assumption that $|V(\mathbf{1})|$ is solvent independent, any apparent solvent dependence of $|V(\mathbf{3})|$ that this FCWDS ratio approach generates can be assessed.²⁵ For the three, structurally similar, dihalomethane solvents, this analysis yields $|V(\mathbf{3})| = 4.2 \pm 0.2 \text{ cm}^{-1}$. The value in acetonitrile is comparable; $|V(\mathbf{3})| = 4.2 \text{ cm}^{-1}$. For the other non-aromatic solvents, this approach yields $|V(\mathbf{3})| = 6.5 \text{ cm}^{-1}$ for THF; 6.2 cm^{-1} for THTP; 8.9 cm^{-1} for chloroform and 10.5 cm^{-1} for ethyl ether. The mean value from this analysis in the non-aromatic solvents is $|V(\mathbf{3})| = 6.1 \pm 2.5 \text{ cm}^{-1}$. Because the ratio of calculated FCWDS for **3** and **1** is relatively solvent independent (filled circles in Figure 8.2), the average FCWDS ratio, 0.074, was also used to evaluate $|V(\mathbf{3})|$ in the non-aromatic solvents. The value of $|V(\mathbf{3})|$ was found to range from 4.5 to 7.2 cm^{-1} , with an average of 5.7 cm^{-1} .²⁶ Use of 0.074 as the FCWDS ratio for the aromatic solvents yielded slightly larger $|V(\mathbf{3})|$ values, ranging from 5.5 to 8.8 cm^{-1} .²⁶ Quite clearly, comparable values of $|V(\mathbf{3})|$ are obtained by direct analysis of the rate data (Figure 8.1B) or by analyzing rate ratios. The smallest and largest $|V(\mathbf{3})|$ differ by a factor of two, and the values in aromatic solvents are roughly a third larger than in non-aromatic solvents.²⁷ Despite large differences in driving force ($\sim 0.3 \text{ eV}$) and acceptor structure, the rate constants ratios demonstrate that the actual *fcwds* for **1** and **3** vary comparably with solvent. With the reasonable success of this benchmark, the rate data from **1** and **2** may be analyzed using FCWDS ratios.

8.6 Experimental Rate Ratios (2:1) for the C-shaped Molecule

The presence of identical D and A in **1** and **2** should produce more comparable *fcwds* values and a more similar solvent dependence than found for **1** and **3**. The $k_{\text{et}}(\mathbf{2}) / k_{\text{et}}(\mathbf{1})$ rate ratio data are shown in Figure 8.3 (diamonds). This graph shows that the solvent dependent electron transfer rate constants of **2** are poorly predicted by the rate constants of **1**. The rate ratio exhibits

large variations for the investigated solvents, even among the four solvents (CH₃CN, CH₂Cl₂, CH₂ClBr, CH₂Br₂) that gave identical values of $k_{\text{et}}(\mathbf{3}) / k_{\text{et}}(\mathbf{1})$. To the extent that an overall trend in the ratios can be identified, it is to larger ratios in the solvents supporting the fastest transfer rates for **1**. The poor correlation between the rate constants of **1** and **2** must arise from either very different solvent dependence of the *fcwds* for **2** as compared to **1** and/or a strong solvent dependence of the D/A electronic coupling in **2**. Based on the analysis of rate data for **1** and **3** and prior investigations,³⁻⁵ a solvent dependence of $|V|$ is the more likely origin of the scatter in the $k_{\text{et}}(\mathbf{2}) / k_{\text{et}}(\mathbf{1})$ rate plot.

As discussed earlier, the continuum values of the FCWDS ratio for **2** and **1** vary weakly with solvent and have an average ratio of 2.24 in the non-aromatic solvents. Presuming that a single FCWDS ratio is appropriate for all solvents, the D/A coupling for **2** in each solvent may

be estimated as $|V(\mathbf{2})| = |V(\mathbf{1})| \times \sqrt{\frac{k_{\text{et}}(\mathbf{2})}{k_{\text{et}}(\mathbf{1})}} / 2.24$.

Table 8.2 lists the $|V(\mathbf{2})|$ couplings obtained in this way using $|V(\mathbf{1})| = 19 \text{ cm}^{-1}$. The coupling magnitude varies 3.2 fold: from 0.9 cm^{-1} in ethyl ether to 2.8 – 2.9 cm^{-1} in benzonitrile, *o*-dichlorobenzene and methylene bromide. The spread of the $|V(\mathbf{2})|$ values is only 1.6 times larger than that observed for **3**. However, the influence of solvent on $|V(\mathbf{2})|$ is significantly larger in comparisons made between structurally similar solvents. The predicted FCWDS ratios (**3:1** and **2:1**), experimental $k_{\text{et}}(\mathbf{3}) / k_{\text{et}}(\mathbf{1})$ ratios and $|V(\mathbf{3})|$ values are each nearly constant among the three dihalomethane and acetonitrile solvents. By contrast, the $k_{\text{et}}(\mathbf{2}) / k_{\text{et}}(\mathbf{1})$ ratios and $|V(\mathbf{2})|$ values for these four solvents vary 7-fold and 2.6-fold, respectively. Among aromatic solvents, $|V(\mathbf{3})|$ values vary by 60% whereas $|V(\mathbf{2})|$ values vary by 210%. Overall, the rate constant and coupling results from **2** provide considerable evidence for solvent dependent coupling.²⁸

8.7 Origin of the Solvent Dependent Values of $|V(2)|$

A number of factors influence the magnitude of solvent mediated coupling. Within superexchange models, the number of “pathway” sites (n), the exchange interactions among “pathway” sites (β_{ij}), and the energy gap (Δ) between the tunneling level and the virtual state, defined by charge transfer to the “pathway” site, determine the coupling.^{2,29} If a single solvent molecule comprises the coupling pathway, $n = 1$ and the D / A coupling scales as Δ^{-1} ; *i.e.*,

$$|V| = \beta_{D^*S} \beta_{SA} / \Delta \quad (8.6)$$

If the D / A coupling is mediated by vacant orbitals of the solvent (electron mediated superexchange), the relevant superexchange state is D^+S^-A and the corresponding energy gap, Δ , depends on the vertical electron affinity of the solvent. In contrast, if D / A coupling is mediated by filled orbitals of the solvent (hole mediated superexchange), the appropriate superexchange state is $D^*S^+A^-$, and the corresponding energy gap, Δ , depends on the solvent’s vertical ionization potential. Previous investigations have found a rough correlation between solvent mediated coupling magnitudes and solvent vertical electron affinities for systems employing excited donors.^{3,5} The larger set of solvents in Table 8.2 allows more extensive investigation of such correlations. Explicit expressions for the energy gap, Δ , between the electron transfer transition state and the mediating superexchange state are likely to be complicated. If the mediating state primarily employs the solvent HOMO, Δ should vary among solvents as $\sim E_{\text{HOMO}} + \text{constant}$. If the mediating state involves the solvent LUMO, Δ should vary among solvents as $\sim -E_{\text{LUMO}} + \text{constant}$. Either dependence can be probed by plotting $|V|^{-1}$ versus Δ or E_{MO} .³⁰ Plots of $|V(2)|^{-1}$ versus the solvent HOMO energy are scattered about a best fit regression line that is horizontal. To the extent that the Koopman's theorem applies and the HOMO energy provides a reasonable estimate of the solvent molecule’s vertical ionization potential, this result indicates that hole

mediated superexchange does not contribute significantly to the electronic coupling. As discussed below, the couplings for **2** display a good correlation with the solvents' LUMO energies. Within the accuracy of Koopman's theorem (i.e., to the extent that the LUMO energy determines the vertical electron affinity), this correlation indicates that the electronic coupling for **2** is dominated by electron mediated superexchange involving solvent molecules.

A plot of $|V(\mathbf{2})|$ versus Δ^{-1} should be linear if the exchange coupling terms do not change dramatically with solvent (see eq 8.6). Although vertical electron affinity provides a good measure of the changes in Δ among different solvents, this quantity is not available for many of the solvents in Table 8.1. For this reason, the solvent LUMO energy was used instead. Calculations were performed at the Hartree-Fock level using a 6-31G** basis set.³¹ The geometry of each solvent molecule was first optimized and then the LUMO energy was determined (see Table 8.2).

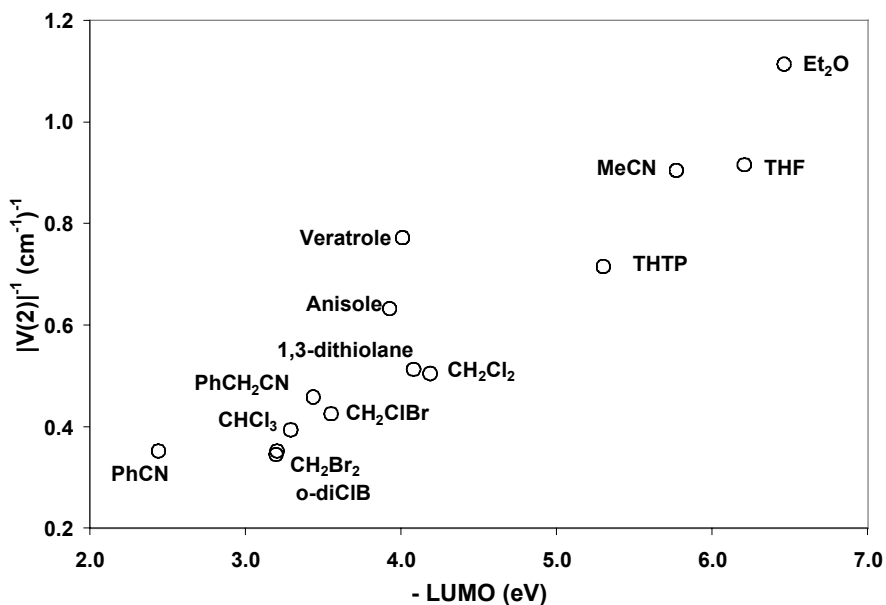


Figure 8.4 The reciprocal D/ A coupling magnitude for **2** ($|V(\mathbf{2})|^{-1}$) in each solvent is plotted as a function of the HF 6-31G** LUMO energy of that solvent molecule.

Among the solvents for which experimental data is available, the calculated LUMO energies are 2.8 ± 0.3 eV more negative than the literature values of the vertical electron affinity.³² Figure 8.4 displays a plot of $|V(\mathbf{2})|^{-1}$ versus solvent LUMO energy. By any reasonable expectation, this plot is linear and provides strong evidence of a correlation between the LUMO energy and the coupling magnitude. This result demonstrates that the D / A mixing for **2** changes significantly as a function on the solvent's electronic structure and that the solvent / solute exchange interactions, β_{ij} , across the 10 Å cleft of **2** are reasonably constant for this group of solvents. The magnitude of $|V(\mathbf{2})|^2$, which is obtained from the experimental rate constants, represents a weighted average over all configurations of solvent molecules within the cleft. The linearity of the correlation in Figure 8.4 indicates that, in the majority of configurations, a single solvent molecule comprises the superexchange pathway ($n=1$). The slope of a linear regression fit of this data yields an average value of $|\beta_{ij}| = 210 \text{ cm}^{-1}$.

8.8 Discussion

A number of highly curved DBA molecules, employing electronically excited donors, exhibit greatly accelerated electron transfer rate constants in electron deficient aromatic and halogenated solvents. The fast rates in these solvents have been attributed to enhanced D* / A coupling involving low energy, unoccupied solvent orbitals. Low lying vacant orbitals support low energy D⁺S⁻A superexchange states, which enhance mixing between the D* and A sites. This scenario provides a reasonable explanation for the large and rather unusual solvent dependence of electron transfer rate constants in **2**. However, the solvent dependence of the *fcwds* also contributes to the observed rate variation. This dependence is evident from the behavior of **1** and **3**, which exhibit enhanced electron transfer rate constants in aromatic and

halogenated solvents. Because the linear covalent bridge in **1** and **3** mediates the electronic coupling, $|V|$ in these molecules is expected to be solvent independent. Accordingly, the solvent dependence of the rates for **1** and **3** arises from variation of the *fcwds*. A meaningful analysis of solvent dependent rates and couplings in **2** requires accurate estimates of the *fcwds*.

8.8.1 Characterizing the *fcwds*.

The electron transfer rates of **1** and **3** in non-aromatic solvents are, for the most part, in accord with the predictions of semi-classical rate constant models using continuum expressions for $\Delta_r G$ and λ_0 (Figure 8.1). Some deviations are evident and may arise from specific solute-solvent interactions. For example, the transfer rate constant for **1** in THTP is about half as large as predicted by the FCWDS calculation. By contrast, the transfer rate constant for **3** in THTP is in good agreement with the FCWDS prediction. The cyclobutenediester group in **3** is a much less potent electron acceptor than nitroethylene. The latter acceptor has been reported to form charge transfer complexes with good donors.³³ A specific interaction between nitroethylene and THTP, with sulfur acting as a weak donor, would serve to diminish the *fcwds* for D* to A electron transfer and could explain the large upward displacement of the THTP point for **1** from the regression line. Analogous interactions between the sulfurs in 1,3-dithiolane and nitroethylene may explain why this solvent, which has the largest n_D , yields the fastest transfer rate constants for **3**, but not for **1** and **2**.³⁴ Weak charge transfer interactions between nitroethylene and anisole or veratrole may be part of the reason that the calculated FCWDS for these two solvents fall well above the regression line for **1** but fall below the regression line for **3**. Automatic inclusion of specific D-solvent or A-solvent interactions is a potential advantage of

using the solvent dependent, experimental rate constants from one DBA molecule to gauge the solvent dependent $fcwds$ for a second DBA containing the same D and A groups.

The presence of identical D and A groups in two different molecules is not sufficient to ensure comparable $fcwds$ solvent dependence. Although identical D and A groups lead to comparable λ_v and $h\nu$ parameters, the driving force and solvent reorganization energy vary with bridge length and topology. The continuum expression for $\Delta_rG + \lambda_o$ and for λ_o (the two solvent dependent terms that appear in the exponent of eq 8.4) scale the solvent response by the same geometric factor, $\left(\frac{1}{r_A} + \frac{1}{r_D} - \frac{2}{R_{CC}}\right)$. If the charge transfer distances, R_{CC} , for two different DBA molecules are such that their geometric factors are very similar, then the two sphere continuum models predict that the solvent dependence of λ_o , of $\Delta_rG + \lambda_o$, and of the FCWDS will be similar for both molecules. The small (14%) difference in the geometric factors for **1**, 0.32, and **2**, 0.28, produces a two-fold difference in their FCWDS. This difference also generates dissimilar variations of the FCWDS with solvent, most dramatically in solvents with small static, ϵ_s , and optical, n_D^2 , dielectric constants. This is evident in the FCWDS(**2**)/FCWDS(**1**) ratio for ethyl ether (Figure 8.2, left most diamond) which is two-fold larger than for all the other solvents. For the majority of solvents, the FCWDS change comparably for **1** and **2**. Overall, the analysis indicates that the use of the average FCWDS ratio to extract $|V|$ from the rate constant ratios contributes about a $\pm 15\%$ variation in the estimated couplings and represents a relatively small source of error.

The continuum expressions used here for λ_o and Δ_rG (eqs 8.1, 8.2) apply to the case of spherical donor and acceptor ions, with no intervening bridge. The presence of a bridge and the spatial arrangement of the donor, bridge and acceptor groups influence the magnitude of λ_o and

$\Delta_r G$, principally through variation of the geometric factor. Barzykin and Tachiya³⁵ obtained a continuum expression for λ_0 in a system composed of contacting donor, bridge, and acceptor spheres. They explored the dependence of the geometric factor on the angle defined by the centers of the three spheres. For angles between 180° and 90° , *i.e.*, from a linear to a right angle DBA geometry, the calculated geometric factor amounted to 94% of the two-sphere value. Between 90° and 60° , the geometric factor decreased to 90% of the two-sphere value. Despite the different DBA topologies of **1** and **2**, the Barzykin-Tachiya result suggests that the appropriate geometric factors for both molecules yield λ_0 values that are similar to the two sphere model result and that the topology difference does not produce significant differences in the *fcwds* solvent dependence for the two molecules. The details of the DBA molecule's shape and the D/A ion charge distribution can be included in calculations of λ_0 using finite-difference Poisson-Boltzmann (FDPB) methods.²⁰ The influence of bridge structure on λ_0 was previously investigated using two C-shaped and two linear DBA molecules.⁵ Assuming the FDPB results to be "correct", the two sphere model was found to significantly underestimate λ_0 in C-shaped molecules where R_{CC} is less than or equal to the sum of the D and A spherical radii. The FDPB method's realistic treatment of the donor and acceptor shapes leaves more "continuum solvent" directly between the D and A groups and generates a substantially larger λ_0 than the two-sphere expression. For molecules in which R_{CC} is at least a few Å larger than the sum of the D and A radii, the two-sphere model and the FDPB method generated very similar scaling of λ_0 with R_{CC} , independent of bridge shape. The FDPB results confirm, at least qualitatively, the conclusions reached by Barzykin and Tachiya³⁵. For a given D / A pair, R_{CC} is the dominant term controlling the geometric factor and λ_0 ; bridge topology provides only a minor perturbation. To the extent

that continuum models reproduce the energetics of solvent-solute interaction, the *fcwds* for the linear and C-shaped DBA molecules **1** and **2** should display similar solvent dependence.

The above arguments imply that the *fcwds* ratios for **3** and **1** should vary little with solvent, however the experimental rate constant ratio $k_{\text{et}}(\mathbf{3}) / k_{\text{et}}(\mathbf{1})$ varies four fold in the fourteen solvents. Interestingly, of the five solvents with rate ratios greater than 0.01, veratrole, *o*-dichlorobenzene, anisole, 1,3-dithiolane, CHCl_3 , three are likely to experience specific solvent interactions with the nitroethylene acceptor in **1** but not with the acceptor in **3**. Such interactions reduce the transfer rate constant of **1** and generate a larger value of the rate ratio. A fourth solvent, CHCl_3 , produces an anomalously large rate constant for **3** that may arise from hydrogen bonding interactions involving the acceptor.³⁶ Ignoring these five solvents, the rate ratio changes by only two-fold and $|V(\mathbf{3})|$ varies from 4.5 to 6.8 cm^{-1} with an average of $5.6 \pm 1.0 \text{ cm}^{-1}$.³⁷ This value is indistinguishable from the value of 4.9 cm^{-1} derived from a linear fit of the rate constants in Figure 8.1B. For **3**, D / A coupling is determined equally well from rate or rate ratio analyses. At least a portion of the remaining two-fold variation of the **3**:**1** rate ratio may arise from the presence of different acceptors in **1** and **3**. More sophisticated continuum and molecular solvation models define an *effective* solute cavity radius that is a function of the solvent size.^{7,22,38} The effect of different solvent radii may be mimicked in the simple continuum model by increasing the acceptor radius of **1** and **3** by a constant amount. The hard sphere radii of ethyl ether and THF are $\sim 0.3 \text{ \AA}$ larger than those of CH_2Cl_2 and MeCN.³⁹ Increasing the acceptor radius of both **1** and **3** by 0.3 \AA increases the calculated $\text{FCWDS}(\mathbf{3}) / \text{FCWDS}(\mathbf{1})$ ratio by $\sim 30\%$. This increase is in the same direction, but not as sizeable, as the two fold larger $k_{\text{et}}(\mathbf{3}) / k_{\text{et}}(\mathbf{1})$ ratio found in ethyl ether and THF compared to CH_2Cl_2 and MeCN. Thus, more elaborate continuum

models may be required to obtain the most accurate values of $|V|$ when analyzing rate constant ratios from molecules with different D or A groups.

8.8.2 The Solvent Dependence of $|V|$

The solvent dependence of the $k_{eT}(2) / k_{eT}(1)$ ratios and the $k_{eT}(3) / k_{eT}(1)$ ratios are dramatically different. Because **1** and **2** possess the same D and A groups, specific solvent effects should cause negligible differences in the *fcwds* of the two molecules. Nor should the different bridge structures cause significant differences in the *fcwds* of **1** and **2**. Rather, the ten-fold variation of the **2:1** rate constant ratios arises primarily from solvent dependent electronic coupling in **2**. As the non-adiabatic rate constants are proportional to $|V|^2$, the solvent dependence of the extracted coupling varies less dramatically than the rate constants; by only 3.2-fold for **2** across this set of solvents. Although the following discussion will concern $|V|$, it is important to remember that the kinetically relevant quantity is $|V|^2$.

At least two origins of the solvent dependent electronic coupling in **2** are possible. Solvent may alter the structure of the D, A, or bridge, thus modulating coupling mediated by the bridge. Alternatively, solvent molecules may constitute an independent D / A coupling pathway. Since the same donor and acceptor groups are present in both **1** and **2**, solvent perturbation of D or A structure should appear in both molecules. This might alter the magnitude of bridge-mediated coupling, but the change ought to scale comparably in both molecules and be unobservable in the rate ratio. Solvents might induce changes in bridge structure, *e.g.*, R_{CC} in the clamp might vary with solvent.⁴⁰ However, it would be difficult to explain the correlation between coupling magnitude and solvent LUMO energy (Figure 8.4) in terms of solvent induced changes in bridge structure.^{40a} As suggested previously, the more straightforward explanation

for the solvent dependent coupling in **2** is the existence of D/A coupling pathways involving a solvent molecule, or molecules, within the cleft. The magnitude of solvent mediated coupling depends on many factors: the energy and spatial distribution of solvent orbitals, solvent size, placement, orientation, and the details of the spatial overlap between the donor and solvent and between the solvent and acceptor. Clearly, the coupling is modulated by solvent motion within, as well as in and out of, the cleft. The coupling magnitudes determined in these analyses are averages over active solvent configurations. The correlation between solvent LUMO energy and coupling magnitude (Figure 8.4) provides compelling evidence that unoccupied orbitals of the solvent comprise the dominant coupling pathway for DBA **2** in all of the solvents. The average value of $|\beta_{ij}|$, 210 cm^{-1} , is five to ten times smaller than the exchange interaction determined for aromatic contact ion pairs.⁴¹ Contact ion pairs are more tightly associated than neutral solvent/donor or solvent/acceptor pairs, and the interaction should decrease steeply with increasing separation. These considerations suggest that the derived value of β_{ij} is reasonable for neutral molecules in van der Waals contact.

It is worth noting that use of the average FCWDS ratio to determine $|V(\mathbf{2})|$ (Table 8.2) reduces the apparent solvent dependence of the coupling. Among the non-aromatic solvents, the trend in Figure 8.2 (filled diamonds) is to smaller values of the FCWDS ratio in the solvents with the largest $k_{eT}(\mathbf{1})$. Using the predicted FCWDS ratio for each solvent (in an equation analogous to eq 5) reduces the coupling in ethyl ether by 0.2 cm^{-1} ($|V(\mathbf{2})| = 0.7 \text{ cm}^{-1}$), increases the coupling in CH_2Br_2 by 0.4 cm^{-1} ($|V(\mathbf{2})| = 3.3 \text{ cm}^{-1}$) and alters the couplings in the other non-aromatic solvents by less than 0.1 cm^{-1} . Thus, $|V|^2$ for **2** in CH_2Br_2 is up to 22 times larger than in ethyl ether and is a primary source of the 240 fold difference of the rate constants in these two solvents.

8.9 Conclusion

Solvents strongly influence rate constants of charge separation reactions. In the majority of supramolecular compounds investigated to date, the origin of these rate variations is the solvent dependence of the *fcwds*. For highly curved structures, donor - acceptor electronic coupling can arise from solvent inclusive pathways. In such systems, D / A coupling may be solvent dependent and factoring rate variations into contributions from $|V|^2$ and the *fcwds* is non-trivial. In an effort to identify simple means to effect this separation, photoinduced electron transfer rate constants were determined for three donor-bridge-acceptor structures in a series of fourteen different solvents. Two of the three structures contained a linear bridge. The rate constants from these linear structures were used (1) to identify and characterize solvent effects on the FCWDS, (2) to evaluate the utility of simple dielectric continuum models of solvation and (3) to provide a ‘measure’ of the FCWDS solvent dependence for a C-shaped molecule in which D/A coupling is solvent mediated. The solvent dependence of the electron transfer rate constants in the C-shaped molecule was dramatically different from those of the two linear molecules. Using FCWDS estimates derived from the linear structures, the contribution of $|V|^2$ to transfer rates in the C-shaped DBA was found to vary by more than one order of magnitude among solvents and to decrease as the energy of the solvent LUMO increases. The correlation with the solvent molecule’s LUMO energy demonstrates that unoccupied orbitals of the solvent can be active components of coupling pathways linking excited donor and acceptor groups.

8.10 Acknowledgments

We would like to thank Prof. K. Jordan (Pittsburgh) for informative discussions. Financial support from the National Science Foundation is also acknowledged.

8.11 References

-
- (1) Jortner, J. *J. Chem. Phys.* **1976**, *64*, 4860.
- (2) a) Newton, M. D.; *Chem. Rev.* **1991**, *91*, 767. b) Betts, J. N.; Beratan, D. N.; Onuchic, J. N. *J. Am. Chem. Soc.* **1992**, *114*, 4043. c) Gray, H. B.; Winkler, J. R. *J. Electroanal.* **1997**, *438*, 43. d) Paddon-Row, M. N. *Acc. Chem. Res.* **1994**, *27*, 18.
- (3) a) Kumar, K.; Lin, Z.; Waldeck, D. H.; Zimmt, M. B. *J. Am. Chem. Soc.* **1996** *118*, 243; b) Gu, Y.; Kumar, K.; Lin, Z.; Read, I.; Zimmt, M. B.; Waldeck, D. H. *J. Photochem and Photobiol. A.* **1997**, *105*, 189. c) Kaplan, R. W.; Napper, A. M.; Waldeck, D. H.; Zimmt, M. B. *J. Am. Chem. Soc.* **2000**, *122*, 12039.
- (4) a) Read, I.; Napper, A.; Zimmt, M. B.; Waldeck, D. H. *J. Phys. Chem. A.*, **2000**, *104*, 9385; b) Read, I.; Napper, A.; Kaplan, R.; Zimmt, M. B.; Waldeck, D. H., *J. Am. Chem. Soc.* **1999**, *121*, 10976.
- (5) Kumar, K.; Kurnikov, I.; Beratan, D.; Waldeck, D. H.; Zimmt, M. B. *J. Phys. Chem. A* **1998**, *102*, 5529.
- (6) a) Loken, N. R.; Paddon-Row, M. N.; Koeberg, M.; Verhoeven, J. W. *J. Am. Chem. Soc.* **2000**, *122*, 5075. b) Lawson, J. M.; Paddon-Row, M. N.; Schuddeboom, W.; Warman, J.; Clayton, A. H. A.; Ghiggino, K. P. *J. Phys. Chem.* **1993**, *97*, 13099.
- (7) a) Matyushov, D. V.; Voth, G. A. *J. Chem. Phys.* **1999**, *111*, 3630. b) Matyushov, D. V. *Chem. Phys.* **1996**, *211*, 46. c) Matyushov, D. V. *Mol. Phys.* **1993**, *79*, 795.
- (8) Evidence for a temperature dependence of solvent mediated coupling C-shaped DBA molecules has been found. Napper, A. M.; Read, I.; Waldeck, D. H.; Kaplan, R. W.; Zimmt, M. B. *J. Phys. Chem. A.*; **2002**; *106*(18); 4784-4793.
- (9) A similar analysis of solvent effects on electron transfer rates in highly curved molecules was previously reported. See Ref. 6a.
- (10) Zeng, Z.; Zimmt, M. B. *J. Am. Chem. Soc.* **1991**, *113*, 5107.
- (11) Details concerning the preparation of compounds **1** to **4** have been reported elsewhere. a) Kumar, K.; Tepper, R. J.; Zeng, Y.; Zimmt, M. B. *J. Org. Chem.* **1995**, *60*, 4051. b) Han, H. Ph.D. Thesis, Brown University, 1998. c) Kaplan, R. Ph.D. Thesis, Brown University, 2001.
- (12) Charge transfer distances determined using the Generalized Mulliken Hush Method. See Ref. 13.
- (13) a) Cave, R. J.; Newton, M. D. *J. Chem. Phys.* **1997**, *106*, 9213. b) Cave, R. J.; Newton, M. D. *Chem. Phys. Lett.* **1996**, *249*, 15.

(14) This conclusion is supported by prior determinations of $|V|$ for **1** in three of these solvents; ether, acetonitrile and benzonitrile. See reference 3c.

(15) a) Chen, P.; Mecklenburg, S. L.; Meyer, T. J. *J. Phys. Chem.* **1993**, *97*, 13126. b) Heitele, H.; Poellinger, F.; Weeren, S.; Michel-Beyerle, M. E. *Chem. Phys.* **1990**, *143*, 325.

(16) Vath, P.; Zimmt, M. B.; Matyushov, D. V.; Voth, G. A. *J. Phys. Chem. B* **1999**, *103*, 9130.

(17) Molecular solvation models developed by Matyushov incorporate solvent density contributions and reproduce FCWDS variations with temperature accurately. See Ref. 7,16.

(18) For the nitroethylene acceptor, $E_{\text{RED}} = -1.29$ V. For the cyclobutenediester, $E_{\text{RED}} = -1.62$ V. The donor has $E_{\text{OX}} = 0.87$ V. All potentials were measured relative to the Ag/AgCl electrode.

(19) E_{00} for the S_1 state of the donor varies between 2.98 and 3.04 eV in these solvents. See Kumar, K. Ph.D. Thesis, Brown University, 1995.

(20) a) Sharp, K.; Honig, B. *Annu. Rev. Biophys. Biophys. Chem.* **1990**, *19*, 301. b) Sitkoff, D.; Sharp, K. A.; Honig, B. *J. Phys. Chem.* **1994**, *98*, 1978. c) Zhang, L. Y.; Frieser, R. A. *J. Phys. Chem.* **1995**, *99*, 16479.

(21) a) Reynolds, L.; Gardecki, J. A.; Frankland, S. J. V.; Horng, M. L.; Maroncelli, M. *J. Phys. Chem.* **1996**, *100*, 10337. b) Khajepour, Mazdak; Kauffman, John F. *J. Phys. Chem. A* **2000**, *104*, 9512.

(22) a) Jeon, J.; Kim, H. J. *J. Phys. Chem. A* **2000**, *104*, 9812. b) Ladanyi, B. M.; Stratt, R. M. *J. Phys. Chem.* **1996**, *100*, 1266. c) Perng, B.-C.; Newton, M. D.; Raineri, F. O.; Friedman, H. L. *J. Chem. Phys.* **1996**, *104*, 7153, 7177.

(23) As noted above, the coupling across the bridge of **1** is presumed to be solvent independent. Thus, only the FCWDS vary with solvent.

(24) Including all solvents, the calculated FCWDS ratio is 0.085 ± 0.034 .

(25) For these calculations, $|V|(\mathbf{1}) = 19 \text{ cm}^{-1}$ from a prior evaluation was used. See Ref. 3c.

(26) The $|V|(\mathbf{3})$ values (in cm^{-1}) obtained using a constant FCWDS ratio are: Et₂O 6.7, MeCN 4.5, THF 6.2, CHCl₃ 7.2, CH₂Cl₂ 4.6, CH₂ClBr 4.5, THTP 6.8, CH₂Br₂ 4.8. For the aromatic solvents, the values are Anisole 7.7, Veratrole 8.8, PhCH₂CN 6.9, PhCN 5.5, o-dichlorobenzene 8.4.

(27) A prior analysis of $k_{\text{eT}}(T)$ data for **3** in acetonitrile, dimethylacetamide and benzonitrile yielded $|V|(\mathbf{3}) = 2.7 \pm 0.8 \text{ cm}^{-1.5}$. This value is two-fold smaller than the average values derived using the continuum FCWDS. It should be noted that the ratio calculations

(FCWDS(**3**)/FCWDS(**1**)) are very sensitive to the values of $\Delta_r G$ in the reference solvent (acetonitrile). The above calculations were based on $\Delta_r G_{\text{ref}}(\mathbf{3}) = -0.56$ eV and $\Delta_r G_{\text{ref}}(\mathbf{1}) = -0.86$ eV. Lowering the former and raising the latter value by 0.03 eV yields an average value of $|V|(\mathbf{3}) = 4.1 \text{ cm}^{-1}$ for the non-aromatic solvents. Errors in $\Delta_r G_{\text{ref}}$ of this magnitude are certainly possible given the presence of electrolyte in the redox measurements.

(28) With the exception of CH_2Br_2 , the $|V(\mathbf{2})|$ determined in this analysis are a factor of 2.5 smaller than values derived from analyses of $k_{\text{eT}}(T)$ data.^{3c} $k_{\text{eT}}(T)$ data was analyzed for **2** in MeCN, CH_2Cl_2 , PhCH_2CN , CHCl_3 , PhCN and CH_2Br_2 . The values of $|V(\mathbf{2})|$ in CH_2Br_2 was 4.2 fold larger than that obtained in the present analysis. At this point, it is not possible to determine if the larger disparity arises from errors in the parameters used to determine FCWDS(T) or from a stronger temperature dependence of $|V|$ in this solvent.

(29) McConnell, H. M. *J. Chem. Phys.* **1961**, *35*, 508.

(30) Solvent refractive index may also contribute to Δ as the solvent electronic polarizability also solvates the superexchange state.

(31) The calculations were performed using TITAN, Ver. 1.0.5. Wavefunction and Schroedinger, Inc., 1999.

(32) Discussions of the origin of this offset may be found in the following citations. a) Chen, D.; Gallup, G.A. *J. Chem. Phys.* **1990**, *93*, 8893. b) Burrow, P.D.; Howard, A.E.; Johnston, A. R.; Jordan, K.D. *J. Phys. Chem.* **1992**, *96*, 7570. c) Staley, S.W.; Strnad, J.T. *J. Phys. Chem.* **1994**, *98*, 116.

(33) a) Kushibiki, N.; Ogasawara, M.; Yoshida, H. *J. Polym. Sci., Polym. Chem. Ed.* **1979**, *17*, 1227. b) Irie, M.; Tomimoto, S.; Hayashi, K. *J. Polym. Sci., Part B* **1972**, *10*, 699.

(34) The absence of literature dielectric constant data for 1,3-dithiolane prevents calculation of the FCWDS in this solvent.

(35) Barzykin, A. V.; Tachiya, M. *Chem. Phys. Lett.* **1998**, *285*, 150.

(36) Hydrogen bonding strongly accelerates charge separation rate constants of **3** and other linear DBA molecules containing the same D and A. Hydrogen bonding may arise from HCCl_3 ,^{36a,b} from ethanol present as stabilizer or from HCl produced when the stabilizer is removed. a) Phutela, R. C.; Arora, P. S.; Singh, P. P. *Z. Phys. Chem. (Leipzig)* **1976**, *257*, 945. b) Langner, R.; Zundel, G.; Brzezinski, B. *Spectrochim. Acta, Part A* **1999**, *55A*, 35.

(37) Including *o*-dichlorobenzene, the average value of $|V(\mathbf{3})|$ in the “non-interacting” solvents is $5.9 \pm 1.4 \text{ cm}^{-1}$.

(38) a) Basilvesky, M. V.; Rostov, I. V.; Newton, M. D. *Chem. Phys.* **1998**, *232*, 189. b) Newton, M. D.; Basilevsky, M. V.; Rostov, I. V. *Chem. Phys.* **1998**, *232*, 201.

(39) a) Marcus, Y. *Ion Solvation*, John-Wiley and Sons, Chichester, 1985. Table 6.4. b) Schmid, R.; Matyushov, D. V. *J. Phys. Chem.* **1995**, *99*, 2393.

(40) a) Calculations by Paddon-Row and coworkers^{40b} suggest that pyramidalization of reduced ethylene acceptors reduces the charge transfer separation, R_{CC} , subsequent to electron transfer in C-shaped molecules in a vacuum. The reduction of R_{CC} in **2** could vary with solvent polarity and influence its electron transfer kinetics. The extent of this Coulomb driven reduction of the D / A separation, if it occurs in solution, should be largest in solvents with the smallest dielectric constants. The observed variation of $|V(\mathbf{2})|$ is not correlated with dielectric constant. b) Shephard, M. J.; Paddon-Row, M. N. *J. Phys. Chem. A* **2000**, *104*, 11628.

(41) Gould, I. R.; Young, R. H.; Mueller, L. J.; Albrecht, A. C.; Farid, S. *J. Am. Chem.Soc.* **1994**, *116*, 3147.

Chapter 9. Electron Transfer Reactions of C-shaped Molecules in Alkylated Aromatic Solvents: Evidence that the Effective Electronic Coupling Magnitude Is Temperature-Dependent

9.1 Introduction

The requirements for fast electron-transfer processes are favorable Franck-Condon factors and significant electronic coupling between the donor and acceptor groups. Electronic coupling magnitudes in electron-transfer systems vary from thousands of wavenumbers, e.g., for contact ion pairs,¹ to hundredths of wavenumbers for donor and acceptor groups separated by tens of angstroms, e.g., in proteins and glasses.² Different methods are used to determine coupling magnitudes from experimental data. Systems with moderate couplings (10 – 200 cm⁻¹) often exhibit charge transfer (CT) absorption and/or CT emission bands. Analysis of these bands' transition intensities provides values of the donor-acceptor electronic coupling.^{1,3} For systems with smaller donor-acceptor couplings, CT transitions are usually too weak to detect and analyze. The electronic coupling magnitudes in “weakly coupled” systems may be determined through analysis of electron-transfer rate constants, once the appropriate Franck-Condon factors have been determined or estimated. Despite the indirect nature of this approach, a number of such investigations have successfully identified relationships between the electronic coupling magnitude and the underlying molecular structure and/or properties of the medium between the donor and acceptor groups.^{4,§}

[§] Reproduced with permission from Napper, A. M.; Read, I.; Waldeck, D. H.; Kaplan, R. W.; Zimmt, M. B.; *J. Phys. Chem. A.*; **2002**; 106(18); 4784-4793. Copyright 2002 American Chemical Society

It has long been appreciated that the structure of the medium between the donor and acceptor groups influences the rates of electron transfer. Less widely recognized is the important role that dynamics can exert. For many electron transfer reactions, the structure of the medium through which the electron tunnels is dynamic. Theoretical investigations have indicated that intervening medium motions, including vibrations, librations, conformational changes, and diffusion of mobile components, can significantly modulate donor-acceptor electronic coupling magnitudes.⁵ The size of the coupling magnitude fluctuations depends on the amplitudes of the medium motions and the details of the electronic coupling pathways. A dramatic manifestation of the influence of dynamics is “conformational gating”,⁶ which has been observed for protein and intramolecular electron transfer reactions. This phenomenon occurs in long-range electron transfer systems when the electron transfer rates for a subset of the thermally accessible conformations is fast relative to the transfer rates in the most populated conformations. The observed transfer rate is influenced by the kinetics of interconversion among conformations. Larger coupling magnitudes in the “fast” conformations can contribute to the “gating” effect. The variation of coupling magnitude with conformation constitutes a break down of the Condon approximation.

It is difficult to quantify the influence of structural fluctuations on coupling magnitudes in electron transfer systems with small electronic couplings because electron transfer rates, not coupling magnitudes, are the experimental observables. Extraction of the coupling magnitude from experimental rate data requires reliable evaluation of activation barriers, nuclear factors, and solvation. Generally, it is difficult to ascertain the existence and/or magnitude of coupling fluctuations from such an analysis. In those intramolecular electron transfer systems where a structurally rigid bridge connects the donor and acceptor, structural distortions of the bridge and

coupling magnitude fluctuations are likely small.⁷ For intra- and intermolecular electron-transfer systems in which the structure of the intervening medium fluctuates significantly, the donor-acceptor electronic coupling may also fluctuate significantly. Hence, the electronic coupling, extracted from rate constant analysis, represents a (dynamically) averaged electronic coupling matrix element, or an “effective” coupling magnitude. As the majority of investigations are not posed to investigate these effects, little evidence for or against characterization of medium induced fluctuations of the electronic coupling is available.

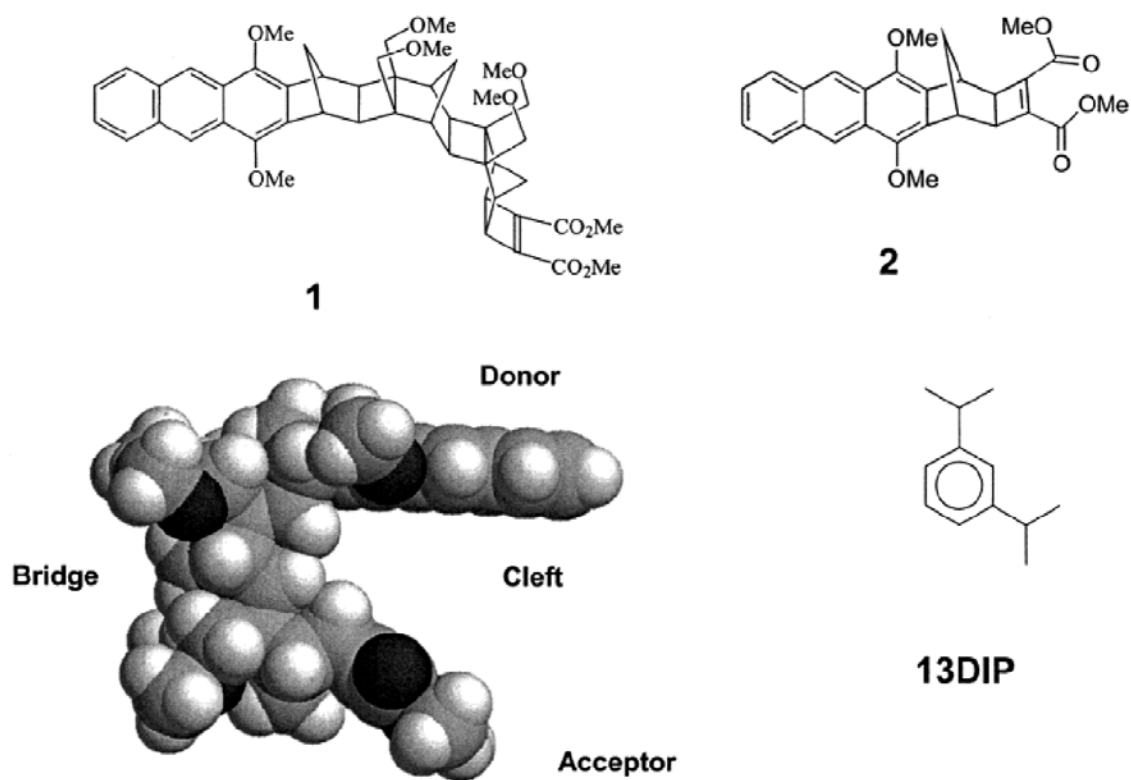


Chart 9.1 Molecular Structures of the Electron Transfer Molecules 1, 2, and the Solvent 1,3-Diisopropylbenzene.

Recent investigations of some highly curved donor-bridge-acceptor molecules indicate that their electronic coupling may derive from “pathways” constituted by solvent molecules.⁸ The coupling magnitudes in these systems are influenced by the solvent molecules’ electronic

structure, size, shape, and the size of the solvent accessible gap between the donor and acceptor groups.⁸ Calculations suggest that the magnitude and sign of the electronic coupling mediated by solvent molecules varies significantly with the latter's placement and orientation relative to the donor and acceptor. Consequently, the relatively rapid and unconstrained motions of the solvent molecules should give rise to a fluctuating electronic coupling magnitude.^{5e} Additionally, environmental variables that alter the solvent dynamics and/or accessible conformations, e.g., pressure⁹ or temperature, may influence the “effective” value of the electronic coupling that is determined through analysis of rate constant data. As is true for systems exhibiting conformational gating,⁶ fluctuation of the donor-acceptor coupling associated with solvent motion constitutes a breakdown of the Condon approximation. Previous investigations have provided some evidence that solvent-mediated electronic coupling magnitudes are temperature dependent.¹⁰ This investigation reports data that indicate a strong temperature dependence of the solvent-mediated, donor-acceptor electronic coupling for a C-shaped molecule, **1** (Chart 9.1). The evidence of temperature-dependent coupling is particularly compelling for extensively alkylated aromatic solvents.

Compound **1** (see Chart 9.1) juxtaposes a dimethoxyanthracene donor and a cyclobutene diester acceptor on opposite sides of a 7 Å cleft that is accessible to solvent molecules. The electron transfer dynamics of **1** have been investigated in highly polar,^{8b} alkylated-aromatic,^{8c,10} and halo-aromatic solvents.¹¹ The electronic coupling magnitude determined for **1** in each solvent depends on the solvent's electronic energy levels and its three-dimensional structure.^{8,10,11} The electron-transfer reactions of **1** in alkylated benzene solvents afford an unusual opportunity for in-depth investigation of the factors that control rate constants. The reaction free energy, $\Delta_r G$, is almost zero for electron transfer from the lowest energy, singlet-

excited state (S_1) of the anthracene donor to the acceptor. An equilibrium between the anthracene S_1 excited state and the charge separated state influences the fluorescence dynamics and allows determination of all three electron-transfer rate constants after the $S_0 \rightarrow S_1$ excitation:^{8c} the charge separation, electron-transfer rate constant for conversion of the anthracene S_1 state to the charge separated state, k_{for} ; the charge recombination rate constant for conversion of the charge separated state back to the anthracene S_1 state, k_{back} ; and the charge recombination rate constant that converts the charge separated state to the anthracene S_0 state, k_{rec} .¹² The free energy gap between the anthracene S_1 excited state and the charge separated state is evaluated experimentally from the first two of these rate constants.

The temperature dependence of the charge separation and charge recombination rate constants of **1** vary dramatically depending on the structure of the alkyl benzene solvent. In benzene, the charge separation rate constant, k_{for} , decreases and the charge recombination rate constant, k_{back} , increases as the temperature is increased. By contrast, k_{for} and k_{back} in 1,3,5-triisopropylbenzene both increase as the temperature increases. The rate constants k_{for} and k_{back} for **1** in 1,3-diisopropylbenzene exhibit more complex behavior, first increasing and then decreasing as the temperature is raised. The nonmonotonic temperature dependence of k_{for} and k_{back} , along with the availability of $\Delta_r G(T)$ data, provide significant constraints on kinetic models used to interpret these rate data. In particular, two possible explanations for the observed rate constant behavior of **1** in 1,3-diisopropylbenzene can be identified. First, the temperature dependence can be explained by a decrease of the effective electronic coupling magnitude with increasing temperature. Second, the temperature dependence could result from a small and temperature-independent value of the solvent reorganization energy, which, in conjunction with the temperature dependence of $\Delta_r G$, moves the charge separation and recombination reactions,

k_{for} and k_{back} , between the Marcus normal and inverted regions. Both interpretations can quantitatively reproduce the observed data for **1** in 1,3-diisopropylbenzene and are consistent with the models used to predict electron transfer rate constants. As discussed later in the manuscript, the combination of these data with earlier data in alkylbenzene solvents argues strongly for the first explanation, a temperature dependence of the electronic coupling magnitude.

This manuscript describes the determination and analysis of the electron-transfer rate constant for **1** in 1,3-diisopropylbenzene solvent. Data collection, rate constant determinations, and determination of the reaction free energy are described in the next section. The two explanations for the temperature dependence of the rate constants are developed in the third section. They differ significantly in the magnitude and temperature dependence of the solvent reorganization energy, $\lambda_s(T)$. The fourth section describes the evidence for and against the two explanations and discusses the implications of these findings for solvent and temperature-dependent rate constants observed earlier. Although it is not possible to reject unambiguously either explanation, the explanation based on a temperature dependence of the effective electronic coupling magnitude is more consistent with prior experimental and theoretical results.

9.2 Data, Rate Constant, and Δ_rG Determinations

The preparation of **1** was reported elsewhere.¹³ Solutions of **1** were prepared with an optical density of ca. 0.05 at the laser excitation wavelength, 375 nm. The solvent 1,3-diisopropylbenzene (98%) was purchased from Aldrich. The solvent was dried with anhydrous magnesium sulfate, filtered, and then fractionally distilled using a vigreux column. The purified fraction was used immediately to prepare the sample. Each sample solution was freeze-pump-

thawed a minimum of three times. The samples were back-filled with argon to reduce solvent evaporation at the higher temperatures.

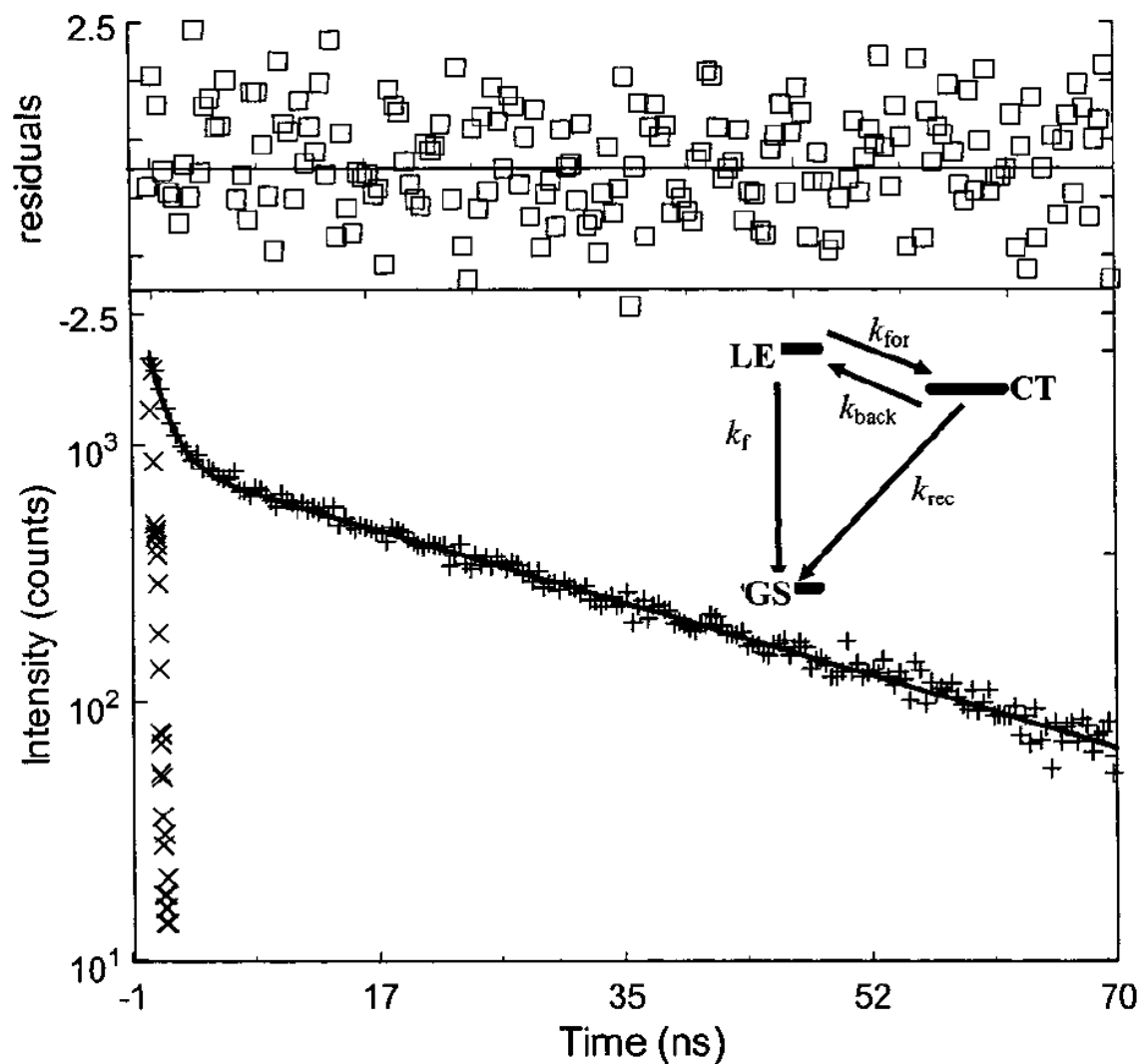


Figure 9.1 Fluorescence decay for **1** in 1,3-diisopropylbenzene at 290 K and the best fit to the data (solid line hidden by the raw data). The impulse response function (\times) and the residuals (\square , at top) are also shown. The fitted curve gives rate constants of 814 ps (68%), 17.7 ns (32%), and a χ^2 of 1.08. The inset shows an energy level diagram for the kinetics.

Excitation of the sample was performed at 375 nm by the frequency-doubled cavity-dumped output of a Coherent CR-599-01 dye laser using LDS750 (Exciton) dye, which was pumped by a mode-locked Coherent Antares Nd:YAG laser. The dye laser pulse train had a

repetition rate of ca. 300 kHz. Pulse energies were kept below 1 nJ, and the count rates were kept below 3 kHz. All fluorescence measurements were made at the magic angle. Other specifics of the apparatus have been reported elsewhere.¹⁴ Instrument response functions were measured using a sample of colloidal BaSO₄ in glycerol. Fluorescence decays were fit to a sum of two exponentials (the decay law was convolved with the measured instrument function) using the Marquardt-Levenberg nonlinear least squares algorithm. Figure 9.1 shows a fluorescence decay for **1** in 1,3-diisopropylbenzene at 290 K, the calculated best-fit, biexponential decay curve, the impulse response, and the fit residuals. For temperatures above 260 K, the sample cuvette was placed in an aluminum block whose temperature was controlled by a NESLAB RTE-110 chiller. Temperatures were measured using a type-K thermocouple (Fisher-Scientific), accurate to within 0.1 °C. Slush baths were used for the lower temperature points: 247 K (*o*-xylene/liquid N₂), 240 K (chlorobenzene/liquid N₂), 235 K (acetonitrile/liquid N₂), and 218 K (chloroform/liquid N₂). The slush bath temperatures varied by ±2 K from the stated temperature.

9.2.1 Kinetic and Thermodynamic Analyses.

Photoexcitation of the anthracene donor moiety creates a locally excited state (S₁ or LE) whose energy is similar to that of the charge separated state in 1,3-diisopropylbenzene solvent. The inset to Figure 9.1 shows the kinetic scheme that is used to describe the kinetics following formation of the locally excited state by the light pulse. There are four unknown rate constants. The intrinsic decay rate constant of the locally excited state, k_f , is obtained from the LE decay kinetics of an analogue to molecule **1** that has no electron acceptor. Fitting the time-resolved fluorescence decay of **1**'s LE state to a biexponential form provides three additional parameters: a fast rate constant, a slow rate constant, and the amplitude fraction of the fast decay. The

electron-transfer rate constants k_{for} , k_{back} , and k_{rec} are calculated using the fit parameters that reproduce the time-resolved fluorescence decay.¹⁵ The Gibbs free energy of the charge separation reaction is determined at each temperature from the ratio of the forward and back rate constant, (eq 9.1)

$$\Delta_r G = -RT \ln(k_{\text{for}}/k_{\text{back}}) \quad (9.1)$$

The availability of experimental $\Delta_r G$, at each temperature, and of the internal reorganization energy parameters (vide infra) make it feasible to interpret the temperature-dependent rate constant data in terms of only two parameters: the solvent reorganization energy and the donor-acceptor electronic coupling.

9.3 Rate Constant Temperature Dependence and Possible Explanations

Figure 9.2 summarizes the temperature-dependent rate constant and $\Delta_r G$ data. Panel A displays the temperature dependence of the charge separation and charge recombination rate constants for molecule **1** in 1,3-diisopropylbenzene. Starting at 218 K, 8° above the solvent's melting point, both the charge separation and charge recombination rate constants increase upon increasing the temperature. The charge separation rate constant, k_{for} , reaches a maximum near 270 K and then decreases sharply at higher temperatures, dropping more than 20-fold by 356 K. The charge recombination rate constant, k_{back} , increases up to 320 K and then decreases 2-fold by 356 K. The maximum rate constants for the charge separation and charge recombination reactions are nearly equal, $\sim 9 \times 10^8 \text{ s}^{-1}$. Panel B presents the experimental $\Delta_r G$ for the charge separation reaction as a function of temperature. The free energy of charge separation varies nearly linearly from 280 to 350 K. However, as the temperature approaches the freezing point of the solvent, $\Delta_r G$ changes less steeply with temperature.

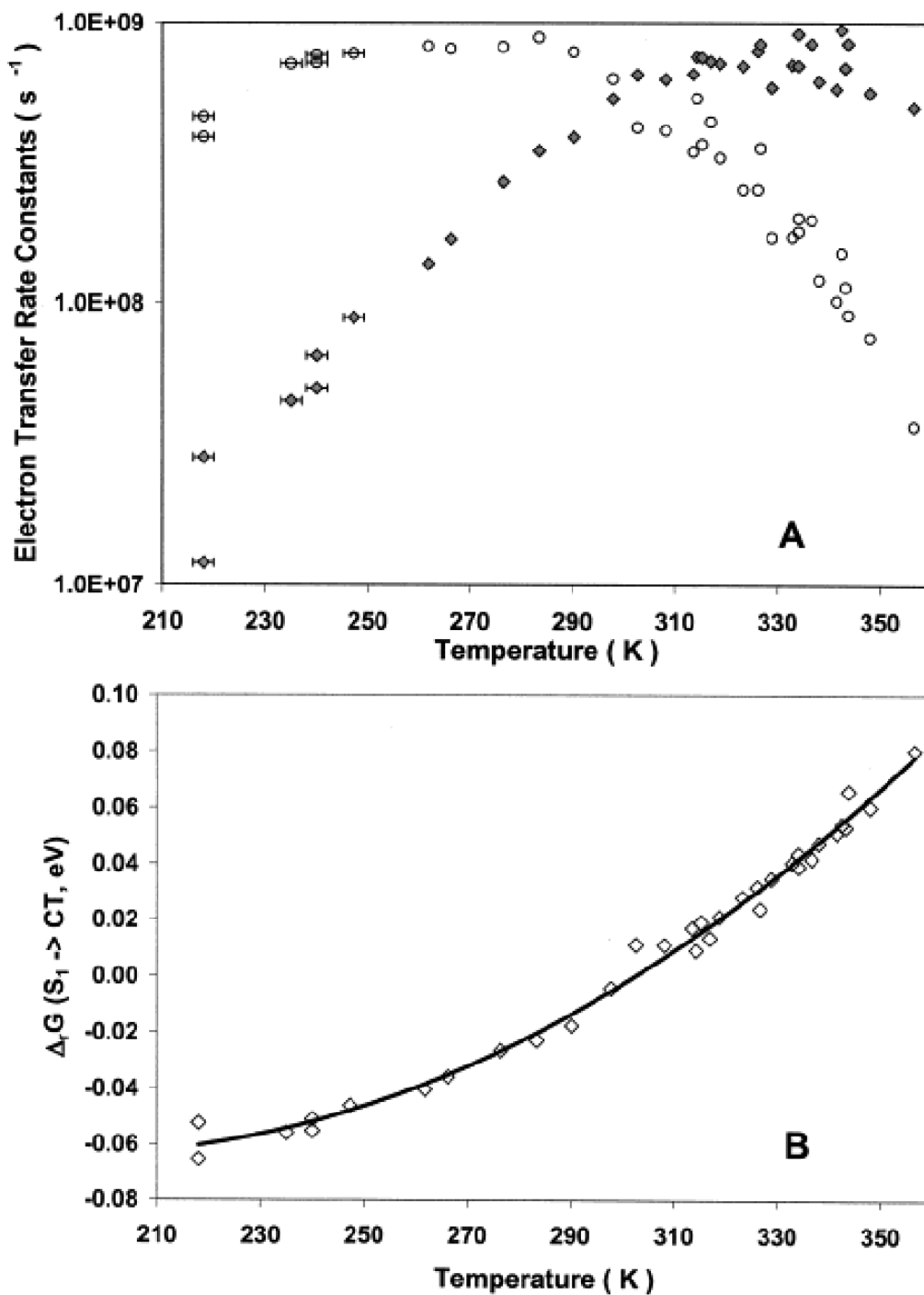


Figure 9.2 (Panel A) Charge separation (k_{for} , o) and charge recombination (k_{back} , \blacklozenge) rate constants for molecule **1** as a function of temperature in 1,3-diisopropylbenzene. Panel **B** plots the free energy change for charge separation (k_{for} , \diamond) as a function of temperature for **1** in 1,3-diisopropylbenzene. The solid line represents a best fit of the data to a quadratic equation.

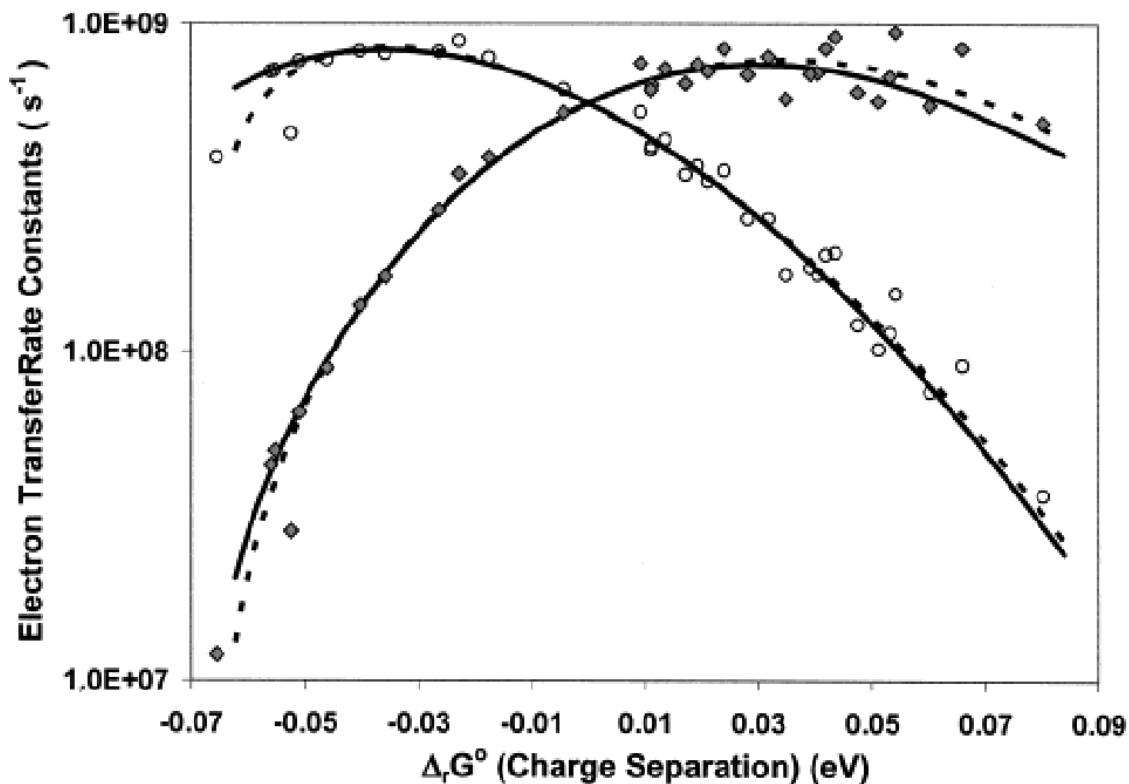


Figure 9.3 Plots of the charge separation (k_{for} , O) and charge recombination (k_{back} , \blacklozenge) rate constants versus the free energy change for charge separation. To minimize overlap, both plots use the charge separation $\Delta_r G$ as the abscissa. The solid lines were calculated using eq 9.2 assuming $|V| = 2.25 \text{ cm}^{-1}$ and $\lambda_s = 0.033 \text{ eV}$. The dashed lines were calculated using the parametrized Matyushov model to predict $\lambda_s(T)$ and the regression estimates of $|V(T)|$ (see text).

The solid line shows a fit to the full temperature dependence of $\Delta_r G$ that is obtained with a quadratic expression. This fit is used later to aid in the analysis of the rate data.¹⁶

Semi-log plots of electron-transfer rate constant versus reaction free energy have been used to determine solvent reorganization energy and electronic coupling magnitudes. For **1**, the logarithms of k_{for} and k_{back} increase, plateau, and then decrease in a plot versus $\Delta_r G$ for the charge separation step (Figure 9.3). This shape suggests that k_{for} and k_{back} both span the Marcus normal and inverted regions and that the solvent reorganization energy is very small (vide infra). In a conventional Marcus plot, the temperature and solvent reorganization energy for all points are

held as constant as possible. In Figure 9.3, however, the temperature for each data point varies from 218 (left side) to 356 K (right side). As a result, the variation of $\Delta_r G$ (abscissa) is attended by significant variation of $k_B T$ and, possibly, of the solvent reorganization energy and the electronic coupling. These variations must be considered in any interpretation of the rate constant plots in Figures 9.2 and 9.3 (vide infra).

The temperature dependence of the charge separation and recombination rate constants may be simulated using a semiclassical formulation¹⁷ for the electron-transfer rate constant (eq 9.2)

$$k_{\text{ct}} = \frac{4\pi^2}{h} |V|^2 \frac{1}{\sqrt{4\lambda_S \pi k_B T}} \times \sum_{n=0}^{\infty} \exp(-S) \left(\frac{S^n}{n!}\right) \exp\left[-\frac{(\Delta_r G + \lambda_S + nh\nu)^2}{4\lambda_S k_B T}\right] \quad (9.2)$$

In this equation, $|V|$ is the donor-acceptor electronic coupling, λ_S is the solvent reorganization energy, $h\nu$ is the quantized mode energy spacing, and S is the ratio of the internal reorganization energy, λ_V , to the quantized mode energy spacing, $S = \lambda_V / h\nu$. The quantity S is assumed to be temperature independent. Estimates of λ_V (0.39 eV) and $h\nu$ (0.175 eV) were previously determined using a combination of quantum chemistry calculations and CT emission spectra from related molecules.¹⁸ Given these values for the internal reorganization parameters and the experimental values of $\Delta_r G$ at each temperature (Figure 9.2B), only the magnitude and temperature dependence of λ_S and $|V|$ may be “adjusted” to reproduce the experimental data. The extensive curvature of the k_{for} and k_{back} versus $\Delta_r G$ plots places significant constraints on the magnitude and temperature dependence of the solvent reorganization energy and/or of the

electronic coupling. As discussed below, two possible explanations for the highly curved plots of k_{for} and k_{back} versus temperature (i.e., versus reaction free energy) have been identified.

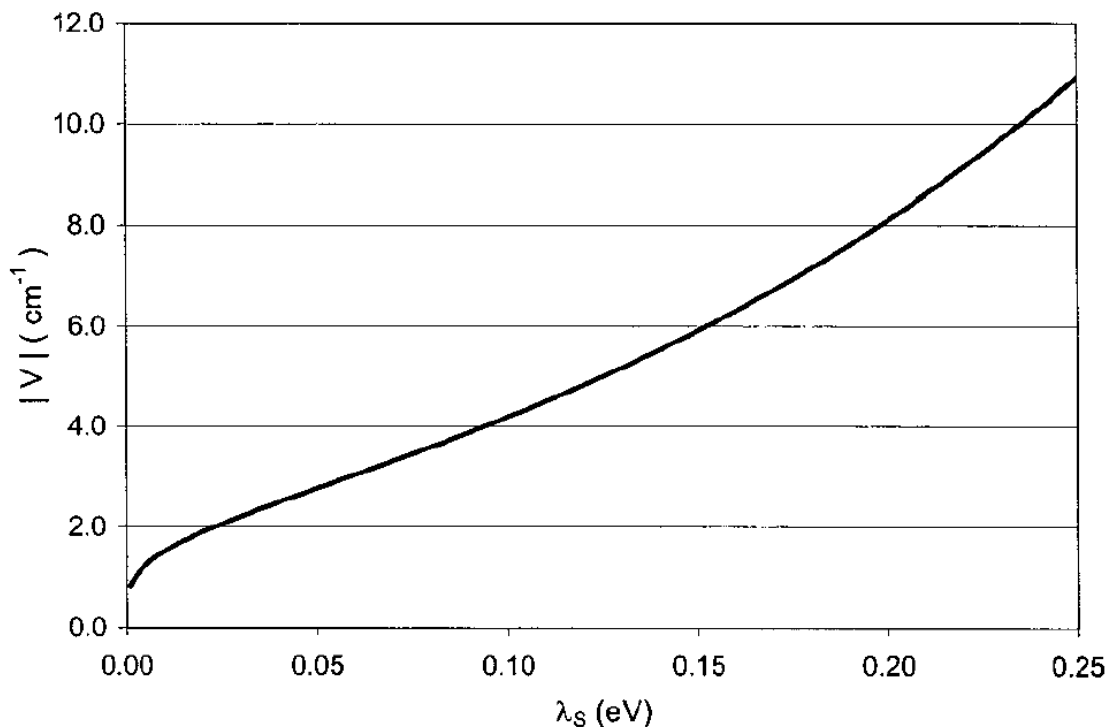


Figure 9.4 Correlation between $|V|$ and λ_S for **1** derived from the experimental transfer rate constant at 297 K, where $\Delta_r G = 0$ eV.

The experimental k_{for} and k_{back} rate constants at each temperature establish a parametric relationship between the two unknown parameters in eq 9.2: the solvent reorganization energy and the electronic coupling. At 297 K, the temperature at which $\Delta_r G = 0$, the charge separation, and charge recombination rate constants are equal, and only the $n = 0$ term in eq 9.2 makes significant contributions to either rate constant. The electronic coupling may be expressed as a simple function of the solvent reorganization energy, the temperature, and the rate constants by rearranging eq 9.2. Figure 9.4 displays this relationship between $|V|$ and λ_S for **1** in 1,3-diisopropylbenzene at 297 K, with $k_{\text{for}} = k_{\text{back}} \sim 5.8 \times 10^8 \text{ s}^{-1}$, and shows that the electronic coupling increases monotonically as λ_S increases. A previous study of solvent-mediated, donor-

acceptor electronic coupling for **1** determined that $|V| = 6 \text{ cm}^{-1}$ in isopropylbenzene (cumene) and $|V| = 1 \text{ cm}^{-1}$ in 1,3,5-triisopropylbenzene.¹⁰ Furthermore, it was found that an increase in the alkyl substitution at the periphery of the benzene ring caused a systematic decrease of the magnitude of solvent-mediated coupling for **1**.^{8c} Accordingly, the electronic coupling mediated by 1,3-diisopropylbenzene for **1** is expected to lie between the values in cumene and triisopropylbenzene, i.e. between 6 and 1 cm^{-1} , respectively. Using the range defined by these couplings, Figure 9.4 indicates that the solvent reorganization energy in 1,3-diisopropylbenzene at 297 K lies between 0.15 and 0.0 eV, respectively. The experimental values of $\Delta_r G$ for charge separation in 1,3-diisopropylbenzene vary, with temperature, between -0.07 and 0.08 eV. Thus, the charge separation reaction could lie in the Marcus normal region (if $\lambda_s > 0.09 \text{ eV}$) or span the normal and inverted regions ($\lambda_s < 0.06 \text{ eV}$).

By assuming a specific, *temperature independent* value of the electronic coupling, eq 9.2 may be used to determine the value of λ_s that is required at each temperature to reproduce the experimental rate constants. Figure 9.5 displays $\lambda_s(T)$, calculated in this manner, for two assumed values of the electronic coupling: 2.25 cm^{-1} (panel A) and 6.0 cm^{-1} (panel B). For the assumed value of $|V| = 2.25 \text{ cm}^{-1}$, the extracted λ_s has a mean value of $0.033 \pm 0.007 \text{ eV}$ and exhibits a weak, positive temperature dependence, $<0.1 \text{ meV/K}$. If λ_s for **1** in 1,3-diisopropylbenzene is this small and without significant temperature dependence, the charge separation reaction lies in the Marcus inverted region at temperatures below 270 K, and the charge recombination reaction lies in the Marcus inverted region at temperatures above 330 K. The solid lines in Figure 9.3 display the temperature dependence of k_{for} and k_{back} predicted using $\lambda_s = 0.033 \text{ eV}$, $|V| = 2.25 \text{ cm}^{-1}$ and $\Delta_r G$ obtained from the data in Figure 9.2B. The calculated curves reproduce the data well.

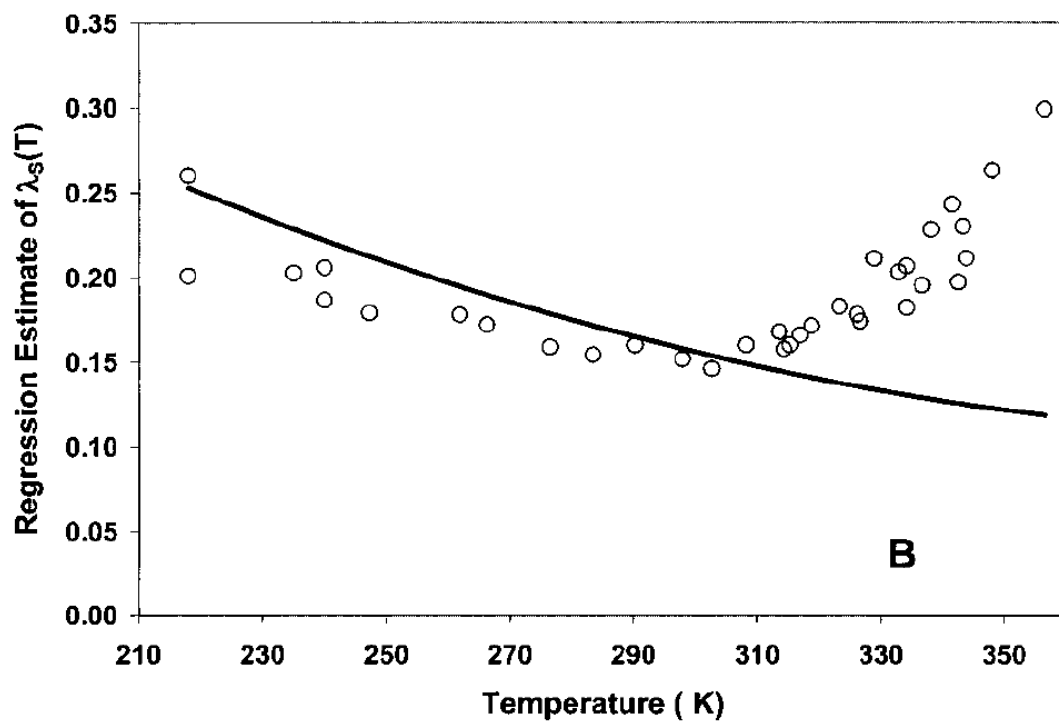
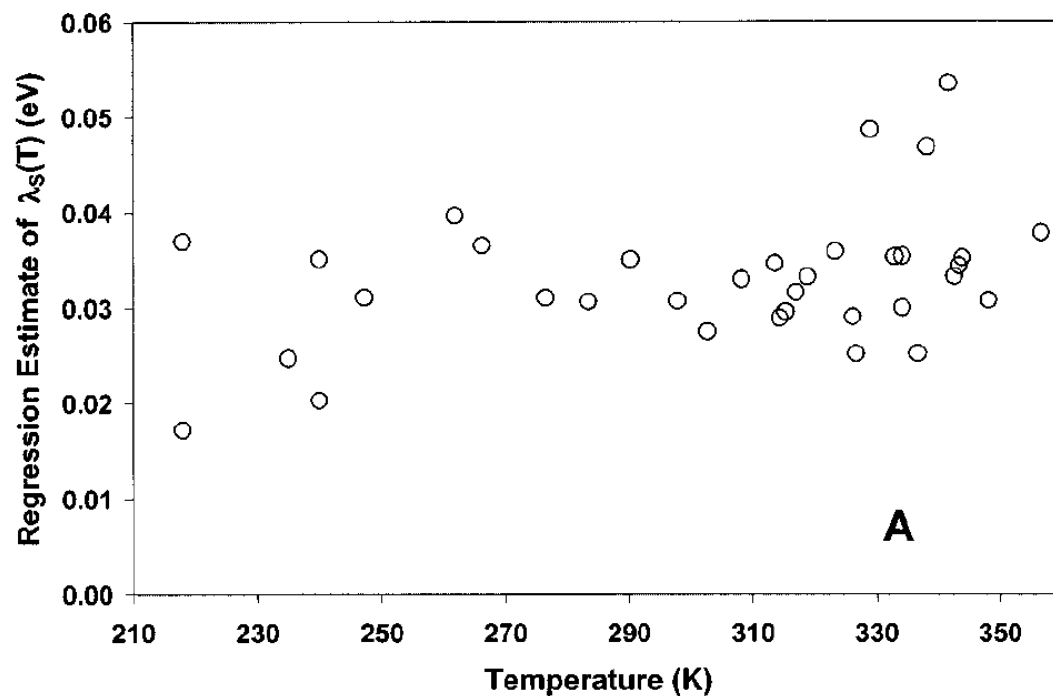


Figure 9.5 Values of $\lambda_s(T)$ obtained from the experimental rate constant data, eq 9.2 and an assumed value of $|V|$. The data in panel A were obtained with $|V|$ set to 2.25 cm^{-1} . The data in panel B were obtained by setting $|V|$ equal to 6.0 cm^{-1} . The solid line in panel B shows the $\lambda_s(T)$ prediction from the calibrated Matyushov model.

Using the larger assumed value of $|V| = 6.0 \text{ cm}^{-1}$, the λ_s values extracted with eq 9.2 (Figure 9.5B, circles) exhibit a U-shaped temperature dependence with a value at 297 K of 0.16 eV. Previous theoretical and experimental studies¹⁹ of the solvent reorganization energy in liquids provide no evidence to substantiate such a U-shaped temperature dependence. Therefore, either the assumed coupling magnitude of 6 cm^{-1} is inappropriate or the assumption that the coupling magnitude is temperature independent is erroneous. From both these analyses it is clear that a meaningful determination of the coupling magnitude requires more information about the solvent reorganization energy.

Table 9.1 Calibrated Solvation Model Predictions of $\lambda_s(295 \text{ K})$, Its First Derivative, and Experimental Values of $\lambda_s(295 \text{ K})$ Determined by Fitting $k_{\text{for}}(T)$ and $k_{\text{back}}(T)$ Data^a

solvent	model: $d(\lambda_s(295\text{K}))/dT$ (eV/ 10^3 K)	model: $\lambda_s(295 \text{ K})^{23}$ (eV)	expt: $\lambda_s(295 \text{ K})$ (eV)
benzene	-1.1	0.27	0.26
toluene	-1.0	0.24	0.22
cumene	-0.83	0.19	0.17
mesitylene	-0.76	0.17	0.14
TMB	-0.75	0.20	0.16
13DIP	-0.63	0.16	
135TIP	-0.74	0.12	0.01

^a TMB is 1,2,4-trimethylbenzene, 13DIP is 1,3-diisopropylbenzene, and 135TIP is 1,3,5-triisopropylbenzene.

As it is not possible to independently measure λ_s for **1**, theoretical estimates and experimental values from related systems need to be considered. Previously, a molecular solvation model, developed by Matyushov,²⁰ was calibrated¹⁰ to reproduce the experimental

values of the charge separation free energy for **1** in alkylated benzene solvents. This calibrated solvation model can be used to predict the magnitude and temperature dependence of the solvent reorganization energy. Table 9.1 presents these predictions for the solvent reorganization energy and its temperature derivative at 295 K in seven alkylbenzene solvents and compares them to values of $\lambda_S(295\text{ K})$ that were obtained by fitting experimental rate constant data for **1**.^{10,21} The model predicts a monotonic decrease of the solvent reorganization energy with increasing temperature and with increasing alkyl substitution of the solvent molecules. For the first five solvents in Table 9.1, the model predictions and the experimental values of $\lambda_S(295\text{ K})$ are in good agreement. Only the regression estimate of $\lambda_S(295\text{ K})$ in 1,3,5-tri-isopropylbenzene deviates significantly from the model's prediction (see below for an alternative analysis of the kinetic data for **1** in this solvent). The good agreement between the experimental and theoretical values of λ_S in five of the six solvents that are structurally related to 1,3-diisopropylbenzene suggests that the model's prediction of $\lambda_S = 0.16\text{ eV}$ at 295 K for this solvent is reasonable. This value is much larger than the λ_S estimate required by assuming $|V| = 2.25\text{ cm}^{-1}$ but quite close to the value required by assuming $|V| = 6\text{ cm}^{-1}$. The solid line in Figure 9.5B displays the parametrized solvation model prediction of λ_S versus temperature for **1** in 1,3-diisopropylbenzene.²² Between 220 and 290 K, the theoretical predictions are slightly larger (by 0.02-0.03 eV) than the $\lambda_S(T)$ values required to reproduce the rate data (circles) for the assumed value of $|V| = 6.0\text{ cm}^{-1}$. These two sets of $\lambda_S(T)$ deviate at higher temperatures.

Both sets of $\lambda_S(T)$ values in Figure 9.5, panel B, are substantially larger than the experimental $-\Delta_rG$ values, suggesting that the charge separation and charge recombination processes lie in the Marcus normal region at all temperatures. In the Marcus normal region, larger λ_S values reduce the electron-transfer rate constant. The apparent increase of λ_S at

temperatures above 310 K (circles, panel B) acts to decrease the transfer rate constant calculated using a temperature independent coupling of 6 cm^{-1} .

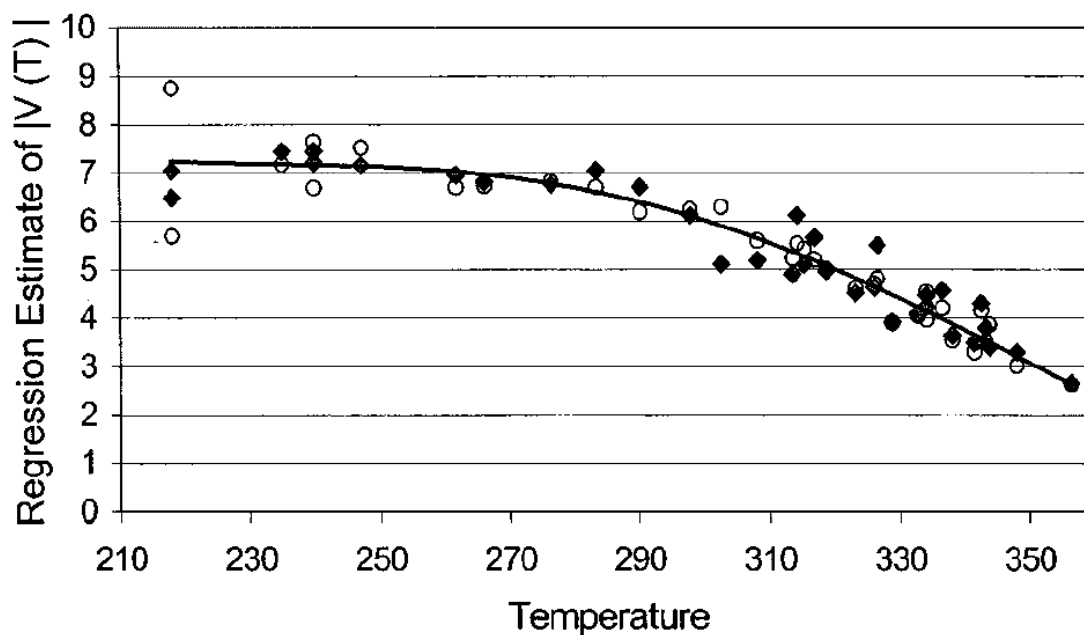


Figure 9.6 Values of the electronic coupling for **1** in 1,3-diisopropylbenzene, obtained by fitting the experimental rate constant data using the calibrated Matyushov model to calculate $\lambda_s(T)$, plotted as a function of temperature: (k_{back} , O), (k_{for} , \blacklozenge).

Given the mobility of solvent molecules and evidence that solvent placement influences coupling magnitude, it is possible that a decrease of the average, effective coupling, rather than an increase of λ_s , may be occurring at temperatures above 310 K. This proposal can be explored by assuming that the parametrized solvation model accurately predicts the magnitude and the temperature dependence of the solvent reorganization energy for **1**. With values for $\lambda_s(T)$, eq 9.2 may be used to determine the value of the electronic coupling required to reproduce the experimental rate constants at each temperature. The coupling magnitude obtained using this procedure (Figure 9.6) is relatively constant between 220 and 260 K, $7.2 \pm 0.5 \text{ cm}^{-1}$, but

decreases by more than 60% between 260 and 350 K.²⁴ The temperature dependence of k_{for} and k_{back} predicted by this analysis is in very good agreement with the experimental data (Figure 9.3, dashed lines).

At this point, two models have been advanced to explain the rate data from **1** in 1,3-diisopropylbenzene. The two models reproduce the rate data using different values and temperature dependences of $|V|$ and λ_{S} . In the next section, evidence is presented that confirms the validity of λ_{S} predictions from the calibrated molecular model and the validity of the $|V(T)|$ explanation. Arguments that discount the accuracy of the “inverted” region model are also presented.

9.4 Pros, Cons, and Consequences of the Two Explanations

The temperature dependence of the charge separation and charge recombination rate constants for **1** in 1,3-diisopropylbenzene are well reproduced by both the “inverted region” and the “temperature-dependent electronic coupling” explanations. At low temperatures ($\Delta_{\text{r}}G(\text{CS}) < -0.05$ eV), the latter model fits the data slightly more accurately. For both explanations, the solvent reorganization energy is small, less than 0.3 eV. Determining which of the two proposed explanations is correct requires accurate information on the solvent reorganization energy magnitude and its temperature dependence, a task that is not experimentally feasible for **1**. As noted above, a molecular solvation model, which previously was parametrized¹⁰ to reproduce the experimentally determined $\Delta_{\text{r}}G(T)$ data for **1** in a series of alkylbenzene solvents, predicts values of $\lambda_{\text{S}}(295 \text{ K})$ for **1** (ranging from 0.12 to 0.27 eV) that are in good agreement with $\lambda_{\text{S}}(295 \text{ K})$ determined by fitting experimental rate constant data. The model’s prediction of $\lambda_{\text{S}}(295 \text{ K})$ for **1** in 1,3-diisopropylbenzene, 0.16 eV, is significantly larger than the 0.033 eV value required by

the “inverted region” explanation. In light of the model’s predictive accuracy in the other alkylbenzene solvents, this discrepancy argues against the “inverted region” explanation.

Although **1** lacks detectable CT absorption and emission spectra, some qualitative information about λ_S can be obtained by studying the CT spectra of a related molecule. Compound **2** employs the same donor and acceptor as **1**, connected by an all-trans three-bond bridge, and exhibits CT emission.²⁵ The donor-acceptor separation in **2** is ~ 6 Å, roughly 1 Å smaller than that in **1**. At 295 K, the maximum of the CT emission, Franck-Condon lineshape from **2** appears at 2.19 eV in 1,3-diisopropylbenzene, 2.12 eV in cumene, and 1.98 eV in benzene.²⁶ This energy is approximately equal to $\Delta_r G(S_0 \rightarrow CT) - \lambda_S - \lambda_V$ or, equivalently, to $\Delta_r G(S_0 \rightarrow S_1) + \Delta_r G(S_1 \rightarrow CT) - \lambda_S - \lambda_V$. The term $\Delta_r G(S_0 \rightarrow S_1)$ amounts to 3.00 eV for the anthracene chromophore in alkylbenzene solvents and the last term, λ_V , is 0.39 eV. Thus, $\lambda_S - \Delta_r G(S_1 \rightarrow CT)$ for **2** at 295 K is equal to 0.42, 0.49, and 0.63 eV in 1,3-di-isopropylbenzene, cumene, and benzene, respectively.²⁷ The same quantity, $\lambda_S - \Delta_r G(S_1 \rightarrow CT)$, calculated for **1** using the experimental $\Delta_r G(S_1 \rightarrow CT)$ data and the calibrated solvation model predictions of λ_S (Table 9.1) amounts to 0.16, 0.24 and 0.37 eV in 1,3-diisopropylbenzene, cumene and benzene, respectively. The variations of $\lambda_S - \Delta_r G(S_1 \rightarrow CT)$ with solvent are nearly identical for **1** and **2**. The offset of 0.26 eV between $\lambda_S - \Delta_r G(S_1 \rightarrow CT)$ for **1** and **2** is consistent with the different charge separation distances of **1** and **2**.²⁸ The similarity of the solvent dependencies of $\lambda_S - \Delta_r G(S_1 \rightarrow CT)$, for **1** and **2**, in conjunction with the accurate reproduction of the $\Delta_r G(T)$ data for **1** shows that the parametrized molecular model’s treatment of solvation by weakly dipolar aromatic solvents and its treatment of solvent structural effects generate meaningful predictions for these anthracene donor, cyclobutenediester electron-transfer systems.²⁹ Although these arguments do not establish unambiguously the accuracy of the model’s $\lambda_S(295\text{ K})$ predictions,

they provide compelling evidence that λ_S for **1** in 1,3-diisopropylbenzene is larger than 0.033 eV. Accordingly, the “inverted region” explanation is not consistent with the available information on λ_S in 1,3-diisopropylbenzene.

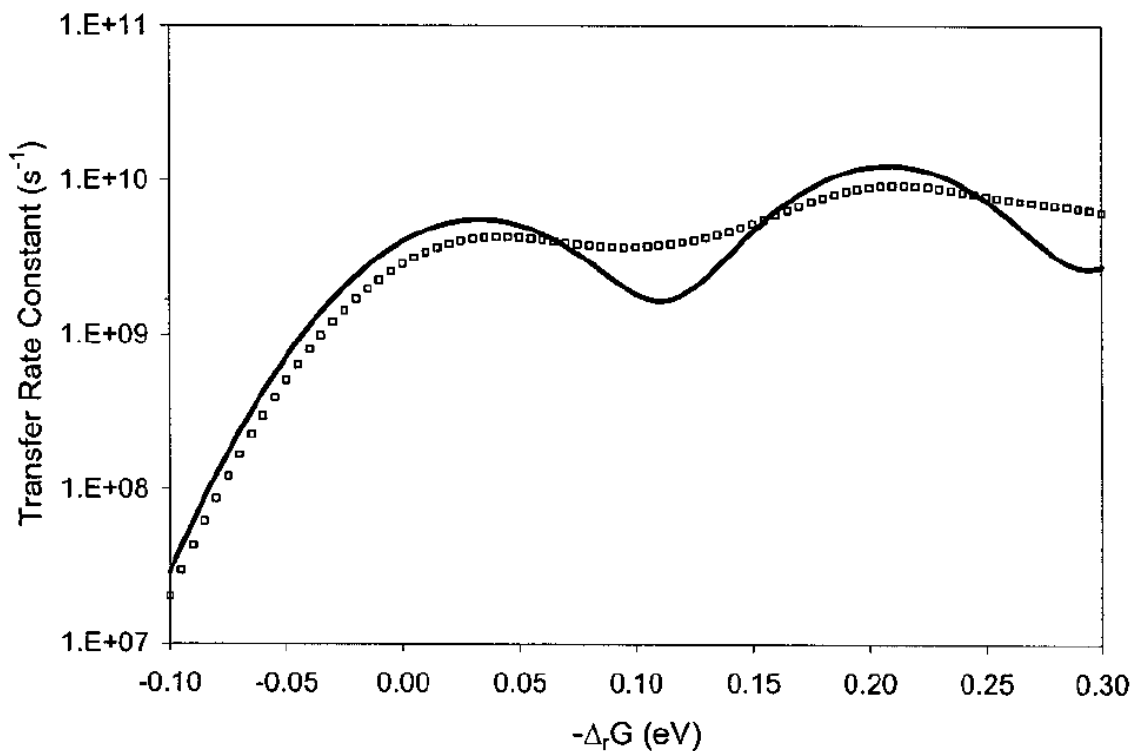


Figure 9.7 Examples of rate constant versus reaction free energy plots calculated using a one-quantized mode (—) and a two quantized mode (□) model. For both models, $|V| = 6 \text{ cm}^{-1}$, $\lambda_S = 0.033 \text{ eV}$, $h\nu_1 = 0.175 \text{ eV}$, $h\nu_2 = 0.087 \text{ eV}$, and the total internal reorganization energy is 0.39 eV. For the two quantized mode calculation, the internal reorganization energies are λ_{V1} (0.175 eV mode) = 0.33 eV and λ_{V2} (0.087 eV mode) = 0.06 eV. For the one quantized mode calculation, λ_V (0.175 eV mode) = 0.39 eV.

Another problem with the “inverted region” explanation for **1** in 1,3-diisopropylbenzene lies in the calculated decrease of the transfer rate when $-\Delta_r G$ is greater than $\lambda_S = 0.033 \text{ eV}$. This prediction may be an artifact of using a single quantum mode model. If λ_S is significantly smaller than the mode spacing, $h\nu$, eq 9.2 predicts a significant drop and recovery of the rate constant for $-\Delta_r G$ between λ_S and $\lambda_S + h\nu$ (Figure 9.7; solid line). A modulation appears in a

semilog plot of rate constant versus $-\Delta_r G$, with rate maxima at values of $-\Delta_r G$ that are close to $\lambda_s + nh\nu$.³⁰ This modulation extends from the “normal” region ($-\Delta_r G < \lambda_s + \lambda_\nu$), through the peak of the Marcus curve and into the region *traditionally* referred to as inverted ($-\Delta_r G > \lambda_s + \lambda_\nu$). If a small portion of the internal reorganization energy is associated with a second quantum mode of lower frequency, e.g., $h\nu \sim 700 \text{ cm}^{-1}$, a two quantum mode rate constant model predicts negligible modulation of the rate constant (Figure 9.7, squares).³¹ Resonance Raman studies of intramolecular CT systems report significant reorganization associated with such intermediate frequency modes in other systems.³² For **1**, modes involving the donor and acceptor rings likely fall in this range, whereas modes associated with reorganization of the donor methoxy and the acceptor ester groups likely occur at somewhat lower frequency. Thus, more realistic treatments of the internal reorganization within the rate constant calculation predict smaller or negligible reduction of the rate constant when $-\Delta_r G$ is greater than λ_s . This raises additional doubts about the validity of the “inverted region” explanation for the transfer rate data from **1** in 1,3-diisopropylbenzene.

If the molecular model prediction of λ_s for **1** in 1,3-diisopropylbenzene is correct, then 1,3,5-triisopropylbenzene is the only alkylbenzene solvent for which the molecular model prediction and the experimentally derived value of λ_s differ significantly. The solvent 1,3,5-triisopropylbenzene differs from the other alkylbenzenes in that the three bulky isopropyl groups spaced around the aromatic ring prevent facile entry of the solvent’s aromatic core into the cleft between the donor and acceptor groups.^{8c} Molecular mechanics calculations indicate that only the isopropyl groups from this solvent extend into the cleft. The absence of a “solvent aromatic ring” between the donor and acceptor groups might cause a larger reduction of λ_s , relative to the other solvents, than predicted by the molecular model. The solvation model treats the CT

molecule as a point dipole contained within a solvent free cavity. Thus, it does not include “cleft” solvent reorganization energy for any of the solvents.³³ If exclusion of the aromatic core of 1,3,5-triisopropylbenzene from the cleft interior is responsible for the 0.11 eV difference between the molecular model prediction and the experimental value (Table 9.1) of λ_S (295 K), then the molecular model must overestimate the “*extra-cavity*” solvent reorganization energy in all of these alkylbenzene solvents by a comparable amount. This line of reasoning suggests that the solvent reorganization energy attending motion of a single solvent molecule within the cleft, ~ 0.1 eV, is comparable to the solvent reorganization energy attending motions of all of the solvent molecules surrounding the donor and acceptor groups. Finite difference Poisson-Boltzmann calculations³⁴ that explicitly account for the shape and presence of a cleft in **1** generate similar values of λ_S whether the solvent is excluded or allowed into the cleft between the donor and acceptor.³⁵ Thus, exclusion of the aromatic core of 1,3,5-triisopropylbenzene from the cleft in **1** is not a likely source for the discrepancy between the calculated and experimental λ_S values. An alternative explanation for the discrepancy between the molecular model and regression estimate of λ_S for **1** in 1,3,5-triisopropylbenzene is that the effective $|V|$ in this solvent is also temperature-dependent. In analogy to the approach employed for **1** in 1,3-diisopropylbenzene, the magnitude and temperature dependence of the effective coupling for **1** in 1,3,5-triisopropylbenzene may be determined by assuming that the molecular model predictions of $\lambda_S(T)$ are correct. The results of this analysis (Figure 9.8) suggest that the effective coupling for **1** in 1,3,5-triisopropylbenzene *increases* with temperature, from 2.9 cm^{-1} at 260 K to 3.5 cm^{-1} at 283 K. A positive value of $d|V|/dT$ provides a simple explanation for the experimental observation that *both* k_{for} *and* k_{back} *increase with temperature* in this solvent.

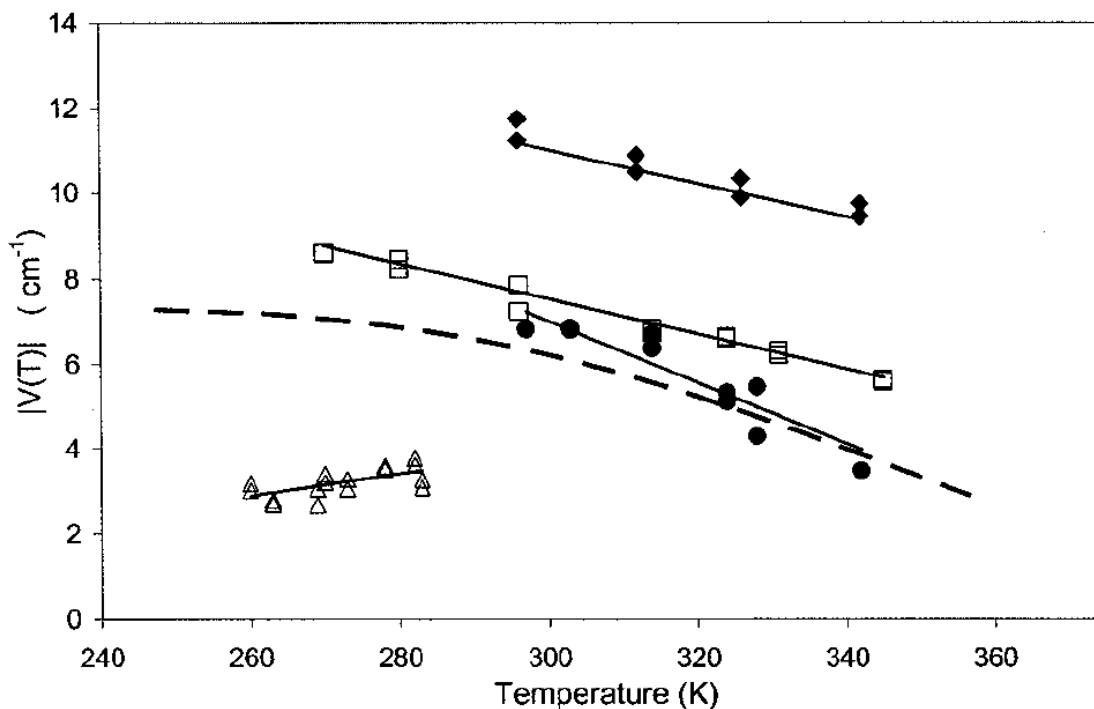


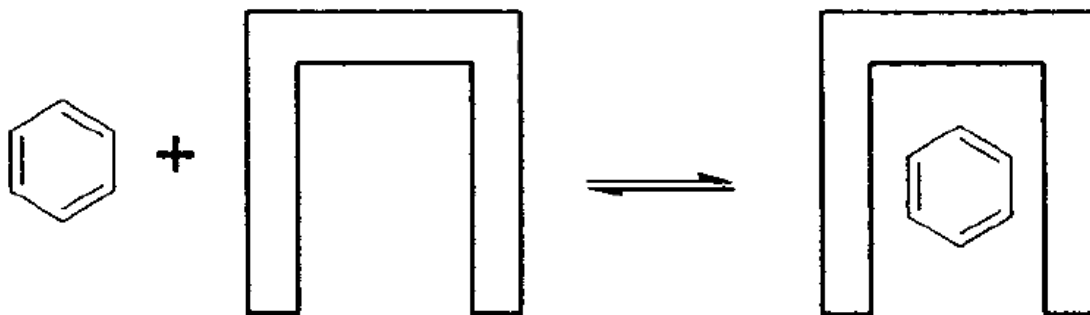
Figure 9.8 Temperature dependence of the electronic coupling for **1** in benzene (◆), cumene (□), mesitylene (●), and 1,3,5-tri-isopropylbenzene (△), obtained by fitting the experimental rate constant data and using the calibrated Matyushov model to calculate $\lambda_s(T)$. Regression lines are drawn through the data for each solvent. The best fit line to the 1,3-diisopropylbenzene $|V(T)|$ data (— —) is reproduced from Figure 9.6.

The magnitude of the coupling obtained from this analysis is larger than the value of 1.0 cm^{-1} previously obtained with the assumption of a temperature independent coupling magnitude and a regression estimate of $\lambda_s(295 \text{ K}) = 0.01 \text{ eV}$. It is not surprising that a larger magnitude of $|V|$ is obtained when larger values of λ_s are used in the analysis (Figure 9.4). Even with this increase, the effective coupling for **1** in 1,3-diisopropylbenzene is still more than 2-fold larger than in 1,3,5-triisopropylbenzene ($260 \text{ K} < T < 283 \text{ K}$). As was suggested previously, increased steric bulk about the periphery of the solvent's aromatic π system results in less effective solvent-mediated coupling.

Figure 9.8 shows the $|V(T)|$ values that are obtained for the other alkylbenzene solvents when the solvation model's predictions for the temperature-dependent reorganization energy are assumed to be correct. The effective coupling magnitude, derived from the rate data and the molecular model $\lambda_S(T)$, decreases with increasing temperature in the solvents benzene, cumene, and mesitylene. The diminution is greatest for mesitylene, for which the coupling magnitude and temperature dependence are similar to that for **1** in 1,3-diisopropylbenzene. The steep decrease of the coupling in mesitylene provides an explanation for the failure of the previous analysis,¹⁰ which assumed temperature independent coupling magnitudes, to reproduce the experimentally observed steep decrease of k_{for} and k_{back} at temperatures above 315 K. The temperature derivative of the effective coupling in benzene and cumene, $-0.04 \text{ cm}^{-1} \text{ K}^{-1}$, is about half as large as that for mesitylene. For the five alkylbenzene solvents, the effective coupling magnitudes at 295 K are 12 cm^{-1} in benzene, 7.4 cm^{-1} in cumene, 6.8 cm^{-1} in mesitylene, 6.3 cm^{-1} in 1,3-diisopropylbenzene, and 3.9 cm^{-1} in 1,3,5-triisopropylbenzene.³⁶ With the exception of the last solvent, these magnitudes are within 20% of the values derived previously from analyses premised on temperature independent coupling.¹⁰

The structure and the number of alkyl groups on the periphery of the solvents' aromatic ring alter the electronic coupling magnitude for **1**. The alkyl groups have a minor effect on the aromatic π system's energy levels. They do influence the probabilities of locating the aromatic π system in positions that offer simultaneous overlap with the donor and the acceptor. Theoretical investigations confirm that such simultaneous overlap is necessary for a coupling pathway constituted by a single solvent molecule to be effective.^{5e} For a C-shaped molecule such as **1**, simultaneous overlap and significant coupling are realized by placement of the solvent's aromatic π system within the 7 \AA wide cleft, directly between the donor and acceptor groups.³⁷

The observed dependence of **1**'s electronic coupling magnitude on the identity of the alkyl groups around the aromatic ring and on temperature can be explained in terms of solvent entry into this cleft. A benzene molecule readily accesses "in-cleft" solvent configurations that provide significant, simultaneous overlap of the solvent with the donor and the acceptor of **1**. For many of these "in-cleft" configurations of the benzene, substituting a peripheral H atom by an alkyl group introduces steric repulsion between the alkyl group and **1**. This repulsion disfavors solvent configurations with the aromatic core situated deeply within the cleft. Solvent configurations in which the (bulky) alkyl groups are farther from the cleft walls and edges are more probable. The latter configurations offer smaller simultaneous overlap of the donor and acceptor with the solvent π orbitals and, therefore, smaller electronic coupling. Larger and/or more numerous alkyl groups more severely reduce the probability of solvent configurations with large overlap and significant coupling. This explains the observed reduction of coupling magnitude with increasing alkyl substitution of the solvent.



Scheme 9.1

Each “in-cleft” solvent configuration affords a unique coupling magnitude. As solvent molecules move within and out of the cleft, the donor-acceptor coupling magnitude fluctuates. The probability of an electron-transfer event is very small during any single initial state-final state level crossing (nonadiabatic transfer). As a result, each molecule of **1** samples a “large number” of solvent configurations before there is significant probability that the ensemble of excited states has undergone electron transfer. Rapid interconversion among solvent-**1** configurations, compared to the electron-transfer rate, generates experimental charge separation dynamics that are well reproduced by a single electron-transfer rate constant with an effective coupling magnitude that is a root-mean-square average of the individual coupling magnitude, $(V_j)^2$, in each possible configuration, $|V| = [\sum_j p_j (V_j)^2]^{1/2}$. The probability of each configuration, p_j , is determined by its free energy and by the temperature. The probability of each solvent-**1** configuration changes differently with temperature, thus altering the distribution of mediating configurations and the average value of the coupling. This provides an explanation for the temperature dependence of the observed electronic coupling.

The different signs of $d|V|/dT$ for **1** in benzene and 1,3,5-triisopropylbenzene may be attributed to the most prevalent “state” of the cleft in each solvent. For example, benzene readily fits within the cleft of **1**, and the equilibrium (see Scheme 9.1) should be characterized by a negative ΔH° and a negative ΔS° .³⁸ Upon increasing the temperature, the equilibrium shifts toward “empty-cleft” configurations. Because the “in-cleft” solvent configurations provide larger electronic coupling than the “empty cleft” configurations, the effective coupling magnitude in benzene decreases as the temperature increases. The rather shallow dependence of $|V|$ on temperature for **1** in benzene and cumene suggests that “in-cleft” configurations predominate throughout the investigated temperature ranges. The steeper dependence of $|V|$ on

temperature for **1** in mesitylene and in 1,3-diisopropylbenzene indicate more significant conversion from predominantly “in-cleft” to “empty-cleft” configurations. The solvent 1,3,5-triisopropylbenzene presents a different situation. Steric repulsion between the isopropyl groups and **1** results in a positive enthalpy for formation of “in-cleft” solvent configurations in which the solvent’s aromatic core is between the donor and acceptor. These configurations provide larger electronic coupling, but ΔG° for their formation is positive (i.e., the equilibrium constant for their formation is less than 1). Higher temperature increases the fraction of these higher free energy, larger coupling, “in-cleft” configurations, and enhances the effective coupling magnitude. Given the excellent correspondence between the experimental rate data for **1** and the rates calculated using the parametrized molecular model in a variety of alkylbenzene solvents, variation of the solvent mediated electronic coupling magnitude with temperature is a likely explanation for the unusual electron-transfer kinetics of **1** in 1,3-diisopropylbenzene.

9.5 Conclusion

The charge separation and charge recombination rate constants for **1** in 1,3-diisopropylbenzene increase, plateau, and then decrease when plotted against temperature or the experimentally determined reaction free energy change. Within the framework of a single quantum-mode, semiclassical electron transfer rate expression, the origin of this rate behavior lies in the temperature dependence of the solvent reorganization energy and/or of the electronic coupling. Two explanations of the kinetic behavior have been advanced. The experimental data can be simulated using a small and temperature-independent solvent reorganization energy or a temperature-dependent electronic coupling magnitude. In the first scenario, the variation of the reaction driving force with temperature shifts the reactions between the Marcus normal and the

Marcus inverted regions and is responsible for the highly curved rate plots. Between 210 and 360 K, Δ_rG for the charge separation and charge recombination reactions are insufficient to populate “products” with one or more quanta of vibrational energy.³⁹ Thus, the electron transfer rate constant in the normal and inverted regions decreases comparably as the reaction free energy shifts away from the optimum value. For this explanation to apply, there cannot be significant vibrational reorganization (energy) associated with modes in the 400-700 cm^{-1} range. The solvent reorganization energy would also need to be extremely small and unusually temperature-independent. Additionally, there are very few examples of charge separation reactions (neutral reactant \rightarrow zwitterionic product) that exhibit rate versus Δ_rG profiles consistent with the Marcus inverted region.⁴⁰ Although many explanations have been advanced to justify the paucity of examples, invoking the inverted region to explain the rate constant data from **1** finds little if any precedent. This would also be the first example of a charge separation reaction in nonpolar solvents lying in the Marcus inverted region.

The alternative explanation for the kinetic data posits that the electronic coupling magnitude varies with temperature. Between 290 and 350 K, the effective coupling for **1** decreases 60% in 1,3-diisopropylbenzene, 50% in mesitylene, and 30% in cumene. The extensive curvature in the bridge of **1** requires an appropriately placed solvent molecule within the cleft between the donor and acceptor to mediate the electronic coupling. The probability of appropriate solvent placement and the efficacy of solvent-mediated coupling both vary with solvent structure and temperature. Although there are theoretical studies that support the feasibility of temperature-dependent, solvent mediated coupling magnitudes,^{5,41} there is not yet *direct* evidence to confirm this explanation. The evidence in this manuscript is indirect, relying on a parametrized solvation model to provide accurate predictions of the solvent reorganization

as a function of solvent structure and temperature. More direct investigation of the temperature dependence in solvent-mediated electronic coupling is clearly desirable. In summary, the experimental rate constant behavior for **1** in a number of alkylbenzene solvents is most reasonably explained by invoking a significant temperature dependence for the solvent-mediated, electronic coupling magnitude. Temperature-dependent electronic coupling may influence electron-transfer dynamics in any system where the composition or the structure of the coupling pathway fluctuates significantly.

9.6 References

- (1) (a) Gould, I. R.; Young, R. H.; Moody, R. E.; Farid, S. *J. Phys. Chem.* **1991**, *95*, 2068. (b) Gould, I. R.; Young, R. H.; Mueller, L. J.; Albrecht, A. C.; Farid, S. *J. Am. Chem. Soc.* **1994**, *116*, 8188.
- (2) (a) Winkler, J. R.; Di Bilio, A. J.; Farrow, N. A.; Richards, J. H.; Gray, H. B. *Pure Appl. Chem.* **1999**, *71*, 1753. (b) Casimiro, D. R.; Beratan, D. N.; Onuchic, J. N.; Winkler, J. R.; Gray, H. B. *Adv. Chem. Ser.* **1995**, *246*, 471. (c) Miller, J. R.; Beitz, J. V.; Huddleston, R. K. *J. Am. Chem. Soc.* **1984**, *106*, 5057.
- (3) (a) Hush, N. S. *Coord. Chem. Rev.* **1985**, *64*, 135. (b) Oliver, A. M.; Paddon-Row, M. N.; Kroon, J.; Verhoeven, J. W. *Chem. Phys. Lett.* **1992**, *191*, 371. (c) Morais, J.; Hung, R. R.; Grabowski, J. J.; Zimmt, M. B. *J. Phys. Chem.* **1993**, *97*, 13138. (d) Bixon, M.; Jortner, J.; Verhoeven, J. W. *J. Am. Chem. Soc.* **1994**, *116*, 7349.
- (4) (a) Closs, G. L.; Miller, J. R. *Science* **1988**, *240*, 440. (b) Paddon-Row, M. N. *Acc. Chem. Res.* **1994**, *27*, 18. (c) Sachs, S. B.; Dudek, S. P.; Hsung, R. P.; Sita, L. R.; Smalley, J. F.; Newton, M. D.; Feldberg, S. W.; Chidsey, C. E. D. *J. Am. Chem. Soc.* **1997**, *119*, 10563. (d) Winkler, J. R.; Gray, H. B. *J. Biol. Inorg. Chem.* **1997**, *2*, 399. (e) Lewis, F. D.; Letsinger, R. L. *J. Biol. Inorg. Chem.* **1998**, *3*, 215. (f) Davis, W. B.; Svec, W. A.; Ratner, M. A.; Wasielewski, M. R. *Nature* **1998**, *396*, 60.
- (5) (a) Chohan, K. K.; Jones, M.; Grossmann, J. G.; Frerman, F. E.; Scrutton, N. S.; Sutcliffe, M. J. *J. Biol. Chem.* **2001**, *276*, 34142. (b) Jones, G. A.; Carpenter, B. K.; Paddon-Row, M. N. *J. Am. Chem. Soc.* **1999**, *121*, 11171. (c) Xie, Q.; Archontis, G.; Skourtis, S. S. *Chem. Phys. Lett.* **1999**, *312*, 237. (d) Balabin, I. A.; Onuchic, J. N. *Science* **2000**, *290*, 114. (e) Cave, R. J.; Newton, M. D.; Kumar, K.; Zimmt, M. B. *J. Phys. Chem.* **1995**, *99*, 17501. (f) Castner, E. W., Jr.; Kennedy, D.; Cave, R. J. *J. Phys. Chem. A* **2000**, *104*, 2869.
- (6) (a) Davis, W. B.; Ratner, M. A.; Wasielewski, M. R. *J. Am. Chem. Soc.* **2001**, *123*, 7877. (b) Graige, M. S.; Feher, G.; Okamura, M. Y. *Proc. Natl. Acad. Sci. U.S.A.* **1998**, *95*, 11679. (c) Hoffman, B. M.; Ratner, M. A. *J. Am. Chem. Soc.* **1987**, *109*, 6237. (d) Intermolecular electron-transfer reactions are influenced by the dependence of electronic coupling on donor-acceptor separation and the nature of the intervening medium. See ref 5f.
- (7) Fluctuations of rigid bridge mediated coupling magnitudes are small compared to the mean coupling matrix element in systems where the donor-acceptor interaction is not symmetry forbidden (see the last column (H_{CR}) of Table 9.1 for **1** in ref 5e. In systems where the donor-acceptor interaction is symmetry forbidden, the mean coupling value is small. Distortions of the molecular structure can generate coupling magnitudes that are larger than the mean value. See the sixth column (H_{CS}) of Table 9.1 for **1** in ref 5e.
- (8) (a) Lawson, J. M.; Paddon-Row, M. N.; Schuddeboom, W.; Warman, J. M.; Clayton, A. H. A.; Ghiggino, K. P. *J. Phys. Chem.* **1993**, *97*, 13099. (b) Kumar, K.; Lin, Z.; Waldeck, D. H.;

Zimmt, M. B. *J. Am. Chem. Soc.* **1996**, *118*, 243. (c) Read, I.; Napper, A.; Kaplan, R.; Zimmt, M. B.; Waldeck, D. H. *J. Am. Chem. Soc.* **1999**, *121*, 10976. (d) Lokan, N. R.; Paddon-Row, M. N.; Koeberg, M.; Verhoeven, J. W. *J. Am. Chem. Soc.* **2000**, *122*, 5075. (e) Kaplan, R. W.; Napper, A. M.; Waldeck, D. H.; Zimmt, M. B. *J. Am. Chem. Soc.* **2000**, *122*, 12039.

(9) The following citation describes the pressure dependence of electronic orbital overlap in hydrogen bonds: Li, H.; Yamada, H.; Akasaka, K.; Gronenborn, A. M. *J. Biomol. NMR* **2000**, *18*, 207.

(10) Read, I.; Napper, A.; Zimmt, M. B.; Waldeck, D. H. *J. Phys. Chem. A* **2000**, *104*, 9385.

(11) Napper, A. M.; Read, I.; Kaplan, R.; Zimmt, M. B.; Waldeck, D. H. *J. Phys. Chem. A* **2002**, *106*, 5288-5296.

(12) The rate constant, k_{rec} , comprises two distinct electron-transfer processes; conversion of the CT state to the molecule's ground singlet state and to the molecule's lowest energy triplet state. This is of no consequence to the current investigation.

(13) (a) Kumar, K.; Tepper, R. J.; Zeng, Y.; Zimmt, M. B. *J. Org. Chem.* **1995**, *60*, 4051. (b) Kaplan, R. Ph.D. Thesis, Brown University, Providence, RI, 2001.

(14) (a) Zeglinski, D. M.; Waldeck, D. H. *J. Phys. Chem.* **1988**, *92*, 692. (b) O'Connor, D. V.; Phillips, D. *Time Correlated Single Photon Counting*; Academic Press: New York, 1984.

(15) The fluorescence decay of **1** is fit to the biexponential form: $I(t) = a_+e^{-k_+t} + (1-a_+)e^{-k_-t}$. The forward electron-transfer rate constant k_{for} is obtained from $k_{\text{for}} = a_+(k_+ - k_-) - k_f + k_-$, and the reverse electron transfer rate constant k_{back} is obtained from $k_{\text{back}} = [(k_+ - k_-)^2 - (2k_f + 2k_{\text{for}} - k_+ - k_-)^2]/4k_{\text{for}}$. See the text for determination of k_f .

(16) The best fit equation is $\Delta_r G(\text{eV}) = 5.2451 \times 10^{-6}T^2 - 2.0156 \times 10^{-3}T + 1.2979 \times 10^{-1}$. The temperature is in units of K.

(17) Jortner, J. *J. Chem. Phys.* **1976**, *64*, 4860.

(18) (a) Zeng, Y.; Zimmt, M. B. *J. Phys. Chem.* **1992**, *96*, 8395. (b) Kumar, K.; Kurnikov, I.; Beratan, D.; Waldeck, D.; Zimmt, M. B. *J. Phys. Chem. A* **1998**, *102*, 5529.

(19) (a) Vath, P.; Zimmt, M. B.; Matyushov, D. V.; Voth, G. A. *J. Phys. Chem. B* **1999**, *103*, 9130. (b) Vath, P.; Zimmt, M. B. *J. Phys. Chem. A* **2000**, *104*, 2626. (c) Derr, D. L.; Elliott, C. *J. Phys. Chem. A* **1999**, *103*, 7888. (d) Matyushov, D. V. *Chem. Phys.* **1993**, *174*, 199. (e) Corte's, J.; Heitele, H.; Jortner, J. *J. Phys. Chem.* **1994**, *98*, 2527. (f) Evidence of increasing λ_s with decreasing temperature for bacterial reaction centers is presented in Ortega, J. M.; Mathis, P.; Williams, J. C.; Allen, J. P. *Biochemistry* **1996**, *35*, 3354.

(20) Matyushov, D. V.; Voth, G. A. *J. Chem. Phys.* **1999**, *111*, 3630.

-
- (21) The only other fitting parameter in these analyses was $|V|$, which was assumed to be temperature-independent.
- (22) Over small temperature ranges, the predicted λ_S appear to vary linearly with temperature. Over larger temperature ranges (140 K for 13DIP), curvature in the $\lambda_S(T)$ plots are evident.
- (23) The predicted values in column 3 of Table 9.1 are larger than previously reported in ref 10. A numerical error in a subroutine was responsible. The results of the corrected code have been checked with code kindly provided by Professor Matyushov.
- (24) The line in Figure 9.6 is a polynomial fit to this derived $|V(T)|$ data. A polynomial fit yields $|V(T)| = 2.257 \times 10^{-8}T^4 - 2.630 \times 10T^3 + 1.106 \times 10^{-2}T^2 - 2.014 \times 10T + 1.423 \times 10^2$. The temperature is in units of K and $|V|$ is in cm^{-1} .
- (25) Compound **2** in the current manuscript is the same as compound **8** in reference 18a.
- (26) (a) The line shape of a CT emission band includes contributions from the frequency dependence of the transition moment in addition to the frequency dependence of the Franck-Condon factors.^{26b} After correcting for the frequency dependence of the transition moment, the Franck-Condon line shape remains. The energy corresponding to the maximum of this line shape is reported in the text. (b) Marcus, R. A. *J. Phys. Chem.* **1989**, *93*, 3078. (c) It is not possible to extract unique values of λ_S and Δ_rG for compound **2** in alkylbenzene solvents. Impurity emissions obscure the blue side of these spectra, making a unique determination of Δ_rG impossible. The absence of detectable CT absorption bands eliminates a second route to unique Δ_rG determination. Consequently, there is substantial, correlated uncertainty in values of Δ_rG and λ_S obtained by fitting the CT emission line shape.
- (27) Both λ_S and $-\Delta_rG(S_1 \rightarrow \text{CT})$ are positive quantities that increase with increasing (nuclear) solvation. As a result, solvation differences provided by various alkylbenzene solvents reinforce, rather than cancel, in the term $\lambda_S - \Delta_rG(S_1 \rightarrow \text{CT})$.
- (28) In alkylbenzene solvents, the Coulomb interaction between the donor cation and acceptor ion amounts to $14.4 \text{ eV } \text{\AA}/(2.3 \times 7.1 \text{ \AA}) = 0.88 \text{ eV}$ for **1** and $14.4 \text{ eV } \text{\AA}/(2.3 \times 5.7 \text{ \AA}) = 1.10 \text{ eV}$ for **2**. The difference of these two values, 0.22 eV, is about the same as the 0.26 eV difference between the $\lambda_S - \Delta_rG(S_1 \rightarrow \text{CT})$ values presented for **1** and **2**.
- (29) Comparison of the magnitude and solvent dependence of λ_S for **1** and **2** would be particularly informative. It is not possible to extract accurate values of λ_S from the CT emission spectra.^{26c}
- (30) Ulstrup, J.; Jortner, J. *J. Chem. Phys.* **1975**, *63*, 4358.
- (31) Figure 9.7 shows that the one quantum mode and two quantum mode models predict different rate constant dependence on reaction free energy for $-\Delta_rG > \lambda_S$. The two models predict

comparable rate constant magnitudes and dependencies for $-\Delta_r G < \lambda_s$, however. Use of the two quantum model with $|V| = 7 \text{ cm}^{-1}$ and the parameters in Figure 9.7 yields rate constants that are indistinguishable from rate constants predicted using $|V| = 6 \text{ cm}^{-1}$ and the one quantum mode model in the range $-\Delta_r G < \lambda_s$. This demonstrates that electronic coupling magnitudes extracted from rate constant data in the Marcus normal region depend weakly on the model used to simulate the vibrational Franck-Condon factors. For further discussion of the influence of zero, one, and multi quantum mode models on Franck-Condon factors and extracted values of the electronic coupling, see refs 18b and 32d.

(32) (a) Hupp, J. T.; Williams, R. D. *Acc. Chem. Res.* **2001**, *34*, 808. (b) Hogiu, S.; Dreyer, J.; Pfeiffer, M.; Brzezinka, K. W.; Werncke, W. *J. Raman. Spectrosc.* **2000**, *31*, 797. (c) Godbout, J. T.; Zuilhof, H.; Heim, G.; Gould, I. R.; Goodman, J. L.; Dinnocenzo, J. P.; Kelley, A. M. *J. Raman Spectrosc.* **2000**, *31*, 233. (d) Lilichenko, M.; Tittelbach-Helmrich, D.; Verhoeven, J. W.; Gould, I. R.; Myers, A. B. *J. Chem. Phys.* **1998**, *109*, 10958.

(33) If reorganization of the cleft solvent makes significant contribution to λ_s , the agreement between the molecular model prediction and the experimental results (Table 9.1) is fortuitous and suggests that the parametrization of the molecular model overestimates the extra-cavity solvation of **1**.

(34) (a) Sharp, K.; Honig, B. *Annu. Rev. Biophys. Biophys. Chem.* **1990**, *19*, 301. (b) Sitkoff, D.; Sharp, K. A.; Honig, B. *J. Phys. Chem.* **1994**, *98*, 1978. (c) Zhang, L. Y.; Frieser, R. A. *J. Phys. Chem.* **1995**, *99*, 16479.

(35) The finite-difference Poisson-Boltzmann calculations indicate that exclusion of the solvent from the cleft of **1** reduces the solvent reorganization energy by less than 10%. See ref 18b.

(36) The value of $|V(295 \text{ K})|$ provided for 1,3,5-triisopropylbenzene is a linear extrapolation of the results obtained at lower temperatures.

(37) An alkyl group within the cleft provides smaller donor-acceptor electronic coupling than an aromatic ring in the cleft because the lowest energy superexchange state, D^+S^-A , has the “transferring” electron localized on the aromatic ring.

(38) (a) Dispersion and electrostatic interactions^{38b} between the anthracene, benzene, and the alkene diester generate a negative enthalpy change for solvent entry. Solvent “complexation” with **1** results in a reduction of translational entropy relative to two, independently diffusing molecules. (b) Tsuzuki, S.; Honda, K.; Uchimaru, T.; Mikami, M.; Tanabe, K. *J. Am. Chem. Soc.* **2002**, *124*, 104.

(39) According to the best fit analysis, approximately 10% of the charge recombination products are formed with one quantum of vibrational energy when the temperature reaches 360 K.

(40) (a) Smitha, M. A.; Prasad, E.; Gopidas, K. R. *J. Am. Chem. Soc.* **2001**, *123*, 1159. (b) Prasad, E.; Gopidas, K. R. *J. Am. Chem. Soc.* **2000**, *122*, 3191.

(41) (a) Segal, D. A.; Nitzan, A.; Davis, W. B.; Wasielewski, M. R.; Ratner, M. A. *J. Phys. Chem. B* **2000**, *104*, 3817. (b) Ashkenazi, G.; Kosloff, R.; Ratner, M. A. *J. Am. Chem. Soc.* **1999**, *121*, 3386. (c) Tang, J. *J. Chem. Phys.* **1993**, *98*, 6263.

Chapter 10. Use of U-shaped Donor-Bridge-Acceptor Molecules to Study Electron Tunneling Through Non-bonded Contacts

A systematic determination of electronic coupling matrix elements in U-shaped molecules is demonstrated. The unique architecture of these systems allows for the determination of the electronic coupling through a pendant molecular moiety that resides between the donor and acceptor groups, quantifying the efficiency of electron tunneling through non-bonded contacts. Experimental electron transfer rate constants and reaction free energies are used to calibrate a molecular based model that describes the solvation energy. This approach makes it possible to experimentally determine electronic couplings and compare them with computational values.[§]

10.1 Introduction

Electron transfer is a fundamental chemical process of immense scientific and technological importance. Consequently, it has received much attention.¹ This study evaluates the electron tunneling efficiency between electron donor and acceptor groups by way of non-covalent molecular contacts. The tunneling efficiency is quantified by the electronic coupling matrix element, $|V|$, which characterizes the electronic interaction between an electron donor (D) and acceptor (A). Donor-Bridge-Acceptor (DBA) molecules have been successfully used to address important issues in electron transfer because they provide systematic control over

[§] Reproduced with permission from Napper, A. M.; Head, N. J.; Oliver, A. M.; Shephard, M. J.; Paddon-Row, M. N.; Read, I.; Waldeck, D. H.; *J. Am. Chem. Soc.*; **2002**; 124(34); 10171-10181. Copyright 2002 American Chemical Society

molecular properties such as bridge geometry,² electronic state symmetry,³ reaction free energy,⁴ and others. Electron transfer in DBA molecules can be viewed as a superexchange mechanism that occurs through the orbitals of the intervening medium along a path between the donor and acceptor groups.⁵ Recent studies have demonstrated significant electronic couplings mediated through covalent bonds,⁶ through hydrogen bonds,⁷ and through solvent molecules.^{8,9} This work quantifies the electronic coupling through molecular moieties in van der Waals contact.

The U-shaped DBA systems designed by the Zimmt^{9,10} and Paddon-Row^{8,13} groups provide insight into the nature of non-adiabatic electron transfer processes that involve electron tunneling through solvent molecules. These systems have the donor and acceptor groups connected by a highly curved, rigid, covalent bridging unit that holds them apart at a fixed distance and orientation. An increase in the electron transfer rate constant has been observed in such systems when solvents of appropriate sizes and orbital energetics are used. This increase has been ascribed to the occupation of the interior cavity by a solvent molecule(s), *e.g.* benzene or benzonitrile, that allows for an enhanced *line-of-sight* electron tunneling between the donor and acceptor groups, as opposed to a longer, through-bond, coupling pathway occurring via the U-shaped bridge. The electronic couplings determined in these systems can be correlated to the size of the solvent molecule^{10b} and its electronic character.¹¹ However, these systems do not provide direct experimental evidence for the presence of a solvent molecule within the cleft.

More recently, Paddon-Row *et al.*¹² have constructed supramolecular systems in which a pendant group, covalently attached to the intervening bridge, occupies the interior of the cleft (Chart 10.1). Comparison of the electron transfer rates for three different systems, **1**, **2**, and **3**¹³, were measured as a function of solvent polarity. It was shown that when an aromatic moiety is positioned in the *line-of-sight* between the donor and acceptor pair, as in **1**, the observed rate

constant is significantly higher than systems in which it is not present, as in **2**, or is not in the *line-of-sight*, as in **3**.¹³ The current work quantitatively analyzes the electron transfer rate data for systems **1** and **2** in toluene and mesitylene solvents and combines it with earlier data¹³ obtained in CH₂Cl₂, THF, and acetonitrile solvents. Electronic structure calculations and the experimental free energies of reaction in the aromatic solvent are used to calibrate a molecular solvation model and subsequently determine the values of the electronic coupling matrix element for **1** and **2**. The electronic couplings are then compared with those calculated for a model system.

A frequently applied analysis of the electron transfer rate constant relies upon a semi-classical version of the Marcus expression. In this treatment, the solute high frequency intramolecular degrees of freedom, which are coupled to the charge separation process, are treated as a single effective quantum vibrational mode and the low frequency intramolecular and solvent modes are treated classically, so that the rate constant can be expressed as

$$k_{\text{eT}} = \frac{2\pi|V|^2}{\hbar\sqrt{4\lambda_o\pi k_B T}} \sum_{n=0}^{\infty} e^{-S} \left(\frac{S^n}{n!}\right) \exp\left[\frac{-(\Delta_r G + \lambda_o + nh\nu)^2}{4\lambda_o k_B T}\right] \quad (10.1)$$

where $\Delta_r G$ is the reaction free-energy, λ_o is the outer-sphere (solvent) reorganization energy, ν is the frequency of the effective vibrational mode, and S is the Huang-Rhys factor given as the ratio of the inner-sphere reorganization energy, λ_i , to the quantized mode energy spacing, $(\lambda_i/h\nu)$.^{1b} The electron transfer rate constants predicted by eq. 10.1 are a strong function of the parameter set used, and an accurate determination of these parameters is necessary when drawing comparisons with experimental rate data. The quantities $h\nu$ and λ_i are typically evaluated using a combination of experimental charge transfer spectra and *ab initio* calculations. Usually, $\Delta_r G$ is estimated through experimental redox data and dielectric continuum corrections to the solvation

energy. This approach is not appropriate in weakly polar and non-polar solvents, however. In this study $\Delta_r G$ is obtained in non-polar aromatic solvents from an analysis of the kinetic data using a two-state model. The model assumes that an equilibrium exists between the locally excited state and the charge-separated species and permits evaluation of the forward and backward electron transfer rate constants. These data are used to calibrate a molecular-based solvation model^{14,15} that is able to reproduce the experimental $\Delta_r G(T)$ values. The same model is used to predict the temperature dependence of λ_o . The electronic coupling $|V|$ and $\lambda_o(295\text{ K})$ are obtained by fitting the experimental rate constant data using the $\Delta_r G$ and $d\lambda_o/dT$ values from the model in conjunction with λ_i and ν values taken from charge transfer spectra.^{10a,16}

10.2 Experimental and Computational Details

Time resolved fluorescence kinetics of **1** and **2** were measured in toluene and mesitylene as a function of temperature. Comparison of the fluorescence decay kinetics with that of the donor-only reference molecules (**1noA** and **2noA**) allowed the electron transfer rate constants to be obtained. In all cases the molecule's excited decay law was found to be bi-exponential¹⁷. This finding is consistent with a small reaction free energy for charge separation, $\Delta_r G$. A previous study¹³ measured the electron transfer kinetics for **1** and **2** in CH_2Cl_2 , THF, and acetonitrile. In these three solvents, a single-exponential decay was observed, consistent with a larger reaction driving force. Simple continuum calculations suggest that the increased dipolar nature of these solvents leads to an increase in the magnitude of $-\Delta_r G$.

The preparation of the electron transfer molecules **1** and **2** were reported previously.¹² The solvents were purified in the manner described previously.¹⁰

Chart 10.1 Electron Transfer Molecules Studied and their Donor Only Analogues.

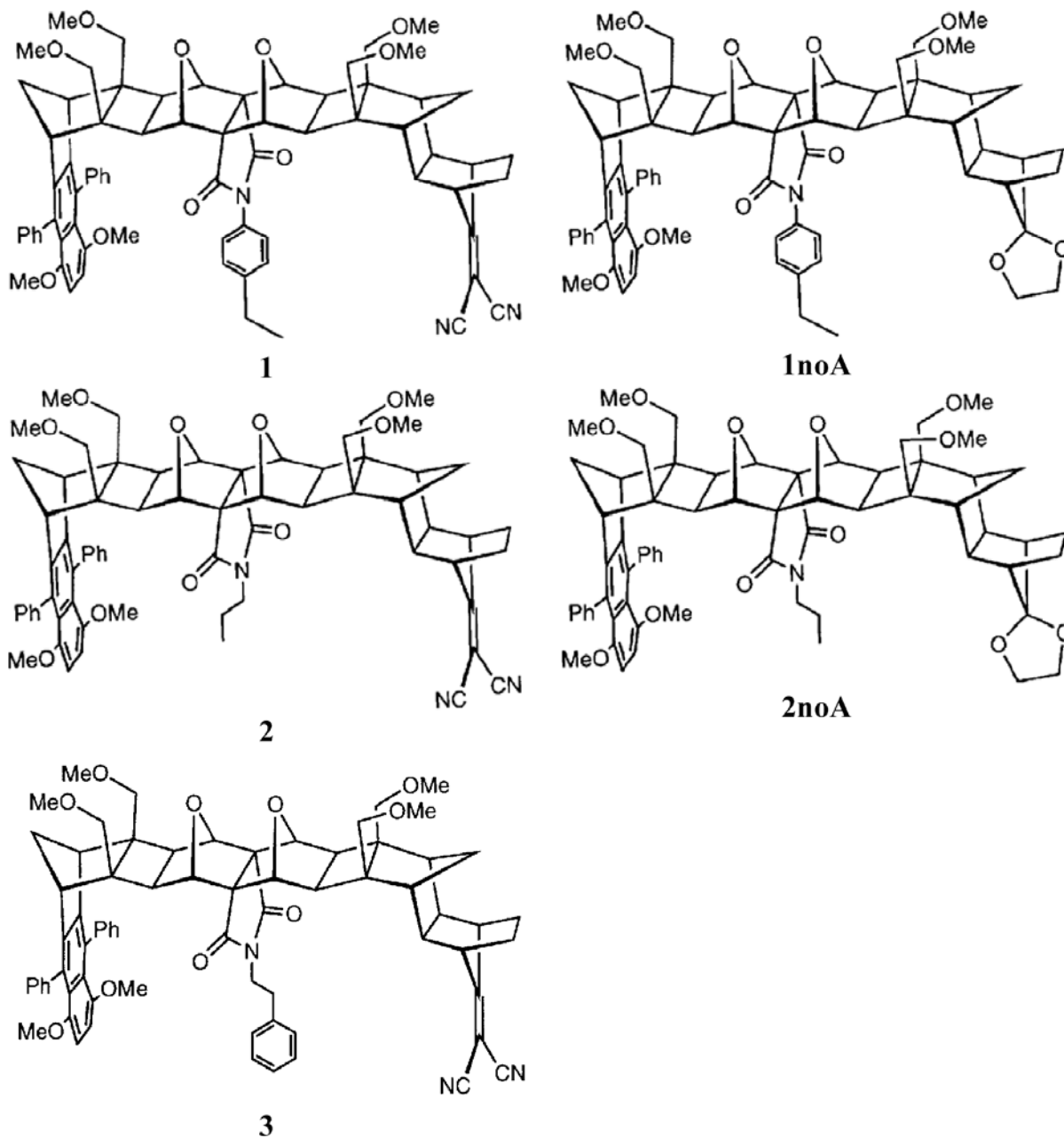
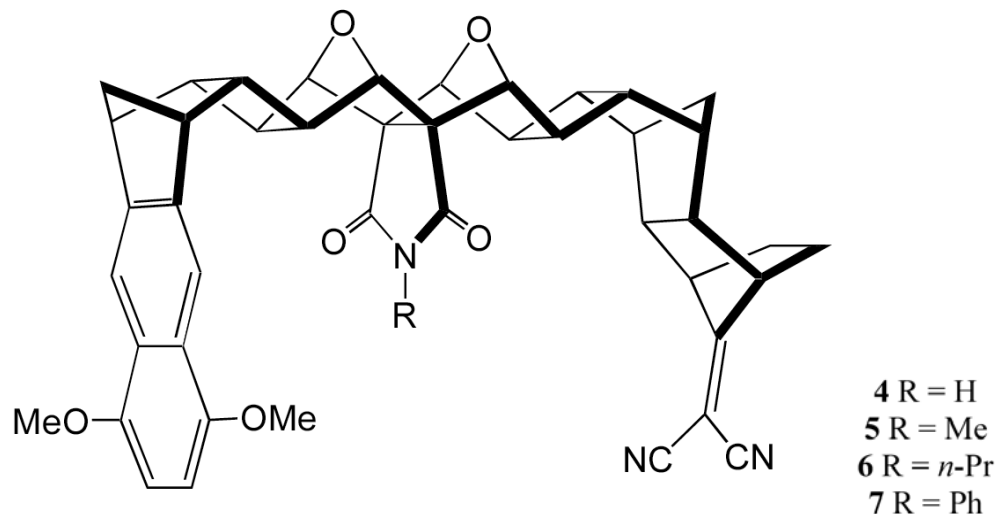


Chart 10.2 Chemical Structures of the Molecules Studied Computationally.



The ground and charge-separated (CS) states of the imido systems **4** - **7** were studied computationally. Ground state geometries of **4** - **7** were optimized at the RHF/3-21G level, whereas the excited singlet CS states were optimized at the UHF/3-21G level. It has been found that the UHF level of theory provides satisfactory optimized geometries of CS states,^{18,19} provided that the CS state is the lowest energy state of that particular state symmetry and multiplicity. As the CS states of **4** - **7** possess $^1A''$ state symmetry, that criterion is satisfied in these molecules. All calculations were carried out using the Gaussian 98 program.²⁰

Salient geometric features of the ground and CS states of **4** - **7** are summarized in Table 10.1. The ground state geometries for **4** - **7** are all very similar with the R group only having a small influence (< 2%) upon the distance between the DMN and DCV groups. The dipole moment varies little (5.3 - 6.0 D) and the total charges on the DMN, DCV, and imide chromophores show little change in going from **4** to **7**. It should be pointed out that the ground state optimized geometry of the N-phenyl system, **7**, was constrained to have C_s symmetry, with the phenyl ring lying in the plane of the imide group, and hence parallel with the DMN and DCV groups. This is not the global minimum however; that structure corresponds to the configuration,

1.35 kcal/mol more stable than the C_s structure, where the phenyl ring is rotated 71° out of the imide plane. Similarly, the N-*n*-propyl system, **6**, possesses a global minimum structure similar to, but 0.23 kcal/mol lower in energy than, the C_s symmetric structure used in these calculations. However, since the UHF level geometry optimization calculation of the CS state required that the molecule possess some symmetry, the C_s symmetry structures were used rather than the global minima structures for **6** and **7**.

In general, there is much to criticize in using a single determinant UHF wavefunction to calculate excited states. Not only does it neglect electron correlation but it fails to give a qualitatively correct description of the open-shell singlet excited state wavefunction - the zeroth-order wavefunction of such states is biconfigurational. Consequently, the UHF wavefunction for singlet excited states is severely spin contaminated. Indeed, we find that $\langle S^2 \rangle \sim 1$ for the UHF CS singlet CS states of **4-7**, implying ca. 50:50 singlet-triplet mixing. The use of such a low level of theory (UHF) to calculate reliable relaxed geometries and dipole moments (but not energies) of CS states has been addressed and fully justified in earlier publications.^{17,18} In particular, we have found that UHF/3-21G optimized geometries and dipole moments for giant CS singlet states related to those studied here are almost the same as those calculated using higher levels of theory, such as CIS which, being multideterminantal, does not lead to spin contamination of the singlet CS state wavefunction. We have also found that, at the UHF, CIS and DFT levels of theory, triplet CS state relaxed geometries and dipole moments of a variety of bichromophoric systems reported in ref 18 are practically identical to those calculated for the respective singlet CS states.

Table 10.1 Selected Data for the Ground and CS States of 4 - 7 and 7' Obtained from Geometry Optimizations at the (U)HF/3-21G Level

system	state	R_c^a (Å)	R_e^b (Å)	θ^c (deg)	μ (D)	charge		
						DMN	DCV	imide ^d
4	¹ A' ground	10.90	11.43		6.01	0.061	-0.191	-0.377
	¹ A'' CS	6.50	9.56	38.9	12.84	0.830	-0.726	-0.340
5	¹ A' ground	10.78	11.38		5.59	0.059	-0.192	-0.358
	¹ A'' CS	6.59	9.33	33.4	14.81	0.845	-0.718	-0.324
6	¹ A' ground	10.70	11.33		5.25	0.058	-0.192	-0.353
	¹ A'' CS	9.03	11.02	36.5	30.81	0.906	-0.749	-0.382
7	¹ A' ground	10.97	11.45		5.75	0.069	-0.187	-0.394
	¹ A'' CS	8.75	10.86	34.4	28.64	0.893	-0.751	-0.378
7'	¹ A'' CS				30.53	0.904	-0.768	-0.381

^a The center-to-center separation between the chromophores (see Fig. 10.1).

^b The bridge edge-to-edge separation (see Fig. 10.1).

^c The degree of pyramidalization of the DCV group (see Fig. 10.1).

^d The charge on the R group is also included in the total charge on the imide group.

This finding is not unexpected, given that charge separation is practically complete in the CS states of these giant bichromophoric systems and that the two radical ion chromophores are only *weakly coupled*, ie the CS states may be regarded as two isolated radical ions interacting almost exclusively by coulombic attraction. Consequently, both singlet and triplet wavefunctions are expected to have nearly the same spatial distribution. This explains why - notwithstanding severe spin contamination, amounting to 50:50 singlet-triplet mixing - the UHF relaxed singlet CS state geometries and dipole moments should be of acceptable quality. Lastly, the geometry for **7** was optimized at the CIS/3-21G level and compared to that obtained at the UHF level. The geometry and dipole moments of the CS singlet state are nearly the same in the two calculations. The CIS dipole moment is 28.56D, compared to 28.64 D (reported in Table 10.1). The only noticeable geometric difference is in the pyramidalisation angle (θ in Table 10.1) about the DCV group; at the UHF level it is 34.4 degrees whereas at the CIS/3-21G level it is 28.2 degrees. This discrepancy is quite small and does not impact the conclusions.

10.3 Evaluation of Through-Bond Mediated Electron Transfer

Given the U-shaped architecture of molecules **1** and **2**, the intervening pendant group should mediate electron transfer between the donor and acceptor chromophores in preference to the two chromophores coupling via the orbitals of the connecting bridge in a *through-bond*, or superexchange, mechanism. The through-bond mechanism has been extensively studied in similar systems.²¹ The importance of the through-bond coupling mechanism, which may be in operation in **1** and **2**, to the overall electronic coupling was assessed by comparing the electron transfer rate of **1** and **2** with that of a reference system, **8**. System **8** possesses a bridge with the

same number of bonds linking the donor and acceptor chromophores as in molecules **1** and **2**, however, it does not possess the U-shaped architecture, so that the most direct coupling of the donor and acceptor is via the bonds of the bridge and not through any solvent molecules. The electron transfer rate of **8** in toluene was found to be less than $2 \times 10^8 \text{ s}^{-1}$ at 293 K and 333 K. In contrast, the electron transfer rate of **1** in toluene was found to be $29 \times 10^8 \text{ s}^{-1}$ at 327 K, and the electron transfer rate of **2** in toluene was found to be $16 \times 10^8 \text{ s}^{-1}$ at 327 K. A comprehensive set of electron transfer rate constant data for **1** and **2** as a function of temperature is provided in the supplementary material. These data show that in the case of **1** and **2** the through-bond coupling mechanism is only weakly present, having only a minor influence upon the overall coupling.

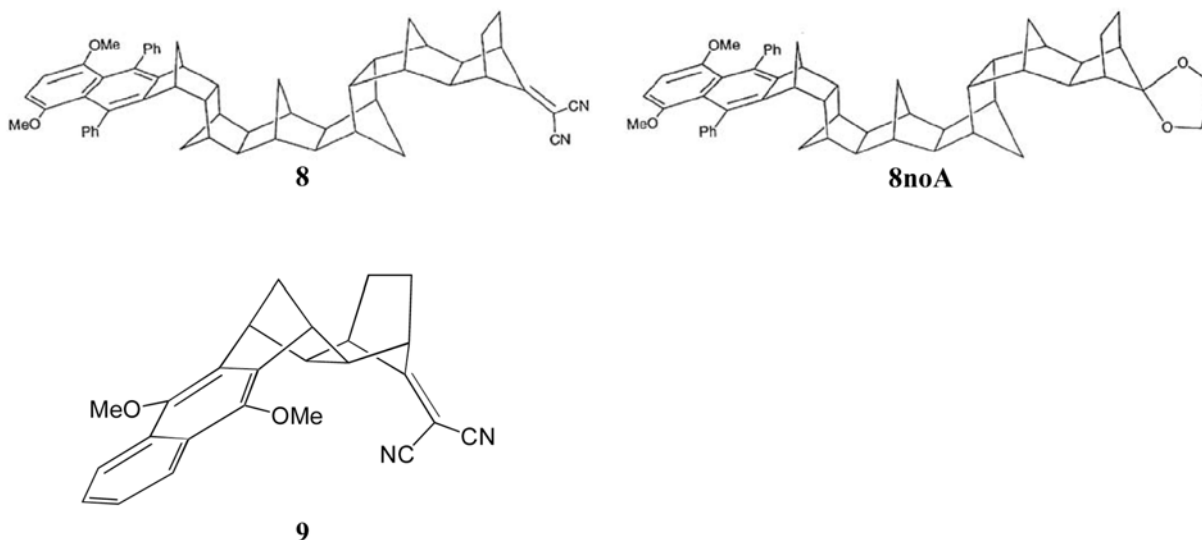
10.4 Determination of λ_i and $h\nu$

Charge transfer absorption and emission band shape analysis provides an effective means of determining the internal reorganization energy associated with the electron donor and acceptor groups. For an electron transfer reaction that is coupled to a single, effective, high frequency vibrational mode, the emission band shape $L(\Delta E)$ is given by

$$L(\Delta E) = \exp(-S) \sum_{n=0}^{\infty} \frac{S^n}{n!} \exp\left[-\frac{(\Delta_r G + \Delta E + n h \nu + \lambda_o)^2}{4 \lambda_o k_B T}\right] \quad (10.2)$$

where ΔE is the photon energy. In practice, the fitting treats $\Delta_r G$, $h\nu$, λ_i and λ_o as adjustable parameters and often gives several parameter sets that provide adequate fits. By combining this analysis with quantum chemical calculations a suitable range of parameter values can be established.¹⁰

Chart 10.3



10.4.1 Charge Transfer Spectra

In the present work, the internal reorganization energy is determined using the charge transfer absorption and emission spectra for a related compound, **9**, in hexane^{21d,22}. Although **9** has a different bridge structure than **1** and **2**, it has the same donor and acceptor groups and can reliably be used to quantify the internal reorganization parameters, since they are primarily associated with the geometry changes of the donor and acceptor upon electron transfer. The Stokes shift, B , is related to the total reorganization energy through

$$B = 2(\lambda_o + \lambda_i) \quad (10.3)$$

and the Stokes shift for **9** in hexane is 1.26 eV. Assuming that λ_o in this solvent is zero, a value of 0.63 eV is obtained for λ_i . The frequency of the effective quantum mode can be determined from the charge-transfer emission bandwidth, $\Delta E_{1/2}$. When the mode frequency $h\nu \gg k_B T$, the emission bandwidth can be written as,

$$(\Delta E_{1/2})^2 \cong 8(\ln 2)(2k_B T \lambda_o + \lambda_i h \langle \nu \rangle) \quad (10.4)$$

Assuming that the outer sphere reorganization energy is zero in hexane, one finds an average intramolecular mode frequency, $h\langle\nu\rangle$, of 1100 cm^{-1} from the emission spectrum shown in Ref. 21d.

10.4.2 Theoretical Calculations

Quantum chemical calculations indicate that electron transfer can result in dramatic geometrical changes between the ground and charge separated (CS) states for these U-shaped molecules, particularly in non-polar solvents.^{18,19} The two major structural features present in the CS state geometries, compared to those calculated for the ground states, is the pyramidalization of the DCV radical anion group at C7 and the degree of distortion in the DMN radical cation group, as shown in Figure 10.1. Some distortion of the connecting bridge also occurs. While the pyramidalization is inherent in the DCV radical anion species^{18,19}, the direction of this pyramidalization and the general distortion of both the DMN group and the bridge arise from the strong Coulomb attraction between the two oppositely charged ends of the molecule. For example, the center-to-center chromophore separation, R_c , contracts, on average, by 3.6 \AA , while the bridge's edge-to-edge separation, R_e , contracts by about 1.5 \AA (Fig. 10.1 and Table 10.1). Unlike the ground state structures, the R_c and R_e values found for the CS state geometries of **4** - **7** depend upon the nature of the imide substituent group, R. For R_c , the range of values for the CS state geometries is 2.53 \AA , whereas for the ground states it is only 0.21 \AA . For R_e , the ranges are 1.69 \AA in the CS states and 0.11 \AA in the ground state. Especially noticeable is the difference in the R_c distances between the molecules with small pendant groups

4 (6.50 Å) and **5** (6.59 Å) as compared to the molecules with more bulky pendant groups, **6** (9.03 Å) and **7** (8.75 Å). This difference arises from the size of the *n*-propyl and phenyl groups, which are fully interposed between the DMN and the DCV groups in **6** and **7**, respectively. The steric bulk of these groups forces the oppositely charged DMN⁺ and DCV⁻ chromophores in the CS state to remain further apart despite the strong Coulomb attraction. In contrast, the H and methyl groups are small enough to allow significant distortion of the DMN and DCV chromophores to occur. Consequently, the charge-transfer state dipole moment that was calculated for molecule **7** was used in the calculations of the outer-sphere reorganization energy and Gibbs free energy of reaction, which are presented below.

We emphasize that all optimized geometries refer to gas phase structures. Consequently, the relaxed gas phase geometries of the CS states will be more distorted than those in solvent because the electrostatic interactions will be attenuated in solvent. Unfortunately, all attempts so far to calculate relaxed geometries by including solvent effects (using solvation continuum models) have failed, owing to lack of convergence in the SCF part of the calculation. Nevertheless, we did manage to calculate the relaxed geometry for the radical anion of 7-dicyanovinylbornane, **10**, in a solvent continuum having a dielectric of 37.5, equivalent to acetonitrile. As with the gas phase structure, **10** displayed a marked pyramidalization about the DCV group. We therefore believe that our relaxed gas phase geometries of CS states reveal structural features that are retained, perhaps to an attenuated degree, in solvents.

Two vibrational modes appear to be coupled to the electron transfer in our systems. First, the formation of the anion involves a pyramidalization of the DCV acceptor group and an out-of-plane bending mode (see Chart 10.4). The frequency associated with out-of-plane bending of the DCV group, schematically depicted by **10a**, is 1088 cm⁻¹.²³

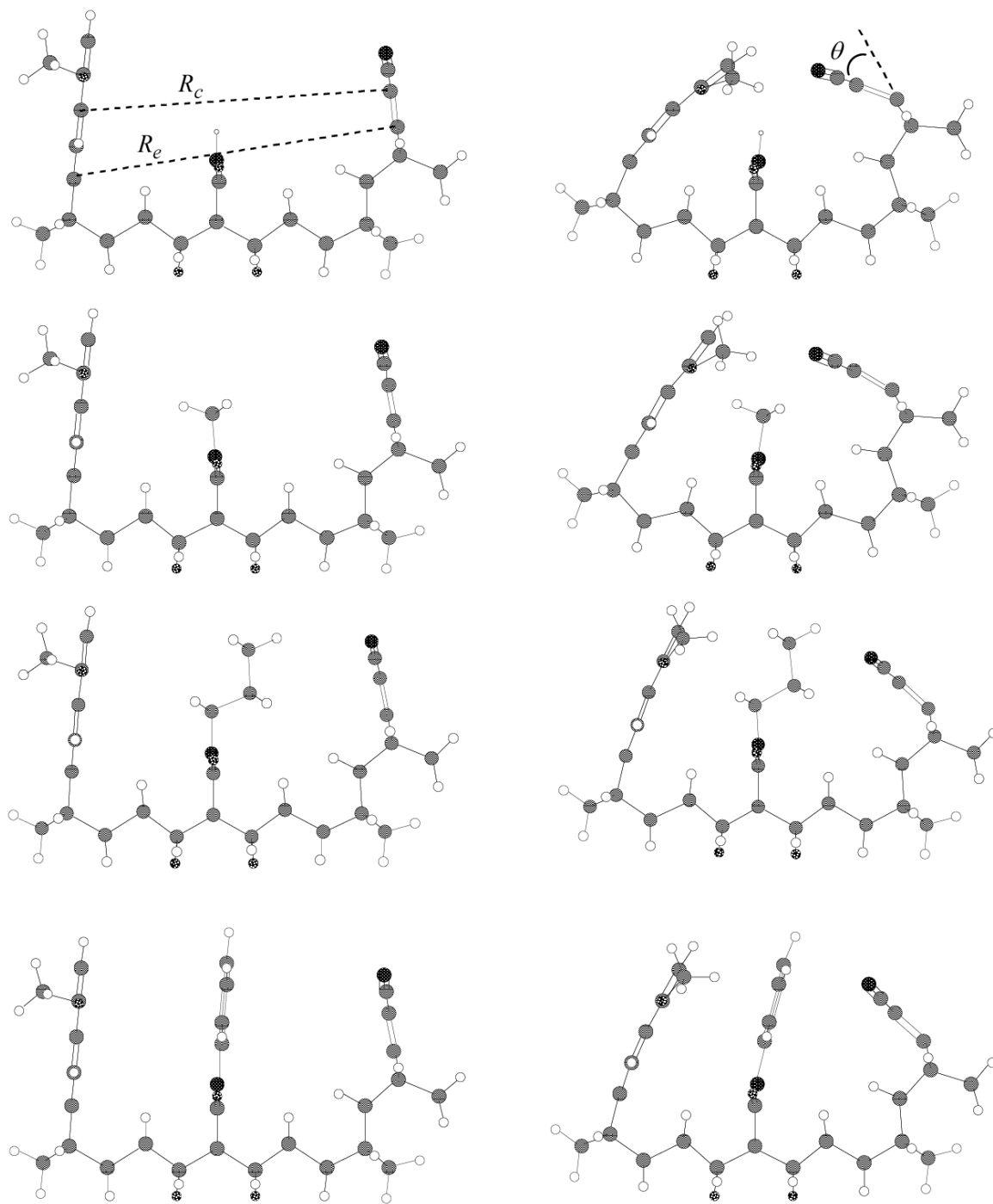
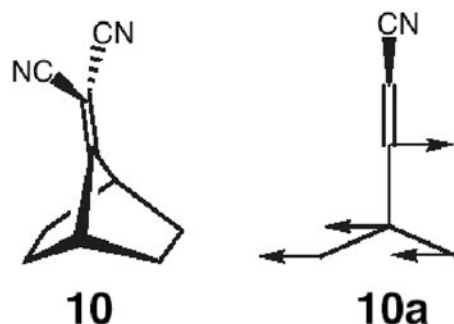


Figure 10.1 Profiles of the ground (left) and CS (right) optimized geometries for the systems 4 (top) - 7 (bottom) obtained at the (U)HF/3-21G level.

Chart 10.4



Second, the naphthalene ring undergoes a ring deformation upon formation of the cation that primarily involves stretching modes at $\sim 1600\text{ cm}^{-1}$. These frequencies bracket the 1100 cm^{-1} effective mode frequency found from the analysis of the charge transfer spectra. Both results are consistent with the large internal reorganization energy observed in these systems. With no information at this time as to the degree of partitioning of the internal reorganization energy with respect to the high-frequency modes, the analysis is largely limited to the case of a single high-frequency mode of 1600 cm^{-1} . This choice is consistent with prior attempts at analysis using the semi-classical equation in related systems with dicyanoethylene acceptors.^{10a} The effect of independently partitioning the inner-sphere reorganization energy between two modes, taken to be 990 cm^{-1} and 1600 cm^{-1} , was explored to examine its impact on the ratio of the electronic coupling matrix element for **1** and **2**. Calculations of the actual partitioning of the inner-sphere reorganization energy are underway and will be published later. Lastly, no matter what partitioning was used, the electronic coupling was always larger for **1** than **2**.

10.5 Determination of $\Delta_r G$

$\Delta_r G$ can be determined from experimental fluorescence lifetime data, provided the locally excited (LE) and charge separated (CS) states lie close in energy, so that an excited state equilibrium occurs.^{10b,24,25} The analysis assumes that the absorption and emission of radiation arises from the LE state of the donor and allows the rate constants k_{for} (LE to CS) and k_{back} (CS to LE) to be determined. Their ratio is used to compute $\Delta_r G$. This behavior was observed for **1** in both toluene and mesitylene. In toluene and mesitylene the reaction free energy for **1** changes systematically with temperature from -0.12 eV and -0.05 eV (see Fig 10.2). At higher temperatures the same effect was observed for **2** in mesitylene. In toluene the fluorescence lifetime decay was clearly dominated by the short time component (*ca.* 99% or greater at all the temperatures) so that it was not possible to accurately determine the reaction free energy for this solvent. In the more polar solvents, THF, CH_2Cl_2 , and CH_3CN , the CS state is sufficiently stabilized so that the back electron transfer is not observed.¹³

The measured $\Delta_r G$ values for **1** (in mesitylene and toluene) and **2** (in mesitylene only) were used to calibrate a molecular-based solvation model. The model was then used to predict the temperature dependence of λ_0 and the reaction free energy in more polar solvents. The model treats the solute and solvent molecules as polarizable hard spheres and accounts for dipole-dipole, dipole-quadrupole, induction, and dispersion interactions. $\Delta_r G$ is calculated as the sum of four components

$$\Delta_r G = \Delta_{\text{vac}} G + \Delta_{\text{dq,i}} G^{(1)} + \Delta_{\text{disp}} G + \Delta_1 G^{(2)} \quad (10.5)$$

where $\Delta_{\text{vac}} G$ is the free energy of the process in vacuum, $\Delta_{\text{dq,i}} G^{(1)}$ is the contribution from first-order dipole, quadrupole, and induction interactions, $\Delta_{\text{disp}} G$ is the contribution from dispersion

interactions and $\Delta_i G^{(2)}$ represents contributions from second-order induction interactions. Details about this model and its implementation are provided in Appendix A and elsewhere.¹⁴

Use of this model requires parameters for both the solute and the solvent. The toluene and mesitylene solvent parameters are the same as those described in earlier work¹⁴. The solute ground and excited state dipole moments were set equal to those calculated at the UHF/3-21G level for **7** (Table 10.1), namely 5.75 D for the ground state and 28.64 D for the CS state. The polarizability was calculated to be $\sim 128 \text{ \AA}^3$ for **1** and 124 \AA^3 for **2**.²⁶ Table 10.2 summarizes the other solute parameters. Calibration of the molecular model requires determination of the parameters $\Delta_{\text{vac}}G$, the solute radius R_o , and $\Delta\gamma'$. The temperature dependent $\Delta_r G$ values in toluene and mesitylene, measured for **1** and **2** (mesitylene only), were simultaneously fit to eq. 10.5 by adjusting these three parameters.

Table 10.2 Parameters used in the molecular solvation model.

Solute Radius (\AA)	7.77
$\Delta_{\text{vac}}G$ (eV) for 1	0.159
$\Delta_{\text{vac}}G$ (eV) for 2	0.114
$\Delta\gamma'$ (\AA^3)	6.2
μ_{ex} (D)	28.64
μ_{gs} (D)	5.75
Toluene polarizability (\AA^3)	12.32
Mesitylene polarizability (\AA^3)	16.14

The fit of the model to the experimental $\Delta_r G$ for **1** in toluene, **1** and **2** in mesitylene, and the predicted $\Delta_r G$ values for **2** in toluene are shown in Figure 10.2. Given the similarity between molecules **1** and **2**, the parameter set was taken to be the same for both solutes with the exception of $\Delta_{\text{vac}} G$. The $\Delta_{\text{vac}} G$ value was chosen independently for the two solutes, so that the $\Delta_r G$ value in **2** was more negative than in **1**, an observation consistent with the experimental data. The difference in $\Delta_{\text{vac}} G$ for **1** and **2** can be rationalized as the difference in the Coulomb stabilization energies for **1** and **2** in vacuum.

Using effective dielectric constants for benzene and hexane in the Coulomb's law expression, the Coulomb stabilization energy for **2** is estimated to be 0.066 eV lower than that for **1**.²⁷ The resulting $\Delta_r G$ values are in qualitative agreement with the experimental data. The difference in the value of $\Delta_{\text{vac}} G$ for solutes **1** and **2** was also estimated by treating $\Delta_{\text{vac}} G$ as an adjustable parameter, which was constrained by fitting the experimental Gibbs free energy data from predictions derived using the molecular solvation model. The best fit difference of 0.045 eV is quite close to the observed difference and that which is estimated. The table in Appendix A gives the predicted $\Delta_r G$ values and lists the contributions from the different terms in eq. 10.5.

With a parameterization of the internal reorganization energy parameters (λ_i and ν) and the reaction free energy ($\Delta_r G$) in hand, it is possible to fit the temperature dependent rate data to the form of eq 10.1 and obtain values for the electronic coupling parameter $|V|$ and the solvent reorganization energy λ_o .

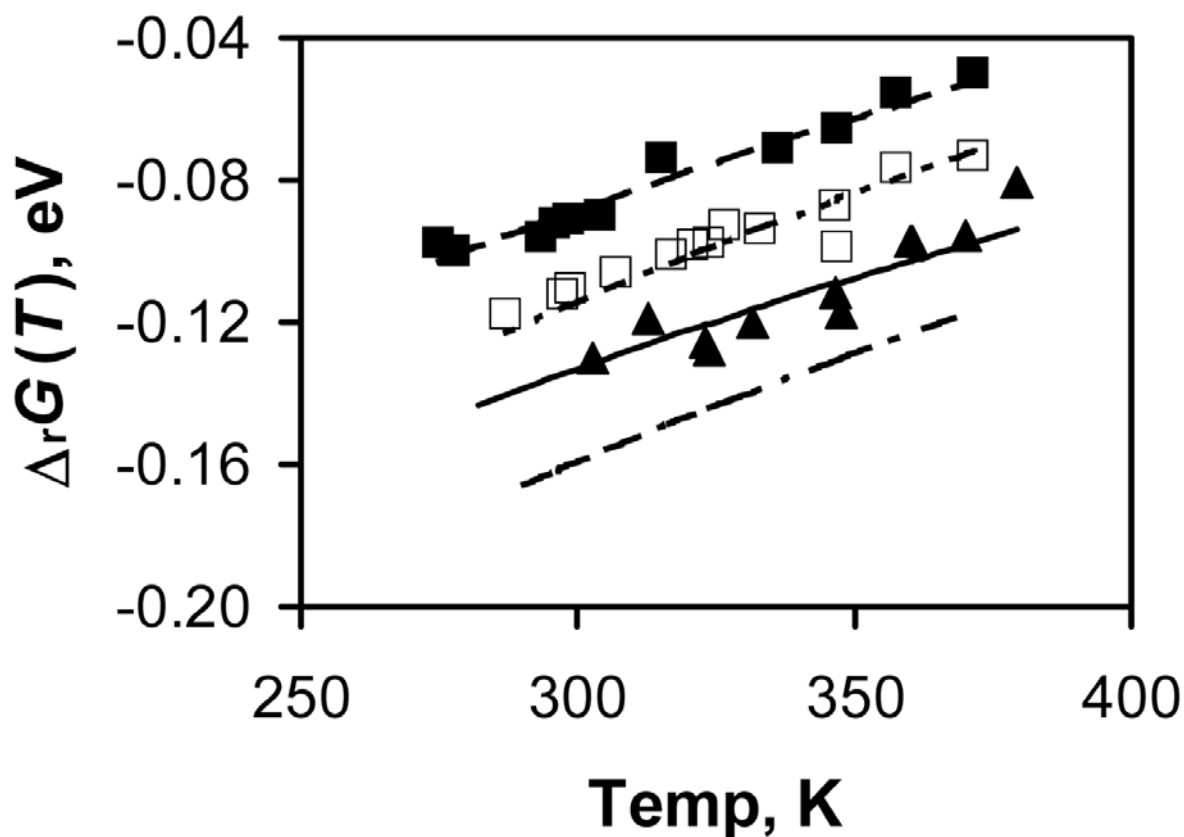


Figure 10.2 The experimental $\Delta_r G$ values are plotted for **1** in toluene (open square) and mesitylene (filled square). The experimental values for **2** in mesitylene are shown as filled triangles. The lines show the $\Delta_r G$ values predicted for all four aromatic systems by the molecular model with the parameters given in Table 10.2. The experimental values for **2** in toluene could not reliably be determined from the fluorescence lifetime data. The $\Delta_r G$ values predicted by the model for **2** in toluene are indicated by the bottom dot-dashed line. See text for details.

This analysis would be straightforward if $|V|$ and λ_o were known to be temperature independent. Although $|V|$ is likely to satisfy this approximation, the solvent reorganization energy is expected to be temperature dependent since the solvation of the solute by the solvent is temperature dependent. For this reason the molecular model that is parameterized to the reaction free energy data is used to treat the temperature dependence of the solvent reorganization energy. The temperature dependent rate constant data can then be used to extract the best fit parameters for the electronic coupling parameter $|V|$ and the solvent reorganization energy at 295K, $\lambda_o(295\text{ K})$.

10.6 Determination of λ_o

The outer sphere reorganization energy is also calculated using this molecular solvation model. The reorganization energy is written as a sum of three components

$$\lambda_o = \lambda_p + \lambda_{\text{ind}} + \lambda_{\text{disp}} \quad (10.6)$$

where λ_p accounts for solvent reorganization arising from the solvent dipole and quadrupole moments, λ_{ind} is the contribution from induction forces, and λ_{disp} accounts for the dispersion interactions. The model treats the solute as a dipolar, polarizable sphere and finds the reorganization energy; see the Appendix and earlier work^{14,15} for further details. The appendix also provides the values of the reaction free energy and the reorganization energy that are predicted by the model. It is well appreciated that continuum calculations are unreliable in non-polar solvents. More importantly, the continuum theory fails to predict the temperature dependence of λ_o , *i.e.*, the sign of $d\lambda_o/dT$, even in polar systems, whereas the molecular model

predicts the correct temperature dependence.^{10a} The continuum model incorporates only the temperature dependence of molecular rotation, whereas the molecular model includes both translational and rotational degrees of freedom so that the temperature dependence of the reorganization energy is more faithfully reproduced. For these reasons the molecular model is used to calculate $d\lambda_0/dT$ and an adjustable offset is used to fit the experimental data. The best fit $\lambda_0(295\text{ K})$ values are reported in Tables 10.3 and 10.4.

10.7 Determination of the Electronic Coupling, $|V|$

Using the values obtained for λ_i , ν , $\Delta_r G$, and $d\lambda_0/dT$, it is possible to fit the temperature dependent rate data to eq 10.1 and obtain electronic coupling $|V|$ and $\lambda_0(295\text{ K})$ values. For these systems, λ_i was taken to be 0.63 eV and ν was taken to be 1600 cm^{-1} . The fitting was performed using $\Delta_r G(T)$ and $d\lambda_0/dT$ values predicted by the molecular model. Figures 10.3 and 10.4 show fits of the model to the rate data for **1** and **2** in toluene and mesitylene as well as three more polar solvents, namely CH_2Cl_2 , THF, and acetonitrile. The rate data for **1** and **2** in the latter three solvents were reported earlier¹³, but until now a quantitative analysis of the data has not been reported. The rate data were fit to eq 10.1 by adjusting $\lambda_0(295\text{ K})$ in each solute-solvent system and adjusting the electronic coupling of the solute. Clearly the fit quality is excellent. The values obtained for $|V|$ and λ_0 are reported in Tables 10.3 and 10.4. The electronic coupling is not dependent on the solvent and the value obtained for **1** is almost four times larger than the value obtained for **2**, namely 168 cm^{-1} versus 46 cm^{-1} .

Table 10.3 Best Fit $|V|$ and $\lambda_0(295\text{ K})$ values for the aromatic systems.

System	$ V $, cm^{-1}	$\lambda_0(295\text{ K})$ in toluene, eV	$\lambda_0(295\text{ K})$ in mesitylene, eV
1	168	0.73	0.69
2	46	0.59	0.56

Table 10.4 Free energy and reorganization energies for **1** and **2** in the more polar solvents.

Solvent	$\Delta_r G^a$ (295 K), eV		$\lambda_0(295\text{ K})$, eV	
	1	2	1	2
THF	-0.37	-0.42	1.13	1.09
CH ₂ Cl ₂	-0.37	-0.42	1.20	1.16
CH ₃ CN	-0.52	-0.57	1.50	1.50

^a The reaction free energy was calculated using the molecular model for solvation. Details may be found in the text and in the appendix.

From eq 10.1, a three to fourfold increase in the electronic coupling should give rise to a nine to sixteen fold increase in the rate constants. However the magnitude of the *FCWDS* term, arising from the differing $\Delta_r G(T)$ data, also changes for **1** and **2** and this change partially counteracts the effect from the change in $|V|$. The best fit λ_o values, evaluated at 295 K, are also reported. From simple continuum arguments, the solvent reorganization energy is expected to be larger for the solvent with the more dipolar character, and this expectation is verified for both **1** and **2** (see Tables 10.3 and 10.4). In addition the reorganization energy for **1** is found to be a bit higher than that for **2** in most of the solvents, which may indicate a small difference in the effective molecular volume or dipole moment between the molecules. The dependence of the electronic coupling ratio ($|V(\mathbf{1})|/|V(\mathbf{2})|$) on the value of the solvent reorganization energy was analyzed in a systematic manner and the electronic coupling of **1** was found to be larger than that of **2** for all reasonable reorganization energies. Details of this analysis are provided in the supplemental information, which contains contour plots of $|V(\mathbf{1})|/|V(\mathbf{2})|$ and χ^2 as a function of λ_o , and plots like that shown in Figure 10.3 under different fitting constraints.

Within the context of a two-state model, the electronic coupling matrix element $|V|$ may be taken to be one half of the energy gap at the avoided crossing of the two adiabatic electronic states, in this case being the locally excited and the CS states, (*i.e.*, $\Delta E = 2V$) as shown in Figure 10.5.

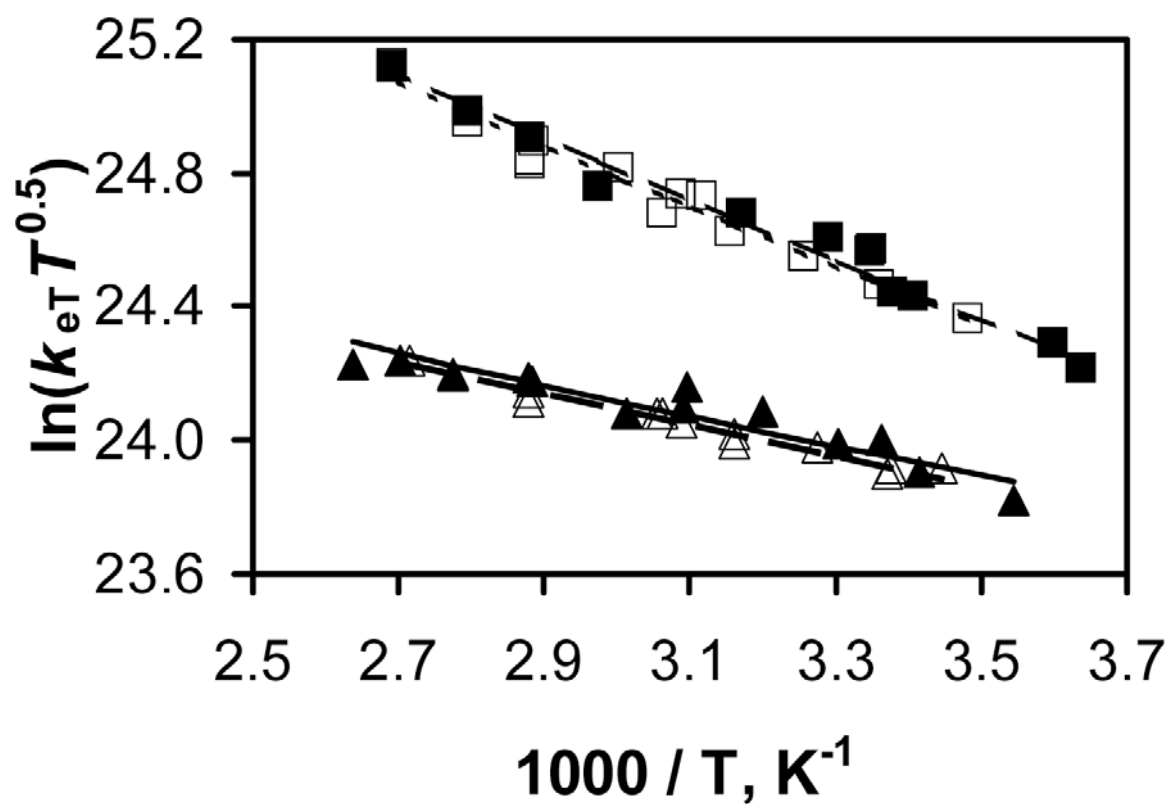


Figure 10.3 Experimental rate data (k_{for}) are plotted versus $1/T$, for **1** in toluene (open square), **1** in mesitylene (filled square), **2** in toluene (open triangle), and **2** in mesitylene (closed triangle). The lines represent the best fits to eq 10.1; see text for details.

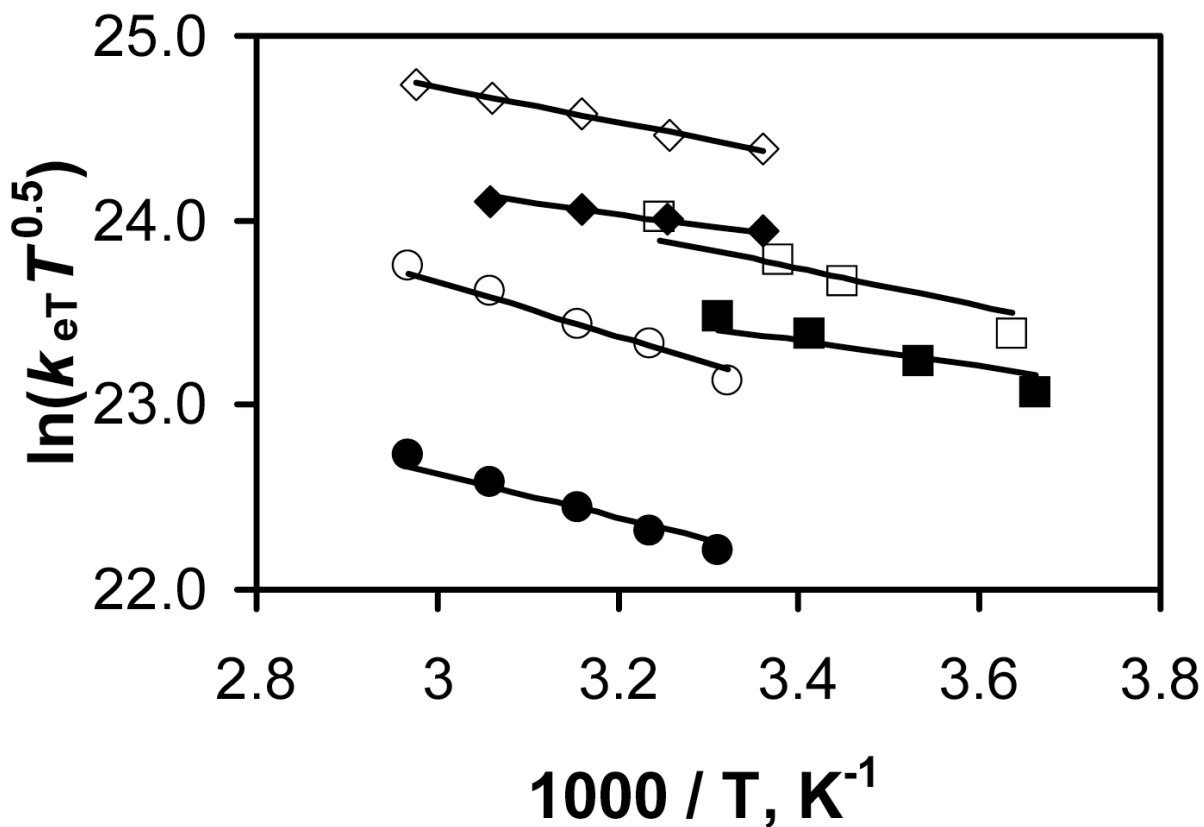


Figure 10.4 Experimental rate data (k_{for}) are plotted versus $1/T$, for 1 in CH_3CN (open circle), CH_2Cl_2 (open square) and THF (open diamond) and 2 in CH_3CN (filled circle), CH_2Cl_2 (filled square), and THF (filled diamond). The lines represent the best fits to eq 10.1; see text for details.

To determine if the electronic coupling between the DMN and DCV groups is in fact mediated by the substituent on the central imide group, or whether the coupling proceeds mainly via a through-bond mechanism,²⁸ ΔE was calculated for model systems based on the N-phenyl system, **7**, using the CIS method. Given the size of these systems two approximations were made in order to make the analysis computationally feasible. First, the model system **7'** was created, which, while possessing the same geometry as the CS state of the N-phenyl imide, **7**, has a hydrogen atom in place of the phenyl group (with an N-H bond length of 1.01 Å).²⁹ Second, it was assumed that the reaction coordinate for the electron transfer in **7** (and **7'**) is the DCV pyramidalization angle, θ , and that all other geometrical parameters are frozen. This assumption was deemed reasonable because exploratory calculations on **7** revealed that the electron transfer process is very sensitive to the magnitude of θ but not other geometrical features. Thus, for both **7** and **7'**, a series of CIS/3-21G single point energy calculations were carried out in which θ was varied until the energy gap between the locally excited state and the CS state reached a minimum value which was then equated to twice the value of the electronic coupling, $|V|$.

In the case of **7**, the avoided crossing is encountered when the DCV is only slightly pyramidalized, with $\theta = 12^\circ$. The electronic coupling, $|V|$, at this point is 16 cm^{-1} . In the case of **7'** the avoided crossing occurs at a slightly larger pyramidalization angle of $\theta = 17.5^\circ$, with $|V|$ equal to 5 cm^{-1} . Thus, $|V|$ for **7'** is significantly smaller, by a factor of three, than that calculated for **7**. While the predicted magnitude of $|V|$ for **7** is substantially smaller than that estimated for **1**, from experimental data, the calculations correctly predict a three to fourfold enhancement of the electronic coupling that arises from the presence of the aromatic ring in the molecular cavity of **7**, compared to **7'**.

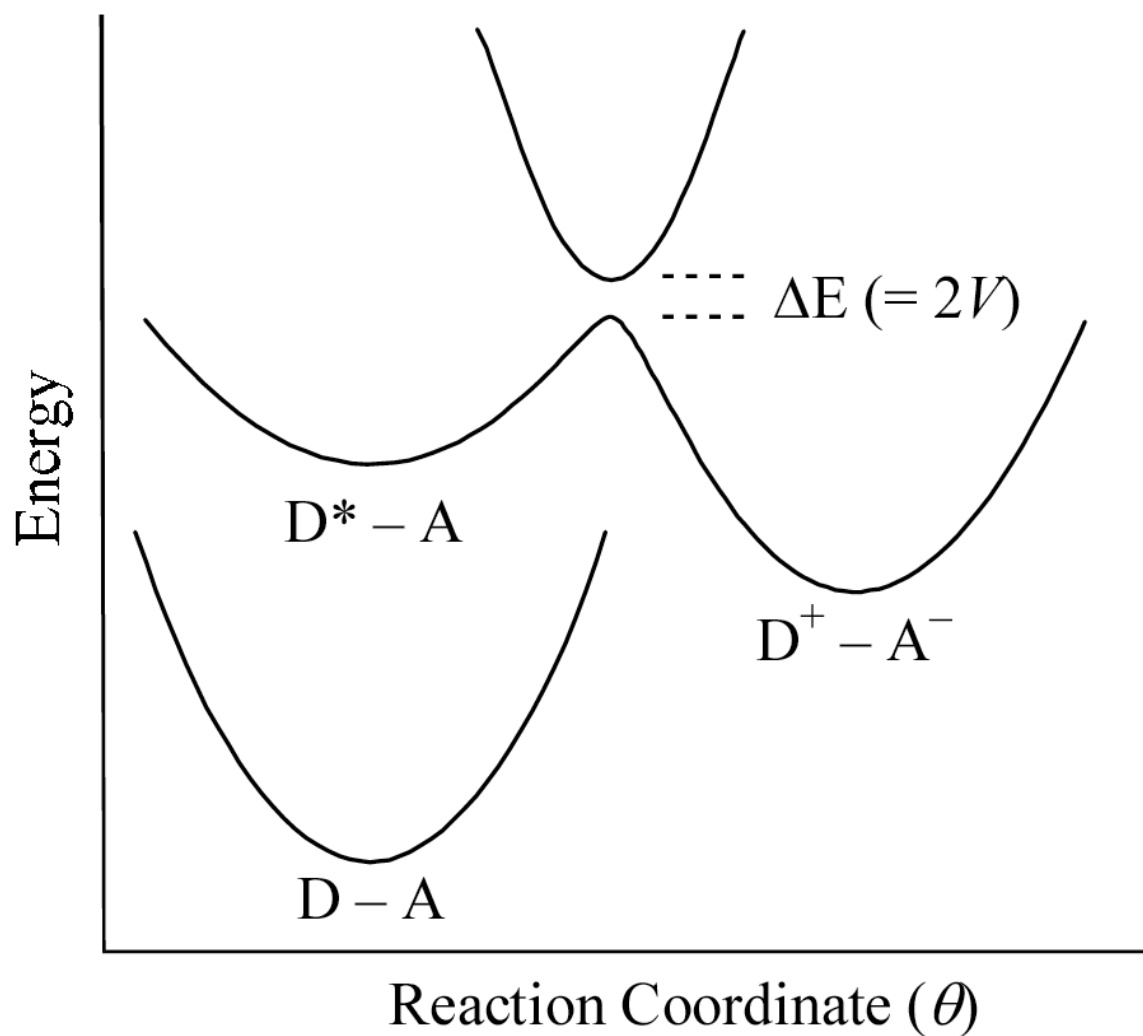


Figure 10.5 A schematic of the potential energy surface for photo-induced electron transfer is shown here. D-A is the ground state surface; D*-A is the locally excited state surface; and D⁺-A⁻ is the CS state surface. At the avoided crossing, the energy gap between the locally excited and CS states, ΔE , is twice the electronic coupling matrix element for electron transfer, $|V|$.

The enhancement in the magnitude of $|V|$ is, no doubt, caused by a superexchange mechanism. These computational results indicate that the central R group is important in mediating the coupling between the DMN and the DCV groups and that a U-shaped system provides a controlled way to analyze effects that different solvents may have upon inter- and intra-molecular electron transfer processes.

The magnitude of the electronic coupling that is extracted from experimental data depends strongly on the value of other parameters in eq 10.1, in particular the reorganization energies, the effective frequency and the free energy. The analysis in mesitylene and toluene uses the experimental free energy and adjusts the outer sphere reorganization energy along with the electronic coupling to fit the rate data. The impact of the modeling for the inner sphere reorganization energy with a single effective quantum mode was assessed by considering a two-mode model (*vide supra*). The use of a two mode model generated results that are consistent with that found from the single mode model; *i.e.*, the electronic coupling in **1** is significantly larger than that in **2**. Figure 10.6 shows how the ratio of electronic coupling magnitudes changes when the partitioning of the internal reorganization energy between the 1600 cm^{-1} mode and the 990 cm^{-1} mode is changed for each of the species **1** and **2**. This analysis shows that the ratio can change over the range of 2.5 to 5, depending on the details of the mode partitioning, but that the electronic coupling in **1** is always larger than that in **2**. In addition, when the partitioning of internal reorganization energy between the vibrational modes is similar in the two compounds (represented by the diagonal in the horizontal plane of the graph that goes from the origin of (0%,0% - a 900 cm^{-1} quantum mode in each compound) to the point at (100%,100% - a 1600 cm^{-1} quantum mode in each compound)), the ratio does not change dramatically.

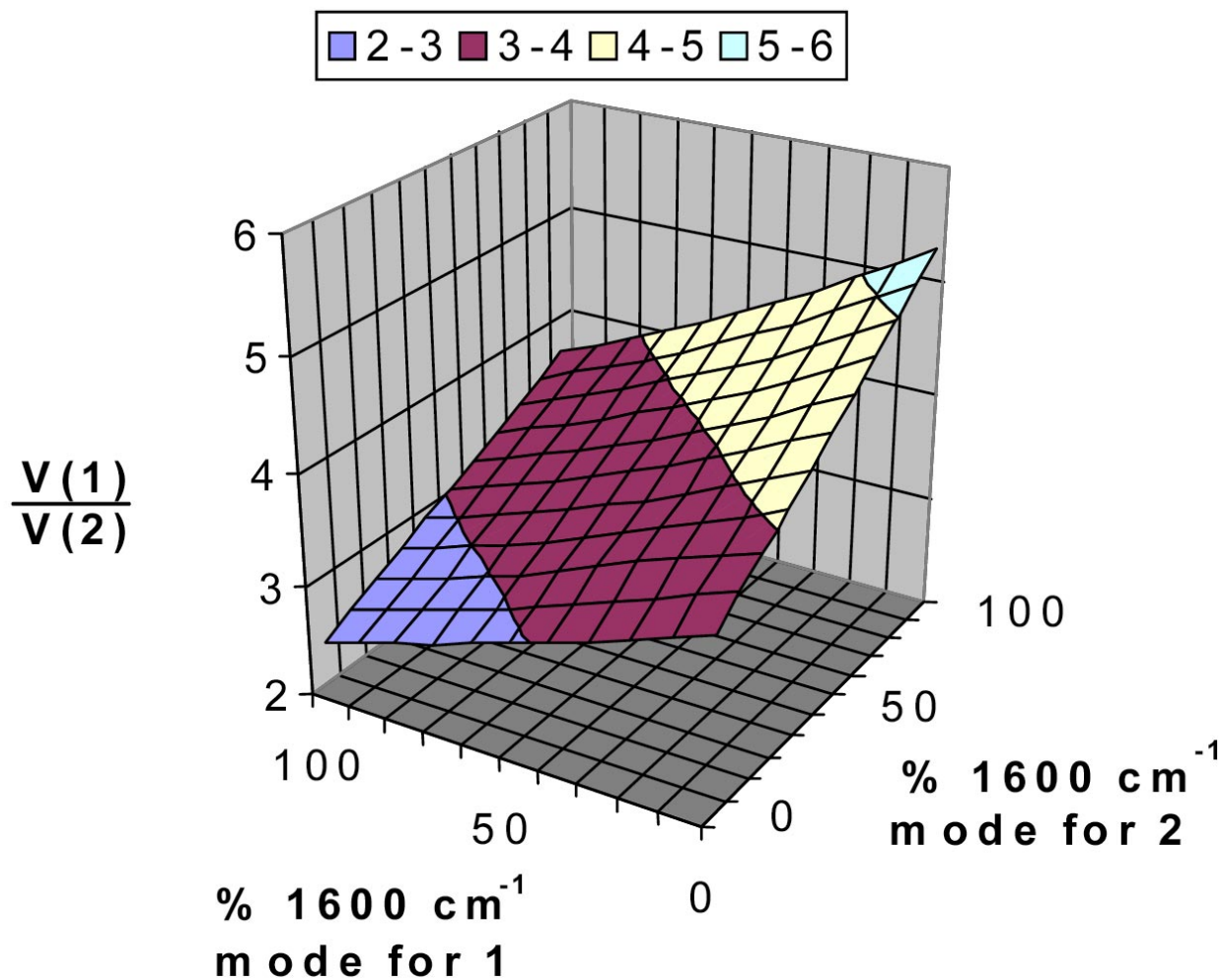


Figure 10.6 The internal reorganization energy is systematically partitioned between a 1600 cm⁻¹ and a 990 cm⁻¹ mode. The three-dimensional plot demonstrates the ratio of $|V|$ that is obtained between **1** and **2** for a given percentage of 1600 cm⁻¹ mode. The lower frequency mode corresponds to a pyramidalization of the cyanoethylene acceptor group, whereas the higher frequency mode corresponds to a skeletal breathing mode of the naphthalene donor.

To the extent that the donor and acceptor groups rather than the pendant moiety controls the partitioning, this observation suggests that the ratio of ca. 3.5 for the electronic coupling magnitudes is robust with respect to the modeling for the internal reorganization energy.

10.8 Conclusions

This work presents electron transfer rate data and computational results that demonstrate efficient electron tunneling through a pendant moiety located in the *line-of-sight* between electron donor and acceptor groups. The electron transfer rates for compounds **1** and **2** were compared with the control molecule **8** to demonstrate that the electron transfer proceeds through the pendant moiety, rather than the covalent bridge. The experimentally determined reaction free energy for **1** in toluene and mesitylene and **2** in mesitylene were used to calibrate a molecular based model for solvation. This model and charge transfer spectra were used to define the reorganization energy and free energy parameters for electron transfer of **1** and **2** in the five solvents studied. By combining the knowledge of these parameters with the temperature dependent rate data, it was possible to experimentally determine the electronic coupling for these two compounds in the solvents. Compound **1** was found to have an electronic coupling that is four times larger than that of compound **2**. The dependence of the empirically derived electronic coupling values on the reorganization energy parameters was evaluated in detail (see Discussion and Supplemental Information). Also, the electronic couplings for the compounds were found to be independent of the solvent. The difference in electronic coupling values reflects the more efficient tunneling through the aromatic moiety of **1** than the alkyl moiety of **2**. The absolute

values of the experimentally derived electronic coupling values obtained for **1** and **2** were shown to be larger than those calculated by *ab initio* molecular orbital theory for analogues of **1** and **2**, but both agree that an aromatic group is better than a propyl group in mediating the electron transfer process.

10.9 Appendix A

The molecular model for solvation in these electron transfer systems has been discussed extensively in earlier work.¹⁴ This model develops explicit expressions for the reaction free energy and the solvent reorganization energy.

The free energy of reaction is given by the sum of four terms in eq 10.5. The most significant contribution in these solvents comes from the $\Delta_{dq,i}G^{(1)}$ term given by

$$\Delta_{dq,i}G^{(1)} = -\frac{(m_e^2 - m_g^2)}{R_{\text{eff}}^3} f(y_d, y_q) \Psi^P(y_d, y_q) \quad (\text{A1})$$

where m_i is the permanent dipole moment of the excited and ground electronic states, $f(y_i)$ renormalizes the solute dipole moment to account for its size and polarizability, R_{eff} is the effective solute radius, and $\Psi(y_i)$ is the polarity response function given by,

$$\Psi^P(y_d, y_q) = \frac{\frac{y_d I_{0s}^{(2)} + y_q I_6^{(2)}}{I_{0s}^{(2)}}}{1 + \frac{y_d^2 \kappa_d I_{0s}^{(3)} + y_d y_q \kappa_{dq} I_{DDQ}^{(3)} + y_q^2 \kappa_q I_{DQQ}^{(3)}}{y_d I_{0s}^{(2)} + y_q I_6^{(2)}}} \quad (\text{A2})$$

In this equation the κ terms account for saturation of the dipolar response that arises from higher order interactions, and the I_{ij} are polynomial representations of the two and three particle perturbation integrals. Their explicit form can be found elsewhere.^{14,30}

The solvent reorganization energy is given by a sum of three terms in eq 10.6. The major contribution in the aromatic solvents comes from λ_p and is given by

$$\lambda_p = \frac{(m_e - m_g)^2}{R_{\text{eff}}^3} [f(y_d, y_q) \Psi^P(y_d, y_q) - f(y_e) \Psi^P(y_e)] \quad (\text{A3})$$

where y_e is the reduced polarizability density of the solvent. The induction term λ_{ind} makes a small but relatively significant contribution to the overall reorganization energy in these solvents (see Table A1) and is given by

$$\lambda_{\text{ind}} = \frac{(m_e^2 - m_g^2)^2}{400 kT \eta \sigma^6} \frac{f(y_e)^2}{(\epsilon_\infty + 2)^2} \left[3 + \frac{8}{3} (\epsilon_\infty - 1)^2 \right] I_{0s}^{(4)} \quad (\text{A4})$$

where η is the reduced packing density of the solvent molecules, σ is the solvent hard sphere diameter,³¹ and ϵ_∞ is the solvent high frequency dielectric constant. Previous work¹⁴ indicated that the absolute values of λ_o predicted from the model are too small. Therefore, only its temperature dependence is used.

Table A1: Individual Contributions to $\Delta_r G$ and λ_0 for **1**. All Values Listed in eV.

T (K)	$\Delta_{\text{sq}}G^{(1)}$	$\Delta_r G^{(2)}$	$\Delta_{\text{disp}}G$	$\Delta_r G$	λ_p	λ_{ind}	λ_{disp}	λ_0
Toluene								
287.15	-2.41×10^{-01}	-1.16×10^{-02}	-2.91×10^{-02}	-1.23×10^{-01}	5.60×10^{-02}	1.07×10^{-02}	4.75×10^{-04}	6.72×10^{-02}
297.55	-2.35×10^{-01}	-1.07×10^{-02}	-2.86×10^{-02}	-1.16×10^{-01}	5.37×10^{-02}	9.91×10^{-03}	4.48×10^{-04}	6.40×10^{-02}
298.75	-2.35×10^{-01}	-1.07×10^{-02}	-2.86×10^{-02}	-1.15×10^{-01}	5.34×10^{-02}	9.83×10^{-03}	4.45×10^{-04}	6.37×10^{-02}
307.15	-2.30×10^{-01}	-1.00×10^{-02}	-2.82×10^{-02}	-1.09×10^{-01}	5.16×10^{-02}	9.27×10^{-03}	4.25×10^{-04}	6.13×10^{-02}
316.95	-2.25×10^{-01}	-9.40×10^{-03}	-2.78×10^{-02}	-1.03×10^{-01}	4.96×10^{-02}	8.67×10^{-03}	4.03×10^{-04}	5.86×10^{-02}
320.85	-2.23×10^{-01}	-9.15×10^{-03}	-2.76×10^{-02}	-1.01×10^{-01}	4.88×10^{-02}	8.44×10^{-03}	3.95×10^{-04}	5.76×10^{-02}
323.85	-2.21×10^{-01}	-8.97×10^{-03}	-2.74×10^{-02}	-9.88×10^{-02}	4.82×10^{-02}	8.27×10^{-03}	3.88×10^{-04}	5.69×10^{-02}
326.65	-2.20×10^{-01}	-8.80×10^{-03}	-2.73×10^{-02}	-9.71×10^{-02}	4.77×10^{-02}	8.12×10^{-03}	3.83×10^{-04}	5.62×10^{-02}
333.15	-2.17×10^{-01}	-8.42×10^{-03}	-2.70×10^{-02}	-9.32×10^{-02}	4.64×10^{-02}	7.77×10^{-03}	3.70×10^{-04}	5.46×10^{-02}
346.55	-2.10×10^{-01}	-7.70×10^{-03}	-2.65×10^{-02}	-8.55×10^{-02}	4.40×10^{-02}	7.11×10^{-03}	3.45×10^{-04}	5.15×10^{-02}
346.95	-2.10×10^{-01}	-7.68×10^{-03}	-2.64×10^{-02}	-8.53×10^{-02}	4.39×10^{-02}	7.09×10^{-03}	3.44×10^{-04}	5.14×10^{-02}
347.05	-2.10×10^{-01}	-7.68×10^{-03}	-2.64×10^{-02}	-8.52×10^{-02}	4.39×10^{-02}	7.08×10^{-03}	3.44×10^{-04}	5.14×10^{-02}
357.75	-2.05×10^{-01}	-7.16×10^{-03}	-2.60×10^{-02}	-7.93×10^{-02}	4.21×10^{-02}	6.60×10^{-03}	3.26×10^{-04}	4.90×10^{-02}
371.45	-1.99×10^{-01}	-6.54×10^{-03}	-2.54×10^{-02}	-7.20×10^{-02}	3.99×10^{-02}	6.04×10^{-03}	3.05×10^{-04}	4.62×10^{-02}
371.55	-1.99×10^{-01}	-6.54×10^{-03}	-2.54×10^{-02}	-7.19×10^{-02}	3.99×10^{-02}	6.03×10^{-03}	3.04×10^{-04}	4.62×10^{-02}
Mesitylene								
274.95	-2.07×10^{-01}	-1.40×10^{-02}	-4.09×10^{-02}	-1.03×10^{-01}	3.35×10^{-02}	1.29×10^{-02}	1.16×10^{-03}	4.75×10^{-02}
277.85	-2.06×10^{-01}	-1.37×10^{-02}	-4.07×10^{-02}	-1.01×10^{-01}	3.31×10^{-02}	1.26×10^{-02}	1.14×10^{-03}	4.68×10^{-02}
293.55	-1.99×10^{-01}	-1.23×10^{-02}	-3.98×10^{-02}	-9.19×10^{-02}	3.07×10^{-02}	1.14×10^{-02}	1.04×10^{-03}	4.31×10^{-02}
295.95	-1.98×10^{-01}	-1.21×10^{-02}	-3.96×10^{-02}	-9.05×10^{-02}	3.04×10^{-02}	1.12×10^{-02}	1.02×10^{-03}	4.26×10^{-02}
298.45	-1.97×10^{-01}	-1.19×10^{-02}	-3.95×10^{-02}	-8.91×10^{-02}	3.00×10^{-02}	1.10×10^{-02}	1.01×10^{-03}	4.21×10^{-02}
304	-1.94×10^{-01}	-1.15×10^{-02}	-3.91×10^{-02}	-8.60×10^{-02}	2.93×10^{-02}	1.06×10^{-02}	9.78×10^{-04}	4.09×10^{-02}
315.35	-1.90×10^{-01}	-1.07×10^{-02}	-3.84×10^{-02}	-7.99×10^{-02}	2.78×10^{-02}	9.85×10^{-03}	9.17×10^{-04}	3.86×10^{-02}
336.35	-1.82×10^{-01}	-9.35×10^{-03}	-3.72×10^{-02}	-6.92×10^{-02}	2.54×10^{-02}	8.63×10^{-03}	8.18×10^{-04}	3.48×10^{-02}
347.05	-1.78×10^{-01}	-8.75×10^{-03}	-3.65×10^{-02}	-6.40×10^{-02}	2.42×10^{-02}	8.07×10^{-03}	7.73×10^{-04}	3.30×10^{-02}
357.75	-1.74×10^{-01}	-8.20×10^{-03}	-3.59×10^{-02}	-5.89×10^{-02}	2.31×10^{-02}	7.56×10^{-03}	7.31×10^{-04}	3.14×10^{-02}
371.55	-1.69×10^{-01}	-7.54×10^{-03}	-3.51×10^{-02}	-5.27×10^{-02}	2.18×10^{-02}	6.96×10^{-03}	6.81×10^{-04}	2.94×10^{-02}
THF								
297.5	-4.92×10^{-01}	-5.36×10^{-03}	-3.27×10^{-02}	-3.71×10^{-01}	2.21×10^{-01}	4.95×10^{-03}	4.88×10^{-04}	2.26×10^{-01}
307.1	-4.83×10^{-01}	-5.00×10^{-03}	-3.23×10^{-02}	-3.61×10^{-01}	2.16×10^{-01}	4.61×10^{-03}	4.63×10^{-04}	2.21×10^{-01}
316.4	-4.73×10^{-01}	-4.67×10^{-03}	-3.18×10^{-02}	-3.51×10^{-01}	2.11×10^{-01}	4.30×10^{-03}	4.41×10^{-04}	2.16×10^{-01}
326.7	-4.64×10^{-01}	-4.33×10^{-03}	-3.14×10^{-02}	-3.40×10^{-01}	2.06×10^{-01}	3.99×10^{-03}	4.18×10^{-04}	2.10×10^{-01}
336	-4.55×10^{-01}	-4.05×10^{-03}	-3.09×10^{-02}	-3.31×10^{-01}	2.01×10^{-01}	3.74×10^{-03}	3.99×10^{-04}	2.05×10^{-01}
Acetonitrile								
301	-6.52×10^{-01}	-1.38×10^{-02}	-2.01×10^{-02}	-5.27×10^{-01}	3.49×10^{-01}	1.28×10^{-02}	1.38×10^{-04}	3.62×10^{-01}
309	-6.47×10^{-01}	-1.37×10^{-02}	-1.98×10^{-02}	-5.21×10^{-01}	3.47×10^{-01}	1.27×10^{-02}	1.32×10^{-04}	3.59×10^{-01}
317	-6.41×10^{-01}	-1.36×10^{-02}	-1.96×10^{-02}	-5.16×10^{-01}	3.44×10^{-01}	1.26×10^{-02}	1.26×10^{-04}	3.57×10^{-01}
327	-6.35×10^{-01}	-1.35×10^{-02}	-1.92×10^{-02}	-5.08×10^{-01}	3.41×10^{-01}	1.24×10^{-02}	1.19×10^{-04}	3.54×10^{-01}
337	-6.28×10^{-01}	-1.34×10^{-02}	-1.88×10^{-02}	-5.01×10^{-01}	3.38×10^{-01}	1.23×10^{-02}	1.13×10^{-04}	3.50×10^{-01}
Dichloromethane								
275	-5.29×10^{-01}	-6.37×10^{-03}	-2.31×10^{-02}	-3.99×10^{-01}	2.51×10^{-01}	5.88×10^{-03}	2.18×10^{-04}	2.57×10^{-01}
290	-5.13×10^{-01}	-5.73×10^{-03}	-2.24×10^{-02}	-3.82×10^{-01}	2.43×10^{-01}	5.28×10^{-03}	1.98×10^{-04}	2.49×10^{-01}
296	-5.06×10^{-01}	-5.49×10^{-03}	-2.21×10^{-02}	-3.75×10^{-01}	2.40×10^{-01}	5.07×10^{-03}	1.91×10^{-04}	2.45×10^{-01}
308	-4.94×10^{-01}	-5.06×10^{-03}	-2.16×10^{-02}	-3.61×10^{-01}	2.33×10^{-01}	4.66×10^{-03}	1.78×10^{-04}	2.38×10^{-01}

Table A2: Individual Contributions to $\Delta_r G$ and λ_0 for **2**. All values listed in eV.

T (K)	$\Delta_{\text{aq}} G^{(1)}$	$\Delta_r G^{(2)}$	$\Delta_{\text{disp}} G$	$\Delta_r G$	λ_p	λ_{ind}	λ_{disp}	λ_0
Toluene								
290.25	-2.38×10^{-01}	-1.12×10^{-02}	-2.89×10^{-02}	-1.19×10^{-01}	5.49×10^{-02}	1.04×10^{-02}	4.67×10^{-04}	6.58×10^{-02}
296.15	-2.35×10^{-01}	-1.08×10^{-02}	-2.87×10^{-02}	-1.15×10^{-01}	5.36×10^{-02}	9.96×10^{-03}	4.52×10^{-04}	6.40×10^{-02}
296.65	-2.35×10^{-01}	-1.08×10^{-02}	-2.86×10^{-02}	-1.15×10^{-01}	5.35×10^{-02}	9.92×10^{-03}	4.50×10^{-04}	6.39×10^{-02}
305.35	-2.30×10^{-01}	-1.01×10^{-02}	-2.83×10^{-02}	-1.09×10^{-01}	5.17×10^{-02}	9.34×10^{-03}	4.29×10^{-04}	6.14×10^{-02}
316.3	-2.24×10^{-01}	-9.39×10^{-03}	-2.78×10^{-02}	-1.03×10^{-01}	4.94×10^{-02}	8.66×10^{-03}	4.04×10^{-04}	5.85×10^{-02}
316.45	-2.24×10^{-01}	-9.38×10^{-03}	-2.78×10^{-02}	-1.02×10^{-01}	4.94×10^{-02}	8.65×10^{-03}	4.04×10^{-04}	5.84×10^{-02}
323.75	-2.21×10^{-01}	-8.93×10^{-03}	-2.75×10^{-02}	-9.80×10^{-02}	4.79×10^{-02}	8.24×10^{-03}	3.89×10^{-04}	5.66×10^{-02}
326.65	-2.19×10^{-01}	-8.76×10^{-03}	-2.73×10^{-02}	-9.63×10^{-02}	4.74×10^{-02}	8.08×10^{-03}	3.83×10^{-04}	5.58×10^{-02}
327.5	-2.19×10^{-01}	-8.71×10^{-03}	-2.73×10^{-02}	-9.58×10^{-02}	4.72×10^{-02}	8.03×10^{-03}	3.81×10^{-04}	5.56×10^{-02}
347.55	-2.09×10^{-01}	-7.62×10^{-03}	-2.64×10^{-02}	-8.42×10^{-02}	4.36×10^{-02}	7.03×10^{-03}	3.43×10^{-04}	5.10×10^{-02}
347.55	-2.09×10^{-01}	-7.62×10^{-03}	-2.64×10^{-02}	-8.42×10^{-02}	4.36×10^{-02}	7.03×10^{-03}	3.43×10^{-04}	5.10×10^{-02}
368.3	-2.00×10^{-01}	-6.65×10^{-03}	-2.55×10^{-02}	-7.29×10^{-02}	4.02×10^{-02}	6.13×10^{-03}	3.09×10^{-04}	4.66×10^{-02}
Mesitylene								
282.15	-2.03×10^{-01}	-1.32×10^{-02}	-4.05×10^{-02}	-9.78×10^{-02}	3.22×10^{-02}	1.22×10^{-02}	1.11×10^{-03}	4.55×10^{-02}
292.85	-1.99×10^{-01}	-1.23×10^{-02}	-3.98×10^{-02}	-9.16×10^{-02}	3.07×10^{-02}	1.14×10^{-02}	1.04×10^{-03}	4.31×10^{-02}
297.45	-1.97×10^{-01}	-1.19×10^{-02}	-3.95×10^{-02}	-8.90×10^{-02}	3.00×10^{-02}	1.10×10^{-02}	1.01×10^{-03}	4.20×10^{-02}
302.75	-1.94×10^{-01}	-1.15×10^{-02}	-3.92×10^{-02}	-8.60×10^{-02}	2.93×10^{-02}	1.06×10^{-02}	9.85×10^{-04}	4.09×10^{-02}
312.55	-1.90×10^{-01}	-1.08×10^{-02}	-3.86×10^{-02}	-8.07×10^{-02}	2.80×10^{-02}	9.98×10^{-03}	9.32×10^{-04}	3.89×10^{-02}
323.05	-1.86×10^{-01}	-1.01×10^{-02}	-3.80×10^{-02}	-7.52×10^{-02}	2.67×10^{-02}	9.34×10^{-03}	8.79×10^{-04}	3.70×10^{-02}
323.65	-1.86×10^{-01}	-1.01×10^{-02}	-3.79×10^{-02}	-7.49×10^{-02}	2.67×10^{-02}	9.30×10^{-03}	8.76×10^{-04}	3.68×10^{-02}
331.75	-1.83×10^{-01}	-9.58×10^{-03}	-3.74×10^{-02}	-7.09×10^{-02}	2.57×10^{-02}	8.84×10^{-03}	8.38×10^{-04}	3.54×10^{-02}
346.65	-1.77×10^{-01}	-8.73×10^{-03}	-3.66×10^{-02}	-6.36×10^{-02}	2.41×10^{-02}	8.06×10^{-03}	7.74×10^{-04}	3.29×10^{-02}
347.45	-1.77×10^{-01}	-8.69×10^{-03}	-3.65×10^{-02}	-6.32×10^{-02}	2.40×10^{-02}	8.02×10^{-03}	7.71×10^{-04}	3.28×10^{-02}
360.25	-1.73×10^{-01}	-8.04×10^{-03}	-3.58×10^{-02}	-5.73×10^{-02}	2.27×10^{-02}	7.41×10^{-03}	7.21×10^{-04}	3.09×10^{-02}
360.35	-1.73×10^{-01}	-8.03×10^{-03}	-3.58×10^{-02}	-5.72×10^{-02}	2.27×10^{-02}	7.41×10^{-03}	7.21×10^{-04}	3.09×10^{-02}
370.15	-1.69×10^{-01}	-7.57×10^{-03}	-3.52×10^{-02}	-5.28×10^{-02}	2.18×10^{-02}	6.98×10^{-03}	6.86×10^{-04}	2.95×10^{-02}
379.25	-1.66×10^{-01}	-7.17×10^{-03}	-3.47×10^{-02}	-4.88×10^{-02}	2.10×10^{-02}	6.61×10^{-03}	6.55×10^{-04}	2.82×10^{-02}
THF								
297.5	-4.88×10^{-01}	-5.34×10^{-03}	-3.27×10^{-02}	-3.67×10^{-01}	2.18×10^{-01}	4.93×10^{-03}	4.88×10^{-04}	2.24×10^{-01}
307.2	-4.79×10^{-01}	-4.97×10^{-03}	-3.23×10^{-02}	-3.57×10^{-01}	2.14×10^{-01}	4.58×10^{-03}	4.63×10^{-04}	2.19×10^{-01}
316.4	-4.70×10^{-01}	-4.65×10^{-03}	-3.18×10^{-02}	-3.47×10^{-01}	2.09×10^{-01}	4.29×10^{-03}	4.41×10^{-04}	2.14×10^{-01}
326.9	-4.60×10^{-01}	-4.30×10^{-03}	-3.13×10^{-02}	-3.37×10^{-01}	2.04×10^{-01}	3.97×10^{-03}	4.18×10^{-04}	2.08×10^{-01}
Acetonitrile								
302	-6.45×10^{-01}	-1.38×10^{-02}	-2.01×10^{-02}	-5.20×10^{-01}	3.44×10^{-01}	1.27×10^{-02}	1.37×10^{-04}	3.57×10^{-01}
309	-6.40×10^{-01}	-1.37×10^{-02}	-1.98×10^{-02}	-5.15×10^{-01}	3.42×10^{-01}	1.26×10^{-02}	1.32×10^{-04}	3.55×10^{-01}
317	-6.35×10^{-01}	-1.36×10^{-02}	-1.96×10^{-02}	-5.09×10^{-01}	3.40×10^{-01}	1.25×10^{-02}	1.26×10^{-04}	3.53×10^{-01}
327	-6.28×10^{-01}	-1.34×10^{-02}	-1.92×10^{-02}	-5.02×10^{-01}	3.37×10^{-01}	1.24×10^{-02}	1.19×10^{-04}	3.49×10^{-01}
337	-6.22×10^{-01}	-1.33×10^{-02}	-1.88×10^{-02}	-4.95×10^{-01}	3.34×10^{-01}	1.23×10^{-02}	1.13×10^{-04}	3.46×10^{-01}
Dichloromethane								
273	-5.27×10^{-01}	-6.43×10^{-03}	-2.31×10^{-02}	-3.97×10^{-01}	2.50×10^{-01}	5.93×10^{-03}	2.21×10^{-04}	2.56×10^{-01}
283	-5.16×10^{-01}	-5.99×10^{-03}	-2.27×10^{-02}	-3.86×10^{-01}	2.44×10^{-01}	5.52×10^{-03}	2.07×10^{-04}	2.50×10^{-01}
293	-5.05×10^{-01}	-5.58×10^{-03}	-2.22×10^{-02}	-3.74×10^{-01}	2.39×10^{-01}	5.15×10^{-03}	1.95×10^{-04}	2.44×10^{-01}
302	-4.96×10^{-01}	-5.24×10^{-03}	-2.18×10^{-02}	-3.64×10^{-01}	2.34×10^{-01}	4.84×10^{-03}	1.84×10^{-04}	2.39×10^{-01}

10.10 References

(1) a) Balzani, V.; Ed. *Electron Transfer in Chemistry*; Wiley - VCH: Weinheim, 2001. b) Barbara, P. F.; Meyer, T. J.; Ratner, M.A., *J. Phys. Chem.* **1996**, *100*, 13148; c) Electron Transfer-From Isolated Molecules to Biomolecules, *Adv. Chem. Phys.* Jortner, J.; Bixon, M. eds. (Wiley, NY, **1999**).

(2) a) Hush, N. S.; Paddon-Row, M. N.; Cotsaris, E.; Oevering, H.; Verhoeven, J. W.; Heppener, M. *Chem. Phys. Lett.* **1985**, *117*, 8. b) Oliver, A. M.; Craig, D. C.; Paddon-Row, M. N.; Kroon, J.; Verhoeven, J. W. *Chem. Phys. Lett.* **1988**, *150*, 366. c) Johnson, M. D.; Miller, J. R.; Green, N. S.; Closs, G. L. *J. Phys. Chem.* 1989, *93*, 1173. d) Paddon-Row, M. N. *Acc. Chem. Res.* **1994**, *27*, 18.

(3) a) Zeng, Y.; Zimmt, M. B., *J. Phys. Chem.* **1992**, *96*, 8395; b) Oliver, A. M.; Paddon-Row, M. N.; Kroon, J.; Verhoeven, J. W. *Chem. Phys. Lett.* **1992**, *191*, 371.

(4) Closs, G.L.; Miller, J.R. *Science* **1988**, *240*, 440.

(5) a) Newton, M. D. *Adv. Chem. Phys.* **1999**, *106*, 303; b) Jordan, K. D.; Paddon-Row, M. N. *Chem. Rev.* **1992**, *92*, 395.

(6) a) Paddon-Row, M. N.; Jordan, K. D. In *Modern Models of Bonding and Delocalization*; Liebman, J. F., Greenberg, A., Eds.; VCH Publishers: New York, 1988; Vol. 6; pp 115. b) Shephard, M. J.; Paddon-Row, M. N., K. D. *Chem. Phys.* **1993**, *176*, 289. c) Paddon-Row, M. N.; Shephard, M. J. *J. Am. Chem. Soc.* **1997**, *119*, 5355.

(7) a) Roberts, J. A.; Kirby, J. P.; Nocera, D.G. *J. Am. Chem. Soc.* **1995**, *117*, 8051. b) de Rege, P. J. F.; Williams, S. A.; Therien, M. J. *Science* 1995, *269*, 1409. c) LeCours, S. M.; Philips, C. M.; DePaula, J. C.; Therien, M. J.; *J. Am. Chem. Soc.* 1997, *119*, 12578. d) Arimura, T.; Brown, C. T.; Springs, S. L.; Sessler, J. L. *Chem. Commun.* **1996**, 2293.

(8) a) Lokan, N. R.; Craig, D. C.; Paddon-Row, M. N. *Synlett* **1999**, 397. b) Lokan, N. R.; Paddon-Row, M. N.; Koeberg, M.; Verhoeven, J. W. *J. Am. Chem. Soc.* **2000**, *122*, 5075. c) Koeberg, M.; de Groot, M.; Verhoeven, J. W.; Lokan, N. R.; Shephard, M. J.; Paddon-Row, M. N. *J. Phys. Chem.* **2001**, *105*, 3417. d) Jolliffe, K. A.; Bell, T. D. M.; Ghiggino, K. P.; Jordan, K.; Langford, S. J.; Paddon-Row, M. N. *Angew. Chem., Int. Ed.* **1998**, *37*, 916. e) Jolliffe, K. A.; Langford, S. J.; Oliver, A. M.; Shephard, M. J.; Paddon-Row, M. N. *Chem. Eur. J.* **1999**, *5*, 2518. f) Bell, T. D. M.; Jolliffe, K. A.; Ghiggino, K. P.; Oliver, A. M.; Shephard, M. J.; Langford, S. J.; Paddon-Row, M. N. *J. Am. Chem. Soc.* **2000**, *122*, 10661. g) Goes, M.; Groot, M. de; Koeberg, M.; Verhoeven, J. W.; Lokan, N. R.; Shephard, M. J.; Paddon-Row, M. N. *J. Phys. Chem. A* **2001**, *105*, 3417.

(9) Kumar, K.; Lin, Z.; Waldeck, D.H.; Zimmt, M. B. *J. Am. Chem. Soc.* **1996**, *118*, 243.

(10) a) Kumar, K.; Kurnikov, I.; Beratan, D. N.; Waldeck, D. H.; Zimmt, M. B. *J. Phys. Chem. A* **1998**, *102*, 5529; b) Read, I.; Napper, A.; Kaplan, R.; Zimmt, M. B.; Waldeck, D. H. *J. Am. Chem. Soc.* **1999**, *121*, 10976; c) Napper, A. M.; Read, I.; Kaplan, R.; Zimmt, M. B.; Waldeck, D. H. *J. Phys. Chem. B* in press.

(11) a) Kaplan, R.; Napper, A. M.; Waldeck, D. H.; Zimmt, M. B. *J. Am. Chem. Soc.* **2001**, submitted. b) Kaplan, R.; Napper, A.; Waldeck, D. H.; Zimmt, M. B. *J. Am. Chem. Soc.* **2000**, *122*, 12039; c) Napper, A. M.; Read, I.; Waldeck, D. H.; Kaplan, R. W.; Zimmt, M. B. *J. Phys. Chem. B*, in press.

(12) Head, N. J.; Oliver, A. M.; Look, K.; Lokan, N. R.; Jones, G. A.; Paddon-Row, M. N. *Angew. Chem., Int. Ed.* **1999**, *38*, 3219.

(13) Napper, A. M.; Read, I.; Waldeck, D. H.; Head, N. J.; Oliver, A. M.; Paddon-Row, M. N. *J. Am. Chem. Soc.* **2000**, *122*, 5220.

(14) Read, I.; Napper, A. M.; Zimmt, M. B.; Waldeck, D. H. *J. Phys. Chem. A* **2000**, *104*, 9385.

(15) Matyushov, D. V.; Voth, G. A. *J. Chem. Phys.* **1999**, *111*, 3630.

(16) a) Marcus, R. A. *J. Phys. Chem.* **1989**, *93*, 3078; b) Lilichenko, M.; Tittelbach-Helmrich, D.; Verhoeven, J. W.; Gould, I. R.; Myers, A. B. *J. Chem. Phys.* **1998**, *109*, 10958.

(17) As described in an earlier report¹³, the fluorescence decay also shows a contribution from an impurity that corresponds to the donor only compound but this feature is accounted for in the data fitting.

(18) Shephard, M. J.; Paddon-Row, M. N. *J. Phys. Chem.* **1999**, *103*, 3347.

(19) Shephard, M. J.; Paddon-Row, M. N. *J. Phys. Chem.* **2000**, *104*, 11628.

(20) Frisch, M. J.; Trucks, G. W.; Schlegel, H. B.; Scuseria, G. E.; Robb, M. A.; Cheeseman, J. R.; Zakrzewski, V. G.; Montgomery Jr., J. A.; Stratmann, R. E.; Burant, J. C.; Dapprich, S.; Millam, J. M.; Daniels, A. D.; Kudin, K. N.; Strain, M. C.; Farkas, O.; Tomasi, J.; Barone, V.; Cossi, M.; Cammi, R.; Mennucci, B.; Pomelli, C.; Adamo, C.; Clifford, S.; Ochterski, J.; Petersson, G. A.; Ayala, P. Y.; Cui, Q.; Morokuma, K.; Malick, D. K.; Rabuck, A. D.; Raghavachari, K.; Foresman, J. B.; Cioslowski, J.; Ortiz, J. V.; Baboul, A. G.; Stefanov, B. B.; Liu, G.; Liashenko, A.; Piskorz, P.; Komaromi, I.; Gomperts, R.; Martin, R. L.; Fox, D. J.; Keith, T.; Al-Laham, M. A.; Peng, C. Y.; Nanayakkara, A.; Gonzalez, C.; Challacombe, M.; Gill, P. M. W.; Johnson, B.; Chen, W.; Wong, M. W.; Andres, J. L.; Gonzalez, C.; Head-Gordon, M.; Replogle, E. S.; Pople, J. A. *Gaussian 98*, Gaussian Inc: Pittsburgh, PA, **1998**.

(21) a) Warman, J. M.; de Haas, M. P.; Paddon-Row, M. N.; Cotsaris, E.; Hush, N. S.; Oevering, H.; Verhoeven, J. W. *Nature* **1986**, *320*, 615. b) Penfield, K. W.; Miller, J. R.; Paddon-Row, M. N.; Cotsaris, E.; Oliver, A. M.; Hush, N. S. *J. Am. Chem. Soc.* **1987**, *109*, 5061. c) Warman, J.

M.; de Haas, M. P.; Verhoeven, J. W.; Paddon-Row, M. N. *Adv. Chem. Phys.* **1999**, *106*, 571. d) Oevering, H.; Verhoeven, J. W.; Paddon-Row, M. N.; Warman, J. M. *Tetrahedron* **1989**, *45*, 4751.

(22) Oevering, H.; Paddon-Row, M. N.; Heppener, H.; Oliver, A. M.; Cotsaris, E.; Verhoeven, J. W.; Hush, N. S. *J. Am. Chem. Soc.* **1987**, *109*, 3258.

(23) A harmonic frequency calculation was carried out on neutral 7-dicyanovinylbornane **10**. The level of theory used was B3LYP/6-311+G(d,p)//B3LYP/6-311+G(d,p), and the geometry optimization was carried out under C_{2v} symmetry constraint. The frequency associated with out-of-plane bending of the DCV group, schematically depicted by **10a**, is 1132 cm^{-1} . Applying the recommended scaling factor of 0.9613 gave a corrected frequency of 1088 cm^{-1} ; see Wong, M. W. *Chem. Phys. Lett.* **1996**, *256*, 391.

(24) Gu, Y.; Kumar, K.; Lin, A.; Read, I.; Zimmt, M. B.; Waldeck, D. H. *J. Photochem. and Photobiol. A.* **1997**, *105*, 189.

(25) a) Paddon-Row, M. N.; Oliver, A. M.; Warman, J. M.; Smit, K. J.; de Haas, M. P.; Oevering, H.; Verhoeven, J. W. *J. Phys. Chem.* **1988**, *92*, 6958. b) Warman, J. M.; Smit, K. J.; de Haas, M. P.; Jonker, S. A.; Paddon-Row, M. N.; Oliver, A. M.; Kroon, J.; Oevering, H.; Verhoeven, J. W. *J. Phys. Chem.* **1991**, *95*, 1979.

(26) The polarizabilities of the molecules were obtained using the HF/3-21+G method and a 'divide and conquer' approach. Calculations were performed for analogues of **1** and **2** that did not contain the phenyl substituents on the naphthalene, nor the four CH_2OCH_3 groups on the bridge. This calculation yielded values of 73 \AA^3 for the analogue of **1** and 70 \AA^3 for the analogue of **2**. Independent calculations for the phenyl and ether substituents gave 9 \AA^3 and 4 \AA^3 , respectively. The polarizability of **1** and **2** were obtained by assuming that the polarizabilities of these components were additive and yielded 107 \AA^3 for **1** and 103 \AA^3 for **2**. A comparison of calculated polarizabilities for a range of molecules whose polarizabilities are known indicated that the calculation systematically underestimated the polarizability by a factor of 0.83. Correction by this factor gives 128 \AA^3 for **1** and 124 \AA^3 for **2**.

(27) The molecular moiety's polarizability was used to estimate the effective dielectric constant of the molecular cleft through the Clausius-Mossotti relationship. The polarizability perpendicular to the propyl group's long axis was taken to be 5.7 \AA^3 , and the polarizability perpendicular to the phenyl axis was taken to be 7.4 \AA^3 . The polarizabilities were taken from Ma, B.; Lii, J.-H.; and Allinger, N. L. *J. Comp. Chem.* **2000**, *21*, 813. The cleft volume was estimated to be 100 \AA^3 . This simple calculation predicts a shift in the reaction free energy between compounds **1** and **2** that is similar to the observed difference.

(28) a) Hoffmann, R. *Acc. Chem. Res.* **1971**, *4*, 1; b) Paddon-Row, M. N. *Acc. Chem. Res.* **1982**, *15*, 245; c) Paddon-Row, M. N. in *Electron Transfer In Chemistry*; Balzani, V., Ed.; Wiley-VCH: Weinheim, **2001**; Vol. 3, Part 2, Chapter 1, 179.

(29) The N-H system, **4**, was not used for these calculations because, given the approximations made, the modified system, **7'**, provides a better comparison to **7** for the influence that the phenyl group has upon the DMN - DCV coupling.

(30) a) Matyushov, D. V.; Schmid, R. *J. Chem. Phys.* **1996**, *105*, 4729; b) Matyushov, D. V.; Ladanyi, B. M. *J. Chem. Phys.* **1999**, *110*, 994.

(31) Ben-Amotz, D.; Willis, K. G. *J. Phys. Chem.* **1993**, *97*, 7736.

Chapter 11. Conclusions.

Each chapter has considered a variety of electron transfer systems. A set of common themes thread their way through this work. How does the structure of the system control electron transfer; and how can we best model this process? The intervening structure between electron donor and acceptor groups is crucial to achieving electron transfer. When the donor and acceptor groups are separated by distances greater than ca. 5 Å in vacuo, the rate of electron transfer is vanishingly small. In order to achieve electron transfer over large distance, detailed knowledge of how the intervening structure impacts electron transfer is required.

Electron transfer in the molecular C-Clamps studied in chapters 2, 3, 5, 7, 8, and 9 was effectively gated by the incorporation of favorably sized solvent molecules into a 7 Å wide cleft. The solvent controlled the electron transfer dynamics through an alteration in both the donor-acceptor electronic coupling as well as the Franck-Condon factor. It is difficult, but not impossible, to extract the individual contributions to the overall rate constant through temperature studies.

The U-shaped dyads studied in chapters 4 and 10 utilized a covalently attached pendant group which was juxtaposed between electron donor and acceptor. In these systems the solvent system offered an ability to alter the FCWDS whilst leaving the electronic coupling effectively unchanged. Both the C-Clamp and the U-Shaped systems show an optimal electronic coupling when an aromatic ring occupies the space between electron donor and acceptor groups. This enhancement in $|V|$ is attributed to the low lying (π^*) LUMO of the aromatic ring systems – a factor that promotes an electron-mediated superexchange interaction.

The development and parameterization of a molecular model of solvation has been undertaken for several systems. It appears as if the molecular model is successful in describing

the temperature dependence of the solvent reorganization energy as well as the free energy of reaction quite successfully for aromatic solvents that are relatively non-dipolar in character. The model correctly predicts the negative sign of $d\lambda/dT$ in these non-dipolar aromatic solvents studied, in stark contrast with the prediction made by that of the unsophisticated continuum treatments. The predictions are somewhat corroborated by charge transfer emission and absorption bands in benzene and other weakly polar solvents.¹

Chapter 9 describes an interesting system consisting of 1,3-diisopropylbenzene and the C-Clamp shaped molecule, A9DCE. The analysis suggests that the electronic coupling matrix element is temperature dependent – a somewhat iconoclastic statement. This is ascribed to a temperature dependent occupation of the cleft by the solvent, resulting in the observed $|V|$ being a weighted average of many different solvent-solute configurations. At higher temperatures, occupation of the cleft by 1,3-diisopropylbenzene may become thermodynamically less favorable, resulting in a reduction in the overall $|V|$, and a negative sign of the differential $d|V|/dT$. Several theoretical studies have suggested the feasibility of temperature dependent solvent mediated electronic coupling. This study supplies (indirect) evidence to support the likelihood of this occurrence.

Chapter 6 examined a self-assembled monolayer on a gold electrode that was terminated in a redox active ferrocene moiety. Chemical modification of the ferrocene tethered alkane chain as well as modification of the diluent alkanethiol led to the discovery that both modifications impacted the rate of electron transfer. Presumably non-covalent pathways through the film as the electron tunnels from the gold to the ferrocenium group (and vice-versa) are important in this system. Since the tilt angle for most alkanethiol films on gold surfaces is on the order of 30 degrees, it may not be surprising that a spatially more direct tunneling route may also play a part

in the electron transfer dynamics. Similar effects have been reported in studies carried out by other researchers.

The superexchange model has proved useful in describing and calculating electronic coupling between electron donor and acceptor through consideration of the intervening orbitals of the spacer or bridge. For photoinduced electron transfer, it seems likely that the electron transfer process is predominantly electron mediated. Superexchange states such as D^+S^-A are the dominant contributors to propagation of the donor and acceptor electronic wavefunctions. There is a direct correlation between the energy of the D^+S^-A state (either by consideration of solvent electron affinity or from electronic structure calculations of the spacer's LUMO level) and the degree to which the donor and acceptor are electronically coupled together. The hole mediated process does not seem to be as important in determining the overall magnitude of V . One reason for this is that the system is prepared in an excited state by optical excitation and lies ca. 3 - 4 eV above the ground state. It seems likely that the electron tunneling state will lie closer to the spacer's LUMO than HOMO.

The ferrocene self-assembled monolayer system shows a significant dependence upon the energetics of the filled orbitals of the alkane monolayer bridge. Calculations based upon transformation of the molecular orbitals into Weinhold's² natural-bond orbital (NBO) basis show that the spacer's sigma manifold is extremely important for propagation of the electronic interaction for the diradical systems $\bullet\text{CH}_2(\text{CH}_2)_n\text{CH}_2\bullet$. The main reason for the decreased electron transfer rate constant in the ether linked systems seems to stem from the lower value of the C-O bond self energies. This results in weaker superexchange interactions stemming from energy mismatching between the tunneling state and the C-O bridge natural-bond orbitals.

Electron transfer reactions constitute one of the most fundamental classes of chemical reactions. Modelling these reactions is a challenging undertaking, requiring detailed knowledge of how the intervening medium between an electron donor and acceptor controls the rate of reaction. This thesis consists of studies into both photoinduced and electrochemical electron transfer systems and demonstrates and rationalizes how the intervening chemical structure affects the reaction rate constant within the non-adiabatic limit. This knowledge obtained from these studies will allow us to better understand electron transfer reactions as well as aid in the design of systems that may be used as transducers of solar energy.

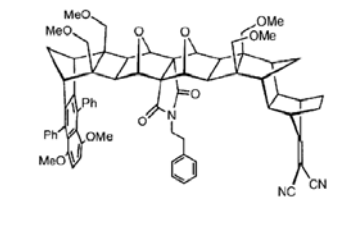
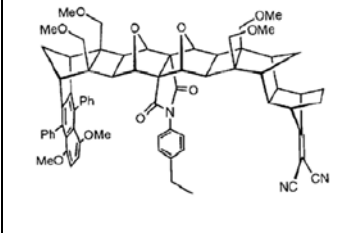
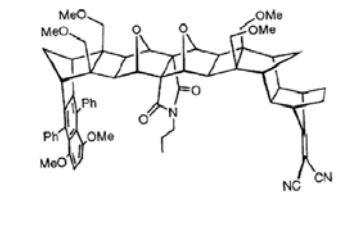
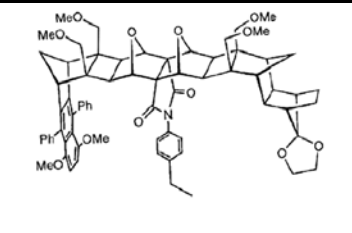
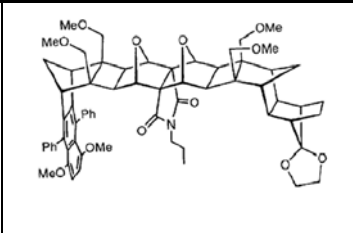
11.1 References.

- (1) (a) Vath, P.; Zimmt, M. B.; *J. Phys. Chem. A.*; **2000**; 104(12); 2626 (b) Tepper, R. J.; Zimmt, M. B. *Chem. Phys. Lett.* **1995**, 241, 566. (c) Cortés, J.; Heitele, H.; Jortner, J. *J. Phys. Chem.* **1994**, 98, 2527.
- (2) (a) Reed, A. E.; Curtiss, L. A.; Weinhold, F. *Chem. Rev.* **1988**, 88, 899; (b) Reed, A. E.; Weinhold, F. *J. Chem. Phys.* **1985**, 83, 1736.

Appendix I

12.1 Kinetic data for U-Shaped DBA Molecules, A1 – A5.

Includes published and unpublished data.

		
A1	A2	A3
		
A4	A5	

Renormalized fluorescence lifetime decays (deconvoluted) are fit to the following functional forms:

$$I(t) = a \cdot e^{-t/\tau}$$

$$I(t) = (A_1 / 100) \cdot e^{-t/\tau_1} + (1 - A_1/100) \cdot e^{-t/\tau_2}$$

etc.

Single Exponential

Double Exponential

χ^2 (if given) refers to the reduced chi-squared obtained from the deconvoluted fit of the experimental fluorescence lifetime decay with the sums of exponentials implied by the column headings of the table.

12.1.1 A1

Acetonitrile:

T(K)	A ₁ (%)	τ_1 (ps)	τ_2 (ps)	χ^2
302	96.8	2873.374	10571.883	1.188
307	97.6	2668.247	12078.658	1.068
317	97.8	2299.678	12225.790	1.049
328	97.8	1965.698	11116.622	1.071
338	97.8	1703.203	10186.576	1.052

Dichloromethane:

T(K)	A ₁ (%)	τ_1 (ps)	τ_2 (ps)	χ^2
275	97.3	1230.589	8388.883	1.096
288	97.3	1021.967	7801.082	1.034
296	97.5	911.735	7609.043	1.144
309	97.6	778.153	7209.359	1.114

Tetrahydrofuran:

T(K)	A ₁ (%)	τ_1 (ps)	τ_2 (ps)	χ^2
294.7	97.494	721.951	7557.977	1.107
308.0	97.510	638.114	6988.646	1.070
316.0	97.497	590.466	6721.012	1.051
320.9	96.808	560.796	6511.230	1.054
335.4	94.332	512.828	6117.696	1.047

Methylcyclohexane

T (K)	A1(%)	T1(ps)	A2(%)	T2(ns)	A3(%)	T3(ns)	χ^2
279.0	63.475	545.740	33.931	2.201	2.595	16.576	1.176
304.9	54.653	451.853	39.225	1.934	6.122	18.162	1.060

12.1.2 A2

Acetonitrile:

T(K)	A₁(%)	τ_1(ps)	τ_2(ps)	χ^2
301	95.2	1378.578	10977.633	1.048
309	95.2	1163.883	7524.628	1.071
317	95.2	1059.591	9006.150	1.113
327	95.2	913.574	7748.864	1.088
337	95.2	809.696	7812.297	1.075

Dichloromethane:

T(K)	A₁(%)	τ_1(ps)	τ_2(ps)	χ^2
275	94.8	1026.209	8457.803	1.107
290	94.9	805.636	7964.127	1.291
296	95.1	725.873	7449.042	1.283
308	95.1	595.082	6893.582	1.225

Tetrahydrofuran:

T(K)	A₁(%)	τ_1(ps)	τ_2(ps)	χ^2
297.5	94.955	414.321	6853.079	1.063
307.1	94.973	380.053	6449.845	1.093
316.4	95.218	352.940	6134.128	1.107
326.7	94.827	330.046	5787.261	1.109
336.0	95.268	310.581	5469.713	1.085

Diethyl Ether

Temp / K	T1(ps)	A1%	T2(ps)
276.3	357.509	84.852	846.1
284	381.376	95.89	1613.705
292.9	362.463	96.637	1727.891

Di-n-pentyl Ether

Temp / K	T1(ps)	A1%	T2(ps)
281.4	270.795	49.452	684.233
292.9	391.906	82.286	829.352
312.1	360.06	92.746	1551.801
331.6	299.831	89.778	1543.275

Toluene

Temp (K)	τ_1 (ps)	A_1 (%)	τ_2 (ps)
287.15	400.23	99.281	45530.395
297.55	369.08	98.962	59434.867
298.75	335.52	98.839	47624.461
307.15	343.32	98.485	76719
316.95	322.95	97.966	58237.609
320.85	292.08	97.607	46296.402
323.85	291.44	97.51	51828.41
326.65	306.97	96.986	55934.547
333.15	272.585	96.872	46016.359
346.55	252.52	95.537	40802.113
346.95	273.14	96.982	41432.098
347.05	270.49	96.963	41804.234
357.75	236.721	93.33	34548.422
371.45	200.96	91.908	28162.916
371.55	203.24	91.836	27814.992

Mesitylene

Temp / K	T1(ps)	A1%	T2(ps)
274.95	442	98.655	13388
277.85	415	98.75	24992
293.55	369	98.201	55211
295.95	365	97.85	26256
298.45	324	97.553	13922
304	316	97.315	13466
315.35	291	94.577	12199
336.35	273	93.326	26278
347.05	237	91.461	28604
357.75	214	87.645	21220
371.55	185	84.645	17156

Methylcyclohexane

T(K)	A1(%)	τ_1 (ps)	τ_2 (ps)	χ^2
278.4	68.059	1498.876	2874.594	1.110
287.8	65.738	1551.604	2881.824	1.131
297.9	63.340	1573.342	2840.292	1.007
306.9	67.211	1671.393	3063.494	1.195
317.4	66.528	1730.149	3357.385	1.151

12.1.3 A3

Acetonitrile:

T(K)	A1(%)	τ_1 (ps)	τ_2 (ps)	χ^2
302	97.9	2952.072	11949.365	1.101
309	98.1	2710.934	11824.104	1.100
317	98.0	2447.824	10961.834	1.162
327	98.1	2199.121	10910.931	1.077
337	97.8	1968.655	9072.971	0.967

Dichloromethane:

T(K)	A1(%)	τ_1 (ps)	τ_2 (ps)	χ^2
273	98.3	1319.246	8868.099	1.026
283	98.1	1147.831	7559.750	1.070
293	98.1	1024.674	6777.087	0.951
302	98.2	942.361	6476.947	1.051

Tetrahydrofuran:

T(K)	A1(%)	τ_1 (ps)	τ_2 (ps)	χ^2
297.5	97.744	621.701	6241.458	1.034
307.2	97.784	588.609	5966.383	1.142
316.4	97.764	565.884	5456.475	1.002
326.9	97.406	545.998	5160.576	0.974

Methylcyclohexane:

T(K)	A1(%)	τ_1 (ps)	τ_2 (ps)	χ^2
278.5	47.321	1055.452	2329.234	1.030
297.7	40.592	1056.429	2103.336	1.028
316.5	46.178	1210.841	2236.759	1.019

Methylcyclohexane

T(K)	A1(%)	T1(ps)	A2(%)	T2(ns)	A3(%)	T3(ns)	χ^2
290.7	37.568	581.682	58.741	2.650	3.690	5.852	1.287
304.3	35.523	525.758	63.744	2.924	0.733	18.337	1.195
317.0	28.634	376.647	69.985	2.531	1.380	8.258	1.236
323.8	24.849	411.675	74.707	2.483	0.444	26.435	1.236

Toluene

Temp / K	T1(ps)	A1%	T2(ps)
290.25	584	99.036	7795
296.15	589	99.305	8785
296.65	593	98.827	6589
305.35	561	99.16	8865
316.3	558	99.238	11059
316.45	544	99.261	12903
323.75	531	99.384	15672
326.65	521	99.382	25657
327.5	521	99.403	27280
347.55	497	99.024	34420
347.55	511	99.224	30981
368.3	465	99.3618	41857

Mesitylene

Temp / K	T1(ps)	A1%	T2(ps)
282.15	614	99.247	7581
292.85	577	99.186	8398
297.45	534	98.873	7415
302.75	543	99.498	12983
312.55	505	99.098	11227
323.05	479	99.207	18801
323.65	504	99.261	15886
331.75	513	98.966	29269
346.65	476	98.384	35611
347.45	472	98.617	25838
360.25	468	97.123	38922
360.35	465	97.102	39368
370.15	451	96.702	31237
379.25	448	94.61	30943

12.1.4 A4

Acetonitrile:

T(K)	A1(%)	τ_1(ps)	χ^2
302	100	11374.715	1.334
307	100	11101.692	1.483
317	100	10471.876	1.365
327	100	9897.308	1.369
338	100	9388.994	1.355

Dichloromethane:

T(K)	A1(%)	τ_1(ps)	χ^2
275	100	8714.392	1.234
287	100	8129.497	1.361
308	100	6900.296	1.369

Tetrahydrofuran:

T(K)	A1(%)	τ_1(ps)	χ^2
287.8	100	7113.268	1.427
306.8	100	6311.336	1.364
326.3	100	5566.494	1.278

Di-n-pentyl Ether

T/K	tau(ps)
281.6	3510.686
292.9	3192.154
312.5	2772.362
332.5	2443.535

Diethyl Ether

T/K	tau(ps)
276.4	5142.405
292.9	4536.171

Methylcyclohexane:

T(K)	A1(%)	τ_1(ps)	χ^2
278.4	100	3333.139	1.145
287.8	100	3177.164	1.258
297.6	100	3002.439	1.152
306.9	100	2895.436	1.146
317.5	100	2756.548	1.199

Methylcyclohexane

T(K)	A1(%)	T1(ns)	χ^2
290.2	100	3.000	1.810
322.3	100	2.694	1.508

Toluene

Temp (K)	Lifetime (ps)
286.75	3843.703
317.75	3248.239

Mesitylene

Temp (K)	Lifetime (ps)
273.15	4233.645
274.95	3937.189
293.15	3525.759
304.15	3307.172
314.85	3135.317
315.95	3408.36
325.15	3016.073
336.45	2866.104
386.85	2572.566

12.1.5 A5

Acetonitrile:

T(K)	A1(%)	τ_1 (ps)	χ^2
302	100	11768.673	1.207
309	100	11284.266	1.195
317	100	10724.881	1.059
327	100	10151.379	1.152
337	100	9556.405	1.129

Dichloromethane:

T(K)	A1(%)	τ_1 (ps)	χ^2
273	100	7919.706	1.282
283	100	7409.797	1.280
302	100	6456.485	1.218

Tetrahydrofuran:

T(K)	A1(%)	τ_1 (ps)	χ^2
292.7	100	6492.299	1.279
310.5	100	5699.771	1.311
325.4	100	4994.447	1.448

Methylcyclohexane:

T(K)	A1(%)	τ_1 (ps)	χ^2
278.5	100	2317.371	1.116
316.7	100	1995.637	1.117

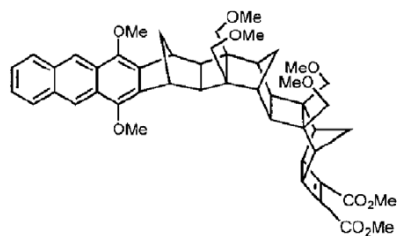
Mesitylene

Temp (K)	Lifetime (ps)
274.45	3008.446
293.15	2360.468
314.85	2116.5
336.45	1921.307
323.15	2675.933
347.05	2591.394
378.85	2349.5
282.85	3154.346

Toluene

Temp (K)	Lifetime (ps)
287.25	4396.628
326.55	3643.304

12.2 Kinetic data for C-Clamp DBA Molecule, A9DCE.



A9DCE:

Chlorobenzene

Temp / K	τ_1 (ps)	A_1 %	τ_2 (ps)
299	243.343	99.71	2359.29
299	244.127	99.866	18401.83
308	236.616	98.86	792.082
319	231.569	98.132	623.473
321	223.015	97.036	540.009
322	224.45	98.001	621.916
322	223.65	95.143	456.181
332	235.266	98.333	636.163
337	232.909	98.945	937.424
337	231.172	98.813	834.364

1,3-dichlorobenzene

Temp / K	τ_1 (ps)	A_1 %	τ_2 (ps)
298	248.5	99.528	2560
308	226.9	99.135	1350
318	215.3	99.232	1250
328	208.7	99.453	1910
338	200.4	99.403	1650

2,5-dichlorotoluene

Temp / K	τ_1 (ps)	A_1 %	τ_2 (ps)
288	397.00	98.54	7810
288	398.00	98.56	7860
288	402.00	98.54	8040
288	386.00	98.63	7740
298	359.00	97.96	8240
298	363.00	98.12	8070
308	343.00	97.27	8560
318	335.00	95.71	9230
318	328.00	95.84	9140
328	325.00	93.47	9960
328	324.00	93.57	10215
338	319.00	90.42	10990
338	321.00	90.324	11170
348	304.00	85.59	12080

3-chlorotoluene

Temp / K	τ_1 (ps)	A_1 %	τ_2 (ps)
298	328.8	99.5	1630
298	316.96	98.539	754.817
308	328.2	99.86	41600
318	322.3	99.84	12300
328	315.2	99.562	3560
338	319	99.5	5270

1,2,4-trimethylbenzene

Temp / K	τ_1 (ps)	A ₁ %	τ_2 (ps)
288	498	92.77	15565
288	468	93.983	15453.12
298	503	87.55	18120
298	503	89.966	20101.18
308	544	83.22	21340
308	481	83.969	19217.57
318	504	72.75	31790
318	555	68.098	28495
328	509	67.44	35230
328	433	65.446	32072.05

1,3-diisopropylbenzene

Temp / K	τ_1 (ps)	A ₁ %	τ_2 (ps)
274	1006.006	83.303	17068.594
276.5	869.081	73.543	11902
277	978.347	81.16	15446.86
283	982.674	75.715	14326.258
283.45	776.776	71.392	17447
290.25	812.27	66.43	17703.783
295	933.201	62.816	28158.031
297.9	822.383	54.096	19805
302.7	875.421	38.143	16383
306	1033.775	49.494	19890.439
308.2	896.388	37.905	15279
312	1072.99	43.453	23727.42
313.6	930.875	33.182	16388
314.35	744.607	41.472	19719.842
315.35	852.449	32.788	19458.783
316.95	820.562	37.987	20567.301
318	1350.832	48.988	19884.559
318	1270.313	31.8	21690.602
318.8	898.802	30.602	17252
320	1452.836	46.666	18834.59
322	1526.891	39.905	19777.971
323.3	977.974	25.668	17611
324	1683.84	23.301	21583.242
326.15	916.701	24.6	20632.057
326.65	810.427	30.487	22343.193
328.9	1201.385	21.35	17770
329	2572.597	22.508	21660.379
332.9	1054.951	18.823	18403

Temp / K	τ_1 (ps)	A ₁ %	τ_2 (ps)
333	4930.293	23.375	21878.088
334.15	1053.055	19.659	18399.811
334.15	866.297	18.332	20784.887
336.65	935.39	19.776	21938.104
338.1	1238.239	15.571	18630
341.55	1308.778	13.589	18009.055
342.55	898.018	14.548	22183.766
343.3	1137.298	13.334	18441
343.85	1039.092	10.186	20934.17
344	17625.646	52.322	25105.463
348.1	1346.987	10.003	17609
356.65	1848.014	8.108	21494.066